THE UNIVERSITY OF WARWICK

Library Declaration and Deposit Agreement

1. **STUDENT DETAILS**

   Tishtrya Ava Mehta
   1763383

2. **THESIS DEPOSIT**

   2.1. I understand that under my registration at the University, I am required to deposit my thesis with the University in BOTH hard copy and in digital format. The digital version should normally be saved as a single pdf file.

   2.2. The hard copy will be housed in the University Library. The digital version will be deposited in the University's Institutional Repository (WRAP). Unless otherwise indicated (see 2.3 below) this will be made openly accessible on the Internet and will be supplied to the British Library to be made available online via its Electronic Theses Online Service (EThOS) service.[At present, theses submitted for a Master's degree by Research (MA, MSc, LLM, MS or MMedSci) are not being deposited in WRAP and not being made available via EthOS. This may change in future.]

   2.3. In exceptional circumstances, the Chair of the Board of Graduate Studies may grant permission for an embargo to be placed on public access to the hard copy thesis for a limited period. It is also possible to apply separately for an embargo on the digital version. (Further information is available in the Guide to Examinations for Higher Degrees by Research.)

   2.4. (a) Hard Copy I hereby deposit a hard copy of my thesis in the University Library to be made publicly available to readers immediately.
   I agree that my thesis may be photocopied.

   (b) Digital Copy I hereby deposit a digital copy of my thesis to be held in WRAP and made available via EThOS.
   My thesis can be made publicly available online.

3. **GRANTING OF NON-EXCLUSIVE RIGHTS**

   Whether I deposit my Work personally or through an assistant or other agent, I agree to the following: Rights granted to the University of Warwick and the British Library and the user of the thesis through this agreement are non-exclusive. I retain all rights in the thesis in its present version or future versions. I agree that the institutional repository administrators and the British Library or their agents may, without changing content, digitise and migrate the thesis to any medium or format for the purpose of future preservation and accessibility.

4. **DECLARATIONS**

4.1. I DECLARE THAT:

- I am the author and owner of the copyright in the thesis and/or I have the authority of the authors and owners of the copyright in the thesis to make this agreement. Reproduction of any part of this thesis for teaching or in academic or other forms of publication is subject to the normal limitations on the use of copyrighted materials and to the proper and full acknowledgement of its source.
- The digital version of the thesis I am supplying is the same version as the final, hardbound copy submitted in completion of my degree, once any minor corrections have been completed.
- I have exercised reasonable care to ensure that the thesis is original, and does not to the best of my knowledge break any UK law or other Intellectual Property Right, or contain any confidential material.
- I understand that, through the medium of the Internet, files will be available to automated agents, and may be searched and copied by, for example, text mining and plagiarism detection software.

4.2. IF I HAVE AGREED (in Section 2 above) TO MAKE MY THESIS PUBLICLY AVAILABLE DIGITALLY, I ALSO DECLARE THAT:

- I grant the University of Warwick and the British Library a licence to make available on the Internet the thesis in digitised format through the Institutional Repository and through the British Library via the EThOS service.
- If my thesis does include any substantial subsidiary material owned by third-party copyright holders, I have sought and obtained permission to include it in any version of my thesis available in digital format and that this permission encompasses the rights that I have granted to the University of Warwick and to the British Library.

5. **LEGAL INFRINGEMENTS**

I understand that neither the University of Warwick nor the British Library have any obligation to take legal action on behalf of myself, or other rights holders, in the event of infringement of intellectual property rights, breach of contract or of any other right, in the thesis.

Please sign this agreement and return it to the Graduate School Office when you submit your thesis.

`Student's signature:` Tishtrya Ava Mehta `Date:` 10/03/2023

A Study of Solar Quasi-Oscillatory Signals

by

Tishtrya Ava Mehta

Thesis

Submitted to The University of Warwick

for the degree of

Doctor of Philosophy in Physics

Department of Physics

December 2022

Contents

List of Tables

List of Figures

Acknowledgments

This thesis is dedicated to my mother, Ava Mehta, who continues to impress me every-day. I'm so grateful for her unwavering support and love, and I know that this work could never have been completed without her. Thank you for always encouraging me to reach for the stars.

I also would like to thank my supervisor, Dr. Anne-Marie Broomhall, who has been an incredible mentor and inspiration to me these past five years. Thank you for being such a brilliant and patient advisor, I feel so lucky to have worked alongside you.

Thank you to all of the people in my life who have filled it with love; Jay- for being my first and favourite teacher, you taught me everything from how to tell the time to trigonometry, and have never stopped guiding me to become better; Gemma- for the late night laughs and the reminders about how much "*I love coding!*"; Olly - for letting me rant to you for hours on end about sunquakes, rats, and embroidery machines, and for always being there when I need you, with a cup of tea and words of support.

To Leanora, Kat, and Will and to all of my other dear friends who have propped me up– thank you for the hundreds of cups of coffee and tea, the puns, the jokes, and the cheering on. To the various members of CFSA, old and new, especially to Dmitrii, Martin, and René, thank you for answering my never-ending list of questions and for the kindness you showed. To Ally Caldecote, thank you for introducing me to the wonderful world of science communication and for helping me build my skills and confidence. Also

thanks must go to Dr. Phil Jemmet, Prof. Margaret Lowe, and the wonderful team at the Warwick Institute of Engagement for their continued help throughout my adventures in outreach.

To instant coffee, Pukka tea, and homemade biscuits, my hot water bottle, ibuprofen, sunshine, walks in the snow, knitting, sewing and Netflix, and to the COVID-19 vaccine, thank you for getting me through the years of long days and late nights. Thank you to the team at St George's Hospital, and to the thousands of vaccine researchers and healthcare workers who worked through the pandemic to enable life to get back on track when things were looking bleak.

I feel so fortunate to have had the opportunity to carry out the research enclosed in this thesis- it really has been a life-changing few years that I will remember with great fondness. I leave you, the reader, with the following quote from the eponymously-named novella by Becky Chambers;
"We step out of our solar system into the universe seeking only peace and friendship, to teach if we are called upon, *to be taught if we are fortunate*"

— Kurt Waldheim, Secretary General of the United Nations, opening audio recording from the Voyager Golden record, launched in 1997

Declarations

This thesis is submitted to the University of Warwick in support of my application for the degree of Doctor of Philosophy in Physics. It has been composed by myself and has not been submitted in any previous application for any degree or other university.

This work presented in this thesis has been completed by the author, excluding the collection and analysis of RHESSI data in Section 7.2 which was performed by Dr. L. Hayes. The relevant sections have been clearly indicated and rewritten in their entirety by the author. The CME catalog used in Chapter 7 was generated and is maintained at the CDAW Data Center by NASA and The Catholic University of America in cooperation with the Naval Research Laboratory. The work given in this thesis is in part based on 4 journal articles (2 published, 1 in the review process, and 1 in prep.):

"Cycle dependence of a quasi-biennial variability in the solar interior".
Monthly Notices of the Royal Astronomical Society, Volume 515, Issue 2, September 2022, Pages 2415–2429
By T. Mehta, K. Jain, S. C. Tripathy, R. Kiefer, D. Kolotkov, A.-M. Broomhall

"Prevalence of non-stationarity in Quasi-Periodic Pulsations associated with M- and X- class solar flares".
Submitted to Monthly Notices of the Royal Astronomical Society, 2023
By T. Mehta, A.-M. Broomhall, L. Hayes

"Reach out, Touch Space!"

Astronomy & Geophysics, Volume 63, Issue 5, October 2022, Pages 5.21-5.23

By T. Mehta, C. McDonald, and B. Nealon

"Evolution of Quasi-Periodic Pulsations in a long duration flare".

(In prep.), Astronomy & Astrophysics, 2023

By L. Hayes and T. Mehta

The work in this thesis has been presented as talks at the following conferences/ workshops: **ISSI TEAM(2022)** "Investigating QPP non stationarity with EMD and the CWT"; **COSPAR (2022)** "A statistical examination of non-stationarity in quasi-periodic pulsations observed on solar flares"; **NAM (2022)** "An investigation into the prevalence of period drift in Quasi-Periodic Pulsations in solar flares over Cycle 24"; **Cool Stars 20.5 (2021)** "Helioseismic investigations of the Quasi-Biennial Oscillation"; **NAM (2021)** "Solar cycle dependency of the Quasi-Biennial Oscillation (QBO)".

This work was supported by the SOLARNET project that has received funding from the European Union's Horizon 2020 research and innovation programme under grant agreement No. 824135. The work also benefited from support from STEM Connections, which was funded by Research England. Some of my work in public engagement was also subsidised by a grant from the Engineering and Physical Sciences Research Council in New and Sustainable Photovoltaics.

A flipbook is visible in the lower corners of this thesis which, when flicked through, traces out the paths taken by p-modes of different harmonic degree. This flipbook was created using a gif found on this here[1], which is maintained by New Mexico State University, supported by National Science Foundation CAREER award and the National Science Foundation under Grant Number 1351311.

[1] `astronomy.nmsu.edu/jasonj/HELIO/outline.html`

Abstract

We observe quasi-oscillatory behaviour frequently in solar data, for example in the quasi-biennial oscillation visible in magnetic activity proxies and quasi-periodic pulsations in flares. These behaviours have to be fully understood in order for our solar models to be complete. We can assess these behaviours using a host of analysis techniques that are capable of tracking the quasi-periodicities inherent in these data. In this thesis we use Empirical Mode Decomposition on helioseismic data to examine the quasi-biennial oscillation and establish that there is a significant risk of spurious detections when used on short duration data. We also use a combination of the Fast Fourier Transform and Wavelet analysis to obtain the prevalence of non-stationarity in quasi-periodic pulsations using GOES data. We find that quasi-periodic behaviours are extremely common in solar data. We determine that the relative amplitude of the quasi-biennial oscillation is correlated with the amplitude of the solar cycle. We obtain evidence of low magnitude non-stationarity in the majority of quasi-periodic pulsations. Finally we conclude that understanding quasi-oscillatory behaviour is essential to form a complete understanding of the Sun, its dynamo, its magnetic field, and all associated behaviours.

Abbreviations

AIA	Atmospheric Imaging Assembly.
BiSON	Birmingham Solar Oscillations Network.
CME	Coronal Mass Ejection.
CoRoT	Convection, Rotation and planetary Transits.
CWT	Continuous Wavelet Transform.
DRAO	Dominion Radio Astrophysical Observatory.
EMD	Empirical Mode Decomposition.
ESA	European Space Agency.
EUV	Extreme Ultraviolet.
FFT	Fast Fourier Transform.
FWHM	Full Width Half Maximum.
FWHM	Full Width Half Maximum.
GOES	Geostationary Operational Environmental Satellite.
GONG	Global Oscillation Network Group.
GWS	Global Wavelet Spectrum.
GWT	Global Wavelet Transform.
HMI	Helioseismic and Magnetic Imager.
HXR	Hard X-ray.
IATL	Institute for Advanced Teaching and Learning.
IDL	Interactive Data Language.
IMFs	Intrinsic Mode Functions.
LMSAL	Lockheed Martin Solar and Astrophysics Laboratory.
NASA	National Aeronautics and Space Administration.

NCCPE	National Co-ordinating Centre for Public Engagement.
NOAA	National Oceanic and Atmospheric Administration.
QBO	Quasi-Biennial Oscillation.
RFU	Radio Flux Units.
RHESSI	*Reuven Ramaty High Energy Solar Spectroscopic Imager*.
SDO	Solar Dynamics Observatory.
SOHO	Solar and Heliospheric Observatory.
SSN	Sunspot Number.
STFC	Science and Technology Facilities Council.
SXR	Soft X-ray.
UT	Universal Time.
XRS	X-ray sensor.

Symbols

P	Pressure.
S_ℓ^2	Lamb Frequency for a given ℓ.
Γ_1	Adiabatic index.
Φ	Gravitational potential.
α	Colour of noise.
ℓ	Harmonic degree.
$\epsilon_{n,\ell}^{-1}$	Inverse fractional mode inertia.
ω	Oscillation frequency.
ρ	Density.
σ	Standard error.
ξ	Displacement.
c	Sound speed.
m	Azimuthal degree.
n	Radial order.
r	Radius or distance.
D	Duration.
$\mathrm{E}_{n,\ell}$	Normalised mode inertia.
G	Gravitational constant.
H_p	Pressure scale height.
Hz	Hertz.
$\mathrm{M}_\odot$	Solar mass.
N^2	Brunt-Väisälä or buoyancy frequency.
$\mathrm{Q}_{n,\ell}$	Inertia ratio.
$\mathrm{R}_\odot$	Solar radius.
Y_ℓ^m	Laplace's spherical harmonics for a given ℓ, m.

Chapter 1

Introduction

In this chapter, I present an introduction to our closest star, the Sun. I describe its basic properties, some interesting features, and its general behaviour. Section 1.1.5 describes the different layers of the Sun and I introduce behaviours such as the Solar cycle, flares, and coronal mass ejections in Sections 1.1.7, 1.1.9 and 1.1.5 respectively. Finally, I outline two phenomenon that are discussed at length in this thesis; the Quasi-biennial Oscillation (Section 1.3) and Quasi-periodic pulsations (Section 1.4). This chapter closes with an overview of the structure of this thesis in Section 1.5

1.1 Overview on our Sun

1.1.1 Solar scale and composition

The Sun, seen in Fig. 1.1, is a magnetically active yellow dwarf, classed as a G2V star. It is 4.6 billion years old and is in its main sequence. To an Earthly observer 1 AU away, the Sun's diameter is 30 arc minutes in the daytime sky, although the true scale of the star is difficult to comprehend. The solar equatorial radius ($R_\odot$) is 6.96 $\times 10^8$ m – the equivalent of almost 55 Earths lined up next to one another. The Sun's sheer size implies a considerable mass. Indeed the Sun makes up 99.86% of the solar system by mass [Woolfson, 2000]. Hydrogen makes up 73% of the Sun by mass, with helium responsible for a further 25%, with the remainder consisting of small amounts of heavier elements such as carbon and oxygen (produced by the CNO cycle, see Section 1.1.5) and trace amounts of iron and heavy elements [Basu & Antia, 2008]. The Sun is made of a plasma, allowing it to exhibit fluid-like properties at extreme temperatures. It also hosts a magnetic field (discussed in Section 1.1.7), which flips the location of its North and South poles every 11 yrs approximately, forming a ∼22 yr cycle.

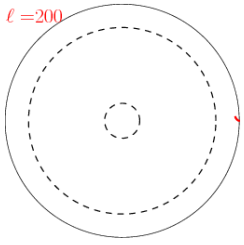

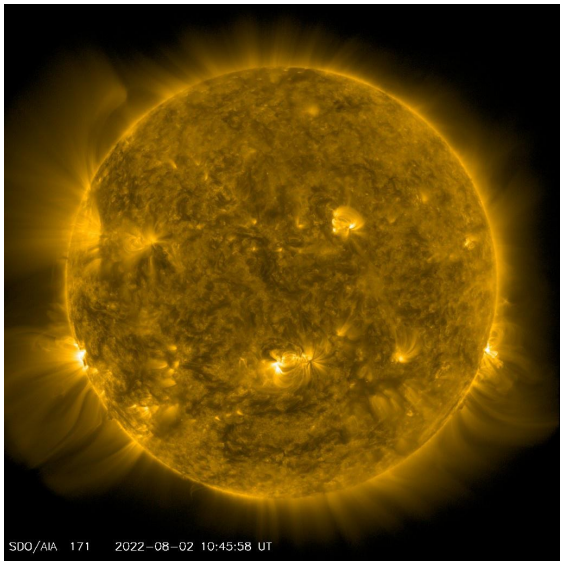

Figure 1.1: An image of the Sun captured by the Atmospheric Imaging Assembly (AIA) in the 171 Å band on 02/08/2022. This waveband allows us to see the Sun's upper transition region/ corona.

1.1.2 Temperature and luminosity

The temperature at the photosphere (commonly referred to as the solar 'surface'– see Section 1.1.5) can be approximated by Weins Law to be 5800 K, with models suggesting the temperature of the core rises to 15.7 $\times 10^6$ K [Phillips, 1995]. The luminosity of the Sun is 3.828×10^{26} W (or equivalently 3.75×10^{28} lm), which we define as 1 Solar Luminosity (1 $L_\odot$).

1.1.3 Differential rotation

A reader may note that we earlier quoted the *equatorial* radius rather than simply a radius. This is because the Sun is not a perfect sphere but instead is slightly flattened at the poles, and spreads at the equator. This is due to the fact that the Sun spins upon its axis, and due to the fluid properties of a plasma, the Sun spins with different speeds as a function of latitude, causing some flattening. The Sun takes 25.6 d at the equator to complete a full rotation and 33.5 d at the poles. We call this phenomenon differential rotation. Observing this motion from Earth, we see the Sun's apparent rotational period is between 27 – 28 days. Fig. 1.2 shows differential rotation at the surface where lower latitudes (0-15 °) show a much higher rotation rate than higher latitudes. As the solar radius decreases and we move towards the deeper layers of the Sun, we see the rotation

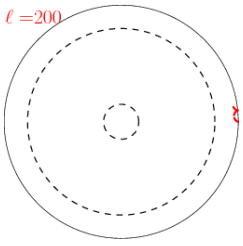

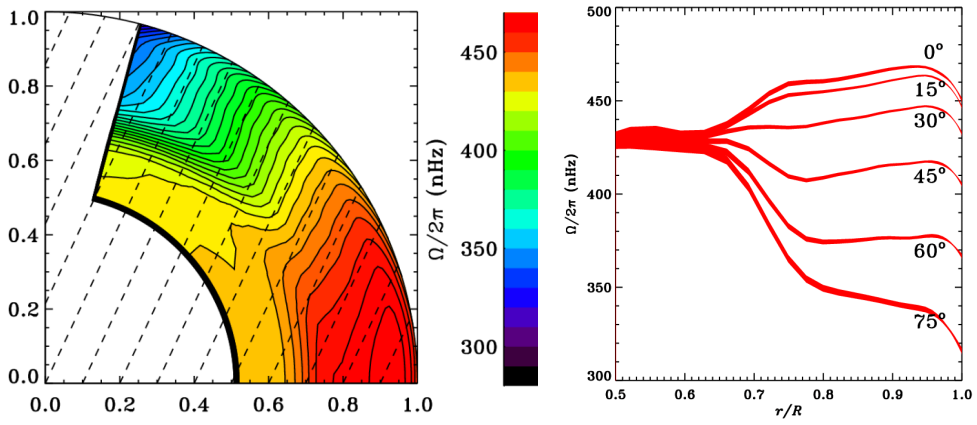

(a) (b)

Figure 1.2: *Left*: Average rotation profile obtained using GONG data using a cut through of the Sun. Note how the rotation rates tend to solid body rotation at lower radii. Solid black lines show contours of constant rotation. Originally published in [Howe et al., 2005]. *Right*: Rotation Rates as a function of solar radius for constant latitudes. Note again the solid body rotation emerging around $0.65\,R_\odot$. Originally published in [Howe et al., 2000].

rates all tend towards similar magnitudes, which indicates solid body rotation at the base of the convection zone. These results were obtained through helioseismic techniques that are discussed at length in Chapter 2.

1.1.4 Why we care about the Sun

Throughout history, the Sun has been the subject of great interest to humankind. Through myths, legends, and rudimentary observations we can observe the field of solar research evolve into what it is today. Our understanding of what the Sun is has gone through many iterations– ancient Egyptians were known to worship a Sun-God named Ra who was said to carry the Sun on his headdress. Anaxagoras, a ancient Greek philosopher from 400 BC was one of the first western astronomers to reason that the Sun was made of materials familiar to us rather than from supernatural origins (he reasoned the Sun was made from fiery rock or metal [Russell, 1961]). In more modern times during the Han Dynasty around 200 BC Chinese astronomers made records of sunspots. Fig. 1.3 shows observations of sunspot migration over several days, taken by Christoph Scheiner, a German astronomer in his publication "Rosa Ursina sive Sol". In modern times, our fascination with the Sun continues because it allows for an unparalleled opportunity to observe a star at such small distances and therefore at remarkably high resolution. The

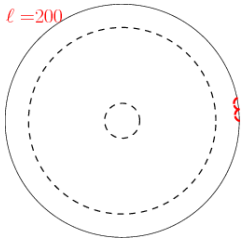

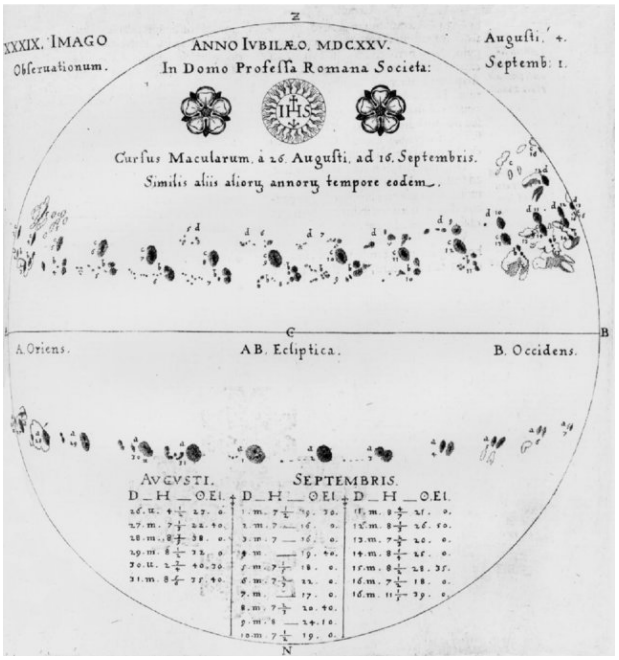

Figure 1.3: Observations from 1625 of Sunspots travelling across the solar disk, taken from Willis et al. [2005]. Originally from Scheiner [1630]

.

Sun is uniquely placed in our universe in that we can access spatially resolved data with incredibly precision. As the brightest object in our sky by far, by virtue of its close proximity (at an average of 1 AU away, $\approx$ 150 million kilometres) we have the ability to gain extremely precise data– something exceedingly difficult for other stars. By learning about our Sun, we can understand the mechanisms governing stars in galaxies we will never be able to visit. Studying the Sun teaches us about our place in the universe.

1.1.5 The layers of the Sun

We commonly divide the Sun into distinct layers, the core, the radiative zone, tacholine, the convection zone, photosphere, chromosphere and corona, all discussed here. We omit discussions of the transition region and a multitude of fascinating features on the Sun such as nanoflares, prominences, steamers, and faculae to name a few, as although they are highly interesting, they are beyond the scope of the work discussed in this thesis.

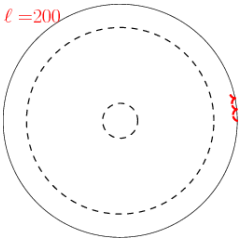

Core

The solar core is where the energy of the Sun is produced. This region, extending from the centre of the Sun to ∼0.25 $R_\odot$ is where nuclear fusion takes place. This mainly consists of the fusion of hydrogen to helium via the proton-proton chain reaction (Eqn. 1.1), producing the vast majority of the Sun's energetic output. The remaining energy is supplied via the CNO cycle, in which helium is still produced, where carbon, nitrogen and oxygen are used as catalysts for the reaction.

$$4H^+ + 2e^- \longrightarrow He^{2+} + 2\nu_e \tag{1.1}$$

The above reaction shows the proton-proton chain reaction, where four hydrogen ions and two electrons are converted into a helium ion, plus two electron neutrinos and excess energy. The core is believed to be 15 million ° K at its centre, dropping considerably to about half this amount at the boundary between the core and the radiative zone where gravity is no longer sufficiently strong to overcome the repulsive coulomb force between atoms and allow fusion to occur [Severino, 2017].

Radiative Layer

The radiative zone extends from 0.25-0.71 $R_\odot$ and in this region energy is transported by radiative diffusion and conduction. This is an extremely slow process as solar photons are emitted and reabsorbed after only a small distance. A photon may be emitted by the core, absorbed by a neighbouring atom, re-emitted and so on for thousands of years before by chance emerging in the regions of the Sun that are less dense and 'escaping' the depths of the solar interior. For a gamma ray, this process may take close to 200,000 yrs.

Tachocline

The tachocline is the region which forms the boundary wherein the Sun goes from solid body rotation to differential rotation, as discussed in Section 1.1.1. The tachocline is remarkably thin and its exact width is difficult to discern as it appears to be close to the inversion resolution at its depth [See Howe, 2009, and references therein for a full discussion on the width and location of the tachocline]. However, estimates by Christensen-Dalsgaard et al. [1991] have been confirmed by Basu & Antia [1997] and accepted since, put the position of the base of the convection zone at 0.713 $R_\odot$. An average of estimates (collated in Table 2. of Howe [2009]) suggest the tachocline width

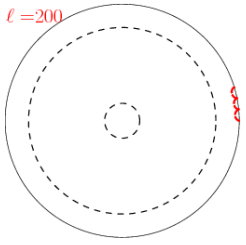

to be $0.05\,R_\odot$. Therefore the tachocline is a region of high shear and so it thought to essential to the generation of the solar magnetic field by means of a solar dynamo.

Convection Layer

Atop the tachocline lies the convection zone, wherein the dominant form of energy transfer is convection. This generates convection currents in the solar interior, where material heats up and becomes buoyant compared to the surrounding solar material. The rising material may have frozen in magnetic flux and 'drag' up flux tubes, causing field lines to erupt at the surface (See Section 1.1.9). The heated material rises, expands, and cools, causing it to sink back toward the tachocline. In massive stars, the majority of a stars' volume is its convection zone, but for the Sun it's close to thirty percent. The density in the convection zone drops significantly towards the photosphere (see Section 1.1.5). This causes the local sound speed to be greater in denser regions (further in the interior) which has significant implications for p-modes (see Section 2.1.2).

Photosphere and Chromosphere

The photosphere is commonly referred to as the solar 'surface' – as misnomer as the photosphere does not delineate a specific surface per se, but is the region of the Sun that becomes optically thick. Because of this we observe many 'surface features' on the region; here we focus on sunspots, active regions, and granulation.

Sunspots appear dark in photometric observations; this is due to the fact that regions that correspond to high magnetic field strengths and this strong magnetic flux inhibits convection. The prevalence of sunspots is directly proportional to the amount of magnetic activity going on in the Sun, and is therefore modulated by the solar cycle (See Section 1.1.7).

Active regions on the Sun are often referred to as 'AR's and are temporary regions wherein the localised magnetic field is strong, and usually complex. As magnetic fields inhibit convection, these regions are cooler than their surroundings and so can usually, but not exclusively, be located by a clustering of sunspots, which are regions that appear relatively dark compared to surrounding areas in spatial observations. Because of their origins in strong magnetic fields, active regions are often associated with phenomenon such as flares and sunspots. Active Regions are more commonly observed towards solar maxima. At the start of solar cycles active regions are more commonly observed at higher latitudes, slowly migrating towards the equator towards solar maxima. This behaviour results in the characteristic 'Butterfly diagram' shown in Fig. 1.4. Active regions are

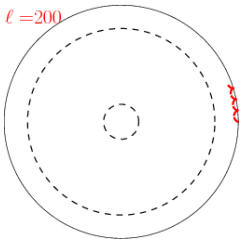

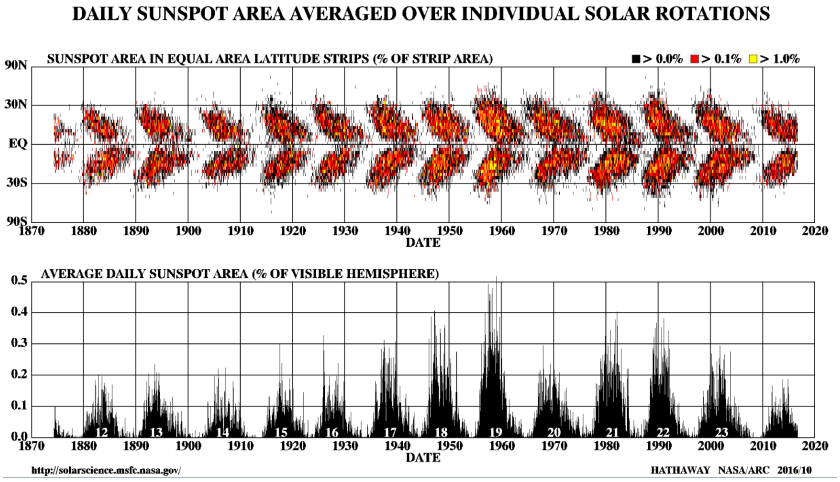

Figure 1.4: (*Top*): Sunspot area with their corresponding latitudes from 1870 – 2016, forming the characteristic butterfly-wing pattern. (*Bottom*): Average Sunspot area, which can be used for a proxy for solar activity, from 1870 – 2016. Data and Figure from NASA, `https://solarscience.msfc.nasa.gov/images/bfly.gif`

.

classed by NOAA with a label of AR***. and usually exist for durations shorter than one Carrington rotation (equivalent to 27.28 d, corresponding to a full solar prograde rotation relative to a latitude of $\pm 26^\circ$ which is the typical sunspot latitude), although some long lasting ARs have been seen to exist for >3 Carrington rotations [Pugh et al., 2017b].

The convection currents generated in the convection zone of the Sun give rise to small scale granulation cells on the photosphere; small regions where the heated material glows, surrounded by a thin shell of cooler material, resembling granules. These granules are short lived (usually only lasting tens of minutes), small in scale (where small is a relative term as they're on the scale of thousands of km) and constantly cover the entire solar surface. Supergranules have also been observed, which last for up to 24 hrs and are on the order of tens of thousands of km in diameters. We observe the effects of granulation in helioseismic data as discussed in Chapter 2.

The chromosphere extends up to 3000–5000 km above the photosphere. Within this region we see the phenomenon of spicules– thin tendril jets of plasma that move with speeds up to 100km/h and last for several minutes. It has been proposed that spicules may be partially responsible for transferring energy into the corona, contributing to the coronal heating problem, discussed below.

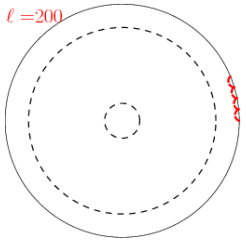

Corona

The corona is the outermost layer of the solar atmosphere, extending millions of kilometres above the photosphere. The corona is made visible during solar eclipses where the solar disk is obscured by the Moon, giving rise to beautiful diamond ring-like formations. The corona is probably most famed for the well studied, but currently unresolved coronal heating problem. The corona has been measured to be 10^6 K– far hotter than predicted temperatures. In fact this temperature is higher than in the chromosphere which is counter intuitively closer to the core of the Sun but has temperatures on the order of 10^4 K [Molnar et al., 2019]. The physics behind this strange seeming disobedience of thermodynamics has not been solved, though most theories suggest transfer of energy into the corona via e.g. MHD waves, spicules [E.g. see Sokolov et al., 2013; Van Doorsselaere et al., 2016; Bate et al., 2022, and references therein]. None have been confirmed as of yet, and the corona remains hot.

A Coronal Mass Ejection (CME) is the rapid release of plasma from a solar or stellar corona, usually into interplanetary space. CMEs typically travel at significant speed, with an embedded magnetic field caused by the ejected proton, electrons and alpha particles. CMEs are often observed by AIA and LASCO (See Chapter 3) and appear as vast structures, usually visible for a number of hours. Most CMEs originate from active regions that have especially complex magnetic fields, such that the destabilisation event is sufficiently energetic to cause such a dramatic phenomenon. It follows that CMEs are more commonly observed towards solar maximum. CMEs may strike the Earth if correctly aligned. This can result in power failures and increased radiation as the Solar Energetic Particles (SEP) interact with the Earths magnetosphere.

Solar wind and space weather

The Sun continually loses mass via the solar wind– a stream of outgoing plasma mainly consisting of electrons, protons and alpha particles, reaching speeds of 250–750 kms^{-1} after only a few solar radii. Collisions between the solar wind and the Earth create space weather where the electromagnetically charged particles from the solar wind (and other interstellar events) interact with the Earth's magnetic field. Among other effects, this may short electronics on orbiting satellites, expose people in flight to high doses of radiation, and cause the northern and southern aurora. Most significantly for human life, satellite shortages may occur and space weather can cause significant radio blackouts, such as the Quebec blackout of 1989[1]. The impact of a significant space weather event

[1] `www.nasa.gov/topics/earth/features/sun_darkness.html`

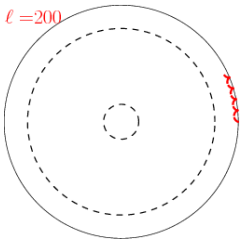

today would be so devastating that the UK government has a 'Severe space weather preparedness strategy' in place to mitigate such events (the policy paper can be read here[2]). Additionally the Meteorological Office, usually abbreviated as the Met Office, continually monitors the Sun in case of such events so that satellites on which we rely, e.g. for GPS and communications, can be warned to minimise solar storm damage. Space weather of course expands beyond the Earth and the solar wind similarly interacts with planets further out, and is for example the cause of the magnificent aurora seen on Jupiter and Saturn.

1.1.6 The life-cycle of Sun

The Sun remains in hydrostatic equilibrium, where the outward pressure caused by hydrogen fusing in the core is matched by the inward pressure due to gravity. This keeps the Sun in a near spherical shape and provides an environment where fusion can continue to take place. The Sun is stable, being half way through it's 'life cycle'. Current models predict that it has another 4-5 billion years of hydrogen in its core to continue fusing, until it reaches a stage known as hydrogen core collapse. At this stage the solar core will contract, temporarily increasing the Sun's luminosity. This gravitational contraction will lead to an increase in hydrogen fusion in a shell surrounding the core, accompanied by an expansion of the star into a sub-giant, and then into a red giant. The luminosity of the Sun will increase by a factor of 1000 at this stage and the Sun will expand in volume until its radius is 0.75 AU (1.1×10^{11} m), likely engulfing the orbits of Mercury and Venus [Boothroyd & Sackmann, 1999]. This Red-Giant-Branch phase (also known as a RGB phase) will last a further 1 billion years in which the Sun will lose a third of its mass. Following this phase the Sun will become increasingly unstable and continue to rapidly lose mass, before the Sun loses its outer envelope which produces a planetary nebula. Finally the core of the Sun, containing about half of the Sun's current day mass, will exist as a white dwarf star which will continue to cool and lose energy via radiative losses until it becomes a black dwarf [Schröder & Connon Smith, 2008].

1.1.7 Solar cycles

The activity of the Sun exists in a cycle of approximately 11 years, which can be seen in sunspot area in the lower panel of Fig. 1.4. This is visible in the strength of the magnetic field, and therefore the number of sunspots, and a number of solar activity proxies, such

[2] ww.gov.uk/government/publications/uk-severe-space-weather-preparedness-strategy

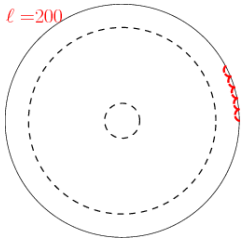

as the $F_{10.7cm}$ radio flux index. We denote solar maxima to be duration when solar activity reaches its greatest amplitude in a given cycle, and denote solar minima the duration corresponding to lowest activity in the cycle. It's important to note that solar minima does not imply that CMEs or flares are impossible, just less likely. The 11 year cycle, often also called the Schwabe cycle after Samuel Heinrich Schwabe, is quasi-oscillatory as the exact period between subsequent minima varies between cycles, with some solar cycles being as short as 9 yrs (Solar Cycle 2), and some extending to almost 13 yrs (Solar Cycle 6). Additionally the duration of a solar cycle has some dependencies on which activity proxy one examines, as the minimal values in each proxy may not necessarily be co-temporal. In the solar physics community the $F_{10.7cm}$ flux is commonly used to characterise the start and end times of solar minima and maxima. Solar cycles have been observed as far back as the late 1700s where astronomer Christian Horrebow observed a 12 year cycle of sunspots. Other scientists, such Rudolf Wolf, built on these ideas and began the solar cycle numbering system that is still used today [Jørgensen et al., 2019]. The solar cycle from 1755–1766 was labelled solar cycle '1', and we have continued labelling solar cycles in this way, with the most recent solar cycle, Solar Cycle 24, finishing in late 2019[3]. Solar cycles also vary in magnitude, with some cycles exhibiting far fewer sunspots and smaller maximal activity proxy amplitudes than others. For example, the Maunder minimum (from 1645–1715) had an exceedingly low number of observed sunspots. This contrasts with the Modern Maxima which occurred from 1933–2008, where relatively high levels of solar activity were observed in Solar Cycles 15–23. Current prediction estimate the solar maximum of Cycle 25 will be in 2026. The magnetic polarity of the Sun swaps between subsequent 11-year cycles meaning it's more accurate to characterise the solar cycle as an approximately 22 year process, but we tend to use the phrase "the solar cycle" to refer to only one of these 11 year oscillations. The 11 year cycle can be clearly seen in a butterfly diagram (Fig. 1.4), where the sunspots initially emerge towards to poles, and grow in density over the years, migrating to the equatorial region. The 11 year cycle is accompanied the quasi-biennial oscillation, an oscillation with a period between 0.5–4 yrs observed in a number of solar activity proxies.

1.1.8 The solar dynamo

The solar dynamo is thought to drive the Sun's magnetic field, converting the kinetic energy from the motion of the solar interior, which is an electrically conductive plasma, into electromagnetic energy. The resulting magnetic field is responsible for the 11 yr cy-

[3] www.weather.gov/news/201509-solar-cycle

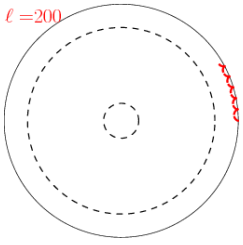

cles seen in solar activity proxies, and all associated dynamic behaviours. There are two large-scale flows in the solar interior that are thought to be essential to the cyclic generation of the Sun's magnetic field; the rotation throughout the interior (Section 1.1.3), and meridional circulation in the upper solar convective layer [Howe, 2009]. The exact mechanism that drives the solar dynamo is not yet fully understood. We cannot directly observe the solar dynamo, only the effects of the magnetic field it generates. Therefore we may turn to observational data of e.g. sunspots and other magnetic features, and backwards engineer the dynamo models that could produce a given phenomenon. The magnetic field of the Sun is complex, resulting in not only the Schwabe cycle (Section 1.1.7) but also smaller oscillations such as the quasi-biennial oscillation (Section 1.3). Therefore the dynamo models that we create must be able to replicate the multitude of the complex observational features we see.

Many solar (and stellar) dynamo mechanisms have been proposed over the past 100 years, but as of yet none have been definitely proven [see Charbonneau, 2020, for a review on the solar dynamo and recent advances in dynamo modelling]. In fact, some of the leading dynamo models of the time were discounted in the 1970s following findings by helioseismic techniques which led to constraints on the solar internal structure [Schou et al., 1998]. Most of the proposed dynamo mechanisms are complex and beyond the scope of this thesis. Here I summarise one of the most prominent models that have been put forwards; the Babcock-Leighton flux transport dynamo mechanism [see Dikpati & Charbonneau, 1999, for an overview on the Babcock-Leighton mechanism]. The Babcock-Leighton dynamo mechanism, first proposed in Babcock [1961] and further built on in Leighton [1964, 1969], relies on the principles of "Joy's law" which describes how a toroidal internal magnetic field can convert a fraction of its flux into a poloidal field. When this effect is paired with significant shear due to differential rotation, the result can be a self sustaining dynamo loop. This model is able to accurately reproduce the 'Butterfly diagram' showing the migration of sunspots towards the equator (first seen in Fig. 1.4), reproduced in Fig. 1.5 using a Babcock-Leighton solar dynamo model simulation. I refer keen readers to Charbonneau [2020] and references therein for further detail on other dynamo generation mechanisms e.g. mean field dynamos. A full understanding of the solar dynamo would represent a monumental step forward in our ability to predict solar behaviour which could allow for better preparation against harmful space weather events (Section 1.1.5). Ultimately, more research is needed to determine which of these mechanisms, or which combination of mechanisms, is responsible for the Sun's magnetic field. By examining the observational properties of large scale behaviours that are produced by the solar magnetic field, e.g. the latitude or depth at

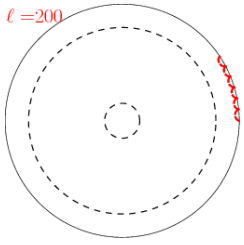

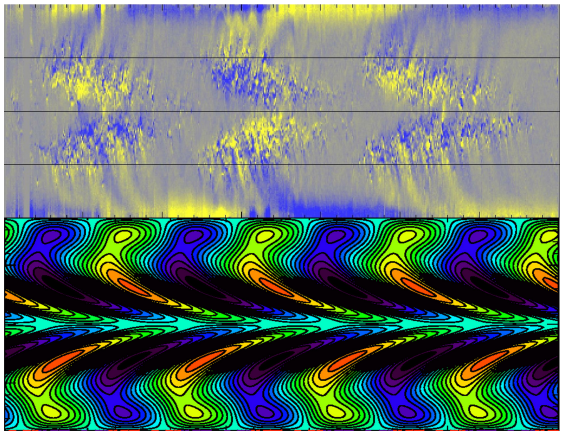

Figure 1.5: (*Top*): Butterfly diagram of magnetic polarities shown in yellow and blue, showing the migration of sunspots towards the solar equator over three cycles, which is similar to the Top panel of Fig. 1.4 (*Bottom*): Butterfly diagram obtained by a Babcock-Leighton solar dynamo model simulation. Figure taken from *Science of European Space Telescope (EST) article* written by Bernadett Beluczest-east.eu/?option=com_content&view=article&id=883&lang=en&Itemid=622

.

which the quasi-biennial oscillation exists in the solar interior, we can constrain solar dynamo models leading to a better understanding of large scale solar dynamics.

1.1.9 Solar and stellar flares

Solar flare

Solar flares are a phenomenon driven by magnetic reconnection and can be characterised by a rapid and localised energy release from an active region on the Sun. The intensity of the electromagnetic radiation produced increases rapidly, in what we call the impulsive phase of the flare, and then after reaching its maximum value gradually falls back down to its pre-eruptive level in what is known as the decay phase. Flares can also be observed on other stars, where they're known as stellar flares. We may classify the amplitude of solar flares by examining the peak X-ray flux observed in the 1–8 Å channel by the X-ray sensor (XRS) instrument on board the GOES-15 satellite measured in Wm^{-2} (See Section 3.8). The flares may then be classified as an X-, M-, C-, B-, or A-class flare with X-class flares being the most energetic (see Table 1.1). A flare is further categorised by a unit between 1 and 9 which indicates its strength within its class (aside for the X-class flares which continues in numbering past 9). The classifications are logarithmic, with a M7 class flare being 10 times more energetic than a C7 class flare. For highly energetic

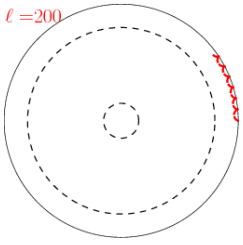

events, such as X- or M-class flares, the impact on Earth can be significant. X-class flares are the most powerful of solar phenomena and can trigger events such as radio blackouts, when the charged particles emitted by the flare are transported as part of solar wind and interact with the Earth's ionosphere. Among the highest classified flares in history is an event that took place on November 4^{th} 2003 which was recorded to have a peak flare emission of 4.0 mW/m^2, putting it in the region of an X40 classification [Brodrick et al., 2005]. Less energetic Earth-directed M-class flares may cause the Northern and Southern lights to increase in intensity as emitted charged particles follow the Earth's magnetic field lines to the North and South poles, where they ionise and excite the atmosphere, causing it to emit in the visible spectrum as aurorae. C-class flares have few noticeable effects on Earth and B- and A-class flares are better known as microflares and are often taken to be the background flux behind more powerful solar phenomena.

GOES Class	**Peak flux (Wm^{-2})**
A	$< 10^{-7}$
B	$10^{-7} - 10^{-6}$
C	$10^{-6} - 10^{-5}$
M	$10^{-5} - 10^{-4}$
X	$> 10^{-4}$

Table 1.1: GOES flare classification

Although the exact mechanisms driving solar flares are still not fully understood the 'standard flare model' is a good approximate model for flare behaviour. Also called the 'CSHKP model' [Carmichael, 1964; Sturrock, 1966; Hirayama, 1974; Kopp & Pneuman, 1976], the standard model attributes the rapid expulsion of magnetic energy emitted during a flare to magnetic reconnection occurring between neighbouring field fluxes. The model suggests that following reconnection at an 'X-point' or null point, charged particles follow the field lines to the foot points where hard X-ray (HXR) emission is generated. This rapid emission of HXR can be used as a tool for spotting reconnection events.

Stellar flare

Flares are not an exclusively solar phenomenon. Indeed white light stellar flares have long since been observed, e.g. in the Carrington event [also see Lacy et al., 1976], and recent advances in ground based surveys have led to the creation of NGTS (Next Generation Transit Survey) from which many stellar flares have been observed across a great range of spectral classes [e.g. Jackman et al., 2021]. Stellar flares must be

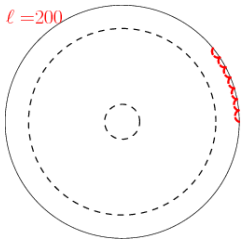

accounted for in exoplanet observations by telescopes such as NASA's Kepler, where the appearance of a stellar flare greatly impacts the success of an exoplanet detection. Kepler has been responsible for the detection of 'superflares' which have energies up to 10^4 times greater than those observed on the Sun [Maehara et al., 2012], and was also used for the successful detections of quasi-periodic pulsations on stellar flares [e.g. Pugh et al., 2017a].

1.2 What are quasi-periodic oscillations

Quasi-periodic oscillations (QPOs) are signals which exhibit a change in their instantaneous period over time. QPOs often have bursty profiles, which can for example be seen in human heartbeats, which have multiple timescales present. We can observe QPOs in climate science e.g. the El Niño– Southern Oscillation is a climate phenomenon which causes non-periodic variations in the surface temperature of the sea and the directions and magnitudes of the accompanying winds around the tropical Eastern Pacific Ocean. Quasi-periodic oscillations can be difficult to characterise for a number of reasons. There is the inherent difficulty in terminology– what differentiates a trend, or two subsequent bursts of emission, to a QPO? The consensus is that at least three approximately consecutive bursts or oscillations are required for a phenomenon to be considered quasi periodic, with roughly similar periodicities. Again these terminologies are up for debate and ultimately arbitrary. For the purpose of this work we use quasi-oscillatory or quasi-periodic to mean at least three consecutive full cycles with periods of similar frequencies. These may originate from two (or more) regimes, each producing an independent time scale, or from a singular regime which causes a change in timescale over time or from something entirely different. We also may refer to QPOs as non-stationary signals and use the terms interchangeably, although a strict mathematical definition differentiates these two terms.

1.3 The Quasi-Biennial Oscillation

1.3.1 Introduction to the QBO

In addition to the largely periodic Schwabe cycle discussed in Section 1.1.7, there is evidence of an oscillation of a shorter time scale similarly observed in solar activity proxies. This is known as the quasi-biennial oscillation (QBO) and has a poorly defined period with observed periods ranging from $\leq$1yr to $\sim$6yrs and a varying amplitude modulated

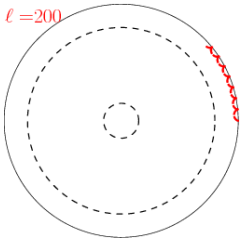

by the Schwabe cycle. The QBO can occasionally be seen as a double peak in solar activity proxies at solar maximum. QBO observations have been reported in a number of indices of solar origin such as the $F_{10.7cm}$ flux, and has also been seen in the interplanetary magnetic field, solar energetic particles and other sources [see Bazilevskaya et al., 2014, and references therein for a full review on observational aspects of the QBO]. Evidence of QBO-like signals have been seen in solar rotational rate residuals at near-surface depths [Inceoglu et al., 2021] and Broomhall [2017] showed that the amplitude of the QBO is highly correlated with sunspot number (SSN) and that the relative amplitude of the QBO to the 11-year cycle is constant across various activity proxies. The process generating the QBO is still not well understood. The QBO has previously been observed in helioseismic data. Both Tripathy et al. [2012] and Simoniello et al. [2013] examined intermediate degree modes using GONG data over Cycle 23 using wavelet analysis and found evidence of oscillations in frequency shifts with a period of approximately 2 yrs. Broomhall et al. [2012] examined the QBO using low degree modes from Sun-as-a-star observations and showed a weak dependence of the QBO amplitude on mode frequency. We explore the presence of the QBO in helioseismic data further in Chapters 2 and 6.

Several mechanisms have been proposed, and it is hoped through the use of modelling [see Inceoglu et al., 2019, and references therein for a summary of suggested generation mechanisms] and observational data we may be able to better constrain the cause of the QBO. These mechanisms include include flip-flop cycles (a complete shifts of the active longitudes on the Sun) [Berdyugina & Usoskin, 2003], unstable magnetic Rossby waves in the tachocline [Zaqarashvili et al., 2010], non-linear tachocline oscillations [Dikpati et al., 2018], secondary dynamos in the solar surface layer [Fletcher et al., 2010]. To date no single mechanism have been confirmed as we have insufficient data, but through helioseismic investigation of the location of QBO we may be better placed to understand the subsurface magnetic field and therefore the QBO that's being created.

1.3.2 Motivation for investigating the QBO

A better understanding of the QBO has wide-reaching impact, for example, the solar wind is in part accelerated and driven by the solar magnetic field and affects us through its interactions with satellites, our energy grid, etc. Due to our incomplete understanding of the generation of the solar magnetic field, we are unable to fully predict its behaviour. By determining where and how the QBO is being generated we can refine our models of the solar magnetic field which will enable us to gain a fuller picture of the magnetic behaviour of our Sun and work towards mitigating some of the solar wind associated

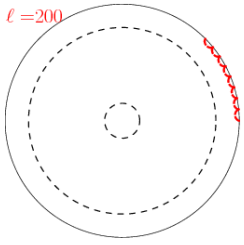

risks. The impacts of QBO research extend beyond our own solar system as there have also been observations of oscillations with mid-cycle periodicities on other fast-rotating stars [see Fig. 1 in Böhm-Vitense, 2007], and in some star systems multiple periodicities are thought to have been seen. It is likely the phenomena responsible for these mid-cycle oscillations is similar to that governing the QBO and so the study of our Sun's QBO should lead to a better understanding of other solar-like star systems.

1.3.3 Difficulties in finding the QBO

The QBO is by definition quasi-periodic and therefore we expect to see a period drift in its profile, where we use the term period drift to imply a change in the instantaneous period of the signal. This makes it poorly suited to Fourier-based or periodogram analysis techniques which anticipate a stationary sinusoidal input. Techniques which do not restrict the input to be strictly sinusoidal, e.g. wavelet analysis, have been previously applied to investigations involving the QBO, see Simoniello et al. [2012]. However, the accuracy of wavelet analysis struggles in noisy conditions and so it may not be well suited for identifying quasi-periodic oscillations in the presence of both white and coloured noise which we see in solar data. Therefore we turn to a data analysis technique which is well suited to handling non-stationary data– the Empirical Mode Decomposition (EMD), which is fully described in Chapter 4. By using a method suited to non-stationary data, we are in a better position to not only detect, but assess the behaviours within the QBO. Ensemble Empirical Mode Decomposition (EEMD), a technique similar to EMD, has previously been applied to low degree modes [see Kolotkov et al., 2015] where the data were obtained from the Birmingham Solar Oscillations Network [BiSON; Chaplin et al., 1996; Hale et al., 2016]. EMD has also been applied to cosmic ray intensity data wherein oscillations with periods in the QBO range were identified [Vecchio et al., 2012], and on rotation rate residuals in Cycles 23 and 24 to investigate the presence of QBO-like signals [Inceoglu et al., 2021].

1.4 Quasi-Periodic Pulsations

1.4.1 Introduction to QPPs

Quasi-periodic pulsations (QPPs) are variations in intensity in the emission of solar or stellar flares. These QPPs are associated with energy release and particle acceleration and usually show three or more bursts with roughly similar periodicities over the duration of the flare [Nakariakov & Melnikov, 2009; Kupriyanova et al., 2020]. Solar QPPs

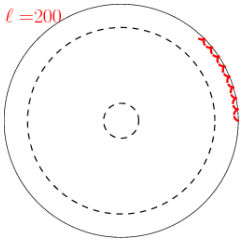

are a multi-wavelength phenomenon, identified in hard X-ray (HXR) emission through to microwave emission, and have been seen in the chromosphere and in interplanetary space [Clarke et al., 2021; Li et al., 2015]. Stellar QPPs have also been extensively observed, (e.g. Zhilyaev et al. [2000], Broomhall et al. [2019], Pugh et al. [2016]), and in some cases have been seen to be multi-wavelength [Kolotkov et al., 2021]. We have observed QPPs with average periods <1 s although solar QPPs are more commonly seen to have periods in of several to tens of seconds. Stellar QPPs have been reported with periods of up to tens of minutes [Zimovets et al., 2021]. Some recent statistical studies of QPPs may be found in Simões et al. [2015]; Dominique et al. [2018]; Hayes et al. [2020a]. Although QPPs are more prominently observed in non-thermal emission, QPPs have also been observed in thermal soft X-ray and extreme ultraviolet (EUV) emission. However as they're less pronounced in thermal emission, some detrending is usually required to identify them [e.g. see Dolla et al., 2012]. It's accepted that QPPs are a reasonably common feature in both solar and stellar flares, although discussions about their prevalence are still ongoing, with estimates ranging from 30–90% of flares [Inglis et al., 2016; Dominique et al., 2018]. This large range is in part due to the ambiguous definition of a QPP, which we have already discussed in Section 1.2. Additionally different analysis methods will vary in what they allow their criteria to detect as a QPP. For example, periodogram based approaches will be poorly suited to detect QPPs that are non-stationary, leading to fewer detections. This is a significant issue as, as the name suggests, quasi-periodic pulsations are rarely periodic. Many QPPs have complex shapes, such as the triangular QPP profile in Fig. 6 of Nakariakov et al. [2019]. This makes them difficult to detect, and trickier still to unify under one definition. QPPs have been observed in all phases of solar and stellar flares, [e.g. Hayes et al., 2016], and in some cases has been seen to extend far into the decay phase. The QPPs seen in solar flares share many characteristics with those observed in stellar QPPs, strengthening the case for a solar-stellar analogy for QPPs [see Zimovets et al., 2021, for an overview on recent advances in observations of stellar QPPs]. Therefore by improving our understanding of the mechanism(s) driving solar QPPs, we will be able to advance our knowledge of stellar QPPs.

1.4.2 Proposed models of QPP generation

Many mechanisms have been proposed to explain the presence of QPPs in solar and stellar flare emission, both from an oscillatory and self-oscillatory perspective [see McLaughlin et al., 2018; Kupriyanova et al., 2020; Zimovets et al., 2021, for recent reviews]. These

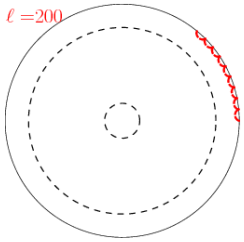

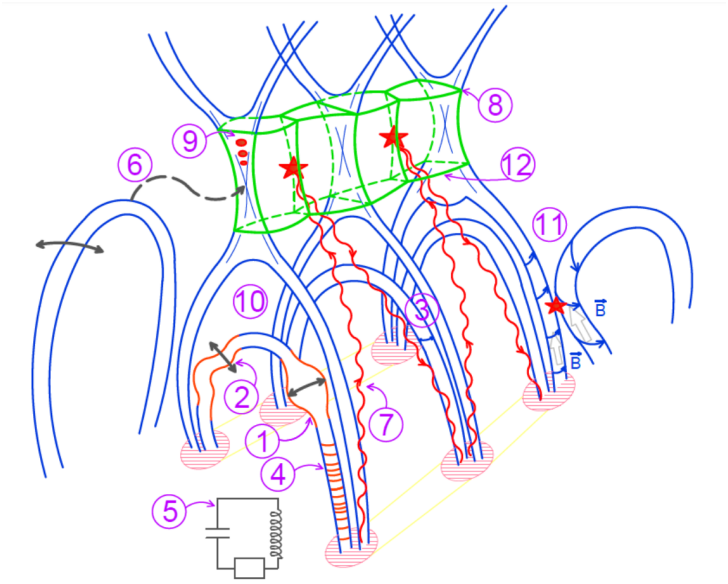

Figure 1.6: Illustration of 12 of the proposed mechanisms of QPP generation. *Originally produced as Fig. 6 in* Kupriyanova et al. [2020]

.

include a broad range of possible scenarios from magnetohydrodynamic (MHD) waves and oscillations in and near the flaring site, to time-dependent reconnection from both oscillatory and multi-island reconnection processes. These mechanisms can be visualised in Fig. 1.6 and as discussed in Zimovets et al. [2021], the mechanisms are labelled as follows (taken from Kupriyanova et al. [2020]): *(1.)* sausage modes; *(2.)* kink mode; *(3.)* torsional Alfvén wave; *(4.)* slow magnetoacoustic mode; *(5.)* equivalent RLC circuit; *(6.)* reconnection triggered periodically by external waves ; *(7.)* autowave processes; *(8.)* flapping oscillations; *(9.)* self-oscillatory processes; *(10.)* thermal overstability; *(11.)* periodic regime of coalescence of two twisted loops; and *(12.)* magnetic tuning fork model.

More mechanisms since the publication of these works have been suggested (e.g. dispersive wave trains and Kelvin-Helmholtz Instability in a flare loop top), and can be read about in further detail in Zimovets et al. [2021] and references therein. It is likely that more mechanisms will continue to be suggested, and that no single mechanism is responsible for the vast multitude of QPPs we see. These mechanisms can be largely sorted into groups, e.g. McLaughlin et al. [2018] sorts them into: (A.) Oscillatory processes (B.) Self- Oscillatory processes and (C.) Autowave processes, whereas Kupriyanova et al. [2020] sorts them into (i) Direct emission modulation by MHD and

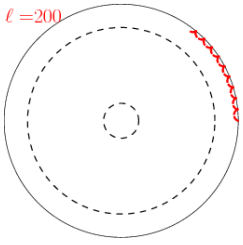

electrodynamic oscillations of all types, (ii). periodic modulation, via MHD oscillations, of the efficiency of energy release processes such as magnetic reconnection, and (iii). spontaneous quasi-periodic energy release.

These groupings are helpful in sorting together similar characteristics, but in many ways arbitrary as there's a significant amount of crossover in the generation mechanisms and in the effects they produce. However such groupings may prove helpful when we obtain more highly resolved QPP data that we can match against these mechanisms, and eventually determine the causes of some of the quasi-oscillatory behaviour we see. Resources such as Table 1. from Zimovets et al. [2021] will be extremely valuable in such studies, as it matches up the generation mechanism to the QPP behaviours we expect it to produce (e.g quality factor, stationarity etc). As of yet no single QPP has been definitively attributed to a specific mechanism, due to insufficient and ambiguous data. Confidently identifying a generation mechanisms for a QPP will be a significant step forward in solar physics as it will substantially improve the Standard Flare Model. The research in Chapter 7 is intended to contribute towards identifying a QPP generation mechanism by assessing the prevalence of non-stationary QPPs.

1.5 Thesis structure

This chapter, Chapter 1, has introduced the background of solar and stellar phenomenon, as well as covering solar structure. In Chapter 2, I address the necessary background for helioseismology and introduce key concepts and terms that will be referred to throughout. In Chapter 3, I discuss the instrumentation and data sources used. Chapter 4 covers the analysis techniques implemented in this thesis. Chapters 5–7 contain the scientific studies in this thesis, covering the effective use of Empirical Mode Decomposition (Chapter 5), searching for the Quasi-Biennial Oscillation in helioseismic data (Chapter 6) and assessing the prevalence of non-stationarity in quasi-periodic pulsations (Chapter 7). In Chapter 8 I present and examine the work in outreach and public engagement that I've done over the past four years. Chapter 9 comprises of a short summary of the findings presented in this work. Additional work and information is presented in the appendix.

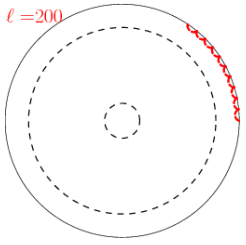

Chapter 2

Waves on the Sun

2.1 Introduction to helio- and astero-seismology

This chapter introduces the field of helio- and asteroseismology and familiarises the reader with terminology and concepts that will be used throughout this thesis. In this section, I introduce the concept of solar and stellar oscillations (2.1.1), and then review the different solar and stellar oscillations that are possible (2.1.2). Next I derive the mathematical conditions for these oscillations to exist (2.1.3). I then focus on discussing pressure modes, which are explored at length in Chapters 5 and 6. I describe the basic generation and properties of pressure modes (2.1.4) and the spherical harmonics that we use to classify them (2.1.5). Next I present how these pressure modes appear in power spectra and how the outputs from these power spectra vary over time (2.1.6). Finally, I present how to correct the frequency shifts for bias (2.1.7), after which the data are ready for analysis in later chapters.

2.1.1 A brief background

The first observations of solar oscillations were in the early 1960s by Leighton et al. [1962] and Evans & Michard [1962] where periodic variations were seen in line-of-sight velocity measurements. These variations were later determined to be the result of globally resonant modes in the Sun, where the dominating modes had frequencies of approximately 3000 µHz, or periods of 5 minutes. In Christensen-Dalsgaard & Gough [1976] it was suggested that the frequencies of these modes can be used to probe the conditions in the solar interior- something impossible to do with typical optical telescopes which are restricted to observing the optically thick photosphere and above. This marked the beginning of helioseismology; the study of waves (seismology), in the Sun (Helios; the

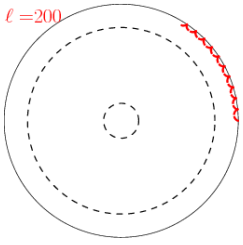

ancient Greek God that was the personification of the Sun). The general methodology of helioseismic studies is to observe these oscillations (usually using spatially resolved line-of-sight Doppler or brightness variations caused by the contractions of the star), perform some processing on these data to obtain oscillation frequencies from power spectra (usually using a Fourier based technique- see Chapter 4), and analyse the oscillation frequencies to infer properties about the solar interior. This process is outlined in the flowchart in Fig. 2.1. We later found similar evidence of oscillations on stars outside of our solar system, in what is now called asteroseismology [Christensen-Dalsgaard, 1986]. Stellar data is usually unresolved, meaning that we cannot observe the more complex modes of oscillations on other stars. However planet hunting missions, such as Kepler, TESS and CoRoT, are still used to great effect in helioseismic studies (for further information, see Harvey [1988] in which Doppler based and photometric methods of observing asteroseismological signals are discussed).

2.1.2 Types of solar/stellar oscillations

Here we define the three types of solar/stellar oscillation, two of which occur within the solar interior, and one on the solar/stellar 'surface'. The interior oscillations are differentiated by their restoring forces, whereas the surface oscillation is governed by a different physical mechanism entirely.

Interior waves are excited by convection currents, which drag solar material up toward the photosphere where the material cools and descends back down towards the base of the convection zone. This motion acts to set up waves that oscillate in fixed cavities, where the boundaries depend on the waves properties (discussed further in Section 2.1.3). The interior oscillations are split into **p-modes** and **g-modes**. P-modes are waves that are excited in the convection zone and have a restoring force of pressure differential. These waves are hence called pressure or p-modes and are analogous to acoustic waves. These p-modes interfere with themselves, setting up spherical standing waves, also known as harmonics, that are visible in Doppler line-of-sight velocity observations. These are the 5 minute oscillations I previously mentioned. We discuss the classification of these p-mode harmonics further in Sections 2.1.4 and 2.1.5. P-modes harmonics are typically seen at frequencies between 1500–4000 µHz, and most prominently at 3000 µHz, but can have frequencies up to the acoustic cut off frequency ($\sim$ 5000 µHz and as low as 200 µHz. However p-modes with frequencies less than $\sim$1000 µHz are difficult to observe due to their low signal to noise ratio. In Sun-as-a-star data, p-mode harmonics have amplitudes from 0.001ms^{-1} to 0.2ms^{-1}, depending on the strength of the mode.

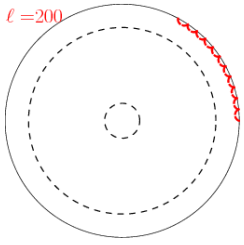

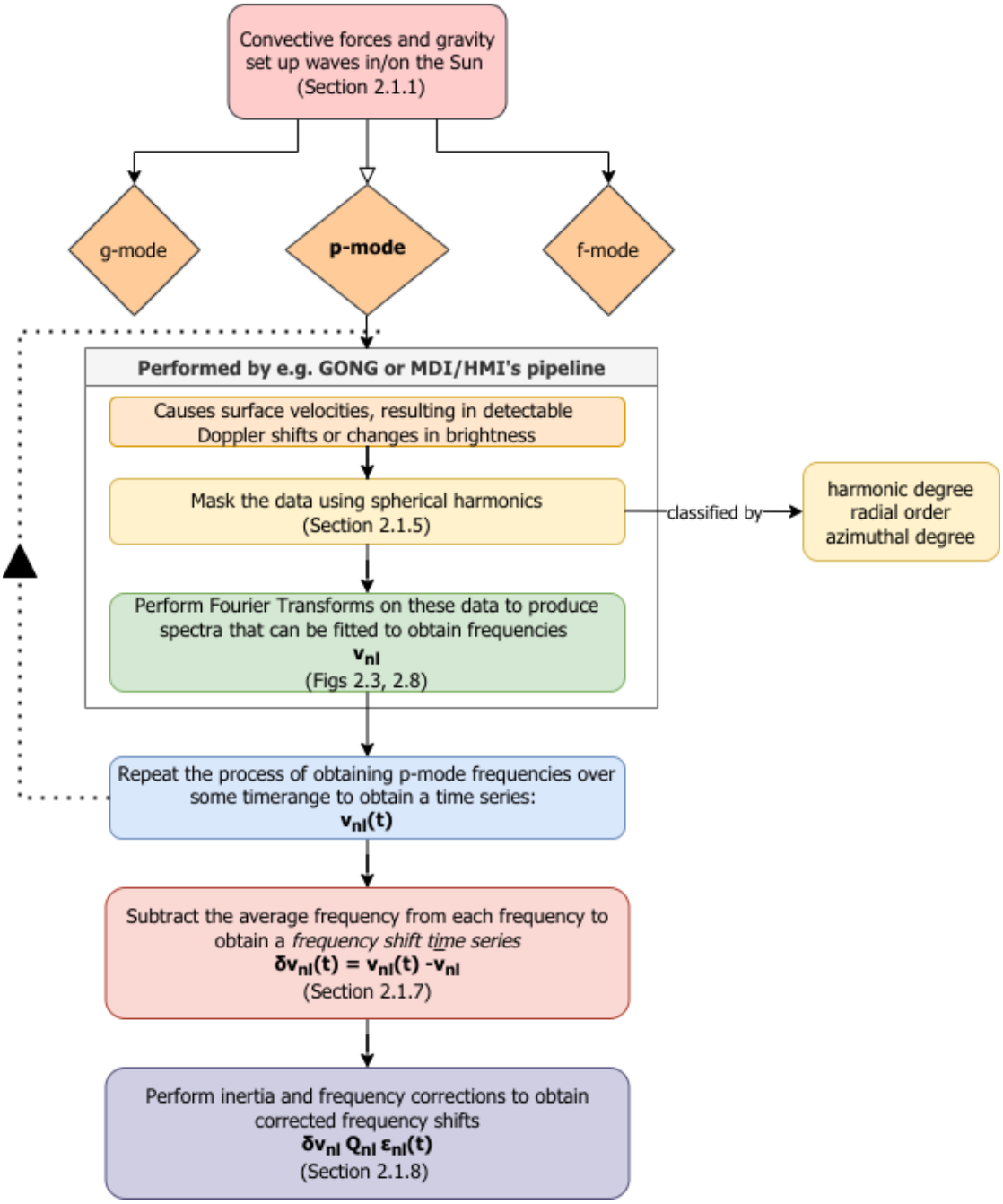

Figure 2.1: Flowchart showing how we obtain the corrected frequency shifts from initial helioseismic data.

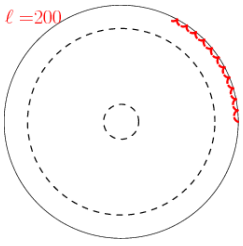

These oscillations compared to the scale of the Sun are quite low and so require precise measurements, prompting the era of global initiatives such as GONG and BiSON (see Chapter 3). P-modes can propagate from near the photosphere down to the solar core. The characteristics of these waves are discussed in more detail in Section 2.1.4. G-modes are also excited in the Sun (although the exact mechanism is still the subject of ongoing debate) and have a restoring force of gravity. G-modes become evanescent in the convection layer and so are trapped within the radiative zone. To date, there have been no conclusive observations of g-modes on the Sun [Schunker et al., 2018; Appourchaux et al., 2010]. In contrast, detections of stellar g-modes are abundant, and have been seen in γ Dor stars [Aerts et al., 1998], subdwarf B stars Green et al. [2003], and white dwarfs Winget & Kepler [2008]. Some sub giant and red giant stars can sustain 'mixed modes', where there is a coupling between the g- and p-mode cavities. These mixed modes can be exceedingly valuable in probing stellar core properties, which have been detected to rotate more than five times the rate of the surrounding radiative zone [Beck et al., 2011]. Surface gravity waves are known as **f-modes**, where no compression occurs, and can be thought of as surface waves on deep water.

2.1.3 Perturbation analysis

Now we derive the equations that govern the behaviour of the two modes of oscillation in the solar/stellar interiors. This derivation closely follows those in Christensen-Dalsgaard [2003]; Basu [2016], which can be consulted for a full derivation.

First, we define an Eulerian perturbation, ξ, around the equilibrium state as

$$\xi = \xi_r \hat{a}_r + \xi_t \hat{a}_t, \tag{2.1}$$

where $\hat{a}_r$ and $\hat{a}_t$ are the unit vectors in the radial and tangential directions.

Using this notation we perturb some of the basic equations that govern solar stellar behaviour; the heat equation, the equations of motion (both radial and tangential), and the Poisson equation. The unperturbed equations may be found in Basu [2016]. The perturbed heat equation is given as

$$\rho_1 = \frac{\rho}{\Gamma_1 P} P_1 + \rho \xi_r \left(\frac{1}{\Gamma_1 P} \frac{\mathrm{d}P}{\mathrm{d}r} - \frac{1}{\rho} \frac{\mathrm{d}\rho}{\mathrm{d}r} \right), \tag{2.2}$$

where Γ_1 is the adiabatic index, where $\Gamma_1 = \delta \ln P / \delta \ln \rho$ taken at constant entropy, and other symbols are defined below. The equations of motion (radial and tangential, respectively), which is also known as the momentum equation, are perturbed as

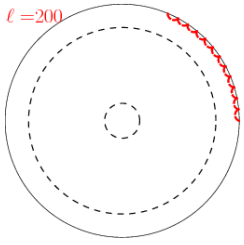

$$\rho\frac{\delta^2\xi_r}{\delta t^2} = -\frac{\delta P_1}{\delta r} - \rho_1 g + \rho\frac{\delta\Phi_1}{\delta r}, \tag{2.3}$$

$$\rho\frac{\delta^2\xi_t}{\delta t^2} = -\nabla_t P_1 + \rho\nabla_t\Phi', \tag{2.4}$$

and the Poisson equation, which characterises the gravitational field, is perturbed as

$$\frac{1}{r^2}\frac{\delta}{\delta r}\left(r^2\frac{\delta\Phi_1}{\delta r}\right) + \nabla_t^2\Phi_1 = -4\pi G\rho_1, \tag{2.5}$$

where we define ρ as density, P as pressure, Φ as the gravitational potential, r as distance, G as the gravitational constant. Where a subscript '1' is applied, the we denote the quantity to be perturbed from its equilibrium value.

For the above equations, we separate out the time dependence from the spatial part as time 't' does not appear explicitly in any of the derivative coefficients. We also may rewrite the perturbations, for a given m, ℓ defined later, and the pressure distribution as spherical harmonics (Y_ℓ^m) that oscillate with time, with frequency ω as:

$$\xi_1(r,\theta,\phi,t) \equiv \xi_r(r)Y_\ell^m(\theta,\phi)\exp(-i\omega t), \tag{2.6}$$

$$P_1(r,\theta,\phi,t) \equiv P_1(r)Y_\ell^m(\theta,\phi)\exp(-i\omega t), \tag{2.7}$$

For now we take ℓ and m to be parameters that govern the shape and complexity of the spherical harmonics. The meaning of spherical harmonics and the parameters ℓ and m are discussed in Section 2.1.5. We use these descriptions of ξ_r and P_1 together with Eqns. 2.3 and 2.5 to obtain the following:

$$\frac{\mathrm{d}\xi_1}{\mathrm{d}r} = -\left(\frac{2}{r} + \frac{1}{\Gamma_1 P}\frac{\mathrm{d}P}{\mathrm{d}r}\right)\xi_r + \frac{1}{\rho c^2}\left(\frac{S_\ell^2}{\omega^2} - 1\right)P_1 - \frac{\ell(\ell+1)}{\omega^2 r^2}\Phi_1, \tag{2.8}$$

where the squared sound speed is given as $c^2 = \Gamma_1 P/\rho$ and the *characteristic acoustic frequency* S_ℓ (or equivalently the *Lamb frequency* S_ℓ^2 is defined by

$$S_\ell^2 = \frac{\ell(\ell+1)c^2}{r^2}, \tag{2.9}$$

We also may write the equation for hydrostatic equilibrium using the above notation as

$$\frac{\mathrm{d}P_1}{\mathrm{d}r} = \rho(\omega^2 - N^2)\xi_r + \frac{1}{\Gamma_1 P}\frac{\mathrm{d}P}{\mathrm{d}r}P_1 + \rho\frac{\mathrm{d}\Phi_1}{\mathrm{d}r}, \tag{2.10}$$

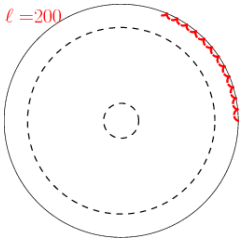

taking N to be the *Brunt-Väisälä* or *buoyancy frequency*, with N^2 defined as:

$$N^2 = g\left(\frac{1}{\Gamma_1 P}\frac{\mathrm{d}P}{\mathrm{d}r} - \frac{1}{\rho}\frac{\mathrm{d}\rho}{\mathrm{d}r}\right), \tag{2.11}$$

with gravitational acceleration g.

The buoyancy frequency defines the frequency at which a displaced fluid parcel will oscillate when perturbed in a stable environment. If N^2 is < 0, the motion of the parcel will become unstable and instead will be subject to convective motions.

We then rewrite Eqn. 2.5 using N^2 to obtain

$$\frac{1}{r^2}\frac{\mathrm{d}}{\mathrm{d}r}\left(r^2\frac{\mathrm{d}\Phi_1}{\mathrm{d}r}\right) = -4\pi G\left(\frac{P_1}{c^2} + \frac{\rho\xi_1}{g}N^2\right) + \frac{\ell(\ell+1)}{r^2}\Phi_1, \tag{2.12}$$

We now make the assumption that we can neglect the perturbation of the gravitational field, making use of the Cowling approximation [Cowling, 1941]. It has been shown that this assumption holds well for large ℓ. We apply the Cowling approximation together with Eqns. 2.8, 2.10, 2.12 to reduce the equations to:

$$\frac{\mathrm{d}\xi_1}{\mathrm{d}r} = -\left(\frac{2}{r} - \frac{1}{\Gamma_1}\frac{1}{H_p}\right)\xi_r + \frac{1}{\rho c^2}\left(\frac{S_\ell^2}{\omega^2} - 1\right)P_1, \tag{2.13}$$

and

$$\frac{\mathrm{d}P_1}{\mathrm{d}r} = \rho(\omega^2 - N^2)\xi_1 - \frac{1}{\Gamma_1}\frac{1}{H_p}P_1, \tag{2.14}$$

where we have introduced the pressure scale height, H_p, as

$$H_p = -\frac{\mathrm{d}r}{\mathrm{d}\,\ln P}, \tag{2.15}$$

Once again we apply several assumptions. Firstly we assume the pressure scale height is large and so terms including H_p^{-1} may be neglected. We also make the assumption that we are interested in modes that are far from the solar core, i.e. r is large. Therefore the $\frac{2}{r}$ term may also be neglected in Eqn. 2.13.

Applying these assumptions, we combine Eqns. 2.13 and 2.14 to finally obtain the equation that characterises the relationship between displacement of a parcel, and its relation to its oscillatory frequency with regards to the Lamb frequency and the buoyancy frequency as follows:

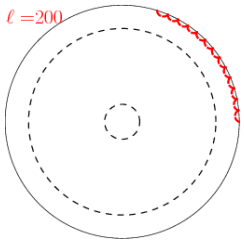

$$\frac{\mathrm{d}^2\xi_1}{\mathrm{d}r^2} = \frac{\omega^2}{c^2}\left(1 - \frac{N^2}{\omega^2}\right)\left(\frac{S_\ell^2}{\omega^2} - 1\right)\xi_r, \tag{2.16}$$

This relation is clearly exponential except for two specific cases, both of which may be visualised in a propagation diagram, seen in Fig. 2.2.

Case (i): This is where both $\omega^2 > S_\ell^2$ and $\omega^2 > N^2$, allowing the mode to be oscillatory in the outer regions of the Sun (see the orange region in Fig. 2.2). These modes are p-modes, with their turning points (the positions of maximal displacement, described fully in Section 2.1.4) defined by $S_\ell(r_t) = \omega$. These turning points are further differentiated into a lower turning point (the closest position the p-mode reaches to the solar core, see Eqn. 2.17) and some upper turning point close to the solar surface. Although the majority of these p-modes spend the majority of their time above the convective zone, some modes may penetrate to the solar core. For most p-modes, $\omega \gg N$, so the displacement of the p-mode is largely determined by the variation of the sound speed. Waves in the p-mode region are further restricted by the acoustic cut off frequency, ω_{ac}. This frequency defines the upper limit of the cavity wherein wave propagation is observed, which is approximately 5000 µHz according to solar models [Jiménez et al., 2011], although 'pseudomodes' with frequencies higher than this have been seen to exist [Kosak et al., 2022].

Case (ii): Both $\omega^2 < S_\ell^2$ and $\omega^2 < N^2$. In this case modes are trapped in the region shown in blue in Fig. 2.2. These modes are g-modes, where the turning points are determined at $N = \omega$. These modes have one turning point at a depth very close to the core of the Sun, and another just below the base of the convective zone. Therefore they are said to be trapped under the convective zone and have not been detected on the Sun, as the displacements are currently undetectable at the solar surface due to their extremely low signal to noise ratio.

2.1.4 Describing pressure modes using harmonics

Now that we have discussed the maths behind the formation of p-modes, we may spend some time discussing their physical characteristics. Here, we discuss the concept of a 'lower turning point' and visualise how p-modes can be approximated by spherical harmonics in the solar/stellar interior. Please note that in this section I use the term 'higher harmonics' as a means to describe harmonics of higher order or equivalently harmonics with a greater number of (anti)-nodes. Strictly speaking, I am referring to modes of greater harmonic degree ℓ, but as I do not introduce the concept of harmonic

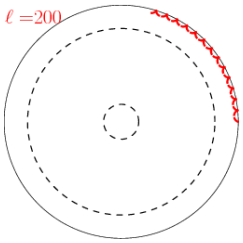

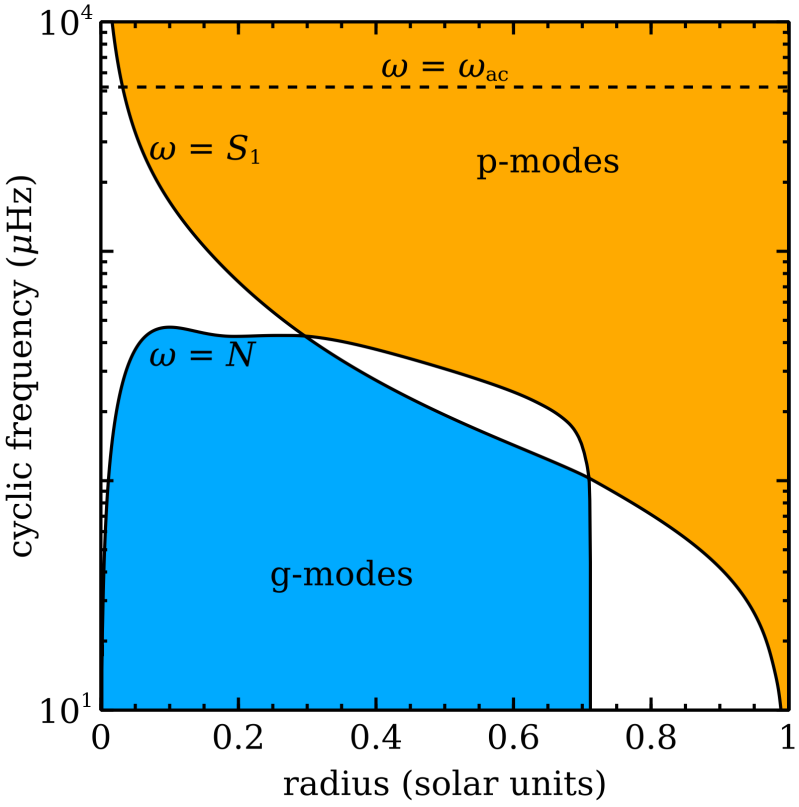

Figure 2.2: Propagation diagram for a standard solar model, showing the relationship between oscillatory frequency ω against solar radius $R_\odot$. The blue region shows where solar g-modes are trapped in the solar interior, bound by the line where oscillation frequency ω equals the buoyancy frequency N. The region in which p-modes are confined is indicated in orange, bound by the line denoting where the oscillation frequency ω equals the Lamb frequency S_1 for an $\ell = 1$ mode. Also indicated is the acoustic cut off frequency at approximately 5000 µHz. *Figure produced by Warrick Ball, displayed here under Wikipedia's Creative Commons.* `commons.wikimedia.org/wiki/File:Propagation_diagram.png`

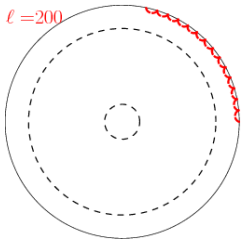

degree ℓ until Section 2.1.5 I will use 'higher harmonics' as shorthand for now.

As discussed in Chapter 1, the interior of most main sequence stars largely comprises of plasma, a state of matter that is susceptible to compression forces. The plasma can therefore act as a fluid, sloshing back and forth when a force is exerted, and can be damped back to an equilibrium positions by some restoring force, much like a mass on a spring in the famous Hooke's Law experiment. However stars have an additional component to consider; heat. The temperature differential in the solar and stellar interiors drives convection currents, and as temperature increases steeply towards the core, the sound speed, proportional to the square root of the temperature follows suit. Therefore a p-mode which propagates towards the interior at an angle to the photosphere will undergo total internal refraction as the deeper edge of the wave travels faster than the surface facing edge. Thus the shallower the angle, the less deep a p-mode will travel. The lower turning point, usually given as r_t or R_{ltp}, is the depth in solar radius at which a p-mode undergoes total internal refraction, as seen in Fig. 2.3. The method of determining R_{ltp} can be found in Section 2.1.5.

As mentioned previously, the global oscillations we observe are the superpositions of many standing p-modes. This is because p-modes have a long lifetime and interfere with themselves, eventually producing resonant oscillations called harmonics. These resonant standing waves are observable in the power spectra of the Doppler velocity data, seen as the prominent peak around 2-4 mHz in Fig. 2.4. Next we examine the properties of harmonics in 1, 2, and 3 dimensions and examine what we explore the p-mode harmonics to look like.

For this discussion we must recall the concept of nodes and anti-nodes. Anti-nodes are the regions in which the standing wave produces maximal displacement, and nodes are where minimal or no displacement occurs. As you move to higher harmonics, more anti-nodes and nodes are present. For a 1D wave with two closed boundaries, such as the standing wave produced when twanging a guitar string, for every x anti-nodes, there are $x+1$ nodes. This concept can be extended into 2D, where we may use Chladni plates to visualise standing waves on a 2-dimensional surface. Chladni plates are covered in a thin layer of sand before being driven by some wave that interferes with itself producing 2D harmonics. This creates anti-nodal regions that undergo significant vibration, forcing the sand away. Sand gathers in nodal areas, producing the patterns seen in Fig. 2.5. These harmonics increase in complexity at higher harmonics, a concept that continues into 3D.

P-modes travelling into the solar interior are a 3D phenomenon, oscillating between the closed boundaries of the acoustic cavity described in Section 2.1.3. We again

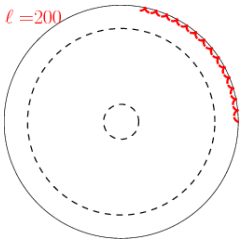

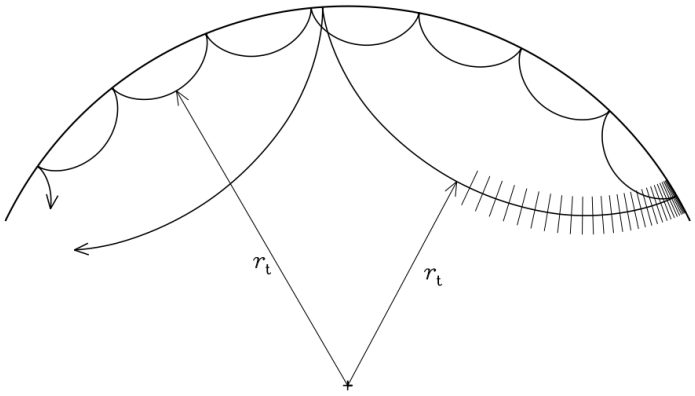

Figure 2.3: Sketch illustrating the propagation of two p-modes in a 2D cross section of a solar hemisphere. The mode travelling to a shallower depth corresponds to a higher harmonic that the mode that penetrates more deeply into the solar interior. The orthogonal dashes on the lower harmonic wavepath correspond to the wave fronts. The deeper edge of the wave front travels slightly faster than the shallower edge, due to the increased sound speed at lower depths, causing the path of p-mode propagation to be curved. *Fig. taken from 5.4 of [Christensen-Dalsgaard, 2003]*

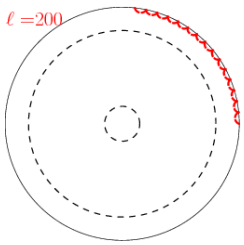

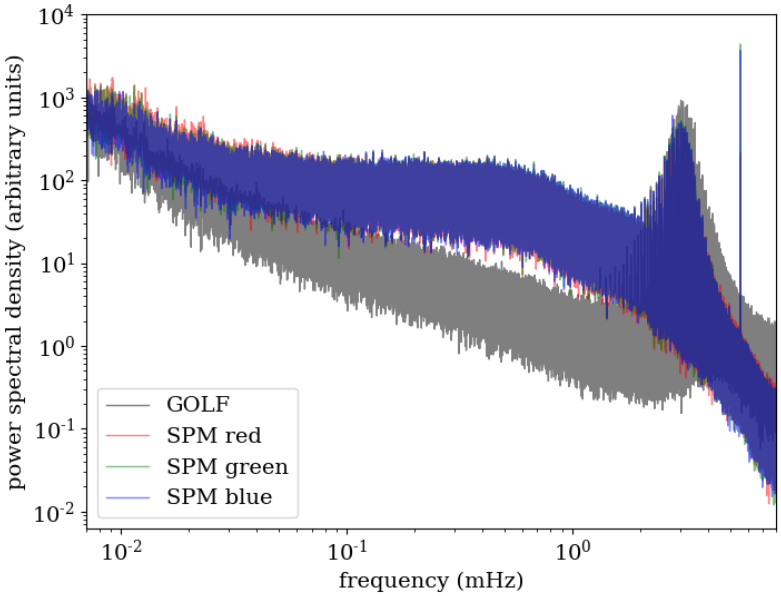

Figure 2.4: Power spectrum of the Sun produced by the analysis of data from the Global Oscillations at Low Frequencies (GOLF) instrument and Sun PhotoMeters (SPM) on Variability of solar IRradiance and Gravity Oscillations (VIRGO) instrument, both aboard SOHO. In all passbands, a modulation centred around 3mHz can be observed- the result of resonant oscillations in the Sun. The slope observed from 10^{-2}-10^{0} mHz is due to the red noise produced by surface granulation, to which GOLF is less sensitive. *Figure produced by Warrick Ball, displayed here under Wikipedia's Creative Commons.* `commons.wikimedia.org/wiki/File:Sun_combined_power_spectrum_loglog.png`

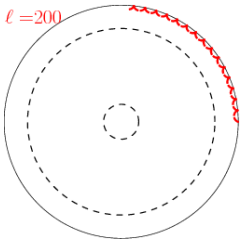

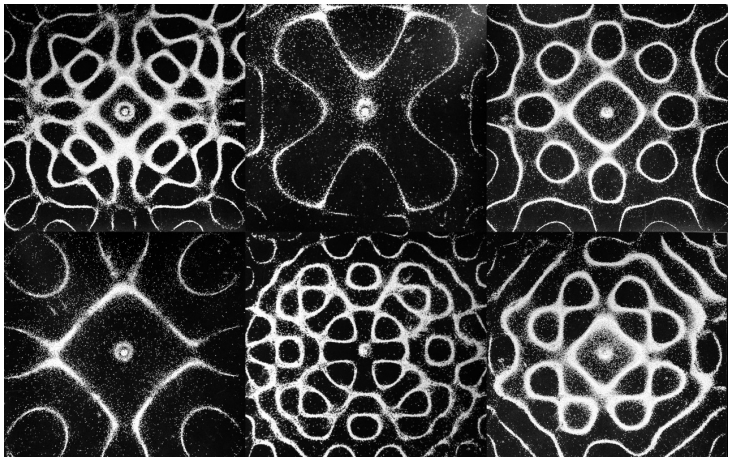

Figure 2.5: Patterns produced by driving waves on a 2 dimensional Chlandi plate covered in a thin layer of sand. Higher harmonics generally create more complex patterns, such as the one seen in the middle of the lower row. Image by *Chris Smith* from Dragicevic & Jansen [2012]

expect to see a pattern of nodes and anti-nodes forming as the p-modes interfere and set up 3D harmonics. We approximate the Sun to be roughly spherical, and therefore must examine spherical harmonics. These spherical harmonics are seen as a 2D static projection of the surface motions in Fig. 2.6. The regions shaded in red show motion away from the reader, and blue toward. As these are oscillations, the regions not associated with a node will oscillate, toward and then away from an observer. Once again, we see that higher harmonics (bottom row of Fig. 2.6) result in more complex patterns than lower harmonics (top row), due to the increasing number of nodes.

We should exercise caution when discussing nodes in 3D spherical harmonics as we need to consider not only radial nodes (that appear at various radii moving out from the core), but also latitudinal nodes (from pole to pole), and longitudinal (that intersect perpendicularly with the equator). Also we may examine the influence of solar rotation on the p-modes and how it impacts the presence or frequency of the harmonics. To do so we must introduce a system to classify the spherical harmonics.

2.1.5 Classifying spherical harmonics

Spherical harmonics can be categorised according to their harmonic (ℓ), radial (n), and azimuthal (m) degrees.

The *harmonic degree*, ℓ is also known as the angular degree, and indicates the number of node lines on the surface. The simplest of oscillations is the ℓ=0 mode,

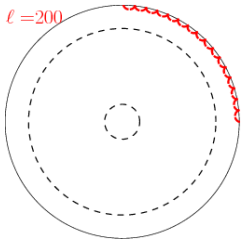

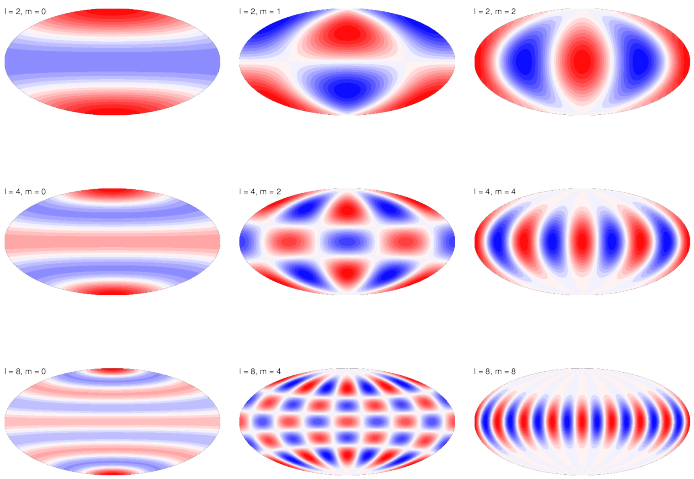

Figure 2.6: 2-D projections of spherical harmonics, with regions in red indicating motion away from the reader and blue towards. Harmonic degree ℓ and azimuthal degree m are indicated. Image courtesy of Thorsten W Becker, Institute for Geophysics, UT Austin, see: `www-udc.ig.utexas.edu/external/becker/contact.html`

known as the breathing mode, where the entire star expands and contracts with each oscillation. This represents a deeply penetrating mode, through to the solar/ stellar core. As ℓ increases, the depth to which the p-mode travels decreases. The p-modes' lower turning point is dependant on ℓ according to the following relation:

$$\frac{c^2(r_t)}{r_t^2} = \frac{\omega^2}{\ell(\ell+1)} \tag{2.17}$$

where r_t is the distance from the core to the lower turning point, $c(r_t)$ is the sound speed at r_t. The distribution of p-mode r_t for modes detected by GONG can be seen in Fig. 2.7a. Typically for p-modes, ℓ is between 0 and 300, with modes of approximately $0 \leq \ell < 3$ considered 'low' degree, approximately $4 \leq \ell < 150$ considered 'intermediate' or 'medium' degree, and approximately $150 \leq \ell < 300$ considered as 'high' degree.

The *radial order* is given by n, which describes how many nodes are in the radial direction. The relationship between mode lower turning point, modal harmonic degree (ℓ) and radial order (n) can be seen in Fig. 2.7b. Each 'n' produces a new ridge in a typical ℓ-ν diagram which compares p-mode frequencies and harmonic degrees (see Fig. 2.8). The nodes in the radial direction are nodal planes extending from the core to the photosphere. For p-modes, the radial order n is confined between 0 and 35, re-

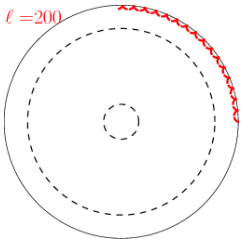

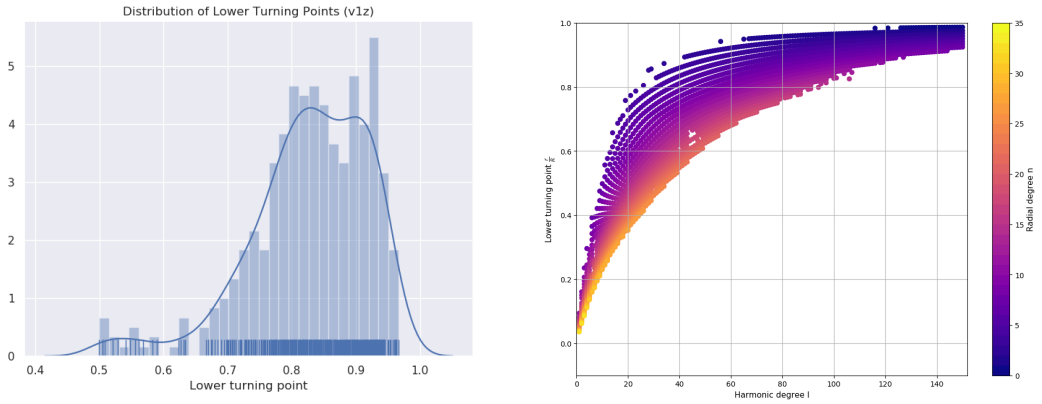

(a) (b)

Figure 2.7: *Left*: Distribution of lower turning points of p-modes observed by GONG between 1995 and 2018, and the associated histogram. *Right*: Relationship between lower turning point, harmonic degree (ℓ), and radial order (n) for GONG obtained p-modes.

strained by the acoustic cut-off frequency. The *azimuthal degree*, $|m|$, describes how many surface nodal lines exist that intersect with the equator, i.e. the nodal lines are arranged longitudinally. Because the Sun revolves p-mode frequencies are split depending on m, as some p-modes travel with the direction of rotation and some against. So different m are split into $2\ell+1$ frequency components, where $-\ell \leq m < \ell$.

A mode with given values for (n,ℓ) is called a multiplet. In this thesis we primarily consider m-averaged multiplets, which is to say we obtain the averaged frequency averaged over all m components for each multiplet. This is because we are primarily interested in the depth dependence of the QBO in helioseismic data (see Chapter 6), rather than the latitudinal dependence, and so we optimised for precision without the loss of pertinent information.

2.1.6 Frequency shifts

The frequency of p-modes are sensitive to both the strong and weak components of the magnetic field, and as such provide a valuable tool to examine them both. The strong component is the dominant force causing sunspots, and the weak magnetic field is seen over a wider range of latitudes [Broomhall & Nakariakov, 2015]. We may assess how the p-mode frequencies change over time by defining the term 'frequency shift', given by

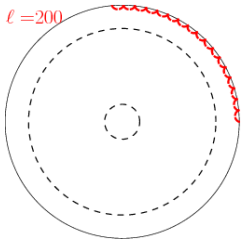

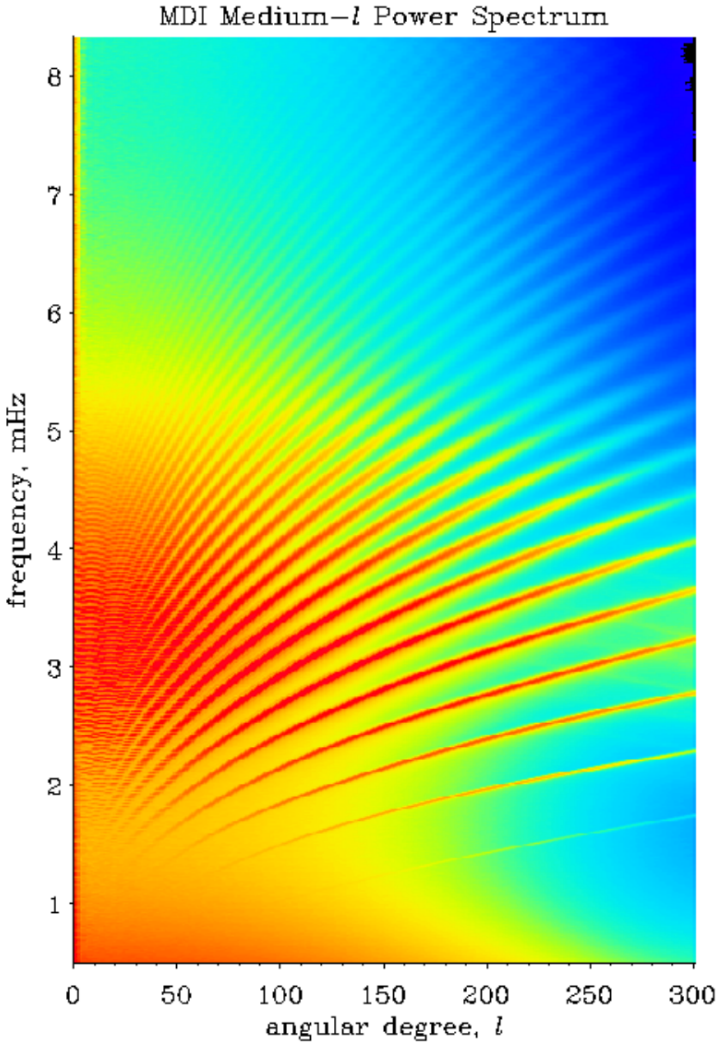

Figure 2.8: A ℓ-ν diagram of frequency verses harmonic degree, produced by 2 months of intermediate degree Michelson Doppler Imager data from The Solar and Heliospheric Observatory from May-June 1996. Each ridge represents a different radial order n, and spectral power density is indicated by colour. Image courtesy of NASA, see `https://soho.nascom.nasa.gov/gallery/Helioseismology/`

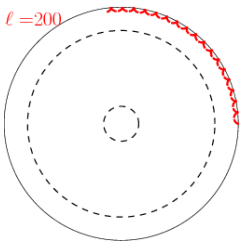

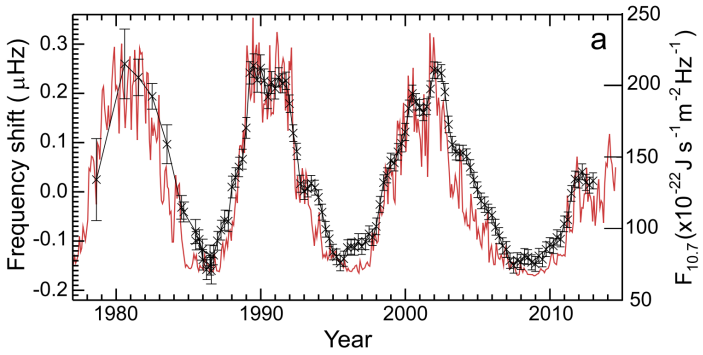

Figure 2.9: Frequency shifts of p-modes observed by BiSON from Solar Cycles 21, 22, and 23 (black) with errors due to uncertainties in the fitting of the p-mode frequencies. The $F_{10.7}$ index solar activity proxy is plotted in red, and has been scaled to appear on the same axis. The two datasets are correlated very closely. Figure is from Balogh et al. [2014] using data courtesy of A.-M. Broomhall, which is an updated figure originally produced in Broomhall et al. [2009].

$\delta\nu_{n,\ell}(t)$ (note that this is different to the small frequency separation, also given by $\delta\nu$)

$$\delta\nu_{n,\ell}(t) = \nu_{n,\ell}(t) - \bar{\nu}_{n,\ell} \tag{2.18}$$

where $\bar{\nu}_{n,\ell}$ is the weighted mean frequency of a mode across the entire time span under consideration, with the weights are given by the inverse of the uncertainty on the fitted mode frequency.

The frequency of p-modes increase with magnetic activity and therefore with solar activity and solar activity proxies, e.g. sunspots. This can be seen in Fig. 2.9 where a strong correlation is visible between frequency shifts and a solar activity proxy-the $F_{10.7}$ index. Therefore we can use frequency shifts to examine the solar activity cycle, or Schwabe cycle, which has an average period of around 11 years (see Section 1.1.7). The link between solar cycles and frequency shift was first shown by examination of intermediate degree modes in Libbrecht & Woodard [1990], and later built on in Anguera Gubau et al. [1992] who found a similar phenomenon for low degree modes.

Solar activity proxies, such as sunspot number, are frequently positive definite meaning that the lower limit at absolute minima is zero. This means that these proxies are well suited for assessments of solar maxima, but poorly attuned for solar minima where a hard lower boundary of zero restricts the amount of information that we can gather. Frequency shifts have no such restrictions and are therefore well suited to assessing solar minima or durations of low activity. Maximal frequency shifts are seen in

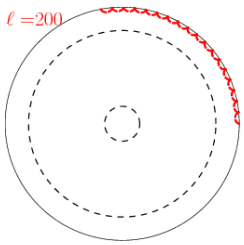

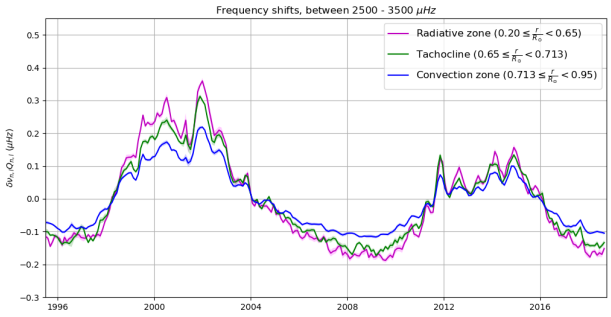

Figure 2.10: Frequency shifts of p-modes observed by GONG from 1995–2018 that had average frequencies between 2500–3500 µHz. The modes have been sorted into three exclusive groups depending on their lower turning points, and are colour coded as seen. Errors are shown as light shading.

modes with the greatest average frequencies, which after mass inertial corrections (see Section 2.1.7) are up to 0.4 µHz between subsequent minima. Evidently, these shifts are very small in magnitude but can tell us a great deal about the associated magnetic field.

The correlation between p-mode frequency and solar activity is primarily driven by how a change in magnetic activity affects the conditions in the outer layers of the Sun beneath the photosphere. Goldreich et al. [1991] showed that the position of a p-modes upper turning point (the upper edge of the acoustic cavity in which the mode oscillates) decreases with increasing magnetic field strength. Therefore as the near surface magnetic field increases the frequency of a given p-mode also increases. This causes positive frequency shifts for growing magnetic activity. It follows that higher frequency p-modes undergo a greater amplitude of frequency shift than lower frequency modes, as discussed in Gelly et al. [2002]. Fig. 2.10 shows the frequency shifts over Solar Cycles 22 ($\sim$ 1996–2008) and 23 ($\sim$ 2008–2014) of GONG-obtained p-modes. These p-modes have been grouped into sets according to the position of their lower turning points (r_t) in the radiative zone, tacholine, or convection zone. The p-modes, all of which have average frequencies between 2500–3500 µHz, all show increased frequency at solar maxima (approximately 2001 and 2014) and decreased at minima. We see that the modes with deeper lower turning points within the radiative zone undergo the largest amplitude of frequency shift, compared to the modes with their lower turning points in the convection zone.

As discussed in Section 2.1.7, the amplitude of the frequency shift varies by the p-modes' frequency and harmonic degree (it also varies by azimuthal degree due to solar

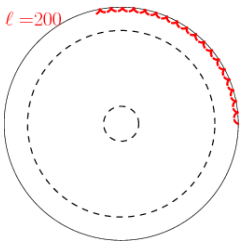

rotation, but for the purposes of this thesis we only examine the m-averaged frequencies and so can neglect this effect). To correct for these factors which could otherwise bias results, we rescale the frequency shifts.

2.1.7 Correcting the frequency shifts

The amount of mass that each mode interacts with varies which means the inertia of each mode varies. We correct for this mode inertia by a normalisation factor. This way we can assess all modes equally, as failing to do so would bias any findings towards the modes that underwent the largest frequency shifts.

Both harmonic degree ℓ and frequency $\nu_{n,\ell}$ are correlated with the amplitude of frequency shift. For a wave with a given frequency $\nu_{n,\ell}$, a wave with a higher harmonic degree ℓ interacts with less mass in the solar interior than a low degree mode, leading to a higher amplitude frequency shift. Similarly, for a given ℓ, a higher frequency $\nu_{n,\ell}$ implies a smaller mode inertia. This is due to higher frequency modes having upper turning points at shallower depths. A shallower upper turning point results in a comparatively larger displacement at the photosphere, and therefore a greater amplitude frequency shift.

Lets introduce the normalisation factors that we use to reduce the biasing from the data. First is the factor that suppresses the biasing towards modes of harmonic degree. From Christensen-Dalsgaard et al. [1991] we define the normalised inertia $\mathrm{E}_{n,\ell}$ as

$$E_{n,\ell} = \mathrm{M}_{\odot}^{-1} \int_V |\xi|^2 \rho \mathrm{d}V = 4\pi \mathrm{M}_{\odot}^{-1} \int_0^{R_{\odot}} |\xi|^2 \rho r^2 \mathrm{d}r = \frac{\mathrm{M}_{n,\ell}}{\mathrm{M}_{\odot}} \tag{2.19}$$

where $M_{n,\ell}$ is the mass associated with the mode, and $\mathrm{M}_{\odot}$ and $\mathrm{R}_{\odot}$ are the solar mass and radius respectively. ξ is the normalised displacement caused by the given mode at the photosphere, with the integration taken over the volume of the Sun given as V. We use Eqn. 2.19 to obtain an inertia 'ratio' which is the term we can multiply frequency shifts to normalise the effect of mode inertia and make frequency shifts largely independent of harmonic degree ℓ.

We define $\mathrm{Q}_{n,\ell}$ as the inertia ratio such that

$$Q_{n,\ell} = \frac{E_{n,\ell}}{\bar{E}(\nu_{n,\ell})} \tag{2.20}$$

where $\bar{E}(\nu_{n,\ell})$ corresponds to the mass of a mode with a $\ell = 0$ and a frequency equal to that of the mode in question. This normalises the frequency shift to its purely

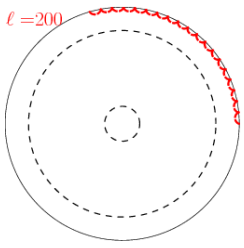

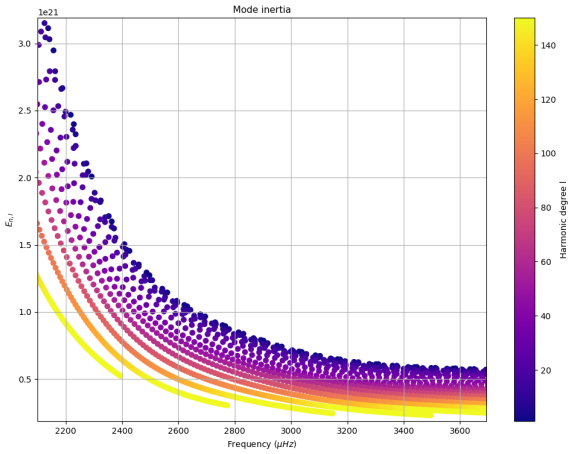

Figure 2.11: Variation of mode inertia term $E_{n,\ell}$ with mode frequency and harmonic degree ℓ, using data obtained by GONG from 1995–2018.

radial equivalent. Fig. 2.11 shows the distribution for normalised inertial values $E_{n,\ell}$ for different mode frequencies and harmonic degree ℓ. Note how for a given harmonic degree ℓ the normalised inertia decreases as frequency increases.

Although the discrepancies in the amplitude of frequency shifts are primarily due to harmonic degree, mode frequency also acts to affect frequency shifts. Following the method described in Chaplin et al. [2001], we introduce the inverse fractional mode inertia $\epsilon^{-1}_{n,\ell}$ as

$$\epsilon^{-1}_{n,\ell} = \left(\frac{E_{n,\ell}}{\bar{E}(3000)} \right) \tag{2.21}$$

where $\bar{E}(3000)$ is the mode inertia of a ℓ=0 mode at $\nu = 3000$ μHz.

As shown in Fig. 2.12, we are able to visualise the impact of these normalising factors on frequency shifts from modes obtained by GONG over solar cycle 23. The top panels show the uncorrected data, with the frequency shifts between solar maximum 23 and solar minimum 23 (*Left)* and minimum 23 and minimum 24 (*Right).* There is a clear harmonic dependence visible, as indicated by colour, and a dependence on mode frequency with much larger frequency shifts over a larger range of amplitudes for greater mode frequencies. The middle row shows the same data, but multiplied by the inertia ratio, $Q_{n,\ell}$. Clearly the harmonic dependence has been largely removed. The lowest panel introduces the inclusion of the inverse fractional mode inertial term $\epsilon_{n,\ell}$ and the dependence of frequency shift and mode frequency has also been predominantly removed.

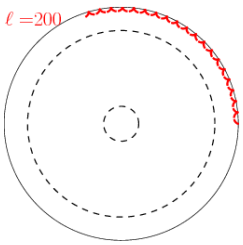

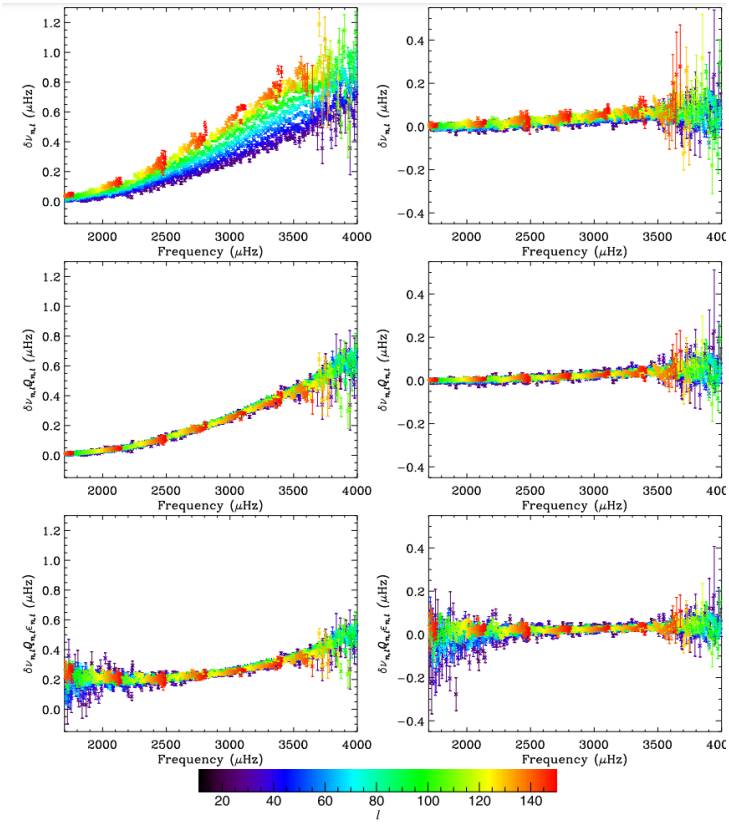

Figure 2.12: Frequency shifts of GONG obtained modes for Solar Cycle 23. Left panels show frequency shifts from Solar Min_{23} to Max_{23}, and right panels from Min_{23} to Min_{24}. Top panels show uncorrected data, middle panels show the same data multiplied by $Q_{n,\ell}$, and the bottom panels show the raw data multiplied by both $Q_{n,\ell}$ and $\epsilon_{n,\ell}$. Harmonic degree is indicated by colour. Figure from Broomhall [2017].

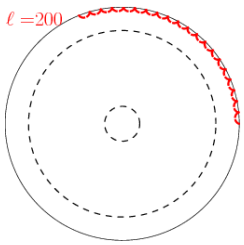

2.2 Helioseismology in context

Helioseismology has already proven itself to be a valuable tool in examining the internal structure of the Sun. For example, GONG data has been used to uncover the solid body rotation found at $0.7R_\odot$ and below (see Fig. 1.2), a finding which significantly impacts the generation mechanism of the solar dynamo. Helioseismology also played a vital role in solving The Solar Neutrino Problem. The Solar Neutrino Problem concerns the apparent discrepancy in the number of electron neutrinos detected on Earth and the number predicted to be produced by the Sun [Christensen-Dalsgaard, 2018]. In some detections, the ratio of detected to estimated electron neutrino abundances fell as low as 1:3, though it was more often around the 1:2 level [Haxton, 1995]. Initially, it was suggested that the solar model used in predicting the production rate of electron neutrinos was incorrect. If the solar model was indeed incorrect, it would require substantial revisions to account for the 'missing' electron neutrinos. New models were proposed that accounted for these electron neutrinos, either by varying the amount of diffusion and mixing in the solar core, and by switching off the ^{3}He + ^{4}He reaction. However helioseismic measurements of the sound speed in the solar interior were incompatible with these models, effectively ruling them out (see Fig. 1. in Bahcall et al. [1997]). Meanwhile the helioseismic sound speed measurements agreed strongly with the so-called standard solar model of the time. This proved that The Solar Neutrino Problem was one of neutrino physics, and not the result of an inaccurate solar model. This later led to the discovery that neutrinos have mixed quantum states, and are able to switch flavours. The missing neutrinos had simply changed from electron neutrinos to other flavours during their journeys to Earth, and were thus undetectable to the electron neutrino detectors. This was proven at the Sudbury Neutrino Observatory where neutrino flavour change was definitively identified [Ahmad et al., 2001]. This discovery contributed to the awarding of the 2002 and 2015 Nobel prizes in Physics, first for advances in neutrino astronomy and X-rays, and later for the discovery of neutrino oscillations and the discovery of neutrino mass.

Helioseismology has also proved useful in measuring solar helium abundance, which is a key parameter in constraining solar evolution. Because the Sun is a cool star, it's difficult to measure the abundance spectroscopically. However the presence of Helium changes the mean molecular weight, and therefore the local sound speed, which means that we can infer helium abundance using helioseismic methods. The first successful attempt at calculating Helium abundance was performed in the early 1990s, [Däppen et al., 1991], with subsequent direct inversions yielding even more precise measurements. Helioseismology has also determined the depth of the convection zone to impressive precision.

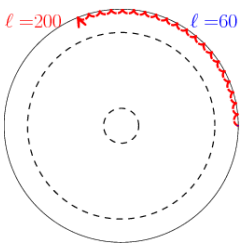

Christensen-Dalsgaard et al. [1991] obtained a relation using sound speed inversions to find that the base of the convection zone, where the temperature gradient changes from adiabatic to radiative, is at 0.713±0.001 $R_{\odot}$, a measurement that has been corroborated by subsequent works.

Asteroseismology is the science of observing oscillation frequencies on stars other than the Sun. Accurate detections of solar oscillation frequencies allow us to better constraint solar models [Guenther & Brown, 2004], and so we apply helioseismic methods to stellar observations in the hopes we can do the same for stellar models. Asteroseismological studies have already obtained measurements of magnetic cycle activity on other stars. This was notably reported in García et al. [2010], where using observations from the Convection, Rotation and planetary Transits (CoRoT) mission, frequency shifts of oscillation frequencies on a solar-type star were linked to activity proxies, showing evidence of an activity cycle. We have also seen solar-like oscillations in red giants, detected by Kepler [Bedding et al., 2010], and in other solar-type stars [Santos et al., 2018], [Kiefer et al., 2017].

The use of asteroseismological techniques has the power to change our understanding of stellar evolution. A recent publication examined 91 stars using Kepler data. The study showed that standard age rotation relations no longer apply after approximately half way through the main sequence, with weakened magnetic breaking being the likely cause of the slowing rotation rate [Hall et al., 2021].

In the recent years we've seen a growing amount of funding dedicated to asteroseismological and helioseismic missions; the highly popularised Kepler mission (and later the K2 mission) for example, produced a plethora of precise data that was successfully purposed for asteroseismic studies. Additionally the recent launch of the Transient Exoplanet Survey Satellite (TESS), a mission from NASA, is capable of producing a near-all sky survey, from which asteroseismology can be performed for solar-type and red giant stars [Campante et al., 2016; Kiefer et al., 2019].

Advances in helioseismology may hold the solution to understanding the solar dynamo. To d ate, many mechanisms have been suggested [Charbonneau, 2020] however we have not yet understood where the solar magnetic field is being generated. Furthermore secondary magnetic behaviour such as the Quasi-Biennial Oscillation can be examined using helioseismic techniques (see Chapter 6). This may lead the way in answering many unanswered questions about the solar magnetic field, its dynamo, and conditions within the core that as of yet are still relatively unknown about.

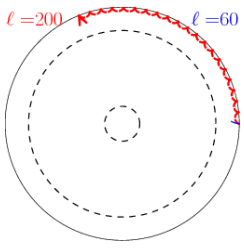

Chapter 3

Instrumentation

This Chapter introduces the instrumentation and corresponding data used within this thesis. SOHO, SDO (and their associated instruments) and GOES are all space-based data sources, whereas GONG, the $F_{10.7}$ index, and BiSON are all derived from ground-based measurements. The Bremen Composite MgII index is an amalgamation of several data sources, both space and ground-based. We use GONG, BiSON, MDI, and HMI to obtain helioseismic data, and the $F_{10.7}$ index and the Bremen Composite MgII index as solar activity proxies, all explored further in Chapters 5 and 6. We use GOES, AIA and LASCO data in Chapters 7 in an examination of non-stationarity in QPPs.

3.1 GONG

The Global Oscillation Network Group (GONG) is a world-wide collaborative initiative that has been taking continuous observations of the Sun since 1995 [Harvey et al., 1996]. It comprises of six sites separated in longitude, located in The Big Bear Solar Observatory in California, USA, The High Altitude Observatory at Mauna Loa in Hawaii, USA, The Learmonth Solar Observatory in Western Australia, The Udaipur Solar Observatory in India, The Observatorio del Teide in the Canary Islands, and The Cerro Tololo Interamerican Observatory in Chile. By using six sites, there is a greater chance of continuous coverage, with an average of 1.8 sites observing at any given time and an typical fill of 80%. GONG provides a range of data products such as magnetogram, velocity and intensity data, which have applications for global and local helioseismology.

Each of the six GONG stations use a Fourier Tachometer [Beckers & Brown, 2013], which use a polarising Michelson interferometer at its centre. Every minute the tachometers measure the Doppler shift of the Ni I Fraunhofer line at 6768Å. As the

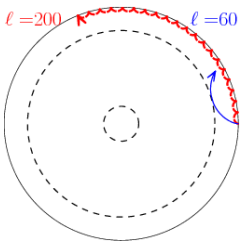

instruments have spatial resolution, the Doppler shifts can be used to produce a full disk Dopplergram and surface velocity field. Solar rotation can be observed in these surface velocity fields as seen in Fig. 3.1. We also see residual velocities caused by the Earth's relative motion. GONG accounts for both of these phenomenon, producing a corrected full disk Dopplergram time series with a cadence of one minute. Through the GONG standard pipeline [Hill et al., 1996] the corrected time series of full disk Dopplergrams are decomposed into spherical harmonic coefficient time series for each set of (m, ℓ) where $\ell \leq$200. Each time series is rebinned to the duration of a 'GONG month', equivalent to 36 days.

Each one month time series is merged into a 3-month set (108 days), centred upon the second month. This time series is processed by a procedure called PSERIES[1], transforming it into the frequency domain and producing a $\ell - \nu$ power spectrum. This Power spectra may be then assessed by *PEAKFIND*[2] to obtain the mean frequency of a mode multiplet, $\nu_{n,\ell}$. *PEAKFIND* does this by applying a non-linear maximum likelihood technique to fit Lorentz profiles to the $\ell - \nu$ power spectrum. The resulting mode frequency (and associated quantities, such as frequency error), are then further processed by a procedure called *PKWORKS* which removes leaks and bad fits. This produces, amongst other products, the *mrv1y* product from which we can obtain the mean mode frequencies, $\nu_{n,\ell}$. We only use the mean frequency of a multiplet in this thesis, $\nu_{n,\ell}$, which depends only on the spherically-symmetric component of the solar structure. However we mention that *mrv1y* product also contains approximations of the frequency splitting of mode multiplets by providing approximations of the first five Clebsch–Gordon splitting coefficients for each multiplet. The frequency splitting for a given mode is related to the Clebsch–Gordon splitting coefficients by the following relationship,

$$\nu_{n,\ell,m} = \nu_{n,\ell} + \sum_i c_{i,n,\ell}\gamma_{i,\ell}(m), \tag{3.1}$$

where $\gamma_{i,\ell}(m)$ are orthogonal polynomials defined in Eqn. 33 of Ritzwoller & Lavely [1991]. The Clebsch–Gordon splitting coefficients are given by $c_{i,n,\ell}$. Mean mode frequencies given in the *mrv1y* tables are measured in µHz, which are used to measure p-mode frequency shifts in Chapters 5 and 6. All GONG data is publicly available here[3].

[1] `https://gong.nso.edu/data/iraf_help/pseries.html`
[2] `gong.nso.edu/data/iraf_help/peakfind.html`
[3] `gong2.nso.edu/archive/patch.pl`

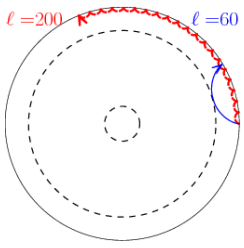

3.2 SOHO

The Solar and Heliospheric Observatory (SOHO) is the result of a collaboration between National Aeronautics and Space Administration (NASA) and the European Space Agency (ESA) and was launched in December 1995 carrying twelve instruments that are capable of studying the Sun from the interior in the deep core to the outer corona and solar wind[4]. SOHO orbits around the first Lagrangian point (L1) and as such can provide continuous coverage of the Sun. The spacecraft was briefly lost in June 1998 in what became known as the 'SOHO vacation' wherein two on-board gyroscopes failed. It was recovered shortly after, but the resulting data gap can be seen in archival data and is discussed in Chapter 6. Of the twelve instruments, this thesis uses two; the *Michealson Doppler Imager* (MDI), and the *Large Angle and Spectrometric Coronagraph Experiment* (LASCO). At the point of writing, SOHO continues to operate and is expected to continue to do so until the end of 2025- almost three decades longer than was originally planned, although several instruments including MDI have ceased operations.

3.2.1 MDI

The MDI instrument aboard SOHO was active from 1st May 1996 to 12th April 2011. The instrument recorded filtergrams of the Sun using use of two tunable Michelson interferometers with a FWHM bandwidth of 94mÅ. These filtergrams provided velocity and continuum intensity readings with an resolution of 4 arcseconds. Using the spatially resolved velocity measurements which, like GONG, have a cadence of 1 minute we obtained p-mode frequencies. These frequencies are produced from time series with a cadence of 72-days [Scherrer et al., 1995; Larson & Schou, 2015, 2018] to identify modes with $\ell \leq 300$ with units µHz. The p-mode frequencies were obtained by the data analysis pipeline run at the SOI Stanford Support Centre [Kosovichev et al., 1997]. The source code on the global pipeline can be found here[5]. This involved using the standard helioseismic data analysis procedure [Hill et al., 1996] to obtain the oscillation power spectra. The spectra are produced by Fourier analysis, similar to the GONG standard pipeline, using the procedure *JTSSLICE*[6]. The package *JPKBGN*[7] extracts mode parametres by fitting symmetric Lorentzians from the resulting Fourier power spectra which are outputted as ASCII files. We use MDI data in Chapters 5 and 6 when measuring p-mode frequency shifts wherein we use the *mdi.vw_V_sht_modes* data product, which follows

[4] soho.nascom.nasa.gov
[5] jsoc.stanford.edu/cvs/JSOC/proj/globalhs/apps/
[6] jsoc.stanford.edu/globalhs/jtsslice.txt
[7] jsoc.stanford.edu/globalhs/jpkbgn.txt

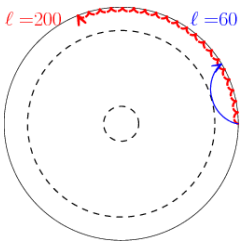

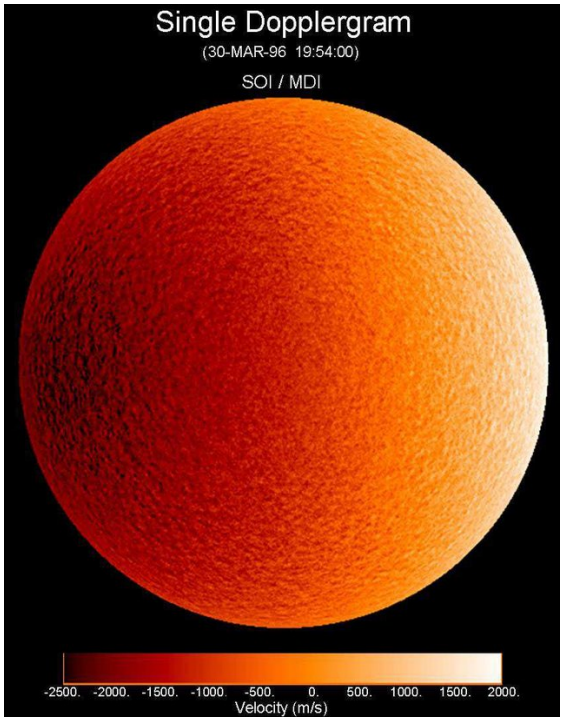

Figure 3.1: Dopplergram of the Sun, taken on March 30$^{\text{th}}$ 1996, by the Michealson Doppler Imager (MDI). Shading represents line-of-sight velocity towards the observer, and the velocity field can be seen to be dominated by solar rotation. *(Figure originally produced/provided by Douglas Gough)*

default processing. Full details on MDI products, and the different processing methods that are applied, can be found here[8]. These data can be found at the Joint Science Operations Center (JSOC) website, which also provides AIA, IRIS and SID data[9].

3.2.2 LASCO

The LASCO coronagraph (Large Angle and Spectrometric Coronagraph Experiment) blocks out light coming directly from the solar disk and instead images the fainter solar corona [Brueckner et al., 1995]. LASCO photographs the solar corona at 1.1 – 32 $R_{\odot}$ by the use of three coronographs, C1, C2, and C3, and can be used to detect and track CMEs. The identification of CMEs is done manually, using data from C2 and C3 as C1 was disabled in June 1998. This data is used in Chapter 7 where we examine whether the presence of a CME impacts the non-stationarity of QPPs. LASCO data is

[8] `jsoc.stanford.edu/MDI/MDI_Global.html`
[9] `jsoc.stanford.edu/ajax/lookdata.html`

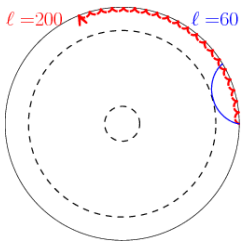

commonly used by the Space Weather Prediction Center (SWPC) to forecast upcoming space weather events. LASCO real time images can be be found here[10] and the LASCO CME catalogue can be found here[11].

3.3 SDO

The Solar Dynamics Observatory (SDO) is a space-based mission launched on 11$^{\text{th}}$ February 2010 [Pesnell et al., 2012]. It carries three instruments; *Extreme Ultraviolet Variability Experiment (EVE)*, *Helioseismic and Magnetic Imager (HMI)* , and *Atmospheric Imaging Assembly (AIA)*. Created and maintained by NASA, SDO is in a geosynchronous orbit at an altitude of 35,789km, which allows near continuous solar coverage.

3.3.1 HMI

Helioseismic and Magnetic Imager (HMI) is commonly thought to be the successor to MDI as it similarly produces Dopplergrams with an improved cadence of 45 seconds [Schou et al., 2012; Scherrer et al., 2012]. HMI examines the Doppler shift of the 6173Å Fraunhofer line with spatial resolution of 1 arcsecond, once again through the use of two Michelson interfermoters. Like MDI, HMI detects the central frequencies in µHz of p-modes for $\ell \leq$300 with a cadence of 72-days. As HMI is effectively the follow on-mission from MDI, it uses the same processing techniques and procedures: *JTSSLICE* and *JPKBGN*, albeit with some improvements in the detection of bad fits and leaks. In Chapters 5 and 6 where this data is used, we use the *hmi.V_sht_modes* product which, like the MDI data, has been fitted using symmetric Lorenzians. Data collected by HMI began on 30$^{\text{th}}$ April 2010 and therefore HMI's data overlaps with MDI by five 72-day datasets. HMI data is used in Chapters 5 and 6. Further information on HMI can be found here[12], and HMI data can be accessed here[13].

3.3.2 AIA

The Atmospheric Imaging Assembly (AIA) is an instrument lead by Lockheed Martin Solar and Astrophysics Laboratory (LMSAL) and provides observations of the solar surface with spatial and time resolution [Lemen et al., 2012]. These observations cover

[10] lasco-www.nrl.navy.mil/index.php?p=content/realtime
[11] cdaw.gsfc.nasa.gov/CME_list/
[12] hmi.stanford.edu/Description/hmi-overview/hmi-overview.html
[13] sdo.gsfc.nasa.gov/data/aiahmi/

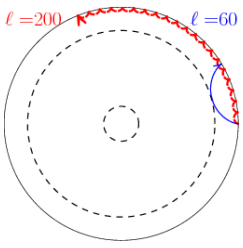

10 channels, focused on wavelengths between 9.4 – 450 nm ranging from regions within the upper corona down to the photosphere. These observations are covered by four individual narrow-band telescopes. AIA observations have a cadence of 12 s, providing near continuous coverage since May 2010. We use AIA data to examine the spatial evolution of a resolved flaring loop in Chapter 7. AIA data is available from the JSOC website[9] and can be also downloaded here[14].

3.4 BiSON

The Birmingham Solar Oscillations Network (BiSON) is a world wide set of six ground-based telescopes and which provide continuous coverage of global p-modes [Broomhall et al., 2009; Davies et al., 2014; Hale et al., 2016]. Funded by Science and Technology Facilities Council (STFC), the six remotely operated observatories are located in Mount Wilson, USA, Las Campanas, Chile, Sunderland, South Africa, Izaña, Spain, Carnarvon, Australia, and Narrabri, Australia. They are operated by the University of Birmingham in collaboration with Sheffield Hallam University. BiSON has been running continually since 1976, making use of resonant scattering spectrometers, containing a silica vapour cell, which measure the Doppler shift of a Franhoufer line, similar to GONG, MDI, and HMI. BiSON provides mode frequencies for low ℓ p-modes, measured in µHz, which are discussed in Chapter 5, and can be found here[15]. These observations are unresolved (meaning that it takes Sun-as-a-star measurements), and so BiSON can only accurately measure $\ell \leq 3$ modes, as modes with higher harmonic degree have too low a signal to noise ratio. These mode frequencies are obtained by fitting asymmetric Lorenzians to power spectra using maximum likelihood functions.

3.5 $F_{10.7}$ index

The flux density of solar radio emission at 10.7 cm is known as the $F_{10.7}$ index and is commonly used as a proxy for solar activity [Tapping & Detracey, 1990; Tapping, 2013]. The $F_{10.7}$ index is well correlated with frequency shifts of low [Chaplin et al., 2007] and intermediate harmonic degree ℓ [Jain et al., 2009] modes, as well as sunspot number data, solar irradiance and UV emissions. The $F_{10.7}$ index is sensitive to quiet Sun, plage and Active Regions, though the exact radiation mechanisms are not understood. The dataset dates back to 1947, and today is measured daily at local noon in the 10.7 cm

[14] `aia.lmsal.com/`
[15] `bison.ph.bham.ac.uk/portal/frequencies`

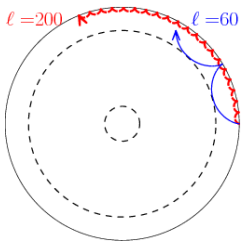

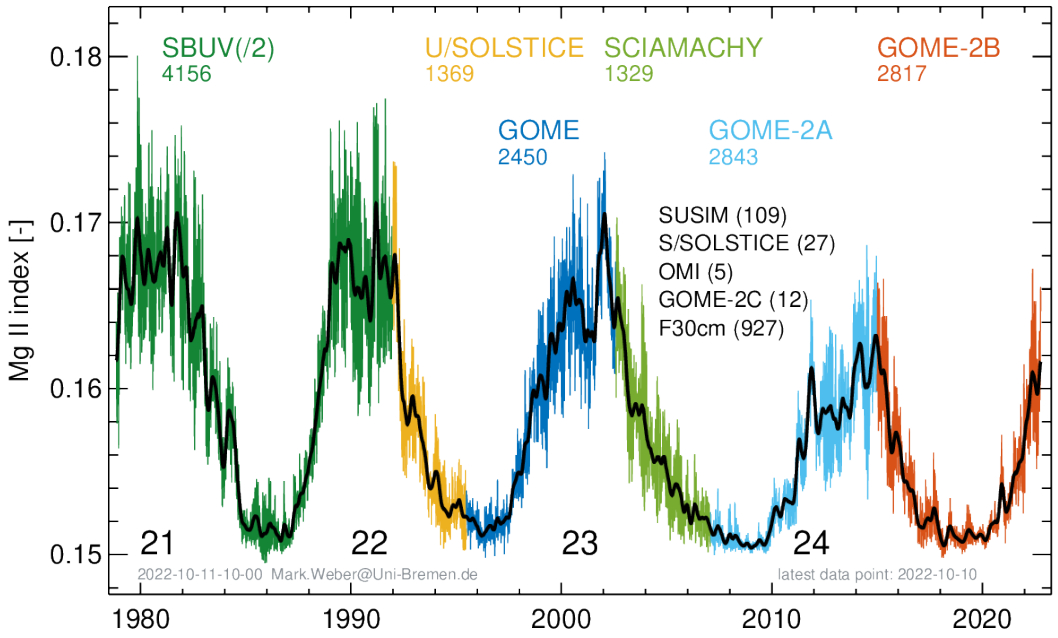

Figure 3.2: Bremen composite MgII index from 1978–2022, with amplitudes that are well correlated with the solar cycle, with solar cycle number indicated in black. Data sources are colour coded, with the number of days contributed by each satellite indicated below the instrument name. Additional data sources that have contributed fewer than 1000 days are shown in black, with the number of days contributed shown in parenthesis. Black curve shows the index twice smoothed by a 55-day boxcar. *Figure from* `iup.uni-bremen.de/UVSAT/Datasets/mgii`

waveband (2800 MHz) at the ground-based Dominion Radio Astrophysical Observatory (DRAO) in Penticton, Canada. The $F_{10.7}$ index is usually given in Radio Flux Units (RFU), where $1\,\mathrm{RFU} = 10^{-22}\,\mathrm{W\,m^{-2}\,Hz^{-1}}$. The data, discussed in Chapters 5 and 6, can be accessed from the Canadian National Research Council website[16].

3.6 Bremen Composite MgII index

The Bremen Composite MgII index gives the core-to-wing ratio of MgII Fraunhofer doublet at 280 nm. The MgII index is also often used as a solar activity proxy as it is well correlated with the Schwabe cycle [Viereck et al., 2001]. The MgII index is sensitive to the conditions in the solar upper corona, and as such is well correlated with Extreme Ultraviolet (EUV). The composite dataset, produced by the University of Bremen for which it is named, is derived from several data sources, most recently GOME (1995-

[16] `nrc.canada.ca/en`

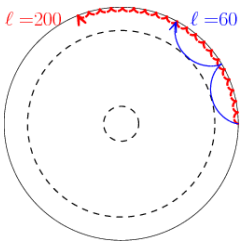

2011) [Weber et al., 1998], SCIAMACHY (2002-2012) [Bovensmann et al., 1999], and GOME-2A, B and C (ongoing) [Callies et al., 2000]. The Global Ozone Monitoring Experiment (GOME) was launched on the European Remote Sensing Satellite-2, and contained a nadir scanning ultraviolet and visible spectrometer, from which the unitless MgII index was measured. SCIAMACHY and GOME-2C work in similar ways, with GOME-2C carried on MetOp, an ESA-run weather probing satellite. The dataset, first discussed in Heath & Schlesinger [1986], produces high cadence and low error data, seen in Fig. 3.2. The data is used in Chapters 5 and 6 and may be found here[17].

3.7 RHESSI

Reuven Ramaty High Energy Solar Spectroscopic Imager (RHESSI) was a solar observatory, launched in February 2002 as part of the Small Explorer program run by NASA [Lin et al., 2002]. It performed high resolution imaging and spectroscopy of solar flares in the range of 3keV–17MeV, in the range of X-rays and gamma Rays.[18] RHESSI uses 9 Rotational Modulation Collimators (RMCs), which together can be used to reconstruct images with spatial resolution up to 2 arcseconds. Each RMc hosts two fine-scale linear grids, made of tungsten and molybdenum, which allow an incoming photon to be modulated as the spacecraft rotates. This modulation is detected and assessed using Fourier analysis. BY combining the readings of all 9 of these RMCs, which each have different slit widths, the flare source can be accurately determined. RHESSI's data is rebinned to produce outputs with cadences of 2 s to milliseconds depending on the quality of the output. RHESSI's orginial mission duration was planned to be 2 years, but RHESSI continued to observe until it ceased operations in April 2018. RHESSI data can be found here[19]. Data from RHESSI is used in tracking peak of an X-ray emitting coronal loop in Chapter 7.

3.8 GOES

The Geostationary Operational Environmental Satellite (GOES) program, operated by NASA and National Oceanic and Atmospheric Administration (NOAA), is a system of 18 satellites to date, which collect data primarily for weather forecasting, meteorology, and environmental observations. We use the X-ray sensor (XRS) aboard GOES 13–

[17] www.iup.uni-bremen.de/UVSAT/Datasets/MgII
[18] www.eoportal.org/satellite-missions/rhessi-reuven-ramaty-high-energy-solar-spectroscopic-imager
[19] hessi.ssl.berkeley.edu/data/

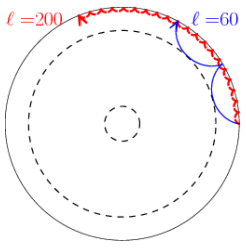

15 to assess solar activity. XRS observes across 2 wavebands in the soft X-ray (SXR) range: 0.5–4 Å (short channel) and 1–8 Å (long channel) [Neupert, 2011]. Gas-filled ion chambers are used to obtain the X-ray measurements in units W m^{-2}. Only X-rays are detected by the use of sweeper magnets which deflect incoming electrons and ions. The short channel detector has a cutoff determined by the ion cell. The long channel instrument has a wavelength cutoff determined by the thickness of the Beryllium filter [Hanser & Sellers, 1996]. In Chapter 7 we use data from these spacecraft to assess the non-stationarity of QPPs during solar cycle 24. The XRS data has a cadence of 2.047 s. In order to get true fluxes for GOES 1-15 the scaling factors of 0.85 and 0.7 for short and long channel data respectively must be divided out (see the GOES documentation[20] for further information) This is due to a depreciated scaling that was done to match up the data from GOES-7 to GOES-8. Hence the data discussed in Chapter 7 has true fluxes, following the removal of these scaling factors. The high cadence data is especially valuable in looking at QPPs, where many QPPs have periods of the order of 10 s of seconds or less. The GOES satellites are also incredibly important when it comes to flare data as we classify the energy of the flare by their peak emission in the long channel (see Section 1.1.9). GOES data can be downloaded here[21].

[20] www.ngdc.noaa.gov/stp/satellite/goes/documentation.html
[21] ngdc.noaa.gov/stp/satellite/goes/index.html

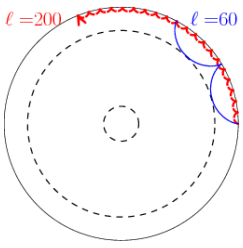

Chapter 4

Data analysis methods

In this chapter, I introduce three data analysis techniques used within this thesis; the Empirical Mode Decomposition (Section 4.1), the Fast Fourier Transform (Section 4.2), and Wavelet analysis (Section 4.3).

4.1 Empirical Mode Decomposition

Empirical Mode Decomposition (EMD) is a method capable of decomposing a dataset, such as a time series, into a set of functions, called Intrinsic Mode Functions (IMFs) which form a complete basis for the input signal. IMFs are described fully in Section 4.1.1, and an example of them can be seen in Fig. 4.1. The benefit of characterising a signal using IMFs is that they're allowed to vary in shape, phase, and amplitude and so are well suited to describe non-stationary processes. The spectral energies of IMFs can be tested against confidence levels, meaning that statistically significant behaviours can be extracted from input signals. The decomposition procedure for EMD was first described in Huang et al. [1998, see Section 5 and equations therein for a full derivation] wherein IMF's are 'sifted' out via the sifting procedure (Section 4.1.2).

4.1.1 Intrinsic Mode Functions

For a signal to be considered an IMF, it must fulfil two criteria;

- The number of zero crossings and the number of IMF extrema should differ by no more than one,
- At any point of an IMF the mean envelope should equal zero.

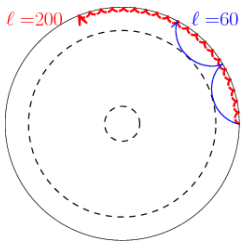

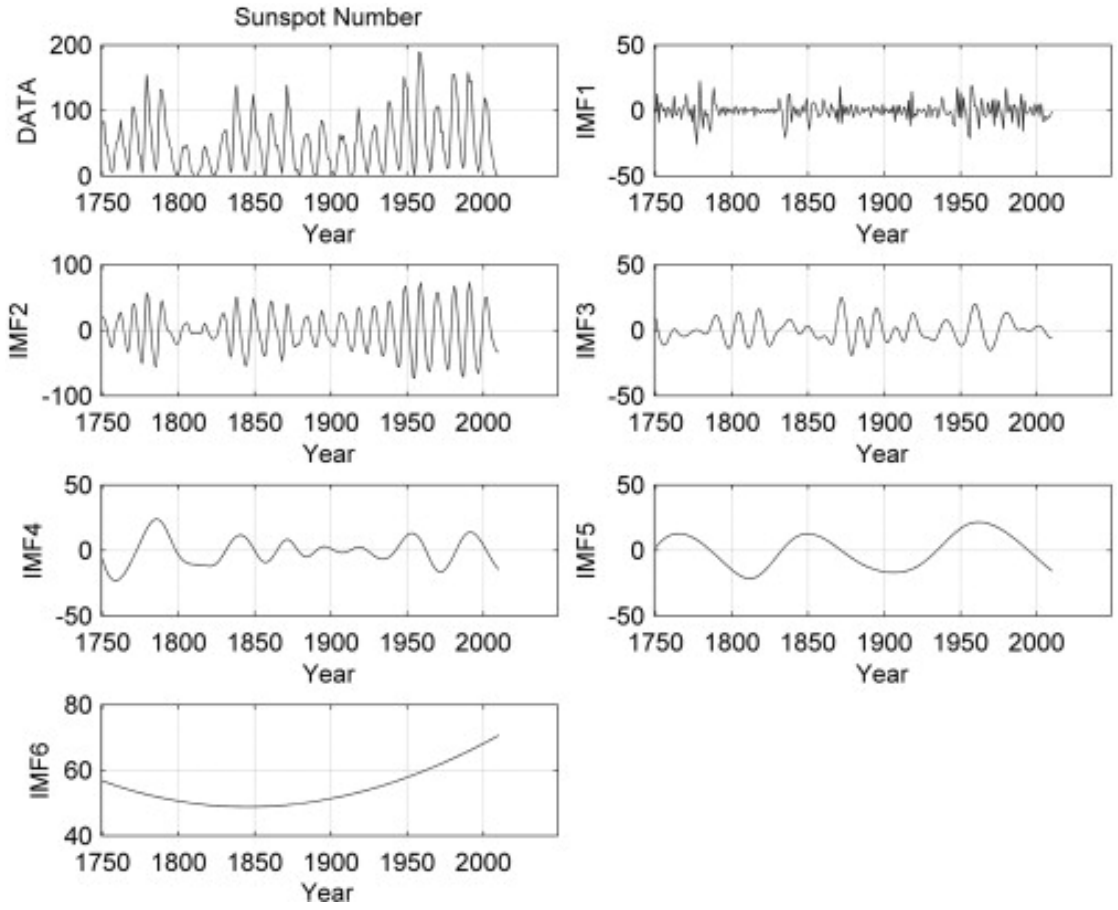

Figure 4.1: Decomposition of Sunspot Number (SSN) data (*Top Left*) from 1750–2010 into 6 IMFs by EMD, originally published as Fig. 1 from Barnhart & Eichinger [2011]

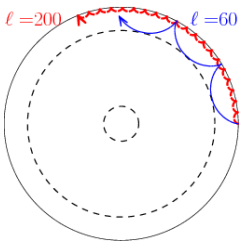

The decomposition of SSN data by EMD results in the IMFs seen in Fig. 4.1. Each of the IMFs (excluding IMF6) are approximately symmetric around the x-axis. IMF6 may be considered part of the trend as its dominant period is larger than 0.7× the duration of the signal (a commonly used 'cut off' for differentiating oscillations from the trend) and as it therefore exhibits fewer than three full cycles of oscillation over its duration. The extraction of IMFs in this way can reveal some enlightening features; for example IMF2 shows the approximately 11 yr Schwabe cycle and even correctly identifies the Dalton minimum from $\sim$ 1790 – 1830. IMF2 changes amplitude and its instantaneous periodicity throughout its duration preserving the valuable features seen in the input data.

4.1.2 Sifting procedure

An iterative sifting process is used to decompose input data into a number of IMFs, with each successive IMF decreasing in average period (although IMFs are often labelled from shortest to longest period, as in Fig. 4.1). For this reason, the final IMF to be obtained can usually be attributed to the trend of the data (although in some cases we reconstruct a trend from several IMFS which have average periods greater than 0.7× the duration of the signal). Therefore we may also use EMD to detrend a dataset.

The sifting process used to obtain IMFs is as follows:

1. First, identify the local maxima and minima of the input signal,
2. Next using these extrema, construct upper and lower envelopes via cubic spline interpolation,
3. Then construct the data's mean envelope, and subtract it from the data,
4. Check whether the new signal (which we call the proto-IMF) *A.* fulfils the IMF criteria detailed in Section 4.1.1 and *B.* whether the standard deviation between this proto-IMF and the input signal from the previous sift is less than the user defined *shift-factor* (see Section 4.1.3). If so the proto-IMF is deemed to be an IMF, if not the proto-IMF becomes the new input signal, and we repeat steps 1-4.

We continue sifting the data in this way, producing, testing, and refining proto-IMFs until they fulfil the IMF criteria and a number of IMFs have been obtained. We introduce a stopping criteria to prevent the process from running indefinitely for sufficiently highly resolved data. The computation stops when either the signal is found to be monotonically increasing or decreasing, such that no more IMFs can be extracted,

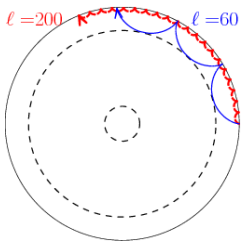

or when the standard deviation between two subsequent sifts is lower than the user defined *shift-factor*. A user may also introduce a maximum number of successive sifts allowed in obtaining an IMF, to prevent excessively long computation time and suppress surplus IMFs that may arise from excessive sifting. A user may also set a threshold for the minimal amplitude of an IMF. What remains of the signal after the sifting process is labelled the residue, or residual of the signal.

4.1.3 Choosing the *shift-factor*

The *shift-factor* is a predetermined user-defined quantity that dictates the sensitivity of the sifting process. We define the *shift-factor* to be the threshold against which we compare the standard deviation between two subsequent shifts (see Eqn. 4.1); if the standard deviation is less than the *shift-factor* then the computation ceases and the proto-IMF is denoted to be an IMF.

$$\text{Standard deviation} = \sum_{t=0}^{T} \frac{|g_{k-1}(t) - g_k(t)|^2}{g_{k-1}^2(t)}, \tag{4.1}$$

where k is the index representing the number of sifting iterations carried out so far, g is a proto-IMF which depends on time t, over duration T.

The choice of a 'large' *shift-factor* (e.g. 1 or 2) results in fewer IMFs, opposed to a 'small' *shift-factor* (e.g 0.01) which results in a large number of IMFs, some of which could be spurious. The ideal choice of *shift-factor* results in usually 3-15 IMFs that each have timescales, amplitudes, and shapes that are approximately constant over their duration and are roughly 'unique' from other IMFs. An IMF produced by analysis with too high a *shift-factor* is thought to be 'under-sifted' and will have two or more vastly different timescales in its profile. Conversely an 'over-sifted' produce could produce two extremely similar IMFs of comparable shapes, amplitudes and timescales.

As finding the optimal *shift-factor* is clearly a user-intensive and sensitive process, we turn to AuTomated Empirical Mode Decomposition (ATEMD)[1]. ATEMD automates the optimal choice of the *shift-factor* by running the sifting process iteratively with 200 *shift-factors*, that are separated in log-space from 0.05 to 1. ATEMD then selects the *shift-factor* that corresponded to the minimal sum of the squared difference between the proto-IMF and the input signal for each IMF. In this way the optimal IMFs are automatically selected. For this reason we use ATEMD in the remainder of this thesis, although we continue to refer to it as EMD for convenience.

[1] `github.com/Sergey-Anfinogentov/EMD_conf/blob/master/atemd.pro`

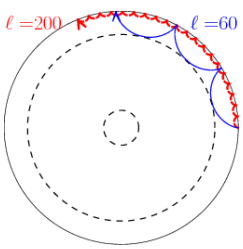

4.1.4 Confidence levels for EMD analysis

In this section we discuss the procedure for obtaining confidence levels on EMD spectra, which follows the methods outlined in Kolotkov et al. [2016] and documented here[2]. An EMD spectrum of the data presented in Fig. 4.2 can be seen in the left panel of Fig. 4.3. IMFs are plotted according to their dominant period (as calculated by the peak value in its Global Wavelet Spectrum (GWS) - see Section 4.3.2) and their energy (the sum of the IMF's squared amplitudes). It is important to emphasise here that many IMFs are non-stationary and so the peak of an IMF's GWS only gives an estimation of the weighted-average period. We assume the energy of an IMF follows a χ^2 distribution (with degrees of freedom as a free parameter to be obtained), which is true for all IMFs except for the IMF with the shortest weighted-average period. Therefore the IMF with the shortest period is excluded from the analysis for all EMD obtained results in this thesis. We also choose to exclude the trend, taken to be the sum of any IMFs with average periods greater than 0.7× the duration of the signal.

We relate an IMF's average period P_m and its energy E_m by

$$E_m {P_m}^{1-\alpha} = \text{constant}, \tag{4.2}$$

where parameter alpha (α) characterises the colour(s) of noise present in the signal. We know that white noise (with α_{w}=0) will exist in any solar data. To determine the value of α for the coloured noise, α_c (which is usually between 1–3.5), we fit the Fourier spectrum of the input signal with a broken power law. The flat slope will represent the region of the spectrum dominated by white noise, and the inclined region is dominated by coloured noise. Therefore we extract the gradient of the sloped region to obtain α_{c}. This is because the signals' power in period space follows the following relationship;

$$S \propto f^{-\alpha}, \tag{4.3}$$

with Fourier power spectral density S, and frequency f, and α as previously defined. Obtaining the value for α_{c} allows us to construct confidence levels for EMD spectra using Monte-Carlo simulations. We create 500 samples of pure noise (250 with $\alpha_{\text{w}} = 0$ and 250 with α_{c} determined from the fitting of the Fourier spectrum). In this thesis EMD will be primarily used to assess frequency time shift series, which have well defined error bars. Although the original code that I have signposted in this thesis uses a constant obtained from the fitting of the data to define the standard deviation of the simulated

[2] `github.com/Sergey-Anfinogentov/EMD_conf`

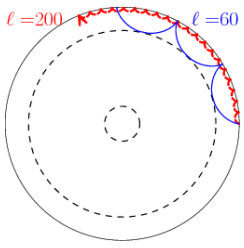

noise samples, the code was modified for this thesis to make the standard deviation of each sample equal to the average error on the frequency shift data. In this way we can incorporate the error from the input data directly into its analysis. We run all of the samples through EMD and obtain all of the average periods and energies of all of the resulting IMFs, which we call test-IMFs. We can use the meta properties of these test-IMFs to create the confidence levels against the IMFs obtained from our signal.

To find the confidence level for the n^{th} IMF, we fit a χ^2 distribution to the energy distribution of the n^{th} test-IMFs (once for the white noise samples, and again for the coloured noise samples), with degrees of freedom a free parameter to be found. We then find the 95% confidence level of this fitting for both noise colours, giving the 95% confidence levels for the n^{th} IMF for white and coloured noise. We now repeat this process across all IMFs and interpolate the confidence levels for white and coloured noise separately, and them sum over them both, giving a single confidence level across the spectrum. This is the 95% confidence level seen in all EMD spectra throughout this thesis.

4.1.5 Errors

We can find the error on an IMF's average period by examining the IMF's GWS. We remind the reader that we denote an IMF's period to be the peak value in the GWS, and so it follows that we use the GWS's Full Width Half Maximum (FWHM) to calculate the IMF's error in period, as seen in Fig. 4.4. Many statistically significant IMFs in this thesis show non-stationary behaviour which will act to distort the distribution of power in a GWS. This effect is compounded by the limited resolution of the wavelet which causes broader peaks in period space for longer periods. Therefore the resulting GWS may naturally show a considerable spread in the period domain leading to large errors. We emphasise that the 95% confidence level used here and throughout the paper relates to the statistical significance of the IMF and the probability that it is not an artefact of noise. Therefore we discuss an IMF with a given period as being above, e.g. a 95% confidence level, implying that there is a 5% probability (or less) that the IMF is the result of noise in the signal. This does not tell us anything about the confidence of the weighted-period of the IMF which is obtained from the IMFs GWS as discussed above.

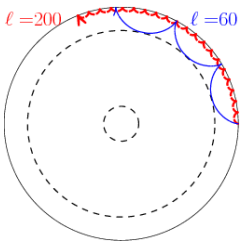

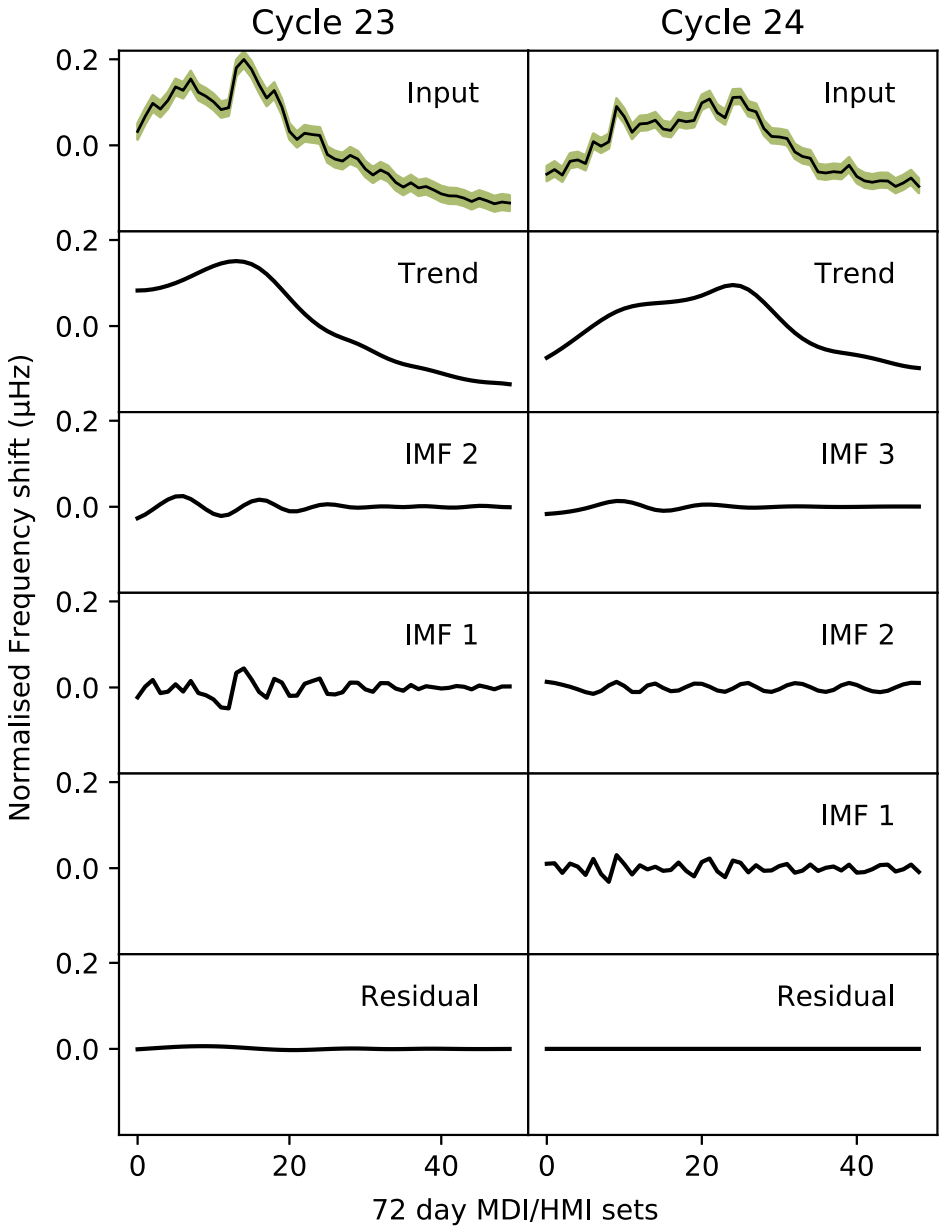

Figure 4.2: Averaged frequency shifts from modes with lower turning points between 0.7–0.75 $R_\odot$ and frequency between 3200–3600 μHz during Cycle 23 (*Top left*) and Cycle 24 (*Top Right*) as measured by MDI/HMI. Frequency shifts have been normalised to have zero mean, with errors seen in green. Lower panels show the IMFs obtained from the decomposition from Cycles 23 (*Left*) and 24 (*Right*). IMF 2 (with an average period of 721 d) from Cycle 23 and IMFs 2 (437 d) and 3 (889 d) from Cycle 24 are statistically significant above a 95 % confidence level. The IMFs with the shortest average periods from each cycle, (IMFs 1) are excluded from the analysis as they cannot be assessed with the confidence levels used.

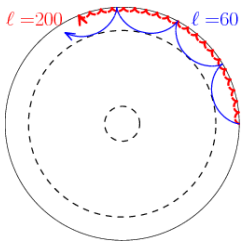

4.2 Fast Fourier Transform (FFT)

The Fast Fourier Transform (FFT) is a well established analysis technique which has been used at length assessing data of solar and stellar origin, and is built on the work by Cooley & Tukey [1965]. The FFT is a more efficient method of computing the Discrete Fourier Transform (DFT), which converts a signal from its original temporal domain to the frequency domain. The resulting spectrum in frequency space shows relative amplitudes of different frequency componants which, when summed back up, reproduce the input signal exactly. The width of the frequency bins in frequency space are restricted by the Nyquist frequency of the data ($(2\delta t)^{-1}$ where δt is the cadence of the input data). FFTs or periodogram based approaches have a long history of applications to solar and stellar data, e.g. Lipa [1978] and more recently Broomhall et al. [2019]. It has the benefit of being an extremely efficient algorithm, and can quickly be applied to large datasets. It can also be performed without pre-processing, although it may struggle with data with large amplitude trends which often dominate the spectrum and obscure higher frequency componants. The inherent assumption of the FFT is that the signal contains a series of stationary sinusoidal signals. Therefore spectral leakage (where spectral power is spread over a number of bins in the frequency domain due to a non-stationary input) can be a significant problem for quasi-oscillatory signals assessed with the FFT. This effect reduces the chance of a given bin containing enough spectral power to be significant. Therefore, for signals with non-stationary and non-sinusoidal properties, such as the QBO, the FFT is a less effective tool in detecting periodicities. In this work we use the FFT algorithm given by SCIPY[3] [Virtanen et al., 2020] and the FFT program built into Interactive Data Language (IDL)[4].

4.2.1 Confidence levels

For the FFT analysis discussed in Chapters 5 and 6, we estimate the confidence level for Fourier spectra in a similar way to EMD. We fit a χ^2 distribution with two degrees of freedom on the energies of estimated white and coloured noise componants, and find the corresponding 95% confidence level, based on a 5% false alarm probability. In Chapter 7 we turn to using the methodology described in Pugh et al. [2017a] to obtain confidence levels. The change in methodology is due to computation being performed with IDL in Chapters 5 and 6 and Python in Chapter 7. The methodology described in Pugh et al. [2017a] is closely based on the work presented in Vaughan [2005] and works by

[3] `docs.scipy.org/doc/scipy/tutorial/fft.html`
[4] `www.l3harrisgeospatial.com/docs/fft.html`

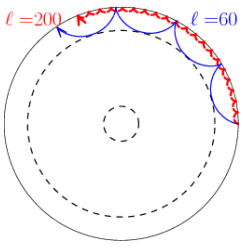

incorporating estimated errors on a fitted broken power law to the signal's periodogram to account for white and red noise. The procedure can be found here[5]. An example of an FFT spectrum with an associated confidence level found by the IDL procedure can be seen in Fig. 4.3.

4.2.2 Errors

In order to calculate errors on results found by FFT, we employ the standard approach. This method incorporates the error in frequency $\delta\nu$, which is equivalent to $\frac{1}{N(\delta \mathrm{t})}$ for a signal with N datapoints, separated in time by $(\delta \mathrm{t})$. We propagate the errors into period space by the following relation;

$$\pm \Delta P = \left| \frac{1}{\nu \mp \delta\nu} - \frac{1}{\nu} \right|, \tag{4.4}$$

where ΔP is the error on the period and ν is the statistically significant frequency found in the power spectrum. We use this method of finding errors on results from Fourier spectra in Chapters 5–7.

4.3 Wavelet Analysis

Wavelet analysis [Daubechies, 1990; Torrence & Compo, 1998] produces a power spectrum that is capable of tracking the evolution of the local time scales of the input data. This is a valuable tool for examining data which contains multiple periodicities or signals that are non-stationary. Wavelet analysis works by convoluting a wavelet function with the input time series, where the width of the wavelet function varies after each pass. The changing width allows for multiple timescales in the data to be examined, over Fourier-based approaches which have a prescribed fixed window width. This method allows the resulting wavelet power spectrum to retain time resolution which we can use to observe changes instantaneous periods in the data. Wavelet analysis can struggle in noisy conditions, which presents problems when assessing low amplitude oscillations. In this thesis we use continuous wavelet analysis (Section 4.3.1) and global wavelet analysis (Section 4.3.2).

[5] `github.com/chloepugh/QPP-confidence-levels`

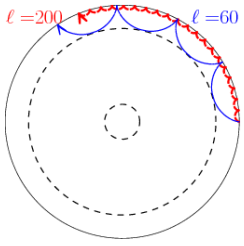

4.3.1 Continuous Wavelet Transform

The Continuous Wavelet Transform (CWT) produces a spectrum that retains time resolution and presents the relative powers of each periodicity over the duration of the signal. An example of a CWT spectrum is given in Chapter 7. CWT spectra usually show time on the horizontal axis, and frequency (or periodicity) on the vertical axis, with power usually indicated with colour. The resulting heat map means that a quick visual inspection can show how the power in the signal changes over time, and how it may be diverted to other periodicities. We do not assess any confidence levels on the CWT examined in this work, and use them for visualising period evolution only. We use a Morlet wavelet as our wavelet function throughout this work as it is a well used and understood wavelet which shows similarity to QPOs by exhibiting multiple oscillations of varying amplitude. The CWT is well tuned to assessing high frequency data, and has poorer resolution in low frequency data as wavelets with increased width are restricted to a lower number of cycles. All CWTs in this thesis are generated using the SCIPY package[6].

4.3.2 Global Wavelet Transform

The Global Wavelet Transform (GWT) sums the spectrum from the continuous wavelet transform over the time domain, to produce a 2 Dimensional spectrum showing the net distribution of periodicities within the data. From this spectrum we gain information about the dominant periodicities, and the spread in periodicities, but we lose the information on how the periodicities evolve. An example of such a spectrum can be seen in the lower panel of Fig. 4.4. This spectrum is valuable for assessing multiple periodicities as we can clearly see the distribution of power across period space. We use the procedure *pwf-gwsfast*[7] to calculate the GWS, which is used to determine all IMF periodicities discussed in Chapters 5–7. Some works select the peak periodicity in a GWS by fitting a symmetric Gaussian function and selecting its' peak value, but this can result in difficulties if you have multiple periodicities. Fitting a GWS with a curve should be performed in cases where the resolution of the data is low or if you wish to fit only a specific region of the spectrum. However this should be done with caution on non-stationary data as the GWS is not necessarily symmetric and a fitting may remove some of the valuable asymmetric data inherent in the spectrum.

[6] `docs.scipy.org/doc/scipy/reference/generated/scipy.signal.cwt.html`
[7] `github.com/Sergey-Anfinogentov/EMD_conf/blob/master/pwf_gwsfast.pro`

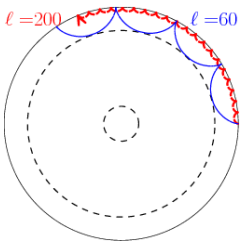

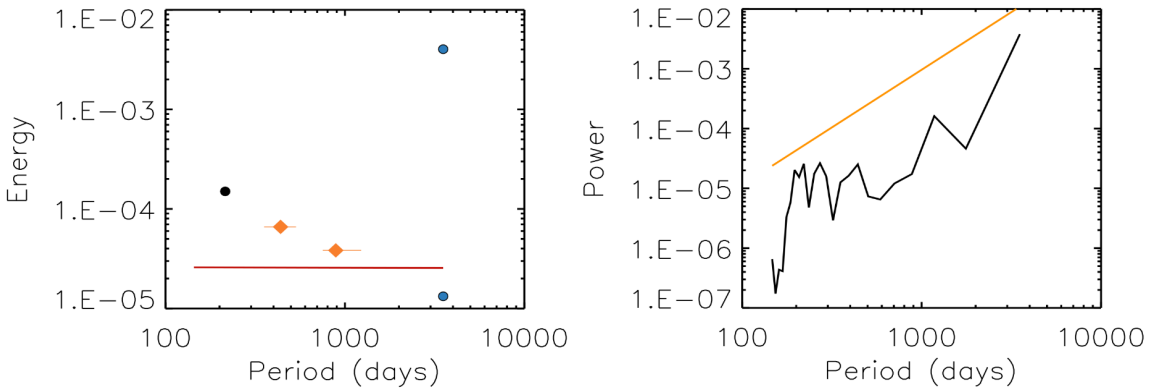

Figure 4.3: (*Left*) EMD spectrum of frequency shift obtained from MDI/HMI data during Solar Cycle 24 seen in the right panel of Fig. 4.2. IMFs are visualised as bullet points indicating the IMFs weighted average period in d against their spectral energy. The 95% confidence level is shown in red. The IMF with the lowest period is shown in black and is excluded from the analysis as it cannot be assessed with the confidence level given. The two statistically significant IMFs and their associated errors in period are shown in orange, with periods of 437 and 889 d. The trend of the data is obtained as the sum of IMFs with periods larger than half of the duration of the signal, here shown in blue. (*Right*) Fourier spectrum of the same frequency shift time series. The red solid line shown on the spectra indicates a 95% confidence level.

4.3.3 Errors

In this thesis we only consider errors on the GWT, as the CWT is only used for illustrative qualitative analysis in Chapter 7. The GWT is used within EMD analysis to calculate the dominant period and its errors for IMFs, and so is used in Chapters 5 and 6. We obtain the errors in the GWS by obtaining the spectrum's FWHM. This is the width in period space corresponding to half the maximal power of the spectrum. The FWHM of a GWS can be seen in the right panel of Fig. 4.4. This method of measuring errors can be especially valuable for non-stationary data, as the spread in the GWS encapsulates the multiple periodicities inherent in a non-stationary signal and provides the reader of the approximate spread of the periodicities. As a result, many of the periodicities discussed in Chapters 6 have large errors, as we are dealing with non-stationary signals. However an uninformed reader may mistakenly take a large error to be an unreliable or measurement, and so it is of great importance to emphasise the meaning behind a large error bar for an non-stationary signal, when using this method of error analysis. We do not assess either the CWT or GWT with confidence levels as we either use them for visualisation methods, or to extract peak values to be assessed by other methods.

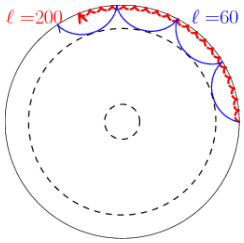

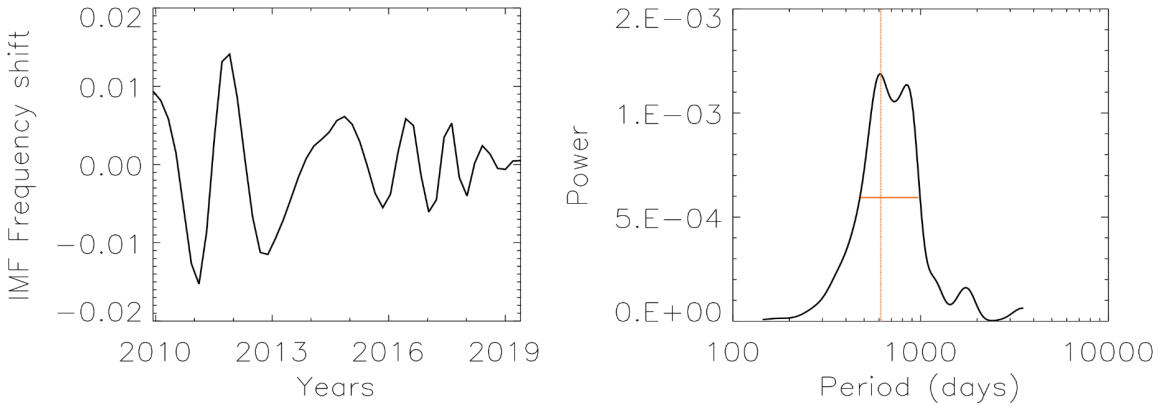

Figure 4.4: Normalised amplitude of a non-stationary IMF (*Left*) from MDI/HMI over the trimmed duration of Cycle 24 and its associated GWS (*Right*). The period associated with maximal power in the GWS is indicated with a vertical orange line. The solid horizontal orange line shows the half-maximum value, used to determine the errors on the average period.

4.4 Visualising IMFs, and EMD, FFT, and Wavelet spectra

We present an example of MDI/HMI data assessed by EMD and the FFT in Figs. 4.2 and 4.3, where Fig. 4.2 shows the decomposition of MDI/HMI data from Solar cycles 23 and 24 (*Left* and *Right* respectively) into their respective trends, IMFs, and residues, and Fig. 4.3 shows the EMD and FFT spectra for the data from Solar Cycle 24.

Visualising IMFs from MDI/HMI data

Fig. 4.2 shows frequency shift time series data from MDI/HMI data, consisting of averaged modes with lower turning points between 0.7–0.75 $R_\odot$ and central frequency between 3200–3600 μHz over Solar Cycles 23 (*Top Left*) and 24 (*Top Right*). Beneath are the IMFs from EMD; the next panels (*Second row*) show the frequency shifts' associated trends (determined as the combination of the two IMFs with the longest periods). The remaining panels show the other IMFs found during the sifting process, and finally the residual of the signals wherein no more IMFs can be extracted as no oscillatory behaviour can be observed. The signal from Cycle 23 (*Left*) decomposes into only two IMFs, whereas the signal from Cycle 24 (*Right*) produces three.

The properties of the IMFs from Cycle 23 are as follows; IMF2 has an average period of 721 d, and was significant above the 95% confidence level, and IMF1, as the IMF

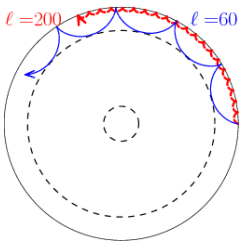

with the shortest average period, is excluded from the analysis as its energy distribution does not follow a χ^2 distribution and so cannot be assessed with the confidence levels used.

For Cycle 24, IMFs 3 and 2 are statistically significant, with periods of 889 d and 437 d respectively, with IMF1 being similarly excluded from the analysis. We examine these IMF further by exploring Cycle 24's EMD spectrum in the Fig. 4.3 (*Left panel*).

EMD and FFT spectra of MDI/HMI data

EMD (*Left*) and Fourier (*Right*) spectra of MDI/HMI data from Cycle 24 can be seen in Fig. 4.3. In the EMD spectrum, we see five IMFs represented by circles, plotted by average period and spectral energy. the 95% confidence level is shown in red. IMF 1, shown in black, has the lowest average period, and we exclude it from the analysis for aforementioned reasons. IMFs 2 and 3, shown in orange, have average periods of 437 and 889 d, with errors on their periods indicated on the spectrum. Both appear above the confidence levels and are therefore considered to be statistically significant. The final two IMFs, shown in blue, both have periods larger than $0.7\times$ the duration of the signal, and so are summed and together are considered the trend of the data. The right panel of Fig. 4.3 shows the Fourier spectrum of the same input data, shown in the Top Right panel of Fig. 4.2. The 95% confidence level is shown in orange. No peaks appear above this confidence level, indicating that the FFT found no significant oscillatory behaviour.

GWS spectrum of non-stationary IMF from MDI/HMI data

Fig. 4.4 shows a statistically significant IMF (*Left*) and its associated GWS (*Right*). The IMF was found by assessing a different frequency shift time series from MDI/HMI data, which occurred during Solar Cycle 24 with $2600 < \nu_{n,\ell} \leq 3000\,\mu$Hz, $0.74 < \mathrm{r_{ltp}} \leq 0.79\,R_\odot$. This IMF has an average period of $613\,^{+360}_{-134}$ d, and can be seen to exhibit amplitude modulation and a period drift.

The IMF's GWS shows significant spread in period space, from approximately 500–1000 d. A double-peak can be seen at roughly 600 and 900 d, which is consistent with a visual inspection of the IMF. A vertical orange line shows the position of the dominant peak in the GWS at 613 d, and emphasises the difficulties in assigning a non-stationary signal a single value for period. A horizontal line shows the spectrum's FWHM, extending from 479–973 d, giving the errors mentioned previously. The large spread in errors are intended to be helpful in communicating the non-stationarity of the IMF to a reader.

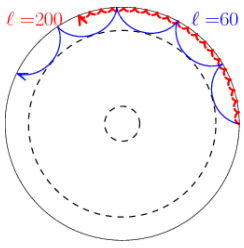

Chapter 5

Effective use of Empirical Mode Decomposition

5.1 Introduction

Empirical Mode Decomposition is a valuable tool in assessing complex signals, and has successfully been applied to solar data [Nakariakov et al., 2010]. However we occasionally observe false positive detections with periods equal to harmonics of the duration of the input signal. These detections appear to be statistically significant above the 95% confidence level set, where periods are equal to $\frac{\text{Duration}}{\text{n}}$ with n = 2,3,4,5. We name these IMFs 'overtones', and we use the shorthand of writing $\frac{D}{n}$ when referring to the n^{th} overtone duration D, with a period $\frac{1}{\text{n}}$ times length of the duration. This phenomenon is not unique to EMD, and has previously been observed in other methods, e.g. Fourier analysis (see Fig. 5.1).

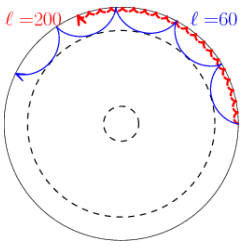

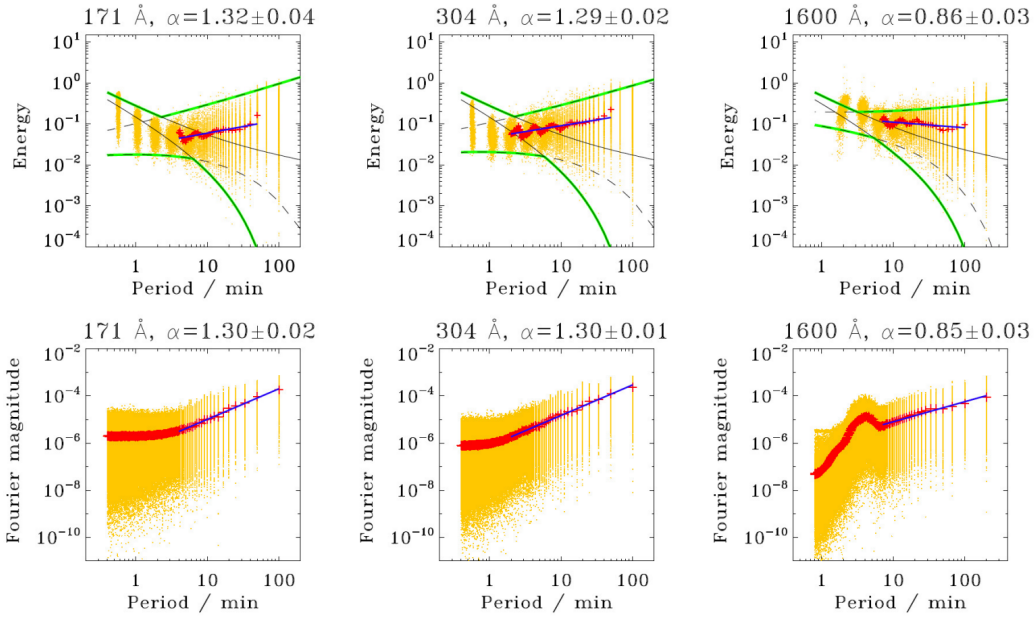

Figure 5.1: *Top panels*: Spectral power and periods of IMFs as yellow dots, where the IMFs have been obtained by EMD assessing SDO/AIA data from the NOAA 11131 active region from 00:00 – 03:20 UT on 8$^{\text{th}}$ December 2010. 99% confidence levels are shown in green and average period energy for each IMF is shown in red, with a linear fit of the mean modal energies shown in blue. *Bottom panels*: Fourier spectral power and periods of Fourier harmonics, again individually shown in yellow dots, with mean Fourier magnitudes shown in red and fitted linearly in blue. We see the Fourier harmonics as vertical stripes, which are analogous to EMD overtones. Figure originally produced as *Fig. 4* from Kolotkov et al. [2016].

This chapter investigates what causes these overtones to appear, what affects their presence, and advises the reader on how to mitigate and account for their appearance. We also discuss when EMD is appropriate to use over other methods. In order to test what factors influence the presence or prevalence of overtones we set up a sample of 'test signals' to be assessed using EMD. Then we alter the colour of noise present in these samples (Section 5.3.1), the duration or cadence of the signal (Section 5.3.2), or the presence of prescribed periodicities slightly offset from the $\frac{D}{2}$, $\frac{D}{3}$, $\frac{D}{4}$ overtones (Section 5.3.3) and assess how this affects any detected overtones.

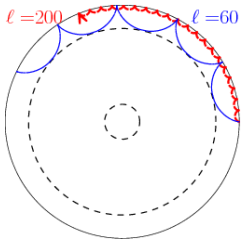

5.2 Are overtones exclusive to EMD?

First we want to see how prevalent overtones are in equivalent signals assessed by EMD and FFT. This will enable us to ascertain the relative risks of using EMD against other methods and allow us to make an informed decision on which method to use.

5.2.1 Setting up a test signal

We test the prevalence of overtones in EMD and FFT by assessing the same simulated signals using both methods and assessing how many detections in the overtone locations are obtained by each. We set up 1000 signals and assess them with EMD and FFT. We set up the signals, with similar properties each differentiated by random noise produced by a different random seed, using the governing parameters given in Table 5.1. The resulting signals have duration, D, of 1000 s, and therefore we expect to see overtones at 500, 333, and possibly 250 seconds.

Table 5.1: parameters, their symbols, and meanings used in constructing a sample of test signals.

N	Number of datapoints	100
c	Cadence	10 seconds
α_w	Colour of white noise	0
α_r	Colour of red noise	2.5
Amp[α_w]	Relative amplitude of white noise	0.25
Amp[α_r]	Relative amplitude of red noise	0.25
Amp[Periodicity]	Relative amplitude of additional periodicity	0.50*
Amp[Trend]	Relative amplitude of the trend	1.0

*Note that for the test signals in this study, and those discussed in Sections 5.3.1, 5.3.2 no additional periodicity is prescribed. This makes the overall duration 1000 s, with a duration to cadence ratio of 100:1.

I assign the signals to have a trend resembling those seen in solar and stellar flares, made by the combination of two exponential functions seen in Eqn. 5.1.

$$x = \begin{cases} t \times \exp[-((t - t_{max})/K_1)^2] & \text{for } t \leq t_{max} \\ t \times \exp[-(t - t_{max})/K_2] & \text{for } t > t_{max} \end{cases} \tag{5.1}$$

where K_1 is a constant, equal to $\frac{1}{5}$ of the duration of the signal, $K_2 = \frac{1}{3}$ of the duration of the signal, and t_{max} is $\frac{1}{3}$ of the duration of the signal. In real solar and

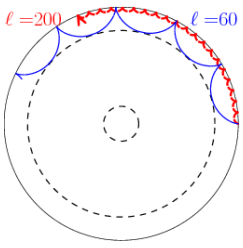

stellar flares, both white and coloured noise is observed. Therefore we add in additional red and white noise. The amplitudes of the noise componants are relative to the amplitude of the trend. The procedure for creating these signals can be found in full under *'EMD synthetic model'* in the repository managed by S. Afinogenov: `github.com/Sergey-Anfinogentov/EMD_conf/blob/master/emd_synthetic_model.pro`. We ran all 1000 of these signals through EMD, and FFT, with a confidence level of 95% and obtain the average periods of any statistically significant IMFs, or peaks in the power spectra respectively. An accurate analysis technique should find no statistically significant oscillations in these datasets, with any spurious detections distributed randomly in period.

5.2.2 Results

The results of the analysis are seen in Table 5.2. We see that in 90+% of cases for both analysis methods, we correctly obtain no statistically significant detections of periodicities in the test signals. We see evidence of overtones in both methods, though the populations of the overtones and their locations vary. We determine a detection to coincide with an overtone location if it is within $\pm$ the cadence of the data, e.g. any detections between 490–510 seconds were counted to be a detection of the $\frac{D}{2}$ overtone. For EMD, we see 79 detections of the $\frac{D}{2}$ overtone at 500 seconds, compared to only 8 detections by FFT. EMD also observed a further 14 detections of the $\frac{D}{3}$ overtone at 333 seconds, and 5 detections of the $\frac{D}{4}$ overtone, whereas the FFT finds evidence of neither. This may be in part due to the fact that EMD can detect multiple periodicities per signal, with their significances being independent from one another, whereas FFT is restricted to detecting only one periodicity, with the most significant energy. Therefore for FFT detections, lower energy overtones may be obscured by higher energy overtones. However seeing as we only detect 8 $\frac{D}{2}$ overtones, it's unlikely that there were a significant number of $\frac{D}{3}$ or $\frac{D}{4}$ overtones obscured. Although we see evidence of overtones in the results from both analysis methods, it's clear that EMD results in a larger population of detections, across a wider ranger of periodicities. Therefore we must fully understand what influences the presence of these overtones and how to account for them before performing any analysis with EMD. We explore which factors contribute to the presence and distribution of overtones in Section 5.3.

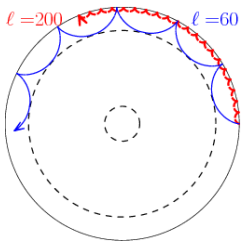

Table 5.2: Results from the testing of 1000 signals using EMD and FFT. The below table shows the number of detections (and their respective percentages out of the 1000 signals) by each method, and the distributions of the dominant periods of statistically significant IMFs from EMD or peaks from FFT spectra. The table indicates how many detections fall into the regions of the $\frac{D}{2}$, $\frac{D}{3}$, $\frac{D}{4}$ overtones and how many signals produced no statistically significant detections.

Periods (seconds)	**EMD**	**FFT**
No stat sig. detections	901 (90%)	992 (99%)
500 ($\frac{D}{2}$)	79 (8%)	8 (0%)
333 ($\frac{D}{3}$)	14 (1%)	0 (0%)
250 ($\frac{D}{4}$)	5 (1%)	0 (0%)
Other	2† (0%)	0 (0%)

†Other periodicities detected were at 68 and 174 seconds.

5.3 An investigation into what influences the presence of overtones

5.3.1 Influence of noise colour on overtone presence

Here, we investigate the impact of noise colour on the presence of overtones. We examine three cases; where the trend is accompanied by only white noise, only red noise, and both red and white noise. Here we remind the reader that noise 'colour' is a way of describing how correlated the noise is. We determine the noise colour according to the slopes of their power spectrum. For example, white noise implies a flat spectral density (meaning it has a slope of 0, and therefore is denoted α_w=0) which is to say each subsequent data point is uncorrelated with the datapoint preceding it. Conversely, coloured, or red, noise implies that the datapoints are well correlated, and so the power spectral density of a coloured noise signal will be sloped with a gradient of around 2–3. In this work we denote red noise to have α_r=2.5.

We produce and assess 100 samples firstly with only white noise, then with red noise, and finally with both red and white noise. Using the same procedure outlined in Section 5.2.1, we run all of these signals through EMD and take note of any detections of IMFs above the 95% confidence level. In Fig. 5.2, we compare the prevalence and distribution of the periods of statistically significant detections via histograms for each of the three cases. The histograms show the periods of the statistically significant IMFs (vertical axis), against their relative populations (horizontal axis). Overtones are shown in light red stripes at the approximate locations of the $\frac{D}{2}$ (500 s), $\frac{D}{3}$ (333 s), $\frac{D}{4}$ (250 s), and $\frac{D}{5}$ (200 s) overtones. Any results corresponding to periods of 0 s imply that no

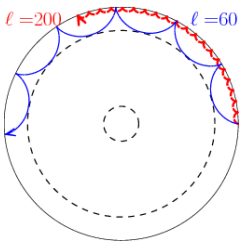

statistically significant IMFs were detected. We emphasise that in some cases EMD detected more than one statistically significant IMF and so the total number of detections on the histograms may exceed 100.

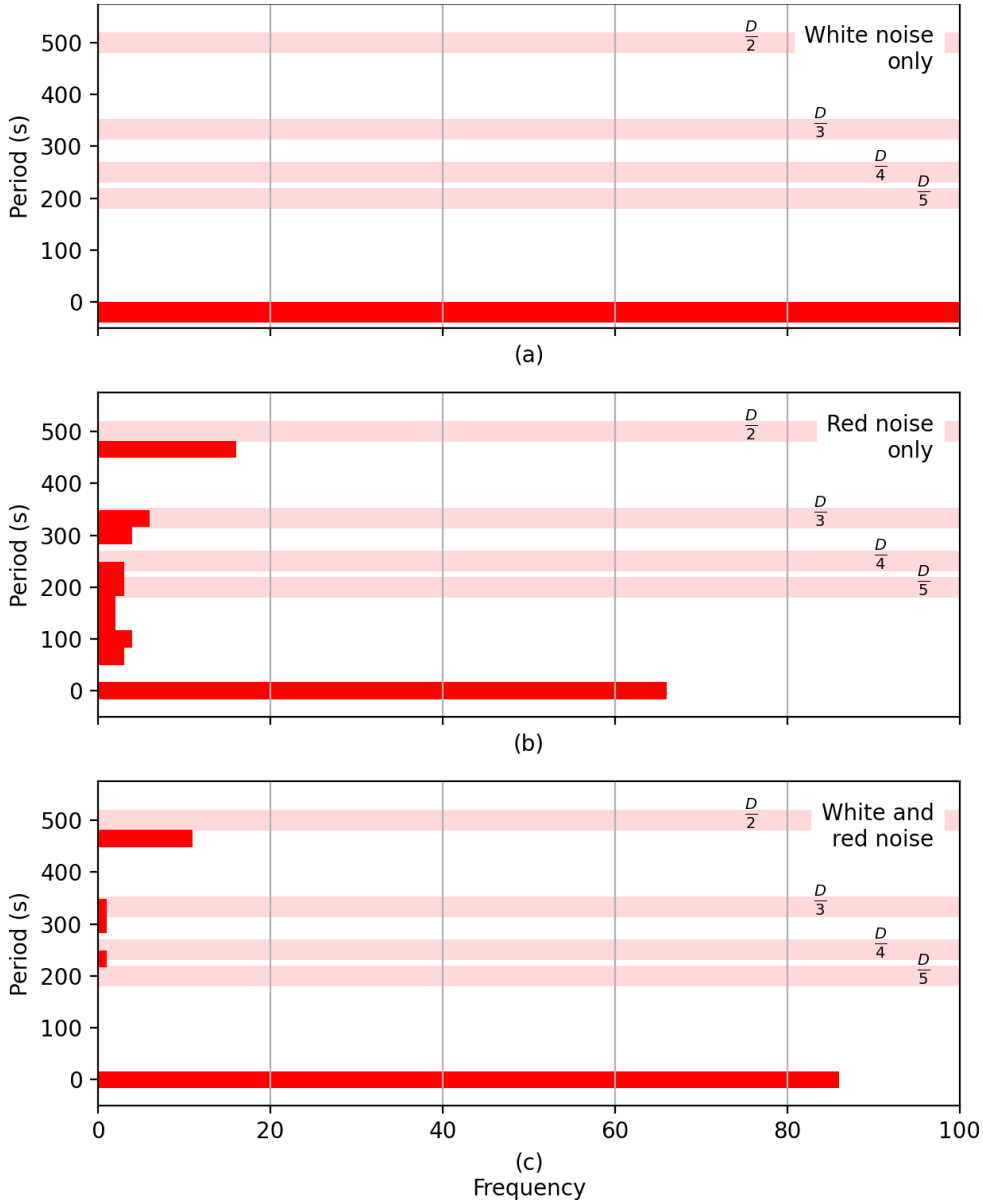

Figure 5.2: Histograms of the periods from statistically significant IMFs from 100 samples per panel, containing white noise only *(a)*, red noise only *(b)*, and both red and white noise *(c)*. Overtones corresponding to $\frac{D}{2}$, $\frac{D}{3}$, $\frac{D}{4}$, and $\frac{D}{5}$ at 500 s, 333 s, 250 s and 200 s respectively are shown in light red, with a width of 40 s as an eye guide for the reader.

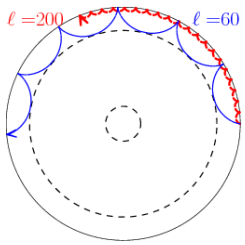

We find that for signals containing only white noise, there are no detections of statistically significant IMFs for all 100 samples. This can be seen in Fig. 5.2a.

For the samples containing only red noise we see that EMD detected (at least one) statistically significant IMF for 35 out of the 100 samples, meaning that EMD correctly identified no statistically significant periodicities in 65 sample signals. These average periods of these IMFs are clustered around approximately 480 s, 350 s, and 50-250 s, close to the $\frac{D}{2}$, $\frac{D}{3}$ overtones and some spurious detections respectively.

We now examine samples that have both red and white noise added, where both noise components each have a relative amplitude of 0.25, corresponding to Fig. 5.2c. We see fewer overtones in this case than when we examined signals with red noise alone. Here, we detect 15 IMFs with periods close to the $\frac{D}{2}$ overtone at around 480 s. We also see a small number of detections of IMFs with periods close to 350 and 250 s, which align closely to the $\frac{D}{3}$ and $\frac{D}{4}$ overtones respectively. The number of samples for which EMD detected no statistically significant IMFs has fallen from 100 in the white-noise only samples to around 85. This means that around 15% of the samples in the combined white and red noise case detected statistically significant oscillations which should be attributed to noise.

This brief study suggests that the current way in which we assess IMF significance is sub-optimal at accounting for coloured noise, but successful at removing artefacts that can be attributed to white noise. As we know red noise is present in solar and stellar data and so we are left with a difficult problem. These results show that the addition of white noise increased the number of results from which no overtones were detected from 65 in the red-noise only case, to 85 in the both red and white noise case. This may suggests that the addition of white noise to real data could help suppress spurious detections.

5.3.2 Influence of the number of datapoints on overtone presence

Now we examine whether the number of datapoints in a signal influences the prevalence or populations of overtones. To do this we perform two short studies in which we vary the signal's duration, and then its cadence, and examine how this affects the presence of overtones. We take the signal with both white and red noise as our 'standard signal'. First, we vary the duration of the signal while maintaining the cadence at 10 s. This results in a change in the number of datapoints, N. We change the duration of the standard signal to: 500 s, 1000 s (the standard signal), 1500 s, 2000 s, and 2500 s. For the fixed cadence of 10 s, this is equivalent to the number of datapoints, N, equalling

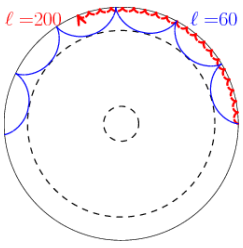

50, 100 (standard signal), 150, 200 and 250.

We run 100 of each of these datasets though EMD as before, and produce histograms of the resulting overtone distributions. Naturally as the duration changes, the locations of the overtones change, as overtones are harmonics of the duration. Therefore to directly compare the results, the histograms in Fig. 5.3 have been rescaled.

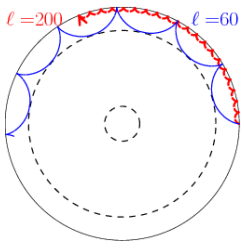

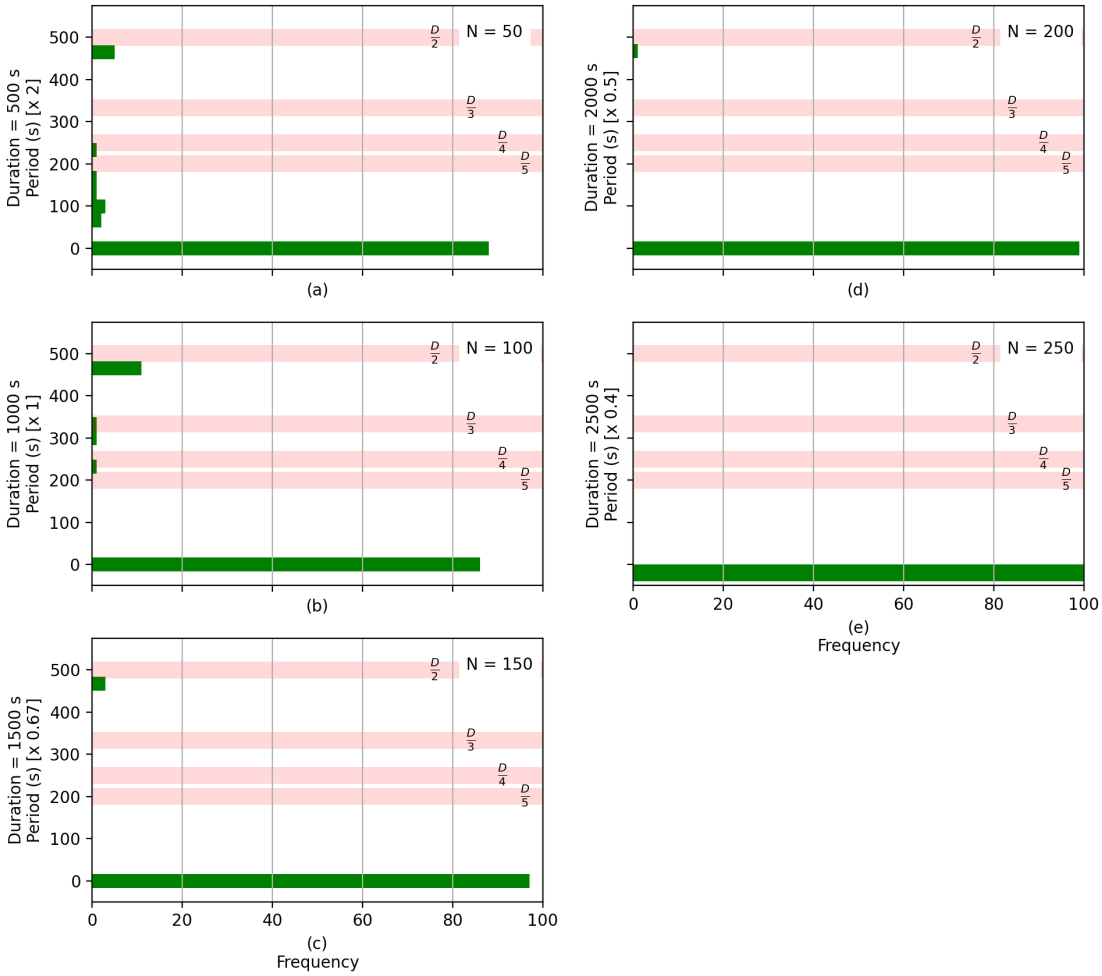

Figure 5.3: Histograms of statistically significant IMF periods from 100 samples of with constant cadence of 10 s, and varying duration, D, and therefore number of datapoints N, with $N = 50$ *(a)*, $N = 100$ *(b)*, $N = 150$ *(c)*, $N = 200$ *(d)*, and $N = 250$ *(e)*. All vertical axes of the histograms have been rescaled to match *(b)* so that results can be directly compared. Red shaded regions indicate the expected locations of overtones $\frac{D}{2}, \frac{D}{3}, \frac{D}{4}$, and $\frac{D}{5}$

.

Fig. 5.3 shows a clear pattern; for a fixed cadence, and increase in duration (and therefore number of datapoints) leads to a decrease in the populations of overtones. For the smallest duration, $N = 50$, $D = 500$ s (Fig. 5.3a), we see evidence of the $\frac{D}{2}$ and $\frac{D}{4}$ overtones, as well as some IMFs with periods around 100 s (rescaled). For the standard

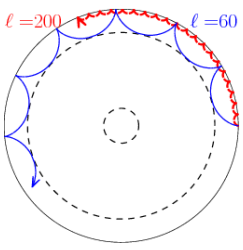

signal, $N = 100$, we see smaller but not insignificant evidence of the $\frac{D}{2}$, $\frac{D}{3}$, and $\frac{D}{4}$ overtones. The $N = 200$, $D = 2000$ s results (Fig. 5.3d), show very little evidence of the $\frac{D}{2}$ overtone, and it is indeed not present at all in the $N = 250$, $D = 2500$ s signal.

We explore this result further by repeating the experiment by holding the duration constant and varying the cadence. We remind the reader that the duration of the standard signal is $D = 1000$ s. We set up four sets of signals, with cadences of 20 s, 10 s (standard signal), 5 s and 2 s. This implies the number of datapoints N is 50, 100, 200 and 500 respectively. Therefore we expect to see the same results for $N = 50$, 100 and 200 and see if the pattern continues for $N = 500$. The results of this analysis can be seen in Fig. 5.4.

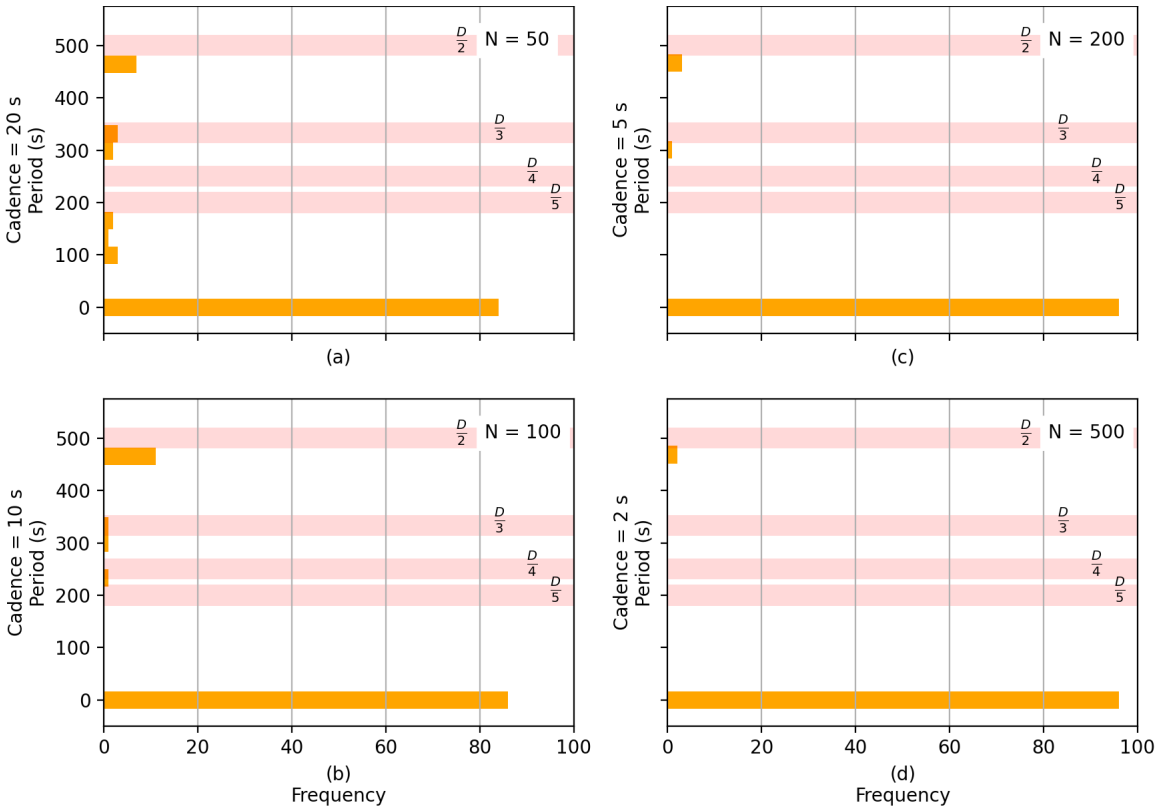

Figure 5.4: Histogram of statistically significant IMF periods from 100 samples of 1000 s with varying cadence from 20 s *(a)*, the standard signal with cadence 10 s *(b)*, 5 s *(c)*, and 2 s *(d)*. Red shaded regions indicate the expected locations of overtones $\frac{D}{2}, \frac{D}{3}, \frac{D}{4}$, and $\frac{D}{5}$

.

Figs. 5.4a,b,c shows the same behaviour for $N = 50$, 100, 200 as seen in Figs. 5.3a,b,

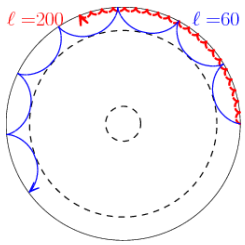

and d respectively. We see confirmation that the presence of the $\frac{D}{2}$ and $\frac{D}{3}$ overtones decreases with increasing N. For $N = 500$, seen in Fig. 5.4d, we see that the presence of the $\frac{D}{2}$ overtone is further reduced compared to the $N = 500$ results, continuing this trend.

Results from this study show that the number of overtones detected fall rapidly for N>150. For $N < 100$, the portion statistically significant of results that can be attributed to overtones appears to be 10% or greater.

5.3.3 Influence of additional periodicities on overtone presence

We now may ask what happens if the signal contains a periodicity of non-noise origin that is equal to that of one of the overtones? Will EMD detect it, and if so will it detect any other overtones? We also need to examine what happens if a non-noise periodicity is close to but not exactly the same periodicity as an overtone? Is EMD capable of differentiating them as two separate signals, or might it detect something in between?

To answer these questions we put forward two studies, in which one examines the output if a periodicity is added that is equal to an overtone, and another which examines the output from an additional periodicity slightly offset from an overtone. For both of these studies, we input a periodicity to our 'standard signal' where the relative amplitude of the additional period is 0.5 (twice that of the white and red noise).

We create 100 samples each of our standard signal with additional periods equal to the locations of expected overtones (500 s ($\frac{D}{2}$), 333 s ($\frac{D}{3}$), 250 s ($\frac{D}{4}$), 200 s ($\frac{D}{5}$)) and offset from them (480 s, 313 s, 230 s, 180 s). We choose an offset of 20 s as it is twice the cadence of the dataset, and so in theory should be differentiable from the overtones.

As before we run these signals through EMD and collate the periods of statistically significant IMFs. Fig. 5.5 shows the histograms signals with periodicities equal to overtone locations, and Fig. 5.6 shows the histograms produced by signals with offset periodicities.

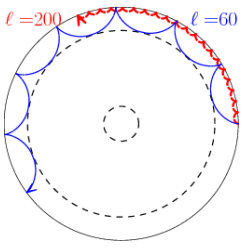

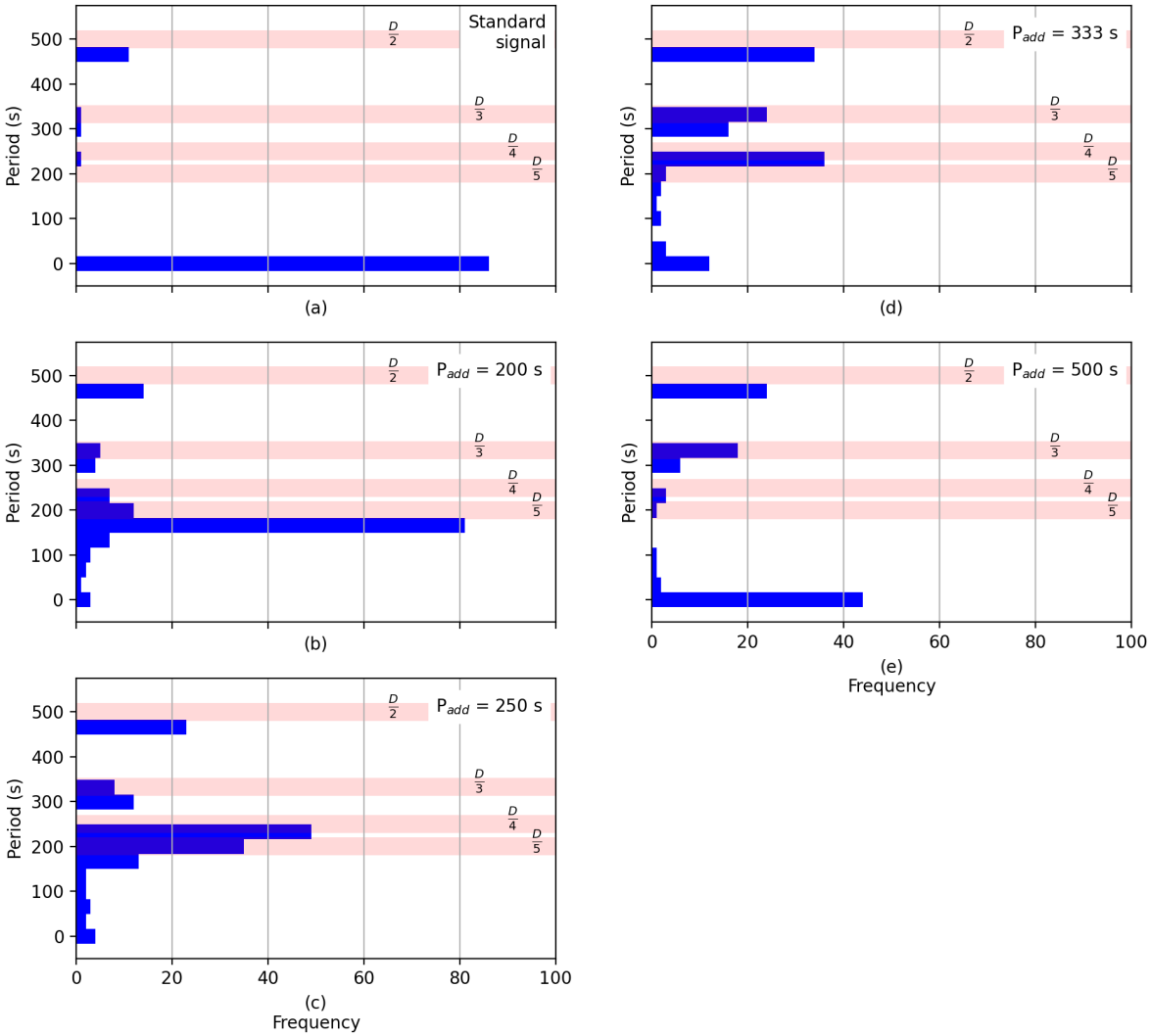

Figure 5.5: Histograms of statistically significant IMF periods from 100 samples with no additional periodicity in the standard signal *(a)*, and inputted periodicities of 200 s *(b)*, 250 s *(c)*, 333 s *(d)*, and 500 s *(e)*. Red shaded regions indicate the expected locations of overtones $\frac{D}{2}, \frac{D}{3}, \frac{D}{4}$, and $\frac{D}{5}$

.

Fig. 5.5a shows the distribution of overtones of our standard signal. We see that the addition of a periodicity at 200 s shown in Fig. 5.5b (equivalent to the $\frac{D}{5}$ overtone) produces a significantly different distribution. EMD has successfully detected 80 IMFs with a periodicity around 200 seconds out of the total 100 sample signals tested. We still see some evidence of overtones at P = 500 s and P = 333 s (the $\frac{D}{2}$ and $\frac{D}{3}$ overtones

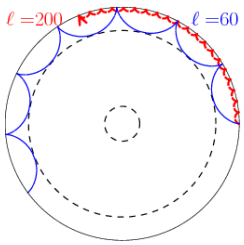

respectively), which show more scatter than in the case for the standard signal. Moving to the addition of the P = 250 s periodicity, seen in Fig. 5.5c, we see a similar increase in detections of IMFs with periods in this region, although less so than the P = 200 s case, falling to only correct detections in only 50 of the 100 samples. Again, we see more scatter around the P= 250 s region, and an increase in significance of the P = 500 s and P = 333 s ($\frac{D}{2}$ and $\frac{D}{3}$) overtones. Examining the addition of the P = 333 s and P = 500 s periodicities, it's clear this trend continues. As we input periodicities we see the following behaviours; firstly there's an increase in detections in the region of the added periodicity when compared to the standard signal, implying that EMD is correctly identifying the periods of these oscillations. Secondly, we see increased scatter in periods around the added periodicity. Thirdly, we see for greater inputted periodicities, the significance of the detected period is reduced when compared to lower periods, i.e. the detection of the P = 500 s signal was correctly identified in approximately ∼25% of datasets (Fig. 5.5e), compared to the addition of the P = 200 s periodicities, which was correctly identified in approximately ∼80% of datasets (Fig. 5.5b).

We now explore whether EMD is able to differentiate slightly offset inputted periodicities from overtones. We perform a similar study as before, but with each additional periodicity offset by 20 s. Fig. 5.6 the results of this analysis, which are largely similar to Fig. 5.5. We see the same trend of lower periodicities, 180 s, 230 s, being better detected by EMD than larger periodicities of 313 s and 480 s. We also see the continued trend of overtones being more prominent for higher added periodicities, e.g. 313 s and 480 s, compared to lower added periodicities. Initial visual inspection of the histograms do not suggest that the location of the prominent bins have changed significantly between the harmonic and offset results. However this may be due to the bin size. To explore it further, we instead consult Fig. 5.7 which compares the distribution of significant IMF periods for the inputted periods of P = 500 and P = 480 s.

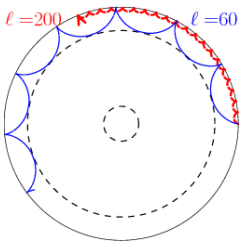

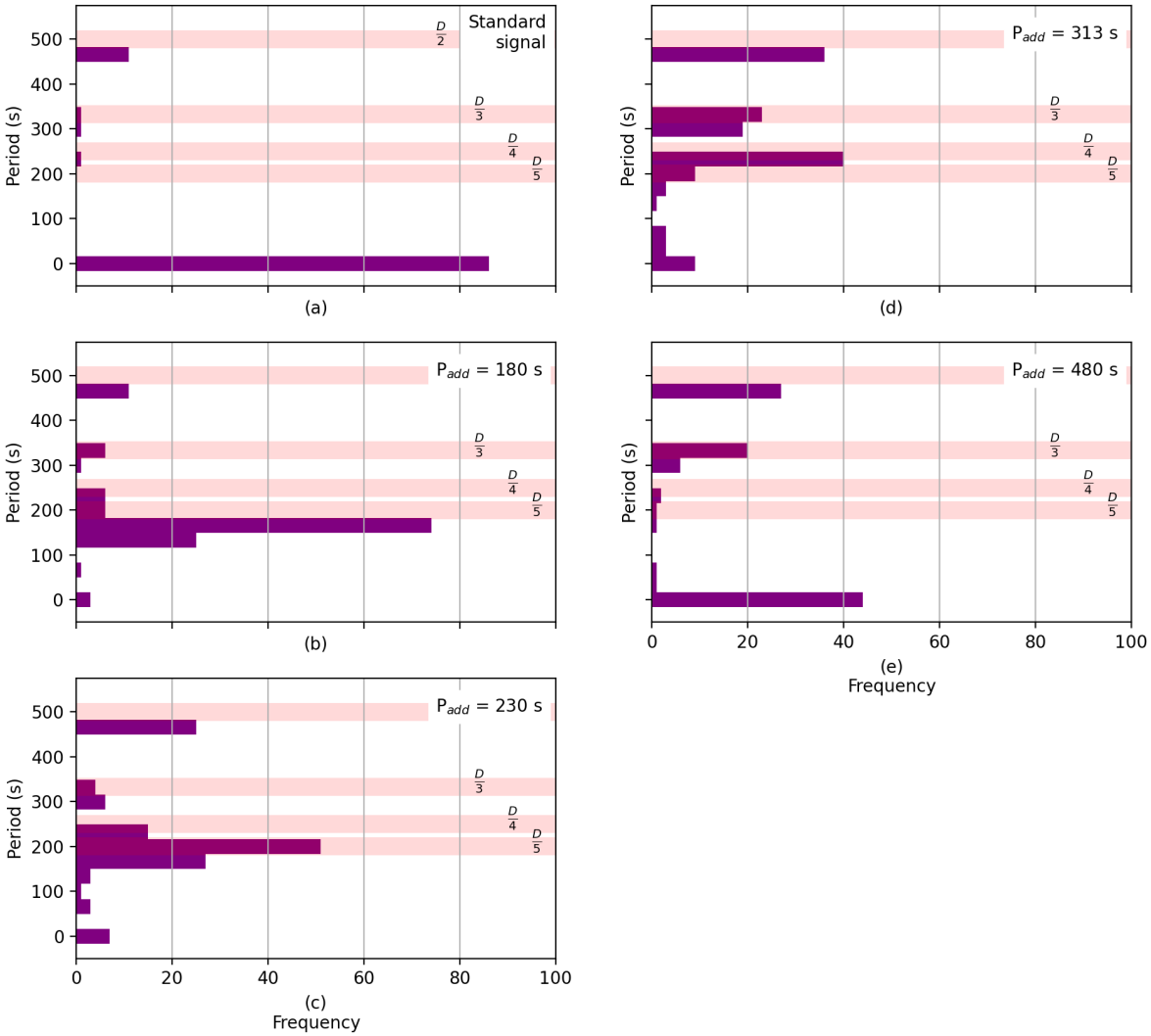

Figure 5.6: Histograms of statistically significant IMF periods from 100 samples with no additional periodicity in the standard signal *(a)*, and inputted periodicities of 180 s *(b)*, 230 s *(c)*, 313 s *(d)*, and 480 s *(e)*. Red shaded regions indicate the expected locations of overtones $\frac{D}{2}, \frac{D}{3}, \frac{D}{4}$, and $\frac{D}{5}$

.

Each point in Fig. 5.7 shows the average period of the statistically significant

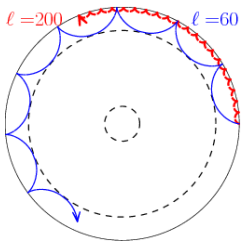

IMF(s) found for a single sample, with their errors shown as a vertical line (found by obtaining the IMF's Global Wavelet's FWHM). The horizontal axis on Fig. 5.7 identifies the sample's ID number and therefore has no physical meaning. Fig. 5.7a shows the results from the inputted P = 500 s (shown as a histogram in Fig. 5.5e) and P = 480 s (Fig. 5.6e). The green region indicating the expected region of the inputted period with width of +/- 10 s, therefore we expect all detections of the inputted periodicities to exist in this region. We instead see that EMD correctly picks up the periodicities in the P = 500 s case, but fails to do so in the P = 480 s case, where the average periods of all of the IMFs fall outside the 470 – 490 s range, with almost all periods at exactly 500 s. This suggests that the average period of the closest overtone at P = 500 s ($\frac{D}{2}$) overpowers the inputted periodicity at P = 480 s, and although this does not change the overall significance of the detections as we can see that both sets of detections around 450–550 s are equally populated in both panels. We conclude that the distribution of periods in both are roughly the same at 500 s despite the difference in inputted periods.

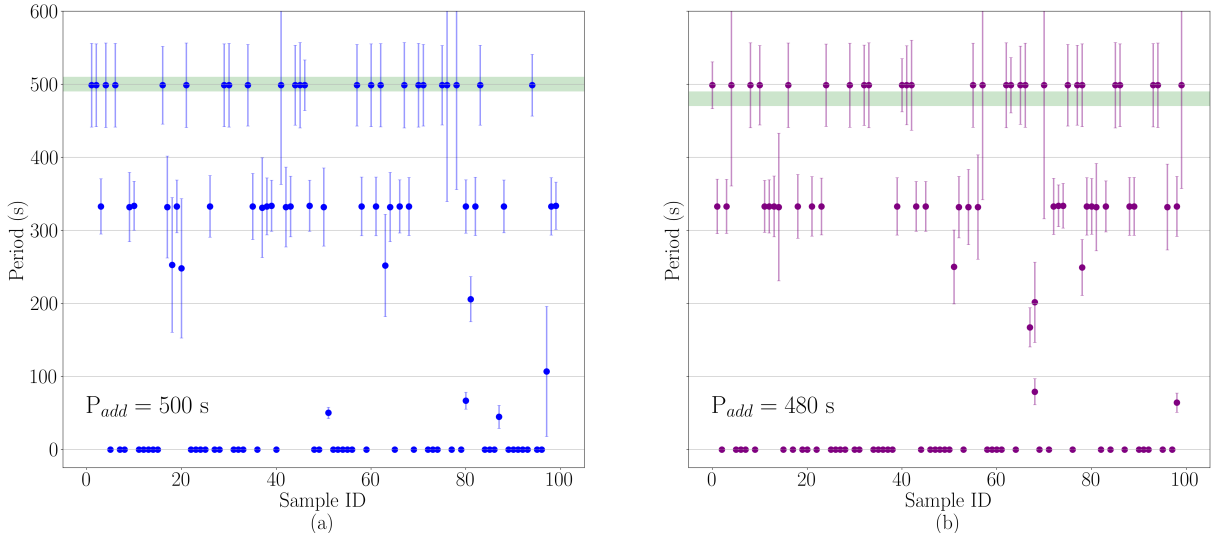

Figure 5.7: Distribution of periods for statistically significant IMFs for 100 samples with an inputted period of 500 s *(a)* and 480 s *(b)*. Green shaded region is an eye-guide for the reader, indicating 490–510 s in panel *(a)* and 470–490 s in panel *(b)*. We indicate that no statistically significant IMFs were detected for a given sample by plotting a period of zero seconds.

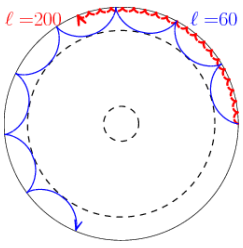

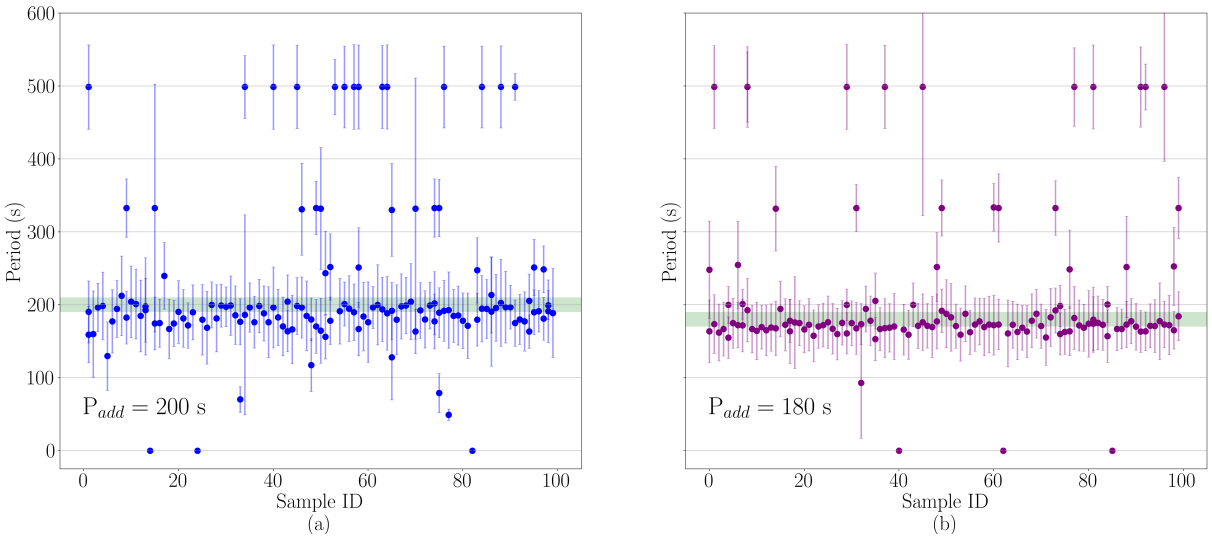

Figure 5.8: Distribution of periods for statistically significant IMFs for 100 samples with an inputted period of 200 s *(a)* and 180 s *(b)*. Green shaded region is indicates 190–210 s in panel *(a)* and 170–190 s in panel *(b)*.

We can examine this again for a lower periodicity in Fig. 5.8 which shows the distributions of the additional P = 200 s signal (Fig. 5.8a) and P = 180 s (Fig. 5.8b). Again we see similar populations in both green regions indicated the expected regions of periodicities (190 – 210 for the left panel, 170 – 190 for the right panel). Both panels show considerable scatter, although less is seen in the right panel. Once again, we do not see a clear separation in the right panel between the inputted signal with P = 180 s and the overtone at P = 200 ($\frac{D}{4}$). We do see a reduced presence of the $\frac{D}{2}$ harmonic however in the right panel with the offset periodicity.

This result is concerning as it brings into question our ability to differentiate overtones and periodicities that are obscured by overtones, as their approximate populations are the same. Further examination is required to determine at what point we are able to distinguish these populations, as it's clear that a difference of twice the cadence is insufficient.

Moving forward, it's essential that we're aware of these phenomenon, as we must be able to comment on whether a result is due to an overtone or a physical process. A conservative reader would discount results corresponding to overtones and then be left with a false negative, which is an equally damaging result. Therefore we must be cautious with how we deal with detections that coincide with exactly an overtone location.

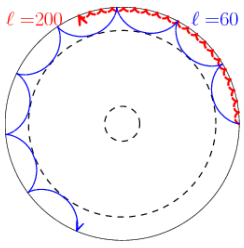

5.4 Examining the presence of overtones in real and simulated data

Now that we have established the prevalence of overtones we expect for a dataset with white and red noise, of a given duration/cadence, and with periodicities of non-noise origin added, we further examine the results we expect to see when assessing real solar data. Here, we move away from assessing the characteristic flare shape, and instead move towards simulated and real solar cycles, which have an approximately sinusoidal shape. In this section, we will analyse the presence of overtones in simulated MDI/HMI data and in real solar proxy data. This will enable us to assess results from Chapter 6 with a better informed eye.

5.4.1 Simulated MDI/HMI data

First we simulate data that resembles the MDI/HMI data. The simulated data were given a cadence of 72 d to match the MDI/HMI p-mode frequencies which will be examined in Chapter 6. We simulate 500 datasets, each inputted with a trend resembling a solar cycle, which we set to have a period of 3528 d (9.6 yrs), which is approximately the same duration of solar Cycle 24. This is to replicate studies on real data performed in Chapter 6, where we consider each solar cycle independently. For a cadence of 72 d, the number of datapoints in the signal, N, is equal to 49. We create a signal that resembles a sinusoid with a period of 3528 d, peaking at half the duration, with white and red noise, with a relative energy of 0.25 compared to the trend as before. We simulate 500 of these datasets, each time slightly varied by the random componants inherent in noise.

We obtain statistically significant IMFs from these 500 sample, take their average periods, and assess whether any of the periodicities can be associated with overtones. From Sections 5.3.2, we see that overtones begin to vanish when N approximately exceeds 100–150. Therefore as $N = 49$, we expect results similar to the $N = 50$ results (Panel (a) from Fig. 5.2) where we saw the number of 'correct' detections of zero statistically significant IMFs to be around 15%. We should expect overtones at $\frac{D}{2}$ (1764 d), $\frac{D}{3}$ (1176 d) , $\frac{D}{4}$ (882 d), with no detections of the sinusoidal trend as it undergoes only a single cycle over the duration of the signal.

The results of the 500 samples assessed by EMD are shown in Table 5.3. The results follow the patterns discussed earlier in this chapter. 80% of the datasets examined correctly detected no statistically significant oscillations (which is consistent for datasets with $N \approx 50$). We see the populations of the $\frac{D}{2}$, $\frac{D}{3}$, $\frac{D}{4}$ decrease in number, again

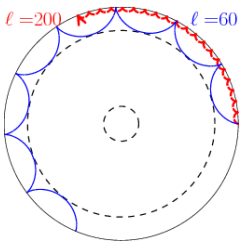

Table 5.3: Distribution of statistically significant IMFs and their corresponding overtones detected in MDI/HMI simulated data

Periods (days)	**Number of detections by EMD**
No stat. sig. detections	400 (80%)
1764 ($\frac{D}{2}$)	51 (10%)
1176 ($\frac{D}{3}$)	10 (2%)
882 ($\frac{D}{4}$)	3 (1%)
Other	43* (9%)

* other periodicities detected were at between 250 – 750 d.

consistent following the patterns shown in earlier studies. We see a large number of detections (equivalent to 9%) that showed considerable scatter for periodicities between 250–750 d. These detections are likely the result of the noise inputted into the signal, and emphasise the importance of multiple tests to obtain accurate results. This study proves that we should expect overtones in our solar cycle studies as well as in QPP studies, and that overtones will be fairly common for datasets with white and red noise and $N \approx 50$.

5.4.2 Presence of overtones in solar activity proxy data

We set up a study to investigate whether overtones occur with the same distribution and prevalence in real data. We choose to examine two solar activity proxies, the $F_{10.7cm}$ index and the MgII index, for four solar cycles: Cycles 21–24. By rebinning the data to artificially vary the cadence of the data, we explore whether the trend of increased number of data points (N) leads to an increase in detections of overtones, and examine whether the populations of overtones change between solar cycles. We also briefly examine whether any other periodicities are observed in these datasets.

We trim the solar activity proxies to their respective solar cycles, and manually remove data corresponding to solar minima. This is to minimise the effect of solar minima on the proxies which are positive definite and therefore poorly suited for assessing solar minima. The resulting start and end dates for each solar cycle are given in Table 5.4. We make note of the durations of each solar cycle, and the expected locations of the $\frac{D}{3}$ and $\frac{D}{4}$ overtones. We exclude searching for the $\frac{D}{2}$ overtone in this analysis as we restrict our results to consist of IMFs with average periods less than or equal to one third of the duration 'D'. This is because we believe that to be reasonably confident of a detection and to differentiate it from the background trend, the signal should exhibit at

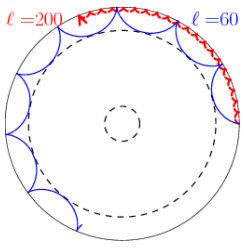

least three full cycles. Both the $F_{10.7cm}$ and the MgII index have cadences of 1 day. We rebin the data to change the cadence to 18, 27, 36, 50 and 72 d for each of the datasets, and run all the data through EMD and extract the dominant periods of statistically significant IMFs as before. We choose these cadences to be approximate factors of the 36 day GONG cadence and 72 day MDI/HMI cadence.

Table 5.4: Start and end dates for solar cycles 21–24, manually trimmed to exclude solar minima. Dates are given in DD/MM/YY format. The durations of the solar cycles and their respective overtones are indicated below, in units of days.

	Cycle 21		**Cycle 22**		**Cycle 23**		**Cycle 24**	
	Start	End	Start	End	Start	End	Start	End
$F_{10.7}$	01/06/76	21/06/86	12/11/86	26/03/97	26/03/97	04/03/08	12/12/09	24/04/19
Duration (D)	3673		3205		4011		3412	
$\frac{D}{3}$	1224		1068		1337		1137	
$\frac{D}{4}$	918		801		1003		853	
	Start	End	Start	End	Start	End	Start	End
MgII	18/01/79	01/11/86	05/06/87	24/04/95	04/08/95	13/08/95	29/11/07	13/01/20
Duration (D)	2844		2880		4392		4428	
$\frac{D}{3}$	948		960		1464		1476	
$\frac{D}{4}$	711		720		1098		1107	

Table 5.5 shows the results of this analysis with cadence varying from 18–72 d for two solar activity proxies, over solar cycles 21–24.

We see clear evidence of the $\frac{D}{3}$ and $\frac{D}{4}$ overtones in all solar cycles except for Cycle 23. Some detected periodicities, e.g. the periodicity of 1103–1108 d detected in Cycle 24 in the MgII proxy for cadences = 36 and 72 d, were remarkably close to the location of overtones, e.g. the $\frac{D}{4}$ overtone in Cycle 24 as seen in the MgII proxy at 1107 d.

We obtain few detections, the results of overtones or otherwise for the datasets with very low cadence (18 d) or very high cadence (72 d). These results suggest that a high resolution, low cadence dataset may lead to fewer overall detections due to a low signal to noise ratio. Increasing the cadence (and therefore decreasing the number of datapoints N), to 27 d leads to an increase in detections, of which one (at 804 d) can be confidently attributed to an overtone. This is likely because the larger rebinning width has lead to increasing averaging out of noise. Increasing the cadence further to 36 and 50 d, we see more detections across all solar cycles, of which roughly half of the results can be confidently attributed to overtones. We remind the reader of the results from Section 5.3.3 which showed that an additional periodicity that had a period close to that of an overtone may be obscured by the overtone. Therefore it is possible that some of these overtone-attributed periodicities may obscure signals of real origin with similar

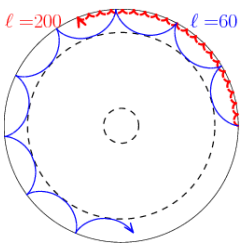

periods. Moving to a cadence of 72 d, we see that the overall number of detections decreases to the level similar to when cadence = 27 d. This is likely because the number of data points has decreased to a level where no signals can be reliably extracted.

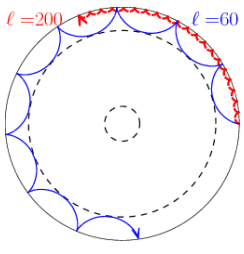

Table 5.5: Average periodicities given in units of days from statistically significant IMFs from EMD analysis on two solar activity proxies, the $F_{10.7cm}$ index and MgII index, rebinned to five different cadences (18, 27, 36, 50 and 72 d) across four solar cycles (21 –24). Periodicites that are close to the locations of $\frac{D}{3}, \frac{D}{4}$ overtones are indicated in brackets. A dashed result indicates that no statistically significant IMFs were detected. Any IMF periodicities with periods greater than one third of the duration of the dataset are excluded from this study and so are not shown.

Cadence = 18 d				
	Cycle 21	Cycle 22	Cycle 23	Cycle 24
$F_{10.7cm}$	-	-	-	-
MgII	-	-	-	-
Cadence = 27 d				
	Cycle 21	Cycle 22	Cycle 23	Cycle 24
$F_{10.7cm}$	-	209, 804($\approx \frac{D}{3}$)	-	251, 856
MgII	-	-	-	-
Cadence = 36 d				
	Cycle 21	Cycle 22	Cycle 23	Cycle 24
$F_{10.7cm}$	-	810($\approx \frac{D}{3}$)	340, 637	1137($\approx \frac{D}{3}$)
MgII	-	955($\approx \frac{D}{3}$)	329, 677	1108($\approx \frac{D}{4}$)
Cadence = 50 d				
	Cycle 21	Cycle 22	Cycle 23	Cycle 24
$F_{10.7cm}$	399, 1210($\approx \frac{D}{3}$)	800($\approx \frac{D}{4}$)	671	304, 1125($\approx \frac{D}{3}$)
MgII	425	347, 944($\approx \frac{D}{3}$)	359	297
Cadence = 72 d				
	Cycle 21	Cycle 22	Cycle 23	Cycle 24
$F_{10.7cm}$	-	-	-	-
MgII	-	-	685, 900	421, 1103($\approx \frac{D}{4}$)

We see that the prevalence of overtones is largely independent of dataset, although slightly more detections of overtones were noted for the $F_{10.7cm}$ index than the

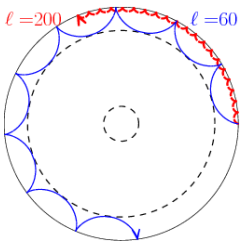

Mgii index.

We see evidence of periodicities that commonly appear that cannot be attributed to overtones. One such periodicity appears at 209–425 d across all solar cycles, and is likely the result of the Earth's annual orbit which we expect to see in both solar activity proxies, as $F_{10.7cm}$ index is measured by ground based instrumentation, and the Mgii index is measured by a composite of Earth orbiting satellites. We also see a periodicity between 637–955 d, which is observed in Cycles 22–24. Several of these periodicities coincide with overtones, but several (e.g. both activity proxies in Cycle 23 at 36 day cadence) do not. We believe these may be evidence of the solar quasi-biennial oscillation (QBO), and these periodicities are discussed at much greater length in Chapter 6.

5.5 Recommendations on the use of EMD

We have shown that the likelihood of obtaining overtones is significant, and when data is improperly handled, a user is at high risk of reporting false positives due to overtones. In light of this, I include some of my recommendations and list some things to consider when assessing data with EMD;

- Consider whether overtones are likely to be an issue for your dataset. Is the number of datapoints in your signal, N, low? (E.g. if $N < 100$, then more than 5% of results are likely due to overtones, if $N < 50$, this rises to more than 15% of your results likely due to overtones). Also consider whether your data is likely to contain a high amount of red/coloured noise. If so the chances of overtones in your results increases.

- Find the locations of the expected overtones, $\frac{D}{2}$, $\frac{D}{3}$, (and $\frac{D}{4}$ if N is reasonably low (< 50)), and treat any results within $\pm 2\times$ cadence of the overtone locations to be potentially due to overtones. Results in these regions are likely due to overtones- but they are also potentially of real origin and are obscured by overtones that have a similar average period.

- If you're questioning whether a result is of non-overtone origin or not, corroborate your results by either assessing a dataset with a different duration (and hence different overtone location), or a different analysis method.

- Be overly cautious when assessing signals with $N < 100$ using EMD, and remember its preferable to obtain a false negative than a false positive.

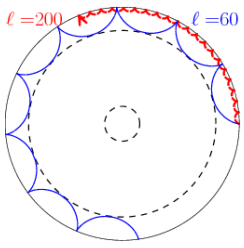

EMD is well suited to assessing non stationary data and is a valuable tool in extracting non-sinusoidal waveform. However the appearance of overtones in low N data is a considerable issue and not one that should be taken lightly given the reasonably high risk of false detections when the method performed with insufficient care. Overall I recommend the use of EMD in cases where the user suspects some element of non-stationarity or complex behaviour, but I would caution its use for low N, high red noise data. In these cases, I would recommend using EMD alongside some other analysis technique which is less susceptible to overtones.

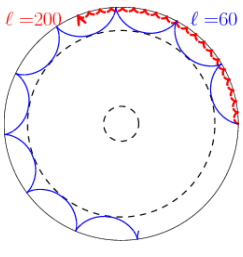

Chapter 6

Searching for the Quasi-Biennial Oscillation

This chapter covers an overview of our study into the cycle dependency of the quasi-biennial oscillation, [Mehta et al., 2022a]. Firstly we explore our motivation for using helioseismic techniques to examine the QBO (Section 6.1), discuss the methodology used (Section 6.2), examine whether we can observe the QBO using helioseismic data and compare its properties in different solar cycles and datasets (Section 6.3), looking specifically at combined solar cycles (Section 6.3.1) and independent solar cycles (Section 6.3.2). We then investigate whether we can identify the QBO in solar activity proxies in the previous four solar cycles (Section 6.4). This chapter concludes with a summary of findings and recommendations on best practises when searching for quasi-oscillatory processes in solar data (Section 6.5).

This chapter was originally published as

"Cycle dependence of a quasi-biennial variability in the solar interior".
Monthly Notices of the Royal Astronomical Society, Volume 515, Issue 2, September 2022, Pages 2415–2429
By T. Mehta, K. Jain, S. C. Tripathy, R. Kiefer, D. Kolotkov, A.-M. Broomhall.

6.1 Motivation

As discussed in Section 1.3, the Quasi-Biennial Oscillation (QBO) has been seen in many datasets; solar rotational rate residuals at near-surface depths [Inceoglu et al., 2021],

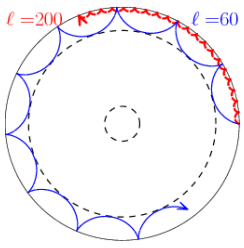

Sunspot Number (SSN) Broomhall [2017], flux in solar energetic particles [Bazilevskaya et al., 2001] and more [see Bazilevskaya et al., 2014, and references therein for a full review on observational aspects of the QBO]. Extracting QBO parameters from any of these datasets has value and can teach us valuable insights into the cause and behaviour of the QBO. However we have not yet determined the generation mechanism of the QBO-some studies suggesting a beating mechanism, and some put forward an entirely separate dynamo [see Inceoglu et al., 2019, and references therein for a summary of suggested generation mechanisms]. Helioseismology offers the unique perspective of examining the QBO in the solar interior. We may examine the Sun at selective radial depths using spatially resolved helioseismic data and examine where, if at all, the QBO can be observed and how its presence changes in different epochs. The QBO has been previously observed in helioseismic data (E.g. see Simoniello et al. [2013]), and so we extend this work by examining two solar cycles, Cycles 23 and 24 across intermediate degree modes, where ℓ varies between $3 \leq \ell \leq 150$, making use of solar oscillation frequencies from GONG, MDI and HMI. We also examined two solar activity proxies, the $F_{10.7}$ index and the MgII index, in order to compare the results from helioseismic data. The analyses were performed using EMD and FFT.

6.2 Methodology

The QBO is by definition quasi-periodic and therefore we expect to see a period drift in its profile. This makes it poorly suited to Fourier-based analysis techniques which anticipate a stationary sinusoidal input. Techniques which do not restrict the input to be strictly sinusoidal, e.g. wavelet analysis, have been previously applied to investigations involving the QBO [see Simoniello et al., 2012]. However, the accuracy of wavelet analysis struggles in noisy conditions and so it may not be well suited for identifying quasi-periodic oscillations in the presence of both white and coloured noise which we see in solar data. In this study we examine p-modes to obtain statistically significant periodicities in the QBO. A full description of the EMD method can be found in Chapter 4. EMD has previously been applied in QBO studies e.g. on cosmic ray intensity data wherein oscillations with periods in the QBO range were identified [Vecchio et al., 2012], and on rotation rate residuals in Cycles 23 and 24 to investigate the presence of QBO-like signals [Inceoglu et al., 2021]. Ensemble Empirical Mode Decomposition (EEMD), a technique similar to EMD, has also been used on data from BiSON where the study was confined to low degree modes [Kolotkov et al., 2015]. We also analyse a subset of datasets using a FFT to examine whether any QBO-like oscillations can be seen in a

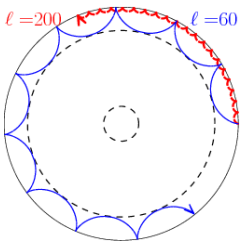

Fourier spectrum, and if so, whether they showed agreement with findings by EMD. The statistical significance of peaks in the Fourier spectra were determined using the methodology described in Pugh et al. [2017a]. The method of obtaining errors on results from EMD are derived from the FWHM of an IMF's global wavelet, discussed in detail in Chapter 4. The errors of significant periods found by the FFT were propagated using the functional approach [See Chapter 4 in Hughes & Hase, 2010, for a description of the methodology used] and were taken to be the width of one frequency bin in frequency space.

6.2.1 Data sources and data selection

GONG data

We use GONG's *mrv1y* dataset (discussed in Section 3.1), which provides the mode frequency $\nu_{n,\ell}$ for all n, ℓ every GONG 'month' (36 d) over the past two solar cycles where there is sufficiently good data. We use this to create a time series $\nu_{n,\ell}(t)$ for both Cycles 23 and 24, and reject modes which are not present in all the datasets, to produce time series with 100% fill. We then calculate the frequency *shift* time series for each common mode as $\delta\nu_{n,\ell}(t)$ where $\delta\nu_{n,\ell}(t) = \nu_{n,\ell}(t) - \bar{\nu}_{n,\ell}$ and $\bar{\nu}_{n,\ell}$ is the average modal frequency. The average modal frequency is the weighted mean frequency of for each n, ℓ mode across the entire time span under consideration, where the weights are given by the inverse of the uncertainty on the fitted mode frequency. The value of $\bar{\nu}_{n,\ell}$ will, therefore, be slightly different depending on whether we are considering the Cycle 23, Cycle 24 or both. We then trim the GONG datasets according to the procedure laid out in Section 6.2.2. This resulted in 474 (with $1 \leq n \leq 19$, $19 \leq \ell \leq 147$) and 743 (with $1 \leq n \leq 20$, $19 \leq \ell \leq 145$) common modes in the trimmed durations of Cycles 23 (GONG months 008–118 inclusive) and Cycle 24 (GONG months 139–244 inclusive).

To examine the frequency and depth dependence of the QBO, we sort these frequency shift time series into bins, according to their modal frequency and lower turning points, r_{ltp}. We choose frequency bins with widths of 400 μHz overlapping by 200 μHz from 1600–4000 μHz and lower turning point bins width width of 0.05 $R_\odot$, staggered by 0.01 $R_\odot$ from $0.05\,R_\odot < r_{ltp} \leq 0.95\,R_\odot$. We choose a depth resolution of the scale of the approximate width of the tachocline [Howe, 2009] because the tachocline plays a key role in some QBO generation mechanisms [for example, see Zaqarashvili et al., 2010]. We sort all frequency shift time series $\delta\nu_{n,\ell}(t)$ into their corresponding bins, rejecting the bin if it contains fewer than three modes in order to reduce the impact of outliers. For a given bin, we calculate the weighted mean frequency, the average frequency shift time

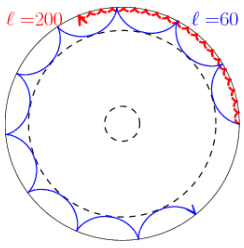

series and corresponding errors. The errors on the individual frequencies were produced by the standard GONG pipeline and used to weight the average frequency shift. Once the modes from GONG have been sorted into bins, and averaged, we obtained 251 mean averaged frequency shift time series for Cycle 23, and 346 for Cycle 24.

MDI/HMI

We used the composite of the *mdi.vw_V_sht_modes* and *hmi.V_sht_modes* data products to obtain mode frequencies and repeat the process of collecting, sorting, and averaging data from MDI/HMI. For convenience, the HMI dataset was chosen over the MDI data for the duration over which the data overlapped. Differences between the MDI and HMI mode frequencies are within 1-sigma (where σ is the uncertainty in frequency determination) for the five overlapping 72 d datasets. The combined dataset uses the MDI data from 2$^{\text{nd}}$ February 1999 to 29$^{\text{th}}$ April 2010 and the HMI data from 30$^{\text{th}}$ April 2010 to 18$^{\text{th}}$ May 2020. This time range was later trimmed via the procedure discussed in Section 6.2.2. Following the same method outlined for GONG data, we again sort these modes by both frequency and lower turning point, using the same frequency and lower turning point bins specified in Section 6.2.1. The MDI/HMI combined data contained 1304 common modes (with $1 \leq n \leq 22$, $5 \leq \ell \leq 150$) in the trimmed durations of Cycle 23 and 1377 modes from MDI (with $1 \leq n \leq 22$, $3 \leq \ell \leq 150$) in Cycle 24. As with the GONG data, the weighted mean frequency shifts and corresponding errors were determined, using the uncertainties given by the MDI/HMI pipelines. Following sorting of these frequency shift time series by lower turning points and average mode frequency, the frequency shift time series were averaged, where this averaging process decreases the total number of mean averaged frequency shift time series to be assessed for Cycles 23 and 24 to be 643 and 679 respectively.

Figs. 6.1a and 6.1b show how the modes are distributed across lower turning point, frequency, and number of modes to a bin for data obtained from GONG and MDI/HMI respectively over the trimmed duration of Cycle 24. For GONG data, the modes follow an approximate Gaussian distribution in lower turning point or depth, centred around $0.8\,\mathrm{R}_\odot$. The median number of modes per bin in this dataset is 5–6, with the maximal number being in the range of 50–52 modes per bin. For the MDI/HMI data, the modes are distributed more evenly across lower turning point or depth, with approximately uniform distribution between 0.4–$0.95\,\mathrm{R}_\odot$. The median number of modes per bin is 8–10 modes, with the maximal number of modes per bin being in the range of 90–92 modes. These distributions are characteristic of their respective datasets for both Cycles 23 and

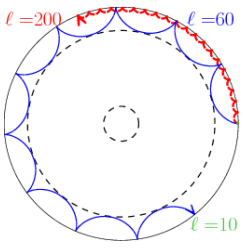

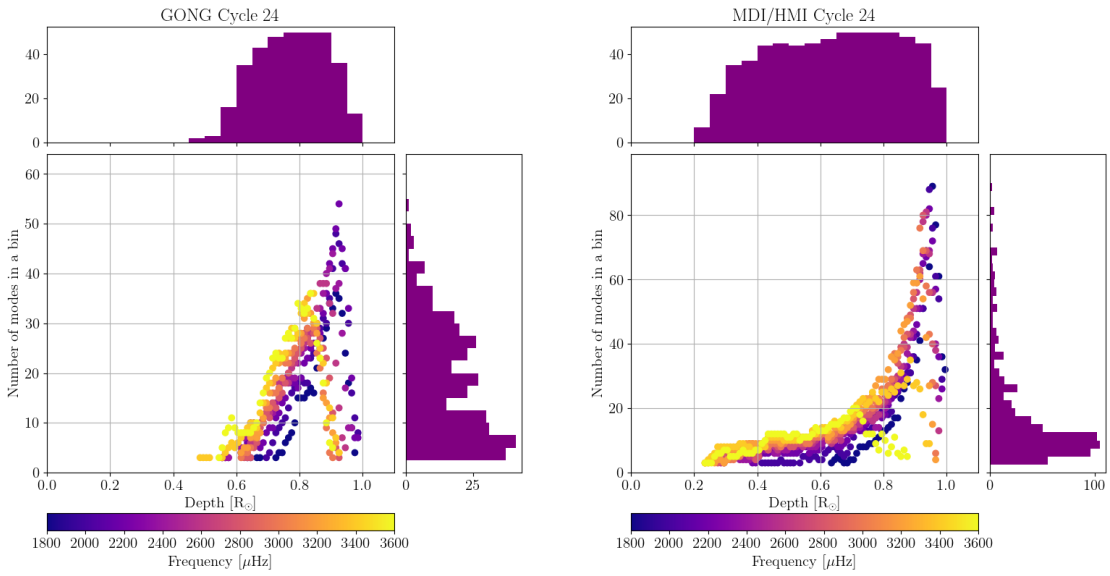

(a) (b)

Figure 6.1: Distribution of mode properties for GONG data *(a)* and MDI/HMI data *(b)* over the trimmed duration of Cycle 24. The scatter plot (centre of both) shows the number of modes in a bin (vertical axis), the average depth given in solar radii ($R_\odot$) to which the modes in the bin penetrate, known as the lower turning point (horizontal axis), and the average frequency of the bin (colour). Histograms of the properties can be seen above (average lower turning points), and to the right (number of modes to a bin) of the scatter plot.

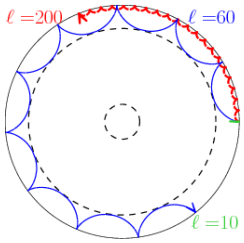

combined Cycles 23 and 24.

$F_{10.7}$ index

The $F_{10.7}$ index measures the flux density of solar radio emission at a wavelength of 10.7 cm and has been shown to correlate well with the frequency shifts of low [Chaplin et al., 2007] and intermediate degree [Jain et al., 2009] modes. It is a widely used proxy for solar activity as it correlates well with sunspot number, UV emissions and solar irradiance and daily observations are available since 1947. The data were obtained from the Canadian National Research Council website[1], and were trimmed over the time periods given in Table 6.1. The data were then averaged over 108 d bins, which each overlap by 36 d to mirror GONG's cadence, and 72 d independent bins to mirror MDI/HMI cadence and trimmed according to the same criteria laid out in Section 6.2.2. $F_{10.7}$ index emissions are measured in radio flux units (RFU), where $1\,\mathrm{RFU} = 10^{-22}\,\mathrm{Wm^{-2}Hz^{-1}}$.

Bremen Composite MgII index

First identified in Heath & Schlesinger [1986], the Magnesium II core-to-wing ratio of the MgII Fraunhofer doublet at 280 nm was found to be a good proxy for solar EUV irradiance. The Bremen composite (also known as the composite MgII index)[2] closely correlates with the Schwabe cycle [Viereck et al., 2001] and has been constructed by combining the data collected by several instruments. The MgII index has been once again trimmed over the time periods given in Table 6.1 via the trimming criteria discussed in Section 6.2.2 and averaged over overlapping 108 d bins with 36 d cadence to mirror GONG's data, and 72 d independent bins to mirror MDI/HMI data.

6.2.2 Trimming the data

It is known that the amplitude of the QBO is modulated by the solar cycle and is greatest at solar maximum [Bazilevskaya et al., 2014]. Therefore to increase the likelihood of observing the QBO we exclude solar minima by trimming the datasets and only assessing the duration wherein we expect to observe the QBO. As the $F_{10.7}$ index is well correlated with GONG 108 d frequency shifts [Jain et al., 2009], we use it to determine when solar activity rises above background levels.

We rebin the $F_{10.7}$ index, averaging over overlapping 108 d bins with a 36 d cadence to match GONG months. These rebinned $F_{10.7}$ index data are then decomposed

[1] nrc.canada.ca/en

[2] http://www.iup.uni-bremen.de/UVSAT/Datasets/MgII

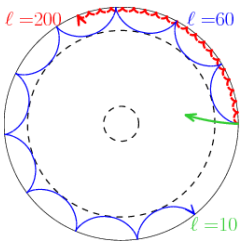

using EMD to produce a number of IMFs, and then the IMF with a period closest to 365 d was selected as the 'annual oscillation'. This annual oscillation (IMF_{365}) was selected because its amplitude typically grows in magnitude towards solar maxima and decays towards solar minima and so it serves as a good tool for determining the bounds of solar maximum. In the case of the GONG data, IMF_{365} has a period of 304^{+79}_{-67} d. We determined the dates where the amplitude of $(\mathrm{IMF}_{365})^2$ is greater than 5% of this average maximum amplitude (the average of the three maximal amplitudes over the solar cycle) and trimmed the data to this duration. This process excludes only the lowest amplitude values in the cycle, analogously trimming solar minima. This was repeated for solar Cycles 23 and 24, with $F_{10.7}$ rebinned to match the 72 d independent sets when used to trim the MDI/HMI data. The different rebinning of the $F_{10.7}$ index leads to a different IMF_{365} profile obtained by EMD which in turn produces the different start and end dates for GONG and MDI/HMI data. These cycle start and end dates are given in Table 6.1.

Similarly we trim the solar activity proxies, covering data from Cycles 21–24. We perform trimming on each dataset twice; once using the overlapping 108 d bins with a 36 d cadence to match GONG months and again to match the 72 d independent sets used by MDI/HMI. This is to ensure the results from solar activity proxies can be directly compared to the results from helioseismic data. We note that MgII data only begins on 20^{th} November 1978 and so a part of the rising phase of Cycle 21 is missing from the analysis.

6.3 Results from helioseismic data

6.3.1 Combined cycles

In this section, we assess the results when we examine two solar cycles (Cycles 23 and 24) as a combined dataset. We perform this twice- once for modes obtained by GONG, and once for modes obtained by MDI/HMI. We take the averaged frequency shift time series and assess them using EMD. We plot the results, as seen in Fig. 6.2, where we compare average modal properties and the periods of any statistically significant IMFs that were observed. Fig. 6.2 shows the results of analysis for both GONG and MDI/HMI data over the time range spanning from the start of Cycle 23 to the end of Cycle 24 and contains the full duration of solar minima for Cycle 24. Fig. 6.2 shows the modes' lower turning point (in units of solar radius, $\mathrm{R}_\odot$) against the periods of the modes' statistically significant IMFs, given in units of days. We also indicate the modes' average frequency, in units of μHz, as a colour bar. The grey shaded regions on the scatter plots (left)

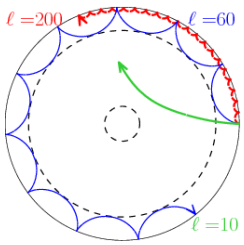

Table 6.1: Trimmed durations for Cycles 21–24 for helioseismic and solar proxy datasets using DD/MM/YY notation. The inclusive time ranges for the below data were determined using the trimming method given in Section 6.2.2 and are therefore shorter than the full durations of Cycles 23 and 24. All of the dates given contain the full duration of the datasets and are inclusive. The regions shaded in grey indicate where there is no data available. Note that the data availability for the MgII index begins after Cycle 21 has started and MDI/HMI data pre-1999 is excluded due to the near loss of the SoHO spacecraft in 1998 which caused a gap in data collection.

Dataset	Cadence [days]	Cycle	
		21	**22**
GONG	36		
MDI/HMI	72		
$F_{10.7cm}$	36	05/01/77 – 28/06/85	08/09/85 – 09/12/95
$F_{10.7cm}$	72	11/01/76 – 28/06/85	30/01/86 – 28/09/95
MgII	36	20/11/78 – 13/05/87	24/07/87 – 12/05/94
MgII	72	20/11/78 – 20/12/86	04/10/87 – 14/01/96
		Cycle	
		23	**24**
GONG	36	14/01/96 – 22/12/06	12/12/08 – 24/05/19
Common modes		474	743
MDI/HMI	72	03/02/99 – 11/12/08	07/12/09 – 04/08/19
Common modes		1304	1377
$F_{10.7cm}$	36	14/01/96 – 22/12/06	12/12/08 – 24/05/19
$F_{10.7cm}$	72	03/12/96 – 16/05/07	07/10/07 – 01/01/19
MgII	36	14/01/96 – 07/10/07	28/02/08 – 01/02/20
MgII	72	14/01/96 – 12/11/07	04/04/08 – 21/11/19

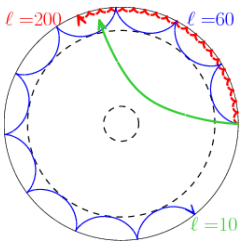

indicate where no high-quality data was available and so no IMFs could be obtained. The same data given in the scatter plots (left) are represented in an adjacent histogram (right), so that the reader may better visualise the distribution of the periods. Following on from discussions in Chapter 5, we mark the expected locations of overtones in pink with a width of $\pm$ 2$\times$cadence of the dataset. We also mark the approximate location of the annual oscillation.

It is difficult to differentiate if a statistically significant oscillation with fewer than two cycles over its duration is part of the signal's trend and caused by noise in the data, or equally a physical phenomenon. Therefore we attribute IMFs with periods of $\frac{D}{2}$ or greater to the general trend of the signal and suggest any detections with period in this range should be studied over longer durations.

The GONG results (Fig. 6.2 *(Top)*) show some evidence of banding, with clustering seen around 300–400, 500–800, 900–1200, 1200–1500 d, and a small number of points between 1700–2200 d where no dominant period can be discerned. The IMFs with periods in between 300–400 d can be attributed to the annual oscillation caused by the Earth's orbit, as GONG data is collected by ground-based instruments. The periods between 1700–2200 d are around the expected locations of the $\frac{D}{4}$ or $\frac{D}{5}$ overtones. We discuss the impact of overtones in more detail in Section 6.3.2. The other bands, clustered at 500–800, 900–1200, and 1200–1500 d may be attributed to the QBO. There is no clear dependence between periodicity and lower turning point or frequency, as the relative clustering of IMFs within the ranges of 0.7–0.9 $R_\odot$ and 2600–3400 μHz, is largely due to selection bias of modes with 100% fill.

The results from MDI/HMI (Fig. 6.2 *(Bottom)*) cover a larger depth range, with IMFs at depths upwards from 0.43 $R_\odot$. The IMFs are clustered with reasonable scatter at 600–1000 d, 1200–1500, and 1900 d. We see no evidence of the annual oscillation in the MDI/HMI data. We consider IMFs with periods between 600–1000 to be exhibiting QBO-like behaviour. Once again there is no correlation between periodicity, lower turning point or mode frequency. The duration of the input signal, D, was 7487 d for this dataset so the resulting $\frac{D}{4}$ overtone is be expected at 1872 d - extremely close to the clustering of modes at 1900 d that is observed. The band between 1200–1500 d partly overlaps with the expected location of the $\frac{D}{5}$ overtone at 1497 d. However the range in periodicity of this band is considerably larger than the one at 1850 d, suggesting that either the overtones at $\frac{D}{5}$ exhibit more scatter, or that some of the IMFs in this range may be of real origin. For visual reasons we have excluded six datapoints from the combined MDI/HMI results (lower panels of Fig. 6.2) that correspond to IMFs with weighted average periods between 2472–2491 d. These average periods are within 25 d

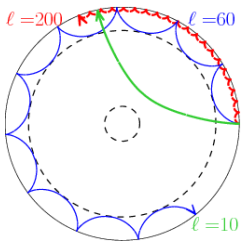

of 2496 d, which is the expected location of the $\frac{D}{3}$ overtone. We have omitted these data points in order to reduce the range on the vertical axis, for both the scatter plot (lower left) and its corresponding histogram (lower right) so that the reader may visualise the datapoints at lower periodicities with greater clarity.

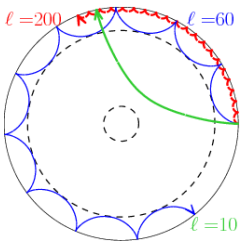

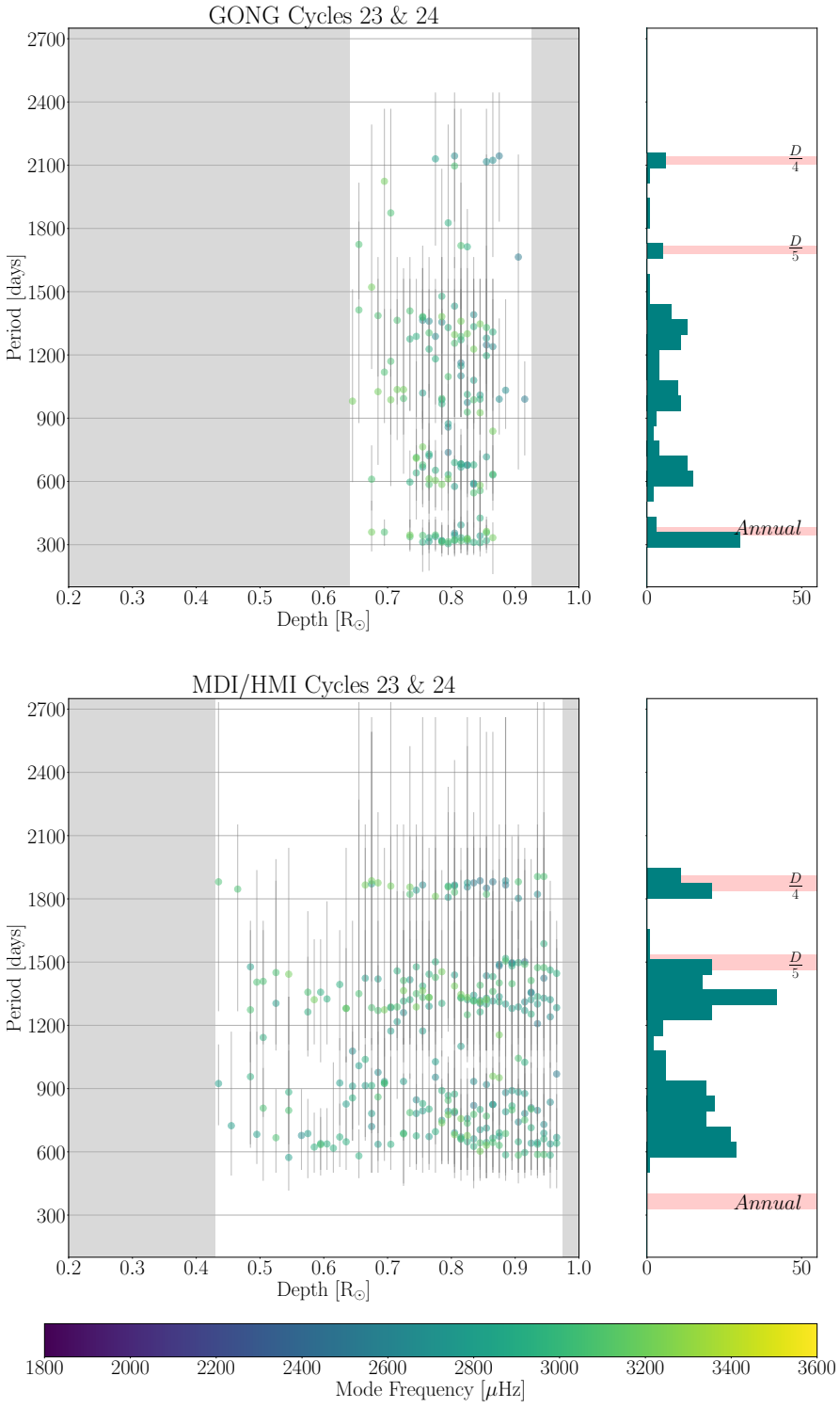

Figure 6.2: (Caption next page.)

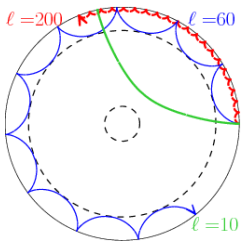

Figure 6.2: (Figure on previous page) Distribution of periods from statistically significant IMFs. The IMFs have been obtained from GONG data *(Top)* and MDI/HMI data *(Bottom)* from the combined duration of Cycles 23 and 24. The depth refers to the lower turning point in solar radius. The colour of the data points indicates the average p-mode frequency, and the error in period (found by the full width half maximum of the IMFs global wavelet spectrum) is indicated by grey error bars. The grey shaded region indicates depths over which no data were available. The adjacent right panel shows the histogram of the distributions with bin-width equal to the cadence of the dataset. We include pink shaded regions (with width equal to twice the cadence of the dataset) as an eye-guide for the reader to visualise the approximate ranges over which overtones are expected, and the location of the annual oscillation. The overtones are labelled as $\frac{D}{3}$,$\frac{D}{4}$, etc., where D is the duration of the input signal. We do not necessarily expect all overtones to be present in all datasets. As discussed in Section 6.3.1, six IMFs from MDI/HMI data with periodicities greater than 2400 d have been removed both from the scatter plot and its associated histogram (lower left and lower right panels) as their errors extend beyond the range plotted.

6.3.2 Independent cycles

Data obtained by GONG

Now we examine the impact of assessing Solar Cycles 23 and 24 separately. Firstly, we reexamine GONG data, where the results of the analysis of modes can be seen in Fig. 6.3 for the trimmed durations of Cycles 23 *(Top)* and 24 *(Bottom)*. Following rebinning in frequency and lower turning point of the 474 common modes from Cycle 23, we obtain 251 averaged modes. Of these 91 produced at least one statistically significant IMF, equivalent to 36% of the sample. For Cycle 24, only 64 (18%) of the 346 input averaged modes produced at least one statistically significant IMF.

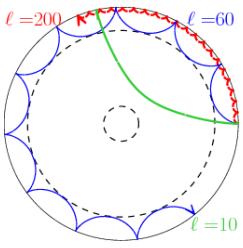

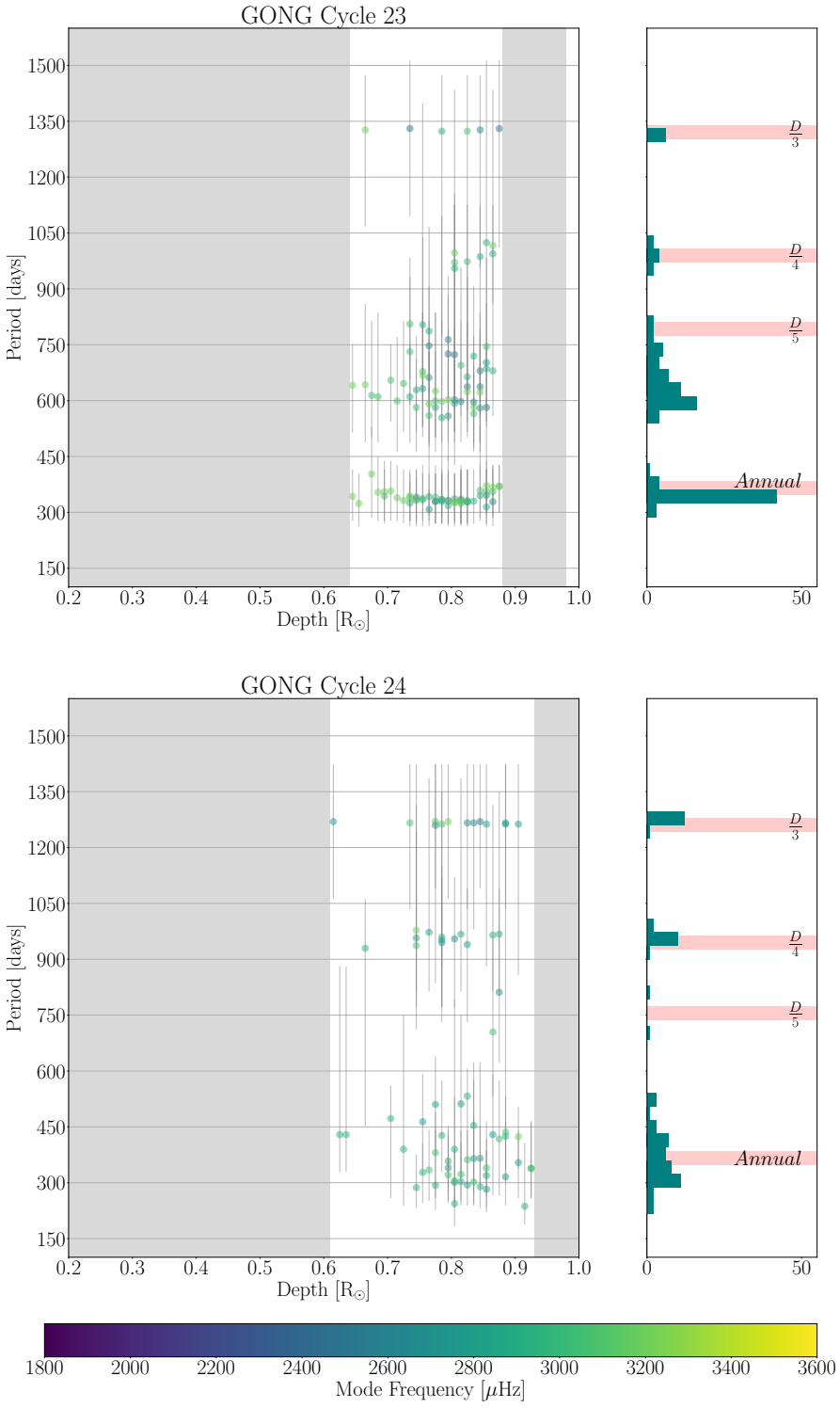

Figure 6.3: Distribution of periods from statistically significant IMFs with IMFs obtained from Cycle 23 *(Top)* and Cycle 24 *(Bottom)* using GONG data. Colours, shaded regions and axes have the same meaning as in Fig. 6.2.

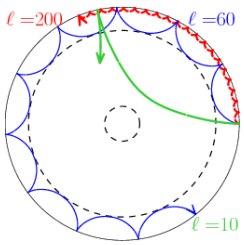

For Cycle 23, the periods of the IMFs are roughly distributed across four bands: 300–400, 500–800, 950–1000, and 1300 d. The bands vary in appearance- e.g. the 500–800 d band is loosely defined and shows a lot of scatter in contrast to the bands at 950–1000 and 1300 d.

The 300–400 d band shows minimal scatter and is believed to be an artefacts of the Earth's annual orbit around the Sun. The 950–1000 d and 1300 d bands are likely overtones of the input signal as they coincide with $\frac{D}{4}$ (990 d) and $\frac{D}{3}$ (1320 d). We also note that the bands are closely packed and show little scatter which are characteristic properties of an overtone.

In contrast the 500–800 d band shows a lot of scatter and contains candidates for quasi-biennial oscillatory behaviour. The band shows some overlap with the location of the $\frac{D}{5}$ overtone which, if present, occurs at 790 d as the duration of the input signal is 3960 d. However the large range of periods covered by this band suggests some IMFs are from non-overtone origin.

There is no clear depth dependence beyond the lack of statistically significant IMFs with lower turning points smaller than $0.6\,\mathrm{R}_\odot$. We do not observe any correlation between the periods of IMFs and their helioseismic frequencies.

The data from the trimmed Cycle 24 seen in the bottom panel of Fig. 6.3 shows similar banding behaviour in the approximate ranges of 250–500, 950–1000 d, and 1275 d. The cluster of results in the 250–500 d range may contain some IMFs which are the results of the Earth's orbit. However, in contrast to the annual bands seen in the upper panels of Figs. 6.2 and 6.3, the annual band seen in Cycle 24 covers a wide range of periods. It is possible that some IMFs with periods in the upper range of this cluster may be attributed to the QBO but there is no clear boundary between IMFs from the annual and QBO-like regime. The bands at 950–1000 and 1275 d show little scatter and coincide with $\frac{D}{3}$ (1260 d) and $\frac{D}{4}$ (945 d) where the duration of the signal D is 3780 d. This suggests that these bands are overtones of the input signal. Due to the shorter duration of Cycle 24, the overtones are more densely packed than those in Cycle 23. A shorter duration naturally leads to more common modes, which in turn results in a greater population of overtones. However we see a weaker QBO presence in Cycle 24 than in Cycle 23 despite the increased number of common modes in Cycle 24. We observe 49 IMFs with periods in the range of 500–800 d which can be associated with the QBO for Cycle 23, with a roughly triangular distribution in its associated histogram, with a median value around 630 d. We contrast this to the same period range for Cycle 24, where we see no distinct peak with only 4 IMFs (a 92% decrease) with a weighted average period between 500–800 d, and a median value of 520 d.

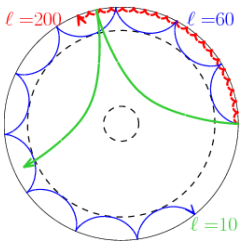

We then perform FFT analysis on the independent helioseismic datasets. For both Cycle 23 and Cycle 24, the ∼11 yr Schwabe cycle was infrequently detected above a confidence level of 95% by Fourier analysis (where a detection is deemed as a statistically significant peak with period $3650 \leq P \leq 4380$ d). This was largely because only one or fewer Schwabe cycles were present in the signals due to the trimming. Although the Schwabe cycle dominated the signal in terms of amplitude, it did not exhibit perfect sinusoidal behaviour and therefore its power was distributed over a number of frequency bins. Therefore, we repeat this analysis with the detrended signal, with the trend being extracted by EMD, as the input signal for both Cycles 23 and 24 (and similarly for the results from MDI/HMI) in order to examine shorter periodicity oscillations, such as the QBO. We assess 251 datasets for Cycle 23 and 346 for Cycle 24.

Of the 251 input signals for the detrended datasets from trimmed Cycle 23, 102 (corresponding to 41%) Fourier spectra had a peak between 333–363 d indicating the presence of the annual oscillation. We estimate the errors on these periods via the so-called functional approach. For the periods between 333–363 d, the corresponding errors to 1sf are -30, +40 d. There were 5 further detections outside this range, all at 666 d (with errors -100, +100 d) which are suggestive of QBO behaviour. Cycle 24 yielded fewer detections overall, in which only 32 of the 346 datasets (9%) produced statistically significant results. The vast majority of these detections had periods between 214–385 d (errors -40, +40 d), with the only other detection at 428 d (error -40, +50 d). It is difficult to determine whether these are truly of solar origin or are indeed false positives due to the low number of detections. To improve confidence in this result we require either more data or an analysis tool which is better suited to detect quasi-periodic signals. These results suggest that solar oscillations with periods less than the Schwabe cycle were less likely to be seen in Cycle 24 compared to Cycle 23.

Data obtained by MDI/HMI

We repeat our analysis once more, this time examining Solar Cycles 23 and 24 separately, using MDI/HMI data. The MDI/HMI datasets have more than twice the number of common modes than the GONG datasets and so produce a greater number of IMFs over a greater depth range. The top panel in Fig. 6.4 illustrates the distribution of periods from IMFs for the MDI/HMI modes detected over the trimmed duration of Cycle 23 which had a duration of 3528 d. There is evidence of banding at approximately 550–800, 800–900 and 1200 d. The $\frac{D}{5}$ overtone if seen is expected at approximately 705 d. This lies within the 550–800 band. The 550–800 band also shows significant scatter which

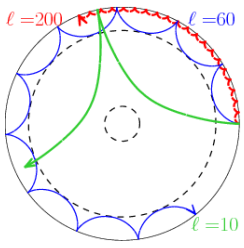

makes it difficult to differentiate overtones and potential QBO candidates. The $\frac{D}{4}$ and $\frac{D}{3}$ overtones are expected at 882 and 1176 d, which correlate with the bands at 800–900 and 1200 d. The periodicities of these QBO candidates again have no correlation with mode frequency.

The results for the trimmed data of Cycle 24 are shown in the bottom panel of Fig. 6.4, producing bands at 400–500, 700–800, 800–900, and 1200 d.

The IMFs with periods of 400–500 d have periodicities greater than what is usually attributed to the annual oscillation, consistent with the periodicities seen in the results from GONG data during Cycle 24. This may be evidence of QBO exhibiting a shorter period in Cycle 24 compared to Cycle 23. A number of IMFs with periods in the range of 550–800 d may also be associated with the QBO. For Cycle 23 we see 105 IMFs with weighted average periods between 550–800 d with a median of 700 d. In assessing the same range in Cycle 24 we see only 36 IMFs (a 66% decrease), with a median period of 730 d. This range does encompass the expected location of the $\frac{D}{5}$ (690-705 d) overtone for both cycles. The $\frac{D}{5}$ overtone (at 690 d, where the duration of the input signal is 3456 d) correlates reasonably well to the band at 700–800 d seen at depths above $0.75\,R_\odot$ However, as the durations of both datasets were roughly the same we would expect the $\frac{D}{5}$ overtone to have similar prevalence in both datasets. Therefore the decrease in IMFs over this range is more likely to be of solar origin than a result of the analysis method. Again differentiating the origin of IMFs in this range poses a challenge as some of the IMFs in this band and the 800–900 d band may be considered QBO candidates. Both bands at 700–800 d and 800–900 d become more densely populated in the region corresponding to $0.75\,R_\odot$ and above and exist across all frequencies for which low error data was available. The locations of the $\frac{D}{3}$ (1152 d) and $\frac{D}{4}$ (864 d) overtones correspond well to the bands at 1200 d and 800–900 d. Although the $\frac{D}{3}$ band is much more densely packed and better defined than its counterpart in the trimmed Cycle 23 MDI/HMI data, overtones corresponding to $\frac{D}{4}$ appear much more sparsely populated than its Cycle 23 counterpart.

Overall, the results from MDI/HMI show a similar pattern to those from GONG: there are proportionally fewer IMFs detected with periodicities in the QBO range in the trimmed Cycle 24 data than in the trimmed Cycle 23 data.

We examine the results from the FFT on the detrended signals both from the trimmed durations of Cycle 23 and 24, at a 95% confidence level. Fourier analysis of Cycle 23 yields 26 detections out of a possible 643 datasets (4%) wherein oscillations at 367 d (with errors ± 40 d) were observed. A further 5 detections (< 1%) of oscillations with periods of 183 d (with errors ± 10 d) were also seen. Interestingly, all of these

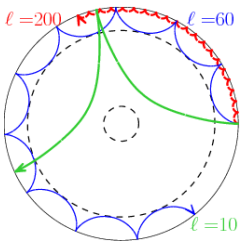

detections occurred for lower turning points greater than $0.76\,R_\odot$. This low number of overall detections from the FFT again may be in part due to the fact that the rising phase of the cycle was omitted so fewer annual cycles could clearly be seen. Out of 679 datasets in trimmed Cycle 24 data, there were 8 detections above the 95% confidence level, all at 1176 d (with errors -300, +600 d), aligning closely with the $\frac{D}{3}$ ($\sim$1200 d) band seen in the bottom panel of Fig. 6.4. This suggests that Fourier analysis also picked up overtones of the input signal. For Cycle 24 data in MDI/HMI, there were no detections of the annual oscillation. This follows on from the previous findings that Cycle 24 appears to show fewer detections of oscillations shorter than the Schwabe cycle.

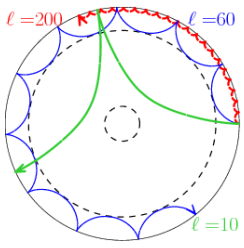

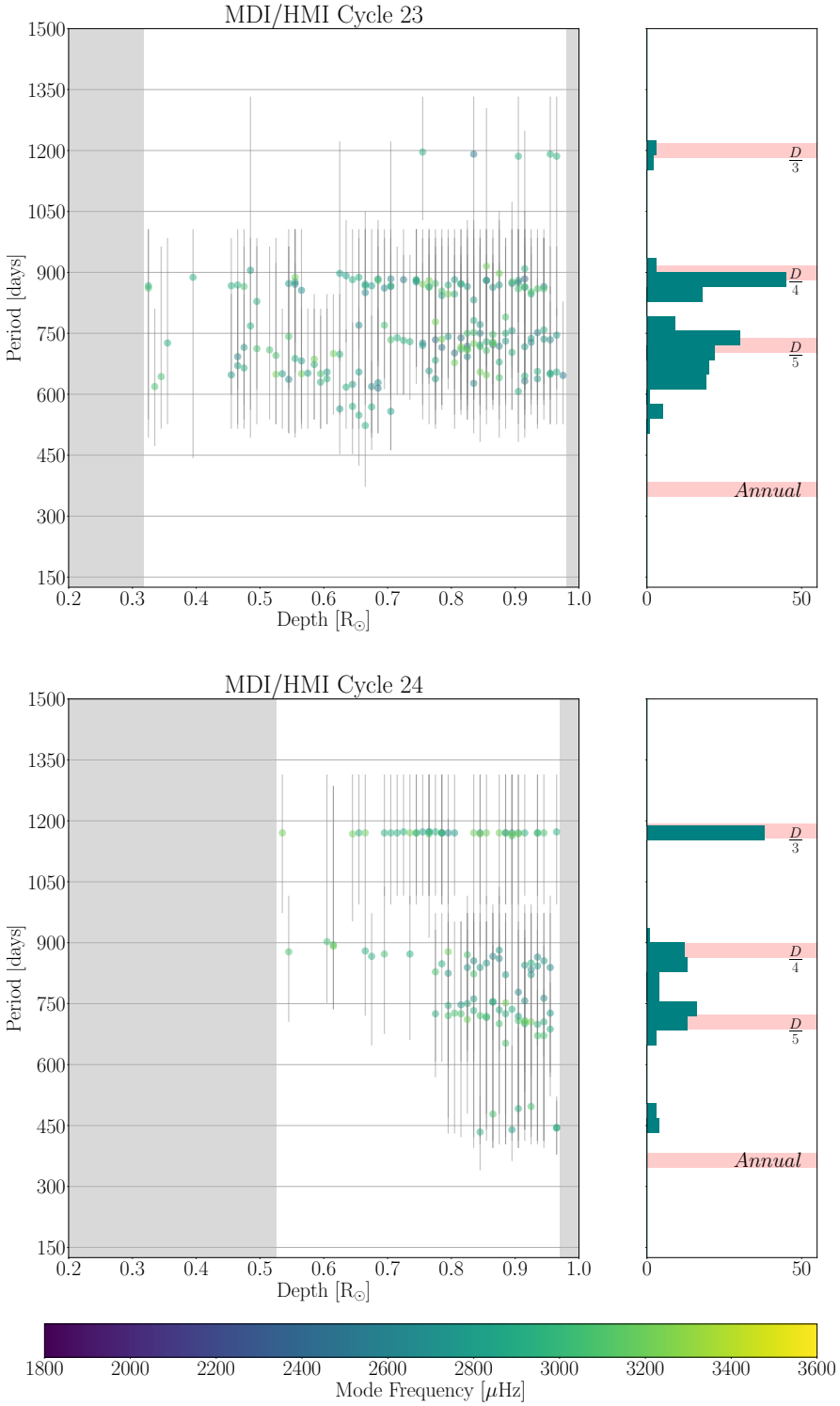

Figure 6.4: Distribution of periods from statistically significant IMFs with IMFs obtained from Cycle 23 *(Top)* and Cycle 24 *(Bottom)* using MDI/HMI data. Colours, symbols etc. are all as given in Figs. 6.2 and 6.3.

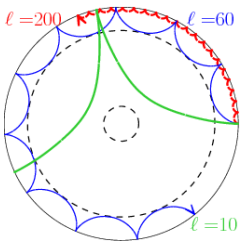

6.3.3 Comparison of analysis techniques

As discussed in Section 6.3.2, the FFT procedure rarely detected the periodic annual oscillation in detrended frequency shift datasets. Therefore it is unsurprising that very few detections of the QBO were seen, as the QBO is expected to be not only lower in amplitude than the annual oscillation, but also its quasi-periodic behaviour spreads its power over several frequency bins. However, it is important to emphasise that FFT analysis was only performed on frequency shifts that had already identified at least one statistically significant IMF and did not investigate signals where no significant IMFs were detected. Therefore these results are useful for a comparison of the methods where EMD found statistically significant oscillations. We also see issues arising due to the non-stationarity of the QBO. For example, the quasi-periodic signal in Fig. 4.4 is symptomatic of the many non-stationary modes examined in this chapter and highlights the difficulty in not only assessing but also describing complex signals. By assigning this mode a single period, we erase the valuable time-dependant period drift behaviour (in this case we see that the period is greatest towards solar maximum of Cycle 24 in 2014 and then decreases during the decay phase), which may provide important information concerning the generation and behaviour of QBO signals. Fig. 4.3 shows the EMD and Fourier spectra of a MDI/HMI frequency shift. Although we see evidence of statically significant oscillations in the EMD spectrum the Fourier spectrum shows no statistically significant peaks above the 95 % confidence level although we do see an enhancement of the Fourier power in the corresponding period ranges. We attribute the lack of detection of significant peaks to spectral power leaking into adjacent bins due to the as the non-stationarity of the signal. This is why Fourier analysis is poorly suited to data with period drifts. The use of FFT in this analysis proved to be useful as an 'eye-guide' only. The QBO also remained undetected in Fourier spectra of solar activity proxies (e.g. see Fig. 6.5).

6.4 Results from solar activity proxies

In order to determine whether the QBO is a cycle-dependent process, we analyse its behaviour over multiple solar cycles using solar activity proxies since MDI/HMI and GONG have only been functional from the rising phase of Cycle 23. We turn to solar activity proxies which have high-quality data dating back several solar cycles. We use data from Cycle 21 through Cycle 24 in the MgII index and $F_{10.7}$ index, and analyse it using EMD in a similar fashion to the oscillation frequency data. These datasets were

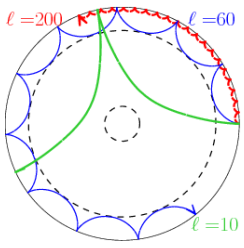

also trimmed according to the method discussed in Section 6.2.2 in order to exclude the time period correlating with low solar activity, where the QBO is less likely to be observed. The start and end dates of the solar activity proxy data are given in Table 6.1. All data were normalised to have a zero mean. We again use a 95% confidence interval, and the periodicities of any statistically significant IMFs found through this method are stated in Table 6.2. We account for errors on the solar proxies by taking the standard error on the mean $\sigma_{\bar{x}}$ where $\sigma_{\bar{x}} = \frac{\sigma}{\sqrt{n}}$. Here σ is the standard deviation of the signal, and n is the number of points we average over. We use this standard error to construct symmetrical error bars, shown in green colour in Fig. 6.5.

Table 6.2: The periodicities, given in days, of IMFs with statistical significance over a 95% confidence interval found by running EMD on data from solar activity proxies. IMFs that we do not attribute to overtones are emphasised in bold. Dashes indicate where no statistically significant IMFs were observed for the given dataset.

Dataset	Cadence [days]	Cycle			
		21	**22**	**23**	**24**
$F_{10.7cm}$	36	**464** $^{+96}_{-151}$	**351** $^{+88}_{-100}$ **893** $^{+163}_{-221}$	**308** $^{+66}_{-59}$ **669** $^{+173}_{-179}$ 1332 $^{+152}_{-444}$	961 $^{+363}_{-225}$
$F_{10.7cm}$	72	–	**286** $^{+167}_{-149}$	747 $^{+205}_{-167}$	–
MgII	36	–	839 $^{+86}_{-110}$	**584** $^{+140}_{-166}$	**448** $^{+113}_{-71}$ 1246 $^{+233}_{-309}$
MgII	72	–	–	**648** $^{+138}_{-116}$	1081 $^{+150}_{-166}$

Across both datasets we see only one detection of a statistically significant IMF for Cycle 21, found in the 36 d cadence $F_{10.7}$ data. This IMF had a weighted average period of 464 d, which is within the range we attribute to the annual oscillation period. This period is similar to another detected in Cycle 24 which is discussed further below.

Cycle 22 yields detections for three out of the four datasets, with only the 72 d

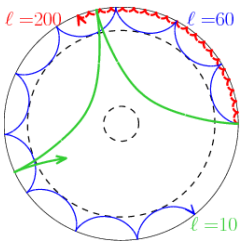

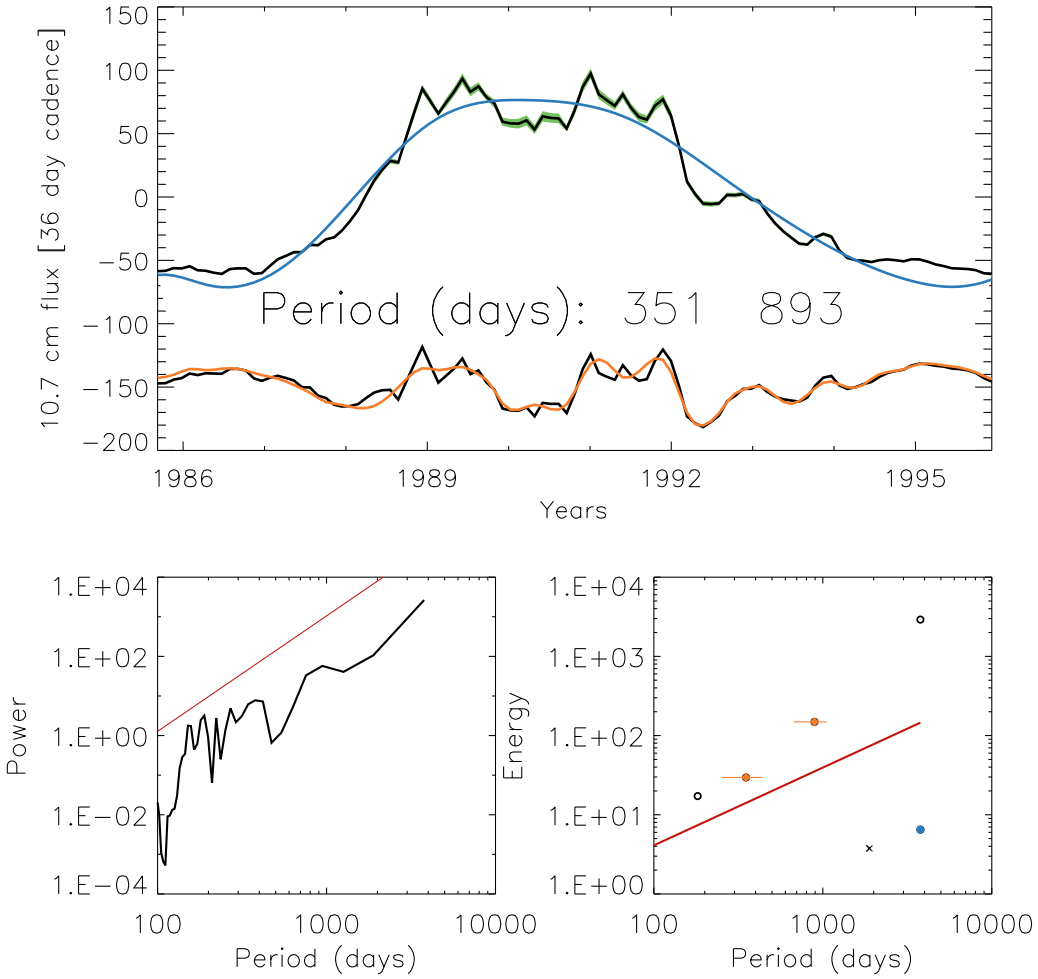

Figure 6.5: Analysis of $F_{10.7}$ data over Cycle 22 where data is averaged over 108 d bins, overlapping by 36 d. *(Top)* Upper curve shows the normalised $F_{10.7}$ data, with errors in green, superimposed with the IMF associated with the trend, shown in blue. Lower curve shows the detrended signal with the overlayed sum of two statistically significant IMFs. These IMFs have periods of 351^{+88}_{-100}, 893^{+163}_{-221} d. *(Lower left)* FFT spectrum of the $F_{10.7}$ data, with 95% confidence level (solid red line). *(Lower right)* EMD spectrum of the $F_{10.7}$ data with IMFs visualised as bullet points, indicating their average periods and spectral energy. The 95% confidence level is shown by red line. The IMF with the lowest period cannot be assessed with the confidence level given and is excluded from the analysis. Statistically significant IMFs with energy over the confidence levels are seen in orange with the error in period shown as a horizontal orange line. The IMF associated with the trend is shown in blue and the residual is indicated by a cross.

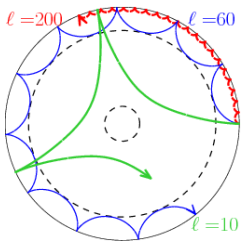

cadence MgII index data showing no statistically significant IMFs. We see IMFs with average periods of 286 and 351 d (both from $F_{10.7}$ index data) which we attribute to the annual oscillation. The remaining detections (seen in 36 d cadence for both $F_{10.7}$ and MgII index data) have periods of 839 and 893 d, and are in the range commonly associated with the QBO. We examine if any of these detections lie close to the expected regions associated with overtones. The durations of 36 d cadence $F_{10.7}$ and 36 d cadence MgII index data were 3744 and 2484 d, respectively. The detection from 36 d cadence MgII index data at 839 d lies close to the $\frac{D}{3}$ overtone, at 828 d. However, the detection in 36 d cadence $F_{10.7}$ data at 893 d cannot be easily attributed to an overtone. Further it correlates well with the other detection in this range suggesting that the IMFs with periods in this range may be of real solar origin.

Cycle 23 shows evidence of the annual oscillation for the 36 d rebinned $F_{10.7}$ data, yielding a detection with an average period of 308 d. We also see detections of IMFs with periods between 584–747 d. Using a similar method as before, we see that the detection at 669 d (for the 36 d rebinned $F_{10.7}$ data) is unlikely to be associated with the $\frac{D}{5}$ overtone which we would expect around 792 d, as in this case the duration of the dataset is 3960 d. The detection at 747 d (from the 72 d rebinned $F_{10.7}$ data) is in the range of what we would expect for the $\frac{D}{5}$ overtone at 763 d, as the duration here is 3816 d. Although the $\frac{D}{5}$ overtone is not commonly observed, it is unlikely that the detection at 747 d is of solar origin and is more likely an artefact of the analysis method. We see another detection from the 72 d rebinned MgII index data at 648 d. This detection is far from the expected range of the $\frac{D}{5}$ overtone at 864 d, as the duration is 4320 d for this dataset, and therefore we suggest this detection is not the result of overtones. The last detection in the QBO range comes from the 36 d rebinned MgII index data with an average period of 584 d. The duration of this dataset is 4284 d, putting the $\frac{D}{5}$ (the overtone with the lowest periodicity that we usually observe) at 857 d. As the periodicity we detected is lower than this value, it's unlikely that this detection is an overtone and an artefact of the analysis method and more likely is of real solar origin. The final detection for Cycle 23 is at 1332 d from the 36 d rebinned $F_{10.7}$ data and closely matches up with the expected location of the $\frac{D}{3}$ overtone at 1320 d.

Finally, we assess the results from Cycle 24. There is a detection of an IMF with a period of 448 d, originating from MgII index data. This result is within the expected range for the annual oscillation but is higher in periodicity than those attributed to the annual oscillation in Cycles 22 and 23. This reflects the findings discussed in Section 6.2 where for both GONG and MDI/HMI data we see an increase in detections of IMFs with periods shifted towards approximately 450 d in Cycle 24 compared to Cycle 23 (see

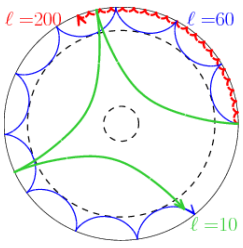

the distribution of the histograms around 450 d in Cycles 23–24 in both Figs. 6.3, 6.4). This shift in Cycle 24 may be due to some mixing between the lower-amplitude, higher periodicity QBO regime and the higher-amplitude, lower periodicity annual oscillation. All other oscillations in the results from Cycle 24 lie close to the expected location of some overtone. The detection at 961 d for the 36 d rebinned $F_{10.7}$ data is close to the location of the $\frac{D}{4}$ overtone at 945 d (where the duration of the dataset is 3780 d). The detections for the MgII index datasets at 1246 and 1081 d for the 36 d and 72 d rebinned data respectively both lie close to the $\frac{D}{3}$ and $\frac{D}{4}$ overtones at 1089 and 1062 d where the durations of their datasets are 4356 and 4248 d respectively. Therefore we see that there is no strong evidence of QBO behaviour in Cycle 24 as observed by solar activity proxies.

To summarise the results of both solar activity proxies excluding the IMFs that we can confidently attribute to overtones, we see oscillations of 464^{+96}_{-151} d in Cycle 21, 286^{+167}_{-149}, 351^{+88}_{-100}, 893^{+163}_{-221} d in Cycle 22, 308^{+66}_{-59}, 584^{+140}_{-166}, 648^{+138}_{-116} and 669^{+173}_{-179} in Cycle 23 and 448^{+113}_{-71} in Cycle 24.

For all solar activity proxy datasets, Fourier analysis did not detect any oscillations above a 95% confidence level other than the duration of the input signal. The annual oscillation was not seen above this level in any of the datasets which may be in part due to the fact that the majority of the power was distributed into longer period oscillations. Through detrending the signal first and then analysing it with FFT, it may be possible to uncover the annual oscillation. This may also reveal further information about the QBO although as the QBO exhibits non-periodic behaviour, power is likely to be distributed over a number of bins in frequency space, reducing its overall significance, and so the annual oscillation may still not be visible. This could be further investigated by rebinning the Fourier spectra [see Pugh et al., 2017a, for further details]. The Fourier spectra of $F_{10.7}$ index data over Cycle 22 can be seen in the lower left panel of Fig. 6.5.

In Kolotkov et al. [2015], a similar analysis was carried out on smoothed $F_{10.7}$ index data which was rebinned to both 108 and 10 d cadences and assessed with the Hilbert-Huang Transform (HHT). These analyses obtained a number of IMFs with periods that are consistent with our results. For example, both the 108 d and 10 d $F_{10.7}$ index revealed IMFs with periods of 1180^{+337}_{-214} and 1110^{+710}_{-340} d respectively which may be compared to the IMFs with weighted-average periods of 1081^{+150}_{-166} and 1246^{+233}_{-309} d detected in Cycle 24 in this study.

Similarly, IMFs with periods of 885^{+117}_{-200} and 833^{+417}_{-63} d found in the previous study can be compared to the detections with periods of 839^{+86}_{-110} and 893^{+163}_{-221} d in Cycle 22. Kolotkov et al. [2015] also observed IMFs firmly in the QBO range with

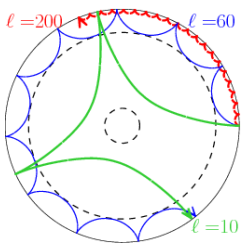

periods of 708^{+215}_{-163} and 690^{+80}_{-200} d which may be compared to our detections in Cycle 23 of 747^{+205}_{-167} and 648^{+138}_{-116},669^{+173}_{-179} d respectively. These authors also detected a number of lower periodicity IMFs with periods of less than 200 d. However, the methodology used in that paper and our study have several differences which may be responsible for these additional IMFs. Additionally, the data used in Kolotkov et al. [2015] spanned over a continuous duration of two-and-a-half solar cycles whereas we use independent cycles which are trimmed to centre around periods of high solar activity. Finally, no significance testing was performed in the earlier study which naturally leads to a greater number of reported IMFs.

6.5 Discussion

We have used both EMD and Fourier analyses to study quasi-periodicities in the time variation of frequency shifts of p-modes observed with GONG and MDI/HMI. The results in this chapter were confined to data that had sufficiently low error, restricting the modes from which we found significant IMFs to roughly 2600–3400 μHz and 0.6–0.9 $R_\odot$. We also examined the $F_{10.7}$ and MgII index over four solar cycles to search for the QBO. This chapter concludes the following.

1. **We find evidence of the QBO in the combined durations of Cycles 23 and 24 in both GONG and MDI/HMI data** (see Fig. 6.2). We observe periodicites in three main groups for GONG data at 500–800, 900–1200, 1200–1500 d and in two groups for MDI/HMI data at 600–1000 and 1200–1500 d which we consider to be evidence of the QBO.

2. **We also observe evidence of the QBO in Cycles 23 and 24 when analysed separately. These observations are accompanied by overtones (specifically with periods in the range of $\frac{D}{3}$, $\frac{D}{4}$ and possibly $\frac{D}{5}$). The ranges where potential QBO candidates were observed overlap with periods where overtones are expected making a definitive classification difficult.** The observed periodicities not solely attributed to artefacts or overtones were approximately between 500–800 d for Cycle 23 across both datasets. MDI/HMI data revealed periodicities over a similar range of 550-800 d in Cycle 24 which we attribute to the QBO. Conversely GONG data did not produce strong evidence of the QBO in Cycle 24, where the majority of IMFs overlapped with a region associated with an overtone making it difficult to ascertain whether these IMFs are an artefact of the analysis procedure or true QBO

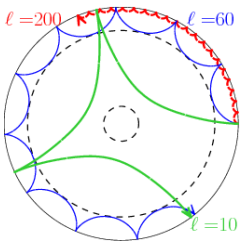

candidates. The EMD technique uncovered consistent measurements of $\frac{D}{3}$ and $\frac{D}{4}$ overtones at approximately 1300 and 1000 d for GONG data over both cycles. Similarly, MDI/HMI datasets yielded detections of $\frac{D}{3}$, $\frac{D}{4}$ and $\frac{D}{5}$ overtones with periods of approximately 1200, 900, and 700 d across both cycles.

3. **We see a weaker presence of the QBO in Cycle 24 compared to Cycle 23 which we do not attribute to data sparsity or analysis methods.** This is because we see fewer IMFs in the approximate QBO range from 500–800 d in Cycle 24 than Cycle 23 (shown in the lower panels of Figs. 6.3 and 6.4), despite the number of common modes increasing for GONG data (by 57%) and remaining roughly constant for MDI/HMI data (an increase of 3%).

We further note that the increase in common modes between Cycles 23 and 24 for GONG data has not changed the overall number of detections of the annual oscillation, although Cycle 24 shows significantly more scatter in the 250–450 range compared to the tight banding seen in Cycle 23. This implies that an oscillation of physical origin is still visible in Cycle 24 data which contrasts with the sparsity of IMFs corresponding to the QBO range. The annual oscillation is not observed by MDI/HMI, however, we see the same trend in data from both instruments - a lower population of IMFs with periods between 500–800 d in Cycle 24 when compared to their Cycle 23 counterparts.

The relative significance of the overtone oscillations at $\frac{D}{3}$,$\frac{D}{4}$ (which could be mistakenly attributed to high periodicity QBO candidates) were largely unaffected between the cycles, whilst the apparent presence of the QBO candidates reduced. This may lead a reader to the incorrect interpretation that the periodicity of QBO increased between Cycles 23 and 24.

Since the weaker signature of the QBO in Cycle 24 is seen in two different datasets and does not depend on the number of common modes, we believe that this cannot be attributed to the analysis procedure. The reduced presence of the QBO in Cycle 24 further suggests that the QBO is a cycle-dependent process and its generation mechanism is in some way linked with that of the Schwabe cycle.

4. **There is some evidence of the QBO in solar activity proxies, specifically during Cycles 22 and 23. This may suggest some form of correlation between the observational properties of the Schwabe cycle and the QBO.** We observe QBO candidates with periods of around 450 d in Cycle 21 and 24, approximately 900 d in Cycle 22 and around 650 d in Cycle 23. Significant IMFs with periods that corresponded to overtones and Earth's annual orbit were also uncovered. The detection

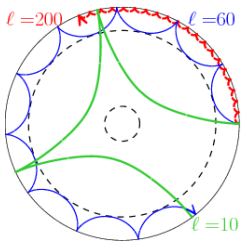

at 450 d in Cycle 24 is interesting as that was also seen in the MDI data, and potentially in the GONG data, although here it is hard to distinguish from the annual periodicity. We point out that the periodicities detected in the QBO range occurred during the more active solar Cycles; Cycles 22 and 23. This may suggest a that the amplitude of the QBO in both frequency shift data and solar activity proxy data scales with the activity of the solar cycle.

5. **The presence of the QBO was not affected by the depth to which the p-mode travelled, nor the average frequency of the p-mode. The analysis further suggests that the magnetic field responsible for producing the QBO in frequency shifts of p-modes is anchored above approximately 0.95 $R_\odot$.** The QBO candidates seen in Figs. 6.2, 6.3 and 6.4 are present across almost all depths where data is available. There is no dependence with lower turning points of any of the modes with the appearance of the QBO, other than in Cycle 24 for MDI/HMI data where the 700–800 and 800–900 d bands are more densely populated at radii greater than 0.75 $R_\odot$. As the intermediate degree modes penetrate to all depths, this suggests that the magnetic field generating the QBO must be anchored above the highest lower turning point of any mode which shows QBO behaviour. The upper turning points of these modes could be analysed in order to better determine the location of the magnetic field.

6. **There is difficulty differentiating overtones and the QBO due to spread in periodicity and large errors.** The errors associated with the periods of statistically significant IMFs are large (see Figs. 6.3, 6.4), with upper and lower bounds overlapping across several bands. Neglecting errors, we find that 20% of IMF periods fall within the expected overtone ranges (visualised by pink shaded bands) for GONG data in Cycle 23 (increasing to 30% for Cycle 24). For MDI/HMI data the percentages of IMFs that have a period within the ranges of overtones are 20% and 58% for Cycles 23 and 24 respectively. Including errors, most of the QBO periods overlap with at least one overtone band, making it even more challenging to assess if a statistically significant period is the result of an overtone. However we do expect the errors on these IMFs to be large due to the nature of quasi-periodic signals. Recall that the errors on the average periods of these IMFs are obtained by the Full Width Half Maximum (FWHM) of the IMF's global wavelet spectrum. Therefore a signal with significant period drift will naturally produce large errors. The contrast of this can be seen by examination of the IMFs attributed to the annual oscillation (which has a stationary period) which show considerably smaller errors than the QBO candidates. We also expect the presence

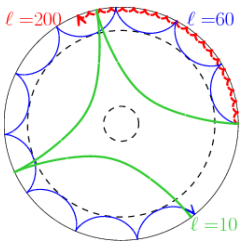

of overtones which are more frequently observed in shorter duration data. This can be seen in comparing the presence of overtones in single cycle data (Figs. 6.3, 6.4) to the longer duration combined cycled data (Fig. 6.2). Although the large errors and presence of overtones are to be expected, the combination of the two leads to difficulty in interpreting the origin of IMFs. At present there is no technique by which we can reliably identify which regime an individual IMF belongs. This can be mitigated by addressing the behaviour of clusters of IMFs instead of individual IMFs but is beyond the scope of this thesis.

7. **The Fast Fourier Transform is poorly suited to assessing signals with significant period drift.**

We assessed helioseismic data using the Fast Fourier Transform and rarely found oscillations with periods in the QBO range. Similarly, we found no evidence of the QBO when assessing solar activity proxies with the Fast Fourier Transform. We believe this is mainly due to spectral leakage between adjacent period bins in the power spectra of the signals, due to the period drift present in QBO signals. In order to properly analyse quasi-oscillatory signals, we must ensure we make use of techniques capable of handling period-drifting signals for quasi-oscillatory processes such as EMD or wavelet analysis.

Helioseismic data spanning a larger time range would improve this study as it would not only allow us to look at the longer-term evolution and behaviour of the oscillations in the QBO range, but would also reduce the presence of overtones, which have an inverse dependence on the duration of the input signal. Therefore we raise the importance of long-term synoptic helioseismic datasets, such as GONG and HMI, which is needed if we hope to study the temporal evolution of phenomena confined to or generated in the solar interior. It would be of interest to the community to revisit this study following Cycle 25.

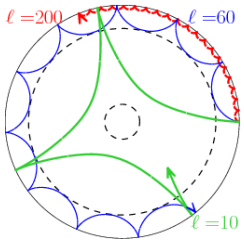

Chapter 7

Non-stationarity in Quasi-Periodic Pulsations

This chapter compiles the work of two papers; the former examines a case study on non-stationarity in QPPs from a single flare[a], and is in the stages of being submitted to a journal for publication (Section 7.2), and the latter examines a larger study on non-stationarity in QPPs in 98 flaring events[b], with the paper currently in the review process (Section 7.3). Our specific contributions to each study are detailed at the start of the respective sections. We summarise the findings from this chapter in Section 7.4.

[a] **"Evolution of Quasi-Periodic Pulsations in a long duration flare"**.
(In prep.), Astronomy & Astrophysics, 2023
By L. Hayes and T. Mehta.

[b] **"Prevalence of non-stationarity in Quasi-Periodic Pulsations associated with M- and X- class solar flares"**.
(Under review) Monthly Notices of the Royal Astronomical Society, 2023
By T. Mehta, A.-M. Broomhall, L. Hayes.

In this chapter we explore the prevalence of non-stationarity, or period drift, in QPPs and discuss the implications of these findings. We look into factors that may cause the appearance of non-stationarity and present our recommendations on how to meaningfully assess QPPs with non-stationary periods.

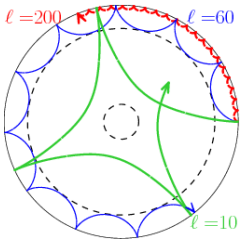

7.1 Motivation of looking at non-stationarity

A signal is considered 'non-stationary' when the instantaneous period of the signal varies with time. This may be seen via a period growth or shrinkage, where the instantaneous period increases or decreases by the end of the signal. We denote this change in instantaneous period a *period drift*. We note that the period drift corresponds to a change in period in two phases of the QPP and is therefore measured in seconds, and is not a rate of change. These effects can originate from a number of causes; for example the properties of the driver of the periodic motion may change with time, creating a shift in the period of the resultant motion. Another cause could be through multiple drivers, each with different stationary periods, e.g. if the motion due to a driver with a short stationary period were to decrease in tandem with the motion from a driver with a higher stationary period growing, we would see an apparent increase in period of the overall motion. These effects may similarly be caused by evolution of the region where the signal originates from.

Most statistical studies of QPPs use analysis methods that assume a stationary output, where a detection is recorded if there's strong evidence of a stable periodic oscillation. This is largely done for convenience, as several of these methods do not require any pre-processing and are well equipped to handle data with red noise processes [Inglis et al., 2015; Pugh et al., 2017a]. These methods have been proven to be efficient, and accurate, and have avoided the pitfalls that arise in detrending data [Pugh et al., 2019]. However considering non-stationarity is important when examining periodic solar and stellar periodicities, as discussed at length in Nakariakov et al. [2019]. A growing number of studies have shown case studies of QPPs that increase in instantaneous periods towards the decay phase of the flare [E.g. Simões et al., 2015; Hayes et al., 2019]. Firstly, if we incorrectly assume a signal is stationary we risk failing to detect non-stationary signals, leaving us with missing or incomplete data that poorly describes the true phenomenon at play. Secondly, we have to think about the implications of non-stationarity on our models and the way we interpret the data. What does the presence of non-stationarity in solar QPPs data imply about the mechanisms driving flares, for example. If we fail to consider the possibility of non-stationarity in our data, we fail to study the universe in its true complexity.

For these reasons we assess QPPs in solar flares in this chapter with an open mind, and search for evidence of non-stationarity. We begin by assessing a case study of a QPP from 2012, and examine whether we can link any period drifts with the changes in flaring loop's height (Section 7.2). We then perform a larger study (Section 7.3),

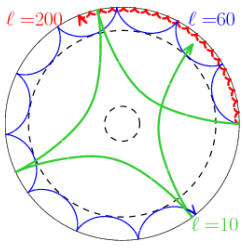

examining non-stationarity in 98 flare events.

7.2 Linking flare loop height to period drift in a QPP: A case study

This section contains work that was part of a collaboration between myself and Dr. Laura Hayes. I contributed the analysis discussed in Section 7.2.3, on the period evolution of QPPs, and L.H. contributed the analysis discussed in Sections 7.2.4 and 7.2.5, on confirming the QPPs origins with AIA data and tracking the flaring loop's height. Figures that have been made by L.H. are indicated in all relevant captions, and Sections 7.2.1–7.2.5 were originally written by L.H. but I have rephrased them in my own words for this thesis.

7.2.1 Introduction

Although there is no scientific consensus on which mechanism(s) drive QPPs in flares (see Section 1.4.2), we are still able link QPPs to observable physical processes which will lead to a better understanding of the processes going on. For example, if we observe a correlation between the properties of a flaring loop and the change in period of an associated QPP, we are in a better position to assume that the physical properties of the loop have some impact on the timescales of the QPP. Conversely, a negative result could be useful evidence in ruling out this possibility. To fully understand the mechanisms driving QPPs we will need a much larger study of likely thousands of QPPs, which are located in a way that we can effectively observe their flaring regions, linking their parameters with optical data with high spatial and temporal resolution. Until then, we are restricted to smaller case studies, like this one, that can guide future work. Here, we examine a long duration QPP that was observed from a flare site which had an associated coronal loop and CME. The coronal loop appeared on the edge of the solar Western limb and therefore was optimally placed for us to investigate the peak of the loop's height. In this study, we track the growth in loop height with QPP period to examine whether the two phenomenon are correlated.

7.2.2 The flaring event

We investigate a flare that occurred on 19$^{\text{th}}$ July 2012 at $\sim$ 04:17 UT, continuing for several hours, on the western limb of the Sun. It was an X1.1 GOES class flare, and associated with a large solar eruptive event [Patsourakos et al., 2013]. The flare emission,

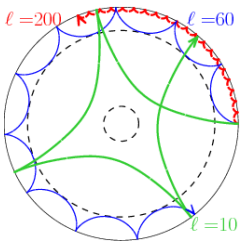

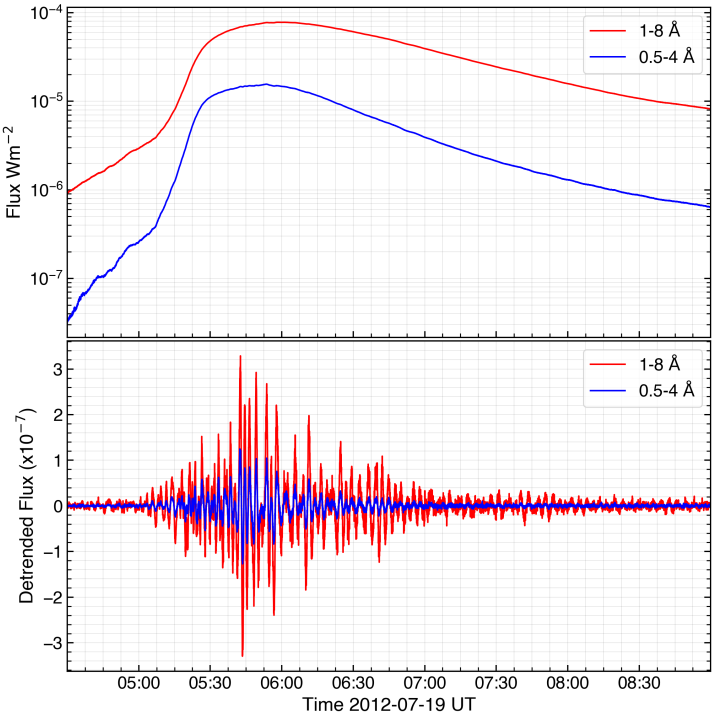

Figure 7.1: The GOES/XRS lightcurves and identified QPPs during the flare. The top panel shows both the 1–8 Å and the 0.5–4 Å channels in red and blue, respectively. The bottom panel shows the detrended lightcurves, calculated by subtracting the slowly-varying components of the flare lightcurves. *Figure created by L. Hayes, from Hayes et al. [In prep.] (2023)*

as observed in GOES 1–8 Å and 0.5–4 Å is shown in the top panel of Fig. 7.1, with peak flare emission occurring at 05:58 UT.

The QPPs associated with the flare are small in amplitude compared to the flare itself, but can be readily seen in the lower panel of Fig. 7.1, which shows the detrended flare emission. The flare was detrended by subtracting a a Savitzky-Golay filter [Savitzky & Golay, 1964] with a window of 151 (∼300 s) and degree 3. We chose these parameters to ensure the window was longer than the periodicity of interest. The QPPs can be seen in both the short and long wavelength channels of GOES, with QPPs extending for several hours past the peak of the flare, and are reasonably coherent. These long lasting QPPs are ideal candidates to study the instantaneous period evolution of a flare as they are measured with high cadence, 100% fill data, and extend for an unusually long time. We now track the QPPs evolution in period using continuous wavelet analysis.

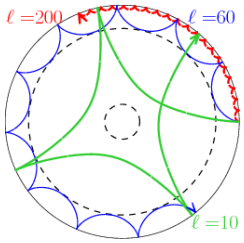

7.2.3 Period analysis

We visualise the variation in the QPPs' instantaneous period using the continuous wavelet transform (CWT). The detrended GOES/XRS 1-8 Å emission is shown in the top panel of Fig. 7.2, with QPPs visible and the impulsive phase (the duration from the start of the flare to peak flare emission as measured in 1-8 Å) is shaded in blue, and the decay phase (the duration from peak flare emission to the return to background levels) is left unshaded. The CWT is sensitive to the amplitude of the oscillations, which presents a difficulty when assessing QPPs as the amplitude of the QPPs decreases significantly in the late stages of the decay phase. Therefore we decide to normalise the QPPs to a constant amplitude before performing the CWT. The QPPs are normalised by dividing the detrended emission with another Savitzky-Golay envelope, this time with a window width of 303 (∼620 s), degree 3. This window length was chosen following an by-eye inspection, as the envelope needed to resemble the local maxima and minima of the data, but not follow so closely as to divide out valuable information. The resulting normalised QPPs can be seen in the middle panel of Fig. 7.2. We finally perform the CWT on this signal, producing the spectrum seen in the lower panel of Fig. 7.2. An approximately linear growth in period is seen between 05:30 – 07:00 UT from ∼100 – ∼200 s followed by a constant period of ∼200 s between 07:00 – 09:00 UT.

7.2.4 Confirming the location of the QPPs

Because GOES/XRS takes full-disk integrated measurements, we need to confirm whether the QPPs identified are indeed from the flaring region. Following on from Hayes et al. [2019], we do this by using AIA data, where we see the flaring loop clearly extending outward from the Western solar limb. It was detected by the AIA instrument aboard SDO, seen in the 131 Å channel in Fig. 7.3 over four hourly intervals. We chose to assess the 131 Å channel as it has a response to the Fe XXI and Fe XXII lines and so will be well correlated with the GOES/XRS channels we are examining for period drift as both instruments are sensitive to temperatures exceeding 10 MK. We used the AIApy [Barnes et al., 2020] software to calibrate the AIA file to a level 1.5 and normalise the exposure times. We note that the images saturate towards the peak of the flare at 06:00 UT, causing some bleeding seen in Fig. 7.3.

We create a lightcurve from AIA 131 Å data by summing the intensity values of the pixels seen in the field of view of Fig. 7.3 for the full four hour duration and create a timeseries. To reduce the impact of time-dependant artefacts introduced by exposure control variability, we sum over every second frame, such that the final timeseries has a

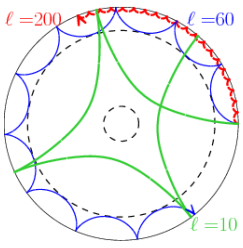

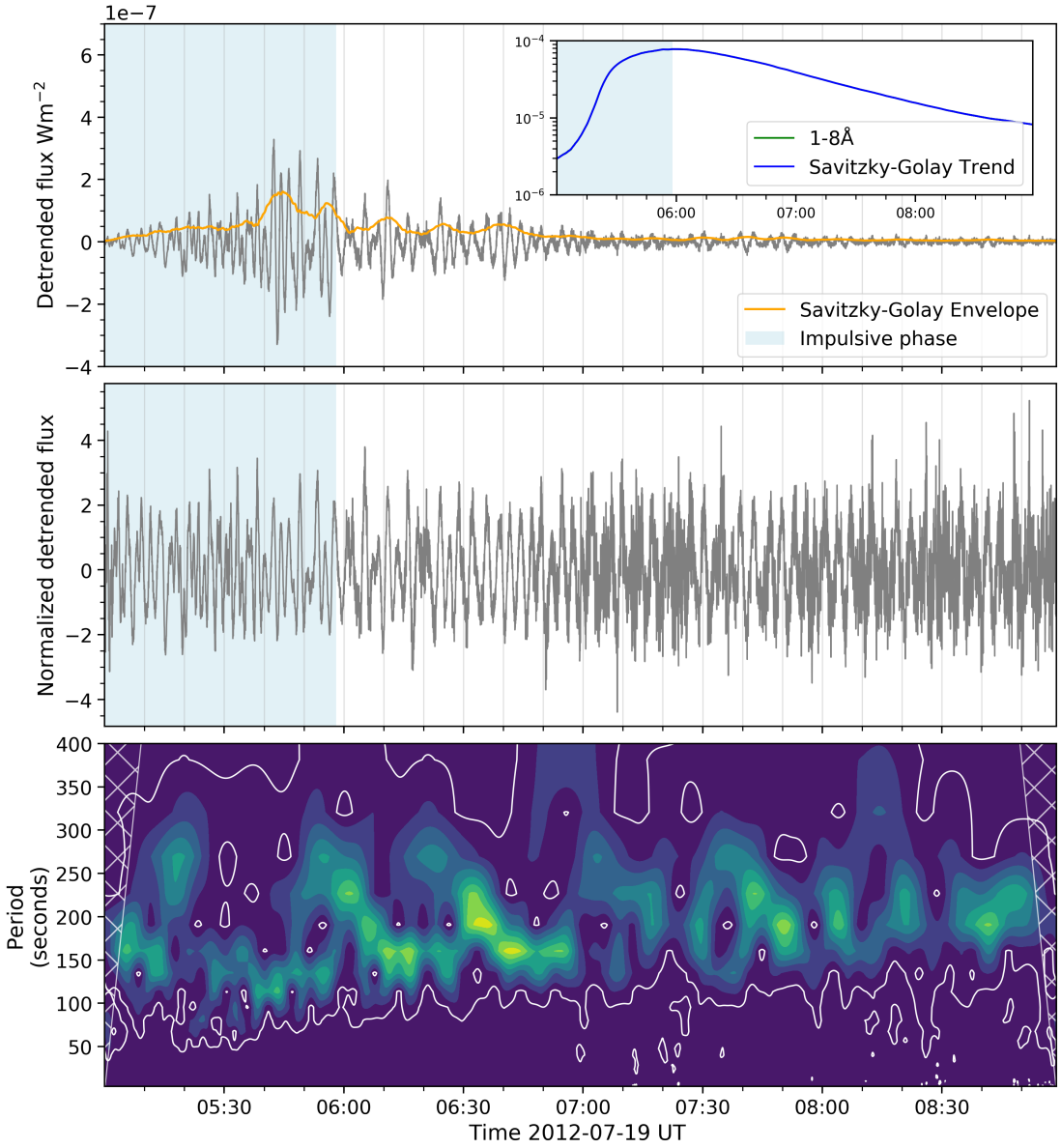

Figure 7.2: Continuous wavelet analysis of the GOES/XRS 1-8 Å emission. The top panel shows the detrended lightcurve (grey) with overlaid Savitzky-Golay envelope (orange). The top panel inlay shows the raw GOES/XRS 1-8 Å emission (green) and the Savitzky-Golay obtained trend (blue), although any differences in amplitude between the two signals cannot be discerned at this scale and so the raw emission (green) cannot be seen. The middle panel shows the detrended normalised emission and the bottom panel shows its continuous wavelet spectrum. Yellow/green indicate regions of higher amplitudes, with lower power amplitudes shown in blue/purple. Power above the 90% confidence level is outlines in white.

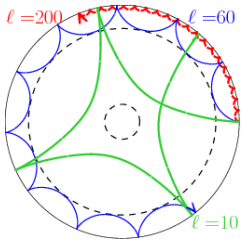

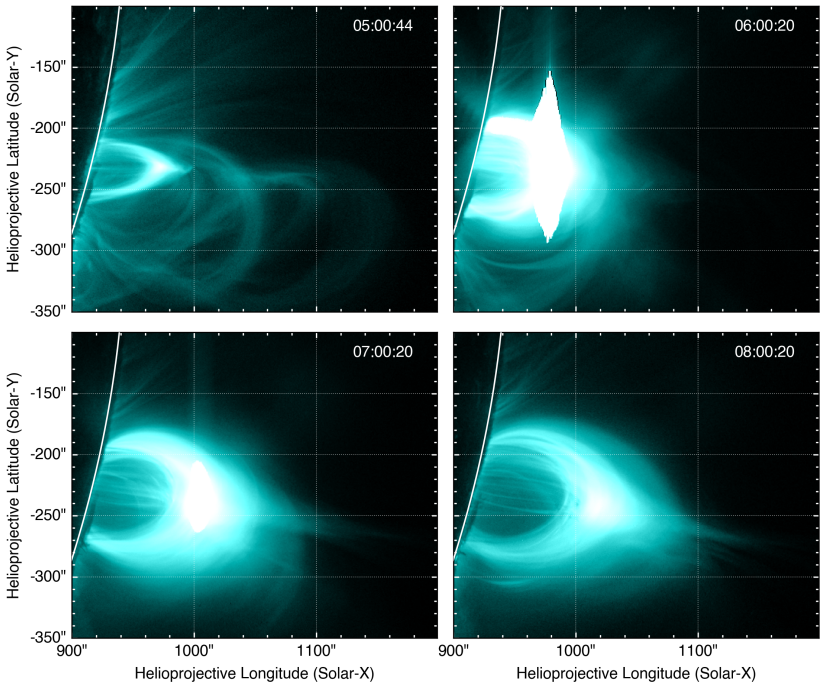

Figure 7.3: Measurements of the flaring coronal loop as measured with AIA in the 131 Å channel. Each image is taken one hour apart and shows the evolution of the structure and the increasing loop length overtime. *Figure created by L. Hayes, from Hayes et al. [In prep.] (2023)*

cadence of 24 s. We ensure all flux is contained within each time interval by selecting a cutout image size which includes all bleeding pixels. As shown in the inset panel of Fig. 7.4, the QPPs seen in the resulting AIA timeseries closely resembles those detected by GOES/XRS, which confirms that our period analysis is indeed assessing varying flare emissions from a single active region and not an instrumental effect. We choose to continue the period analysis with the GOES/XRS data rather than the AIA data even though they were well correlated, as the GOES/XRS data has higher cadence and has been well used in previous QPP studies [Hayes et al., 2020b].

7.2.5 Assessing the loop length

Now that we have confirmed the period evolution of the QPPs, we examine the height evolution of the associated flaring loop. For this, we turn to measurements from RHESSI (See Section 3.7). RHESSI takes image observations of the soft X-ray emitting plasma, from which we extract the location of the X-ray source and track it over time to produce

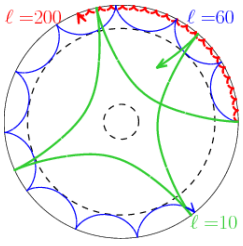

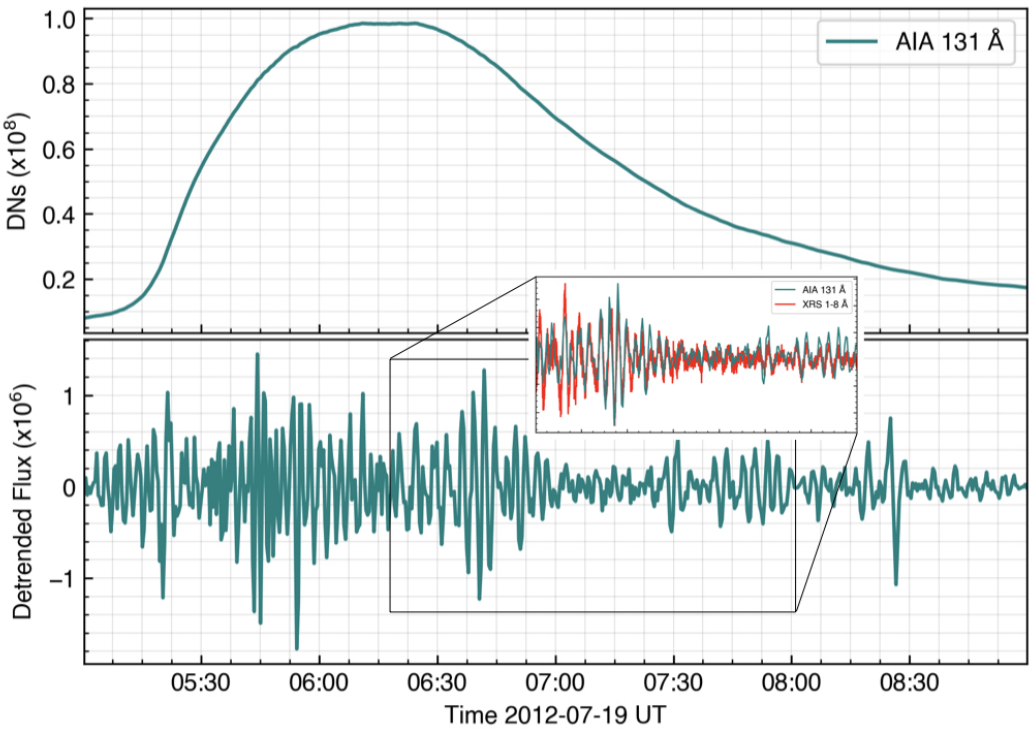

Figure 7.4: The top panel shows the lightcurve generated from AIA images (teal), created by summing over the field of view. The lower panel shows the detrended lightcurve, which is calculated by subtracting a smoothed varying lightcurve. The inset panel of the lower panel shows the AIA data superimposed with the GOES/XRS 1-8 Å detrended lightcurve (red), which reveals the highly correlated properties of the two datasources. *Figure created by L. Hayes, from Hayes et al. [In prep.] (2023)*

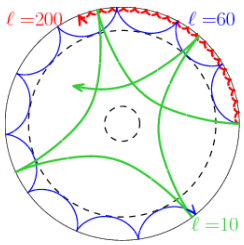

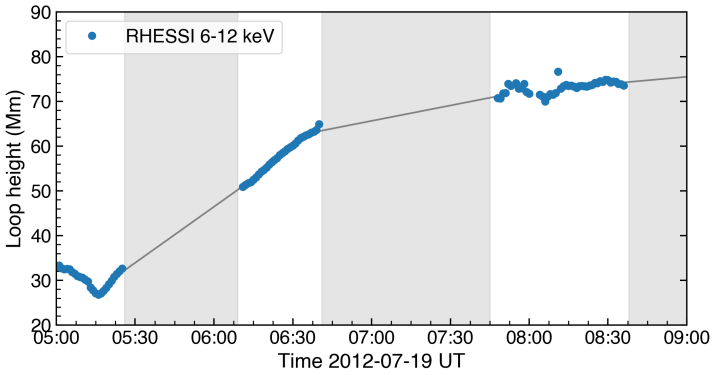

Figure 7.5: RHESSI loop height, measured in the 6-12 keV channel (blue dots). Linear fits (black lines) are shown for the durations when no RHESSI data was available, which are shaded grey. *Figure created by L. Hayes, from Hayes et al. [In prep.] (2023)*

a time series. We do this by reconstructing RHESSI images using the CLEAN algorithm [Schwartz, 2009], with an integration time of 20 s using detectors 3-9. We calculate each image's centroid and track its movement over time to produce Fig. 7.5 which shows the approximate progression of the soft X-ray source at the peak of the flaring loop. The blue marked points are the centroid of each X-ray source in the 6–12 keV energy band. To estimate the loop length times when RHESSI was in nighttime (indicated by the grey shaded regions) linear fits were made to the data between the intervals to make an approximate estimation of the loop source increase as a function of time, similar to Hayes et al. [2019].

7.2.6 Discussion

Both the instantaneous period of the QPPs and the amplitude source height, which we use as a proxy for loop length, show evidence of growth over the duration of the flare. We see initial approximately linear growth in the instantaneous period of the QPPs from 05:30 – 07:00 UT from ∼100 – ∼200 s, which occurs co-temporally with an approximately linear growth in amplitude source height from ∼45 – ∼80 Mm. The QPP period then appears constant from between 07:00 – 09:00 UT at ∼200 s, which matches with the much slower growth of the amplitude source height, which increases from ∼80 – ∼88 Mm over the same time period. We also point out the rapid initial descent and then increase in amplitude source height, which is thought to be caused by the downward contractions of the loops undergoing reconnection.

We know that there must be some link between QPP timescales and flaring

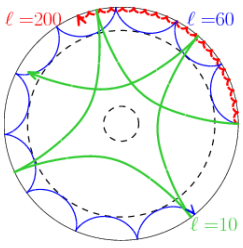

parameters, but this work suggests a link between the timescales of the QPPs and the length scales of the flare. Recent studies [Pugh et al., 2019; Hayes et al., 2020a] have suggested some scaling between QPP period and ribbon separations, which are often used as proxies for loop lengths. To further explore this apparent correlation, we first must establish the prevalence of period drifts, or non-stationarity, in QPPs. In producing a catalogue of non-stationary events, we may be able to repeat this work on a larger scale, looking at flare parametres such as loop length against QPPs with different period evaluations. This will lead to a better understanding of the conditions in which QPPs can exist. Therefore in Section 7.3 we examine the period drift of QPPs in 98 flares and asses their stationarity and links to basic flare parameters.

7.3 Evolution of periods in quasi-periodic pulsations (QPPs) associated with M- and X- class flares

7.3.1 Introduction

Several recent works have suggested that periods within QPPs follow a trend of increasing period rather than stochastic behaviour (e.g. Kolotkov et al. [2018], Hayes et al. [2019]). Following on from the work in Hayes et al. [2020b], we explore this further by investigating whether non-stationarity is an inherent feature of QPPs. We present a comparison of the dominant periods in the impulsive phase of the flare (characterised as the time from the start of the flare to the time corresponding to flare maximum) and the decay phase (from flare maximum to the end of the flaring event) in QPPs from M- and X- class flares from Solar Cycle 24. By examining the prevalence of QPPs that show evidence of non-stationarity we may be in a better position to examine the mechanisms that drive QPPs.

7.3.2 Setting up the study

Data

We obtain a list of flares observed by GOES that were classified as M- or X-class flares, which showed evidence of QPP-like behaviour between 1st February 2011 to 31st December 2018 (i.e., Solar Cycle 24). From this flare list we collate 205 flaring events for which we obtain soft X-ray (SXR) data. We make use of the long channel of GOES-15, which measures emissions in the 1 – 8 Å range. The data have a cadence of 2.047 s and

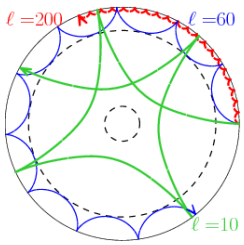

are publicly available here[1]. We use the GOES flare catalogue start times to define the beginning of the flaring event. The start times are defined by NOAA as the start of an X-ray event measured in the long channel as the first minute in a sequence of four minutes wherein there is a steep monotonic increase and the final flux value is greater than the first by a factor of 1.4. We trim the flares to twice the duration from the start of the flare to flare maximum, as measured in the long channel. Flare maximum is the time at which the flare reaches its maximal value as measured in the long channel, which we call peak flare energy. We use this method of choosing the end times rather than the end times stated on the flare database to avoid introducing artefacts due to unequal signal durations in the impulsive and decay phases. This ensures the impulsive and decay phases of the flare have equal duration as can be seen in Fig. 7.6.

We also examine whether the presence of a Coronal Mass Ejection (CME) correlates with the appearance or magnitude of a period evolution in QPPs. We make use of the publicly available CME catalogue[2], which uses LASCO data (Large Angle and Spectrometric Coronagraph Experiment) aboard the Solar and Heliospheric Observatory (SoHO).

Method

The flare was separated into the impulsive and decay phases and then FFTs were performed on each phase separately. Any dominant periods above a 95% confidence level were recorded. We obtain the confidence levels by making use of the technique put forward in Pugh et al. [2017a] which is based upon the work in Vaughan [2005]. This method involves fitting the power spectrum with a broken power law. This is in order to account for both the presence of red and white noise in the signal and avoids the problems that can arise when detrending data. Using this fitting we calculate the 95% confidence level which is used to determine which period, if any, is statistically significant. In some Fourier spectra we see multiple peaks above a confidence level, in which case we only record the most dominant peak above the confidence level, relative to the confidence level.

We note that recent literature suggests that the significance of peaks in non-stationary QPPs can be overestimated in periodograms if segments are poorly selected [Hübner et al., 2022]. We follow a suggested mitigation strategy put forward in Hübner et al. [2022] by searching for a statistically significant QPP with an approximately similar period in the two different phases of the flare. We restrict our QPP period analysis to

[1] ngdc.noaa.gov/stp/satellite/goes/index.html
[2] cdaw.gsfc.nasa.gov/CME_list/

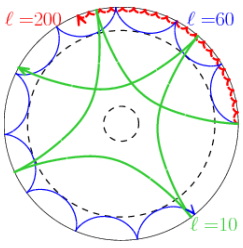

flares which had periods above the 95% confidence level in both the impulsive and decay phases and where both periods were; smaller than one tenth of the full duration of the flare, greater than four times the cadence of the data set, and were separated in magnitude by no more than a factor of eight. We chose these criteria as we expected at least five full oscillatory cycles in both the impulsive and decay phase – fewer and the oscillation may be indistinguishable from red noise. We also restrict our periods to be greater than four times the cadence of the dataset, so the minimal period of QPPs in this study is 8.19 s. This was because we believe detections of periods smaller than this are unreliable when identified in GOES alone and must be accompanied by other data sources with better time resolution. Finally, we believe QPPs that exhibited a change in period by a factor larger than eight to be attributed to a change in the signal to noise ratio i.e. a rapid relative appearance or disappearance of red noise. It is important to state that the absence of the above criteria being met for a given flare event does not necessarily imply that no QPPs were present. Rather there may have been QPPs that were not statistically significant in both phases, or one whose period evolution was outside of the criteria we put forward. However we restrict our study to these criteria in the interest of reliability and consistency of results, and we discount any other data. This resulted in 98 flares which fulfilled the criteria, which are discussed in Section 6.3.

We redefine the term *period drift* to measure the change in period from the impulsive phase to that in the decay phase, equal to Period_{Decay} - $\text{Period}_{Impulsive}$. A positive period drift implies with an increase in dominant period from the impulsive phase to the decay phase and vice versa. We emphasise that there may be multiple processes present in generating the QPPs and a positive period drift does not imply the growth in period of a singular QPP process – for example such an effect could similarly be produced by shorter period QPPs decaying in amplitude in tandem with a secondary longer period process growing in amplitude. This would result in a growth in dominant period across the two phases, i.e. a positive period drift.

We determine the average period of the flare by taking the mean average of the dominant periods in the impulsive and decay phases. As we are examining the prevalence of non-stationarity in QPPs we avoid taking an FFT of the entire duration of the flare to obtain the average period, as a non-stationary signal that has significant period evolution is not well suited to the FFT which assumes a stationary input. It is possible that a non-stationary signal which evolves over several frequencies will show evidence of spectral leakage in its associated power spectrum, leading to any dominant peaks being smeared out, and presenting no statistically significant peaks. This is naturally still an issue to be considered when assessing only the impulsive or decay phase and any quickly evolving

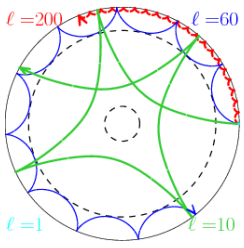

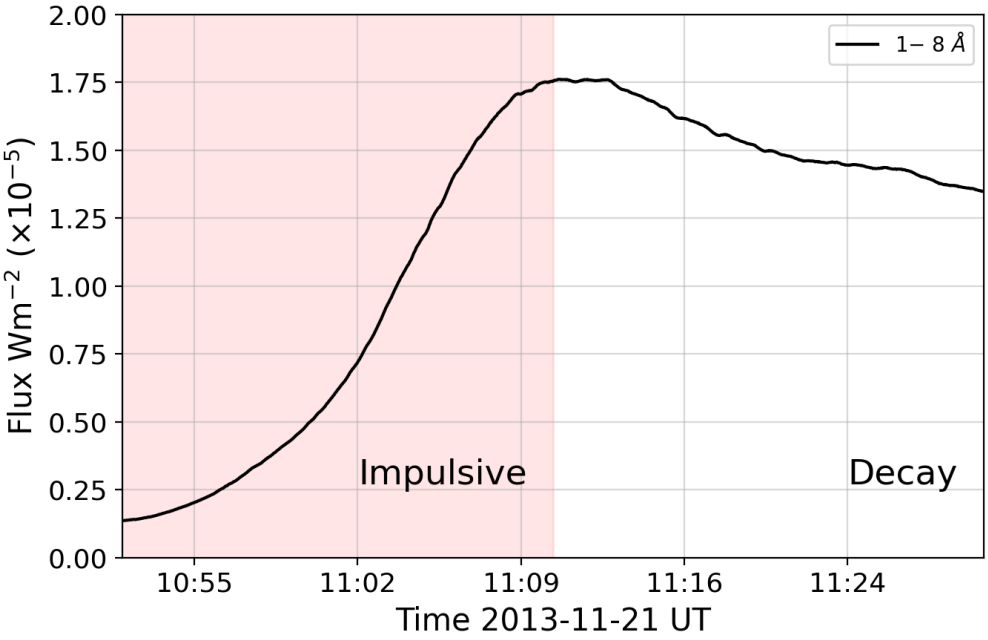

Figure 7.6: Profile of Flare 40 in *GOES* XRS-B 1 – 8 Å, where the impulsive phase is shaded in red and the decay phase is unshaded. The impulsive and decay phases are equal in duration and are delineated by flare maximum which occurs at approximately 11:10 Universal Time (UT).

periodicity is likely to be obscured in the same manner, which may lead to a number of false negatives in our results when statistically significant periods are not found in our analysis. However by splitting the flare into sections we still should be able to observe some periods with sufficiently slow evolution and still pick up on their long-term non-stationarity.

We determine the errors on the periods from the impulsive and decay phases by use of the standard approach (see Equation 4.4 in Chapter 4). The errors in period for the periods obtained for the impulsive and decay phases are propagated when calculating the errors on the average period and the errors on the period drift.

Fig 7.6 shows the 1 – 8 Å lightcurve for Flare 40 where the duration of the flare has been symmetrically split into the impulsive phase until flare maximum, and the decay phase. Fig. 7.7 shows the Fourier spectra of Flare 40's impulsive and decay phases, which show significant periods of $43.3^{+0.8}_{-0.8}$, $54.9^{+1.4}_{-1.3}$ s respectively, corresponding to a period drift of $11.6^{+1.6}_{-1.5}$ s.

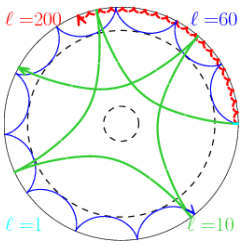

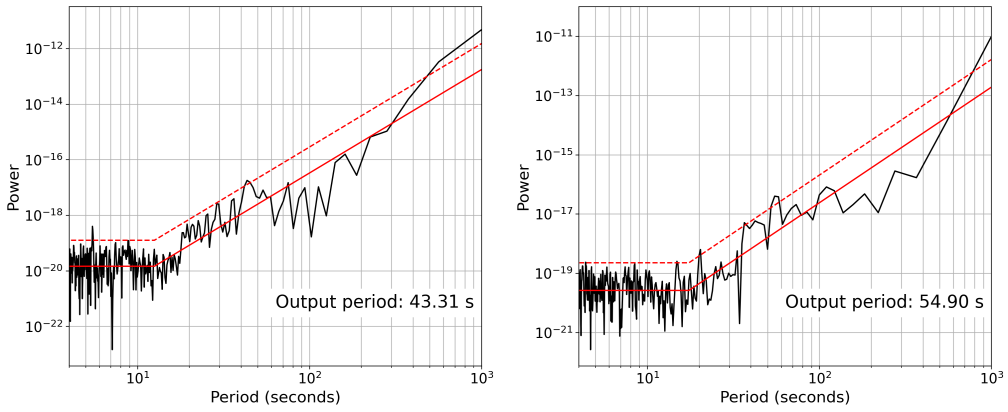

(a) (b)

Figure 7.7: Fourier spectrum of the impulse phase *(a)* and decay phase *(b)* of Flare 40. Fits of the spectra by broken power laws are shown as a solid red lines, and the 95% confidence levels are indicated with dashed red lines. A statistically significant peak can be seen corresponding to 43.3 s in the impulsive phase and 54.9 s in the decay phase.

7.3.3 Results

We examine 205 M- and X- class flares over Cycle 24, resulting in 98 flares that show statistically significant periods in both the impulsive and decay phases of the flare that have both periods greater than four times the cadence of the dataset, less than one tenth of the full duration of the flare, and separated in period by no more than a factor of eight. We consider a period drift to be statistically significant if its absolute magnitude is greater than 4.09 s, which is twice the cadence of the data and significantly larger than all of the error bars presented in this chapter. Of these 98 flares, 19 (equivalent to 19%) showed no significant period drift. 65 QPPs (66% of the sample) exhibited a positive period drift where the dominant period appears to increase from the impulsive to the decay phase. 14 flares (14%) exhibited a negative period drift where the dominant period appears to shrink between the phases.

Fig. 7.8 shows the relationship between the impulsive and decay phase periods (the dominant periods in the impulsive and decay phases respectively) of the 98 flares examined. It can be seen that the majority of results appear above the 1:1 ratio line shown in solid black, which indicates more QPPs have a larger decay period than impulsive period. For the QPPs where the decay period was smaller than the impulsive period, the decay periods are proportional to the impulsive periods by a factor of ∼0.3. For the QPPs showing an apparent period growth, the decay periods are proportional to the impulsive periods by a factor of approximately ∼1.4. This value agrees well with

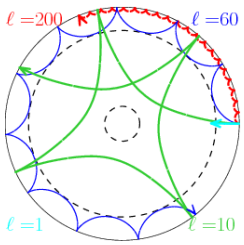

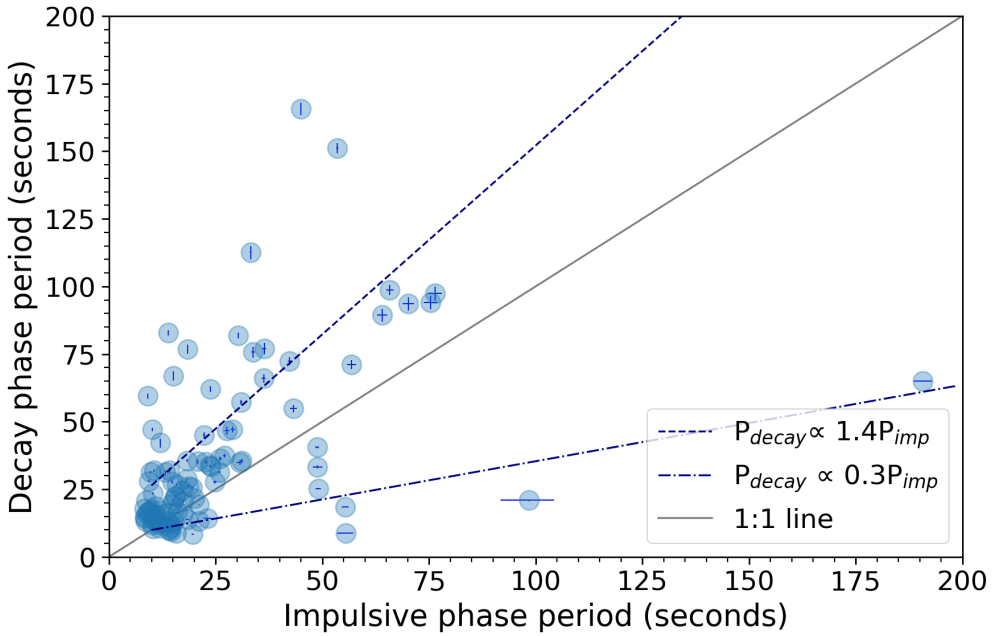

Figure 7.8: QPP dominant periods in the impulsive phase, called 'impulsive phase periods' against dominant periods in the decay phase, called 'decay phase periods'. A 1:1 ratio line (which indicates no period drift) is shown as a solid black line. The line of best fit for QPP periods that grew between the Impulsive and Decay phases is shown as a dashed blue line, and the line of best fit for period that shrunk is shown as a dot dashed blue line. This figure is an updated recreation of Fig. 10 from Hayes et al. [2020b]

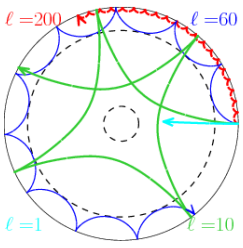

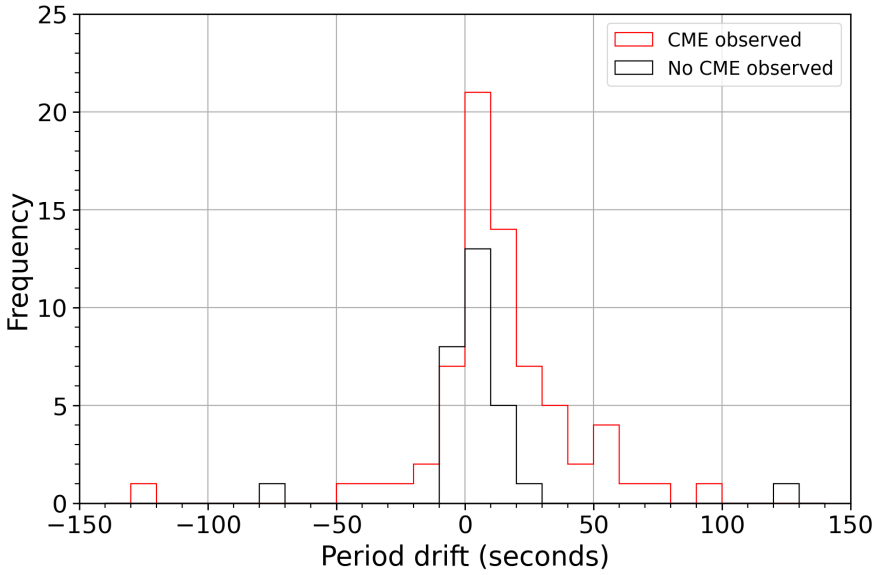

Figure 7.9: Histogram of period drifts (measuring the difference between the dominant period in the QPP's decay phase against the dominant period in the impulsive phase) in QPPs, separated by CME association. The QPPs seen in flares associated with CMEs are given in red, and those not associated with a CME are shown in black.

the factor of ∼1.6 that was found in a similar analysis that can be seen in Fig. 10 of Hayes et al. [2020b]. It should be noted however that the authors found 26 out of the 28 QPP events (92%) showed a larger decay period than impulsive period and their factor is based on the fitting of all 28 events, not just those that show period growth. For the 65 QPPs exhibiting positive period drift, the median period drift is 13^{+13}_{-6} s where the errors correspond to the periods in the upper and lower 25^{th} percentile. Similarly the median negative period drift for the 14 flaring events is -10 $^{+3}_{-24}$ s.

We examine whether the presence of a CME associated with the flare impacts the distribution of period drifts in QPPs. Of the 98 QPPs, 69 were associated with a CME and 29 were not. Fig. 7.9 shows the histogram of period drifts in QPPs from flares associated with CMEs (red) and those from flares not associated with CMEs (black). The distributions of the two sets are reasonably similar with median period drifts of 10^{+13}_{-8} s for the CME associated flares and 5^{+4}_{-6} for the non-CME associated flares. The maximal and minimal period drifts across both groups are also similar with the CME-associated group having maximal and minimal period drifts of 98, -126 s, and the non-CME associated group with 121 and -76 s. There is no discernible difference in period drift between flares with or without CMEs.

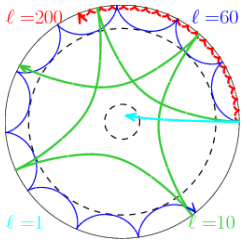

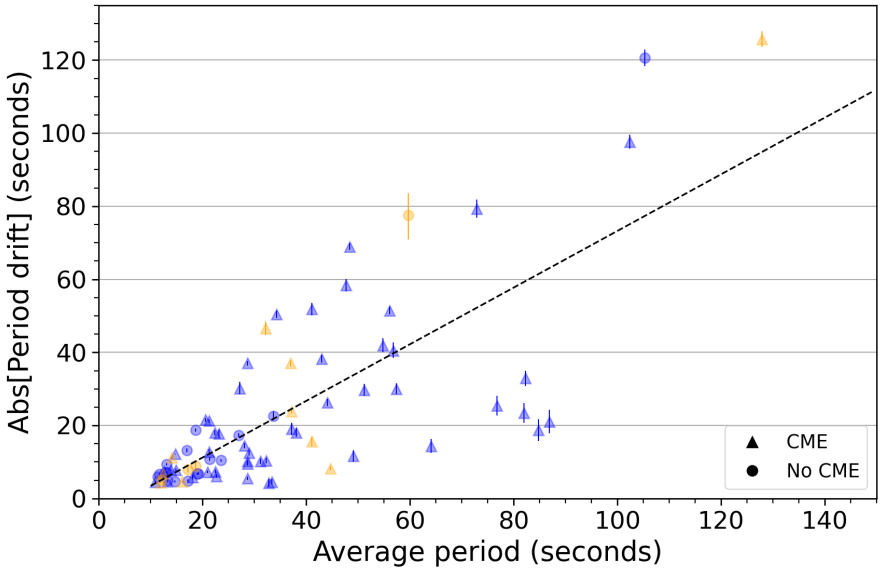

Figure 7.10: Average QPP period plotted against the absolute magnitude of the QPP period drift. Positive period drifts, indicating a growth in dominant period, are shown in blue, and negative period drifts are shown in orange. QPPs from flares associated with CMEs are indicated by a triangle marker whereas those not associated with QPPs are shown with bullet points. The Pearson correlation coefficient is 0.76 indicating a positive correlation. A linear fit of the data is shown in black.

Fig. 7.10 shows the relationship between absolute period drift and average QPP period, where the average period is the mean value of the impulsive and decay periods. Positive period drifts are shown in blue, and the absolute values of negative period drifts are shown in orange. QPPs associated with a CME are shown with a triangle and non-CME associated events are marked with a bullet point. The meanings of the colours and symbols used in Fig. 7.10 are consistent for the remainder of this chapter. A positive correlation, with a Pearson correlation coefficient of 0.76, can be seen between the average period of the QPPs and the magnitude of the period drift. However we emphasise that this correlation is largely an artefact due to the inherent link of period drift and average period. Both are quantities derived from the periods in method used of calculating the average period. The impulsive phase periods largely are between 8 – 75 s, and are approximately similar across the all flares as seen in Fig. 7.8, whereas the decay periods have a larger spread between 8 – 110 s. This results in an apparent correlation between the absolute value of the difference in the two periods, and their average values.

Flare energy and QPP period drift are seen to have no correlation in Fig. 7.11.

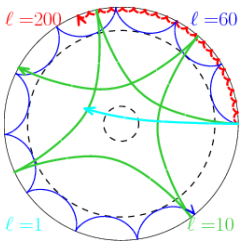

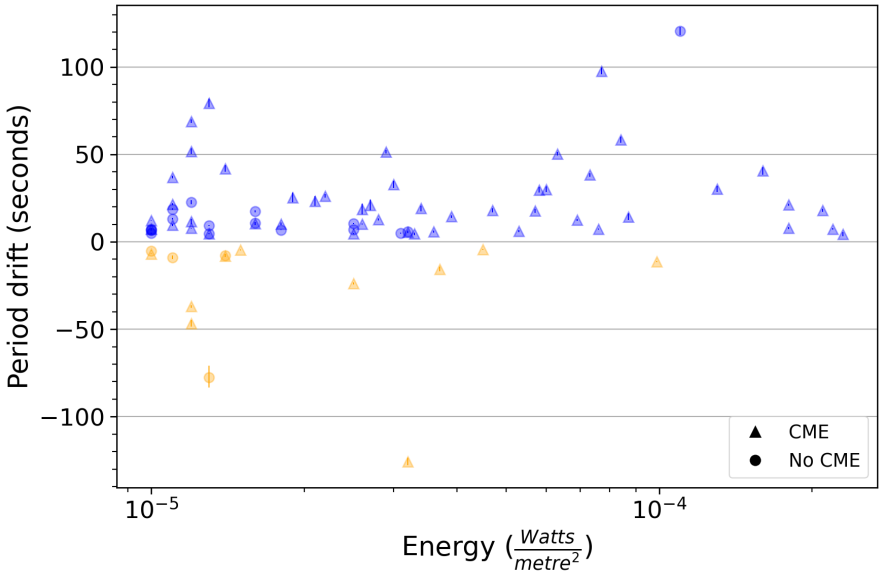

Figure 7.11: Peak flare energy as measured in *GOES* 1 – 8 Å plotted against QPP period drift with no correlation. The meanings of colours and symbols are as given in Fig. 7.10.

Flares not associated with CMEs are more commonly found at lower energies but this distinction has no significant effect on the magnitude or direction of the period drifts observed.

Fig. 7.12 shows a positive correlation between the absolute value of the period drift in QPPs and the duration of the flare, with a Pearson correlation coefficient of 0.82. This relationship can likely be attributed to the fact that longer duration flares allow for more time for any non-stationary QPP periods to evolve which leads to greater magnitude period drifts. There is no noticeable difference between the relationship of flare duration to period drift magnitude for positive or negative period drifts.

We control for the duration of the flares and now examine the rate at which the QPPs evolve. The rate of period drift is defined as the period drift divided by half the duration of the flare, and is therefore a unitless quantity. Fig. 7.13 shows the distribution of the magnitude of the rate of period drift against average QPP period as a scatter plot (Fig. 7.13a) and histogram (Fig. 7.13b). As can be seen, the rates of period drift have considerable scatter with no significant trend visible. The maximal rate of positive period drift is 0.06 and the maximal rate of negative period drift is -0.1, although the majority of the rates of period drift are between -0.02 and 0.3. There is no apparent correlation between the magnitude, sign, or presence of CME to the rate at

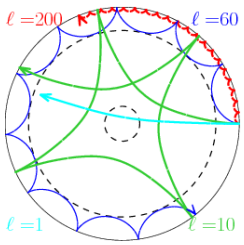

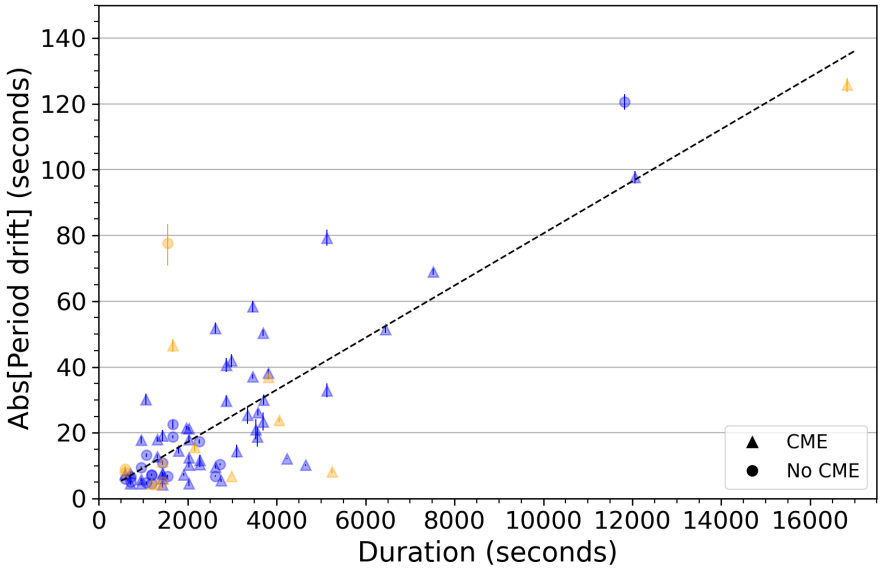

Figure 7.12: Flare duration plotted against the absolute magnitude of the QPP period drift. The Pearson correlation coefficient is 0.82, indicating a positive correlation. A linear fit of the data is shown in black. The meanings of colours and symbols are as given in Fig. 7.10.

which the QPP evolves.

We also find that there is no correlation seen between the rate of period change and the flare energy with significant scatter for all QPPs, which can be seen in Fig. 7.14. There is also no correlation between the rate of period drift and flare duration (Fig. 7.15), which is expected as we obtain the rate of period drift by dividing the period drift by the flare duration.

The period drift of all QPPs in the 98 flares may be visualised in Fig. 7.16 (or explored in Table 1 found in the Appendix). The periods of the QPPs are given in the horizontal axis, with bullet points indicating the period in the impulsive phase, and arrow heads indicating the period at the decay phase. Therefore arrows pointing right and coloured red indicate a positive period drift. Conversely blue arrows, pointing left, indicate a negative period drift. The period drift from a given QPP is plotted against the corresponding flare's duration. The inset axes shows an enlarged region of the plot for flares with durations less than 2500 s. Flares with longer durations naturally allow for more time to evolve, leading to larger magnitude period drifts as discussed previously. The majority of results are clustered for flare durations less than 2500 seconds, with impulsive and decay periods of 40 s or less.

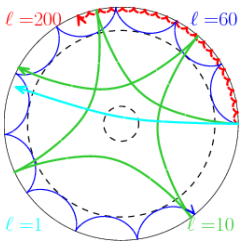

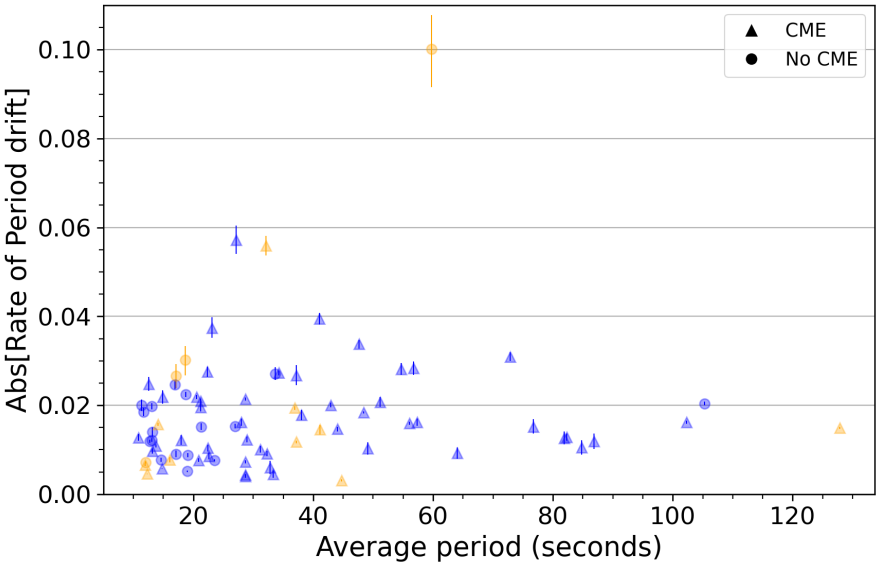

(a)

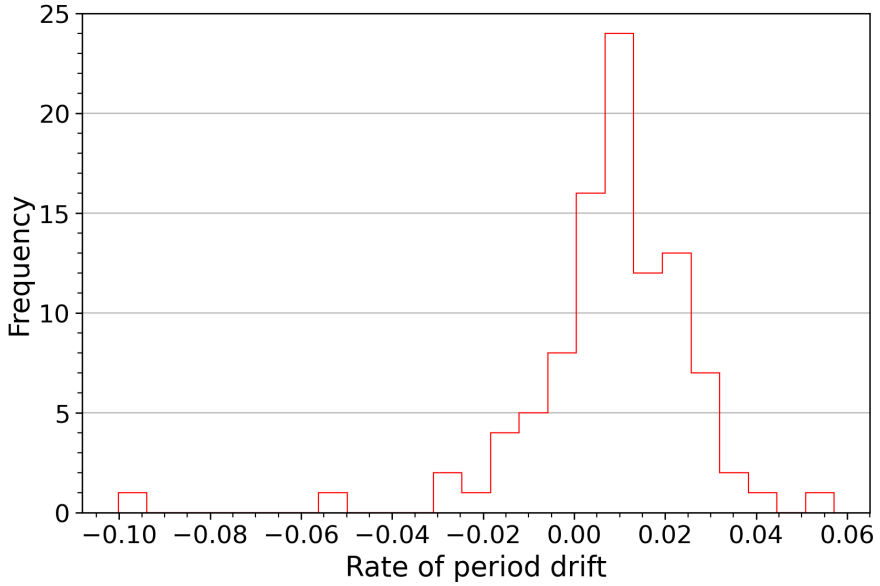

(b)

Figure 7.13: *(a)*: Scatter plot of the absolute magnitude of the rate of period drift, plotted against the average period of the QPP. *(b)*: Histogram of rate of period drift. The meanings of colours and symbols in Panel *(a)* are as given in Fig. 7.10.

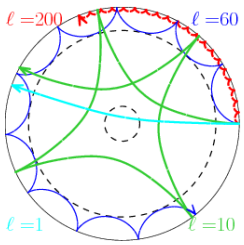

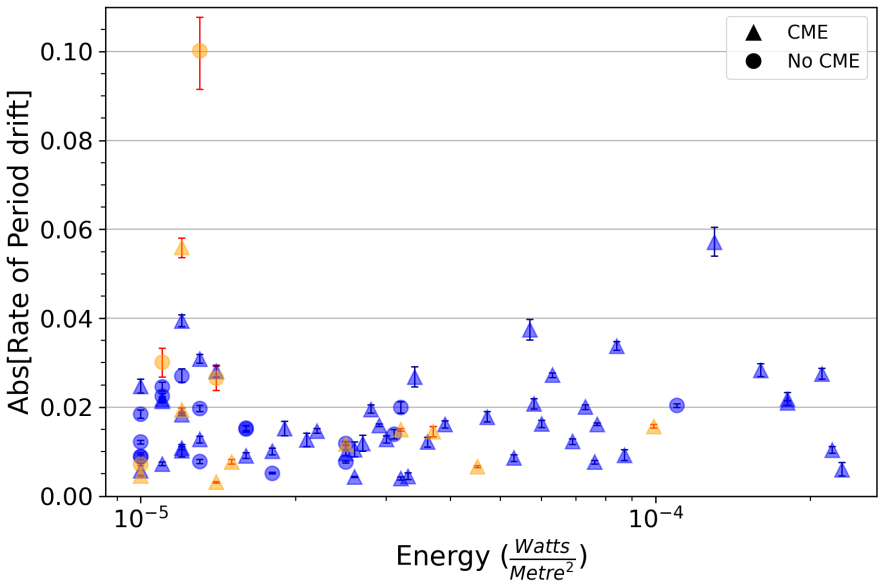

Figure 7.14: Rate of period drift plotted against peak flare energy. The meanings of colours and symbols are as given in Fig. 7.10.

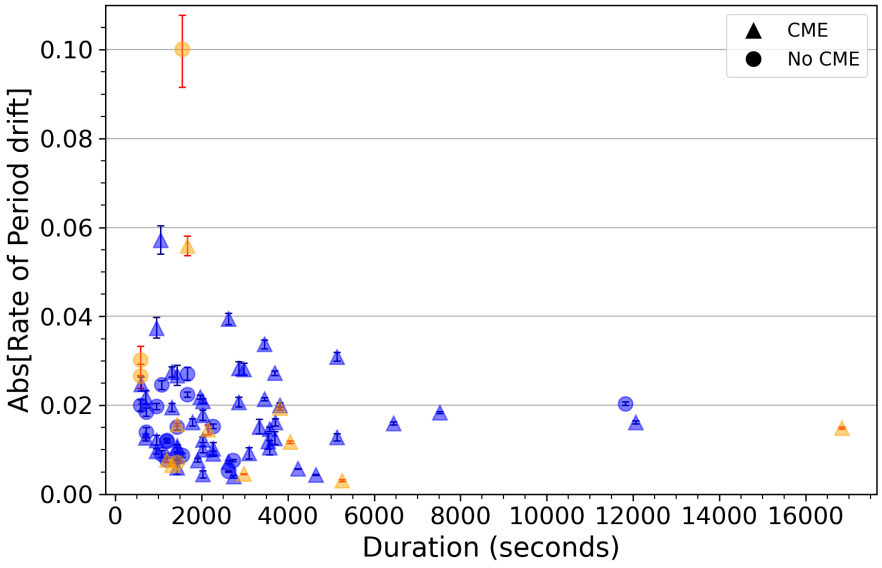

Figure 7.15: Rate of period drift plotted against flare duration. The meanings of colours and symbols are as given in Fig. 7.10.

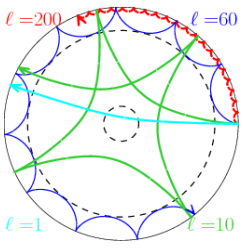

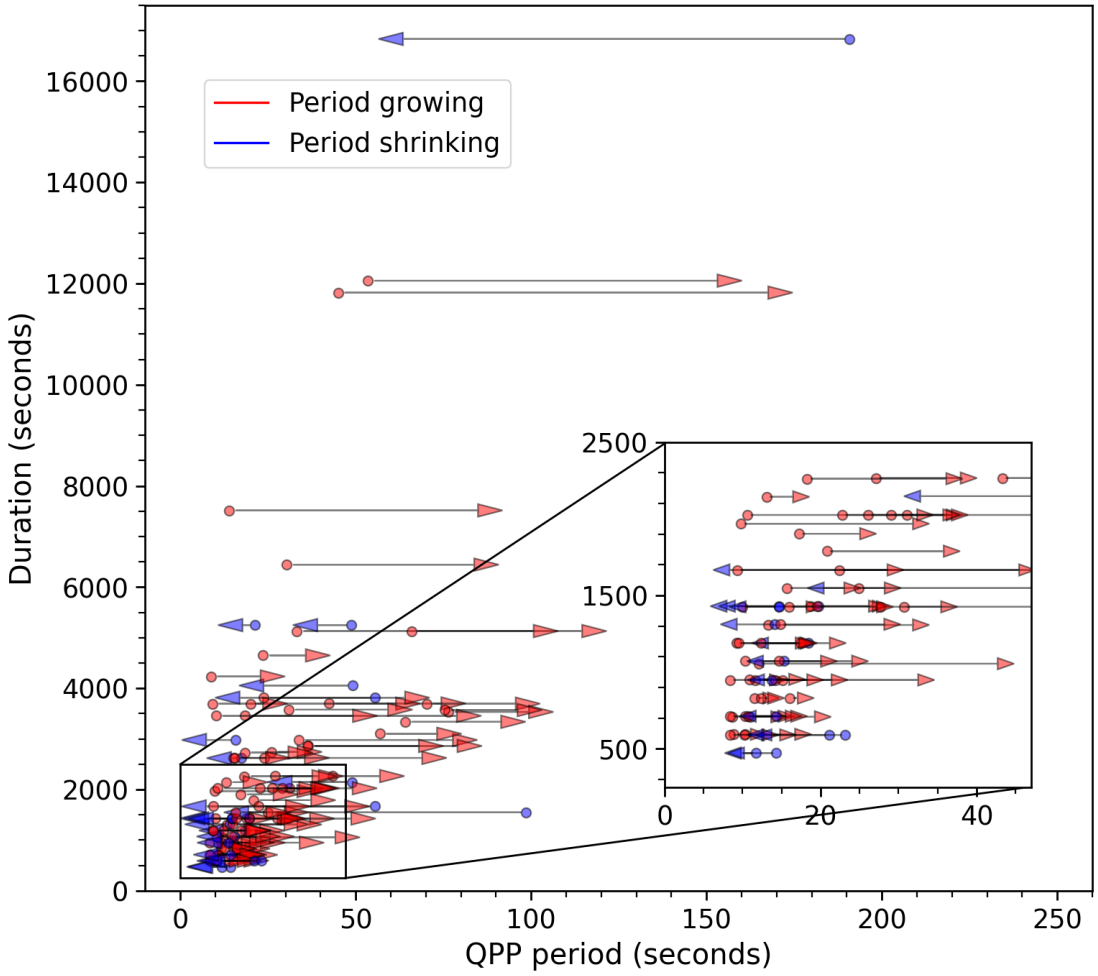

Figure 7.16: Arrows show evolution of statistically significant periods in the impulsive and decay phases of 98 flares, with the arrow pointing from impulsive phase (indicated with a bullet point) to decay phase (arrow head). A period growth, i.e. a positive period drift, is shown in red and a negative period drift is given in blue. The period drift in the QPP is plotted against the flare's duration, both given in seconds.

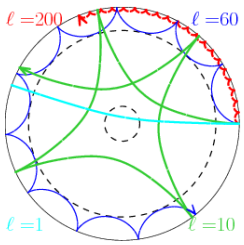

7.3.4 Discussion

We have shown that the majority (81%) of the flaring events which show evidence of QPPs we examined show some evidence of non-stationarity. If this sample is representative of the behaviour of QPPs en masse then we must consider non-stationarity to be a common property of QPPs and account for it in our methodology. If we search for QPPs by utilising methods that assume a stationary output, such as the FFT, we risk false-negative results where the non-stationarity of the QPP may cause spectral leakage. We also risk poorly categorising the behaviour of QPPs by assigning a single value for QPP period. This is because different QPP mechanisms allow for the presence of non-stationarity in different ways and we mustn't omit the valuable data by treating the QPP periods as a fixed value if we are to determine what causes QPPs.

We also would like to note the disparity in the proportion of flaring events showing a positive period drift (66%) compared to those showing a negative period drift (14%). This suggests an apparent growth in QPP period is more common than an apparent shrinkage. We need more data to confirm whether this apparent phenomenon is due to data bias or not. We also note that most of the period drift that we observe is of small magnitude- most commonly between ± 10 s.

We have chosen to split the flare into two phases, a choice which is ultimately arbitrary and done for convenience. It may be that any apparent period evolution is non-linear and follows some different schema. By repeating this analysis with some method that has time resolution, such as a continuous wavelet-transform (CWT) or EMD we may be able to uncover valuable information about the time evolution of the apparent period drifts. This may also be useful in discerning the generation mechanism(s) that are active in the appearance of these QPPs. As discussed earlier, a reader may be misled by these results into thinking that a single process is occurring in which the period is growing or shrinking. It is possible that several mechanisms with different instantaneous periods are growing/shrinking in amplitude- giving the appearance of a single period growing or shrinking. Therefore it would be valuable to make use of a method that can pick up multiple time scales with varied amplitudes with time resolution.

The rates at which the QPPs evolved in period exist over the same ranges and in roughly the same populations for both growing and shrinking QPP periods, without any dependence on QPP average period or maximum flare energy. We note that the presence of CMEs or peak flare energy seem to have no effect on whether the QPP periods grow or shrink, or the magnitudes of the period drifts. We see that longer duration flares are correlated with greater magnitude period drift. It is possible that other properties, such

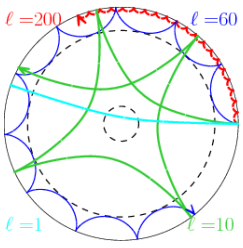

as CME speed or the magnetic configuration of the Active Region could play a role in determining if and how the QPP periods evolve.

7.4 Summary

In this chapter, we investigated whether loop length scales were linked to QPP period timescales and found both quantities were well correlated, both showing an initially approximately linear growth in time, followed by a levelling out. This suggested that there may be a relationship between the two quantities, although much more data is required before we can suggest a causal link. Further observations of well resolved spatial data of flare sites are needed, alongside high cadence measurements of QPP emission data. We also show that there is clear evidence that non-stationarity is a common phenomenon in QPPs observed in M and X class solar flares, with period growth appearing more common than period shrinkage. We must consider this when investigating flaring events for QPPs and be wary about how we assign values to QPP periodicities. It appears that most QPP that show non-stationarity evolve in period at similar rates. It is unlikely that the presence alone of CMEs the peak flare energy impacts the presence of magnitude of QPP period evolution. Further work with spatial resolution of the flare site may be valuable in investigating the cause of QPP period evolution.

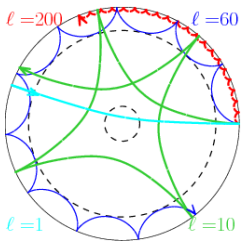

Chapter 8

Outreach, Science communication and Public Engagement

8.1 On the importance of science communication

I am a firm believer that no science is worth doing unless we communicate its motivations, methods, and outcomes to audiences beyond our field.

As a result of the science communication, outreach, and public engagement detailed below, in July 2022 I was awarded **Warwick Award for Public and Community Engagement (*Student Award*)**. Alongside Ally Caldecote and Paul Warwick, in February 2023 I was also awarded the **Warwick Wows Award** as part of the Warwick Wonders and Wows series, in recognition for our work on the Warwick Christmas Lectures. This was preceeded by my election as an Associate Fellow to the Warwick Institute of Engagement. Part of this work references the publication;

"Reach out, Touch Space!"
Astronomy & Geophysics, Volume 63, Issue 5, October 2022, Pages 5.21-5.23
By T. Mehta, C. McDonald, and B. Nealon.

Before jumping into this chapter, I wish to define some common terms that will be used frequently. *Scientific outreach*: the practise of promoting science, scientific findings, or awareness of science to an audience not typically reached, usually in a one-way fashion (i.e. through talks). *Public engagement*: Engaging, usually a specific subset of the population, through two-way dialogue (e.g. school or library visits). *Science*

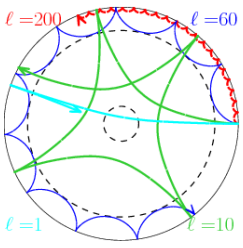

communication: the informing of scientific information, not necessarily to a non-scientific audience.

As can be seen in recent news[1], we are living in a time of mistrust, or hesitancy, in science. Vaccine hesitancy for example is on the rise [Dubé et al., 2013], a phenomenon exemplified by the COVID-19 pandemic, wherein despite substantial public health campaigns, we still saw a significant portion of the public expressing fear or wariness around the vaccine distribution. This was not overcome by overwhelming support from scientists and a wealth of data weighing its safety against the dangers of the virus[2]. Similarly we see this hesitancy crop up in places from politics to industry, where data and scientific advice are not considered to be a reliable sources (See Fig. 8.1). Some of the hesitancy stems from a lack of understanding of the scientific method, leading some people to believe the results of a Google search have a similar weighting in scientific value to a peer-reviewed article in a journal. A lack of understanding or appreciation of the scientific method may lead to friction between sceptics in the public sphere and scientists. While it is sensible, even essential, to have a healthy scepticism of the information being presented to you (as even publications in scientific journals are prone to bias and errors), this mistrust of the scientific method and the results that are born from it has dangerous implications both for individuals and society. To combat this we must promote trust, understanding, and enthusiasm for the scientific method, not just for those who go into scientific jobs, but for society as a whole. As public engagement professionals, we are tasked with encouraging an understanding and appreciation of the scientific method so that the public are better equipped to do meaningful research and find answers they can analyse and trust.

Scientific literacy and trust has huge impacts for the world we live in, through decisions made in e.g. policy making and national investments. We need to instill this trust from a young age and continue to encourage it throughout a child's education. We also need to ensure there's substantial communication between scientists and those outside the discipline. By building these bridges early and and maintaining them, the valuable science that is done in offices and labs can impact the world outside journals and conferences. Without trust in the scientific method, the decisions that affect the world are open to being led by ideology and prejudice. I am aware this is an overly gloomy outlook and also not one that will be solved by the outreach I detail in the following pages. However I do believe a well-planned movement by scientists in improving the way we do scientific communication, increasing public trust in research bodies, engaging

[1] `www.bbc.co.uk/news/science-environment-59251912`

[2] `www.bbc.com/future/article/20211209-how-to-talk-to-vaccine-hesitant-people`

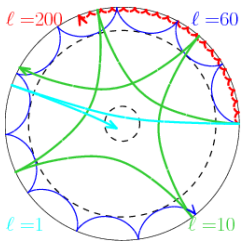

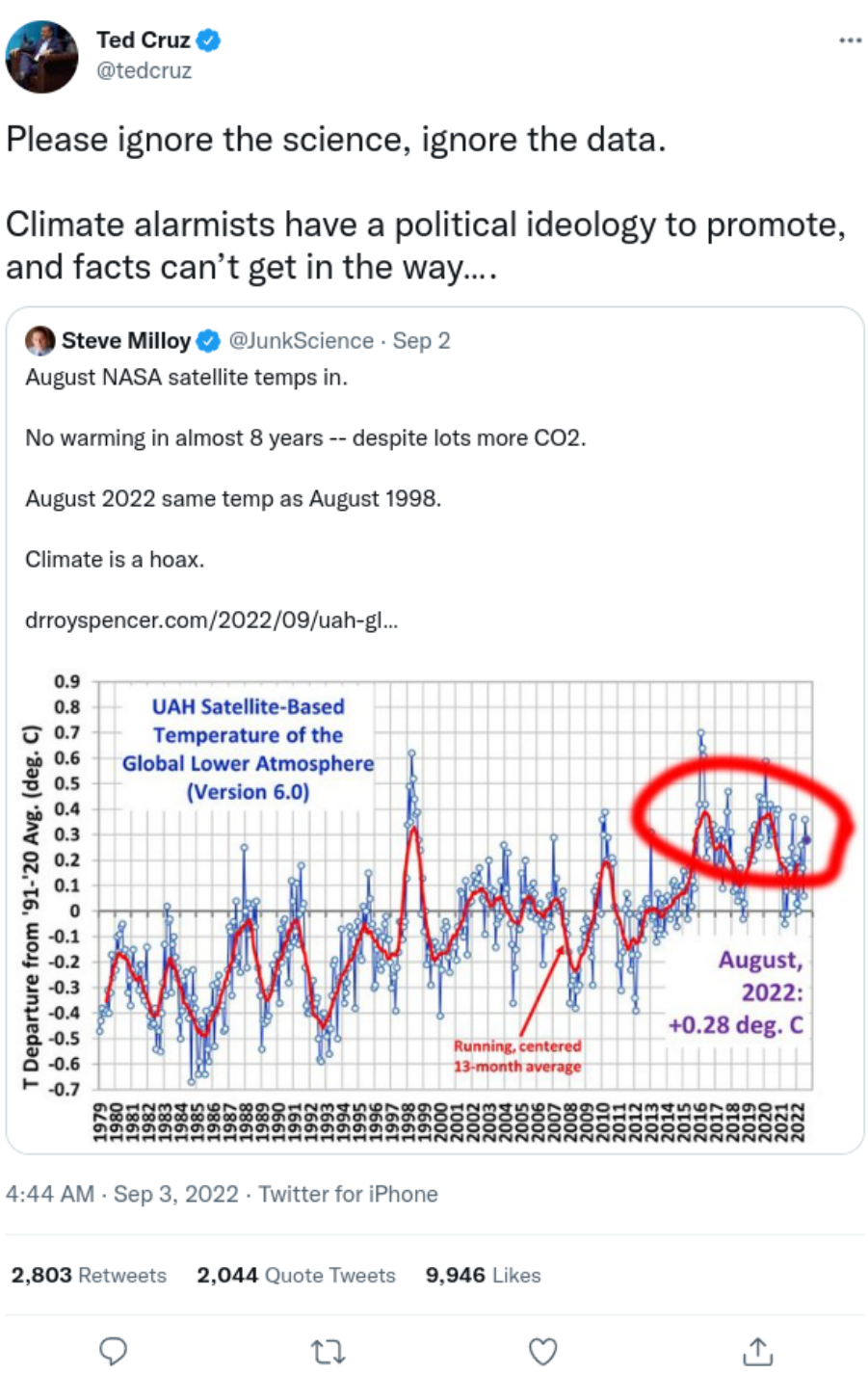

Figure 8.1: Tweet from United States Senator Ted Cruz (@tedcruz) encouraging followers to "...ignore the science, ignore the data", posted at 4:44 AM UT, Sep 3, 2022 [Downloaded on Sep 4, 2022]. The tweet is quoting Steve Milloy (@JunkScience) whose graphic allegedly uses NASA data to claim Climate [change] is a hoax.

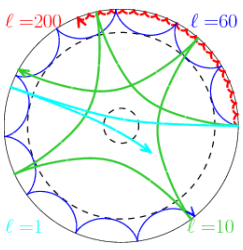

the public from an early age and making an inclusive environment can, and will, lead to better informed and more scientifically led nations. This is what I hope to contribute to.

Another factor to consider is why there is so much hesitancy around science. Much of the distrust is rooted in the historic, and often ongoing, exclusion of audiences who don't fit a particular mold. People have been historically excluded from science due to their gender or sex [Barthelemy et al., 2016] or their race [e.g. Suite et al., 2007, discusses the history of racism in medicine]. Marginalised groups also face a lack of representation in science, ultimately leading to a cycle of exclusion. Factors such as these lead to a cycle of the people sharing the same characteristics being the face and voice of science. To build trust we need to directly target these under-represented groups and ensure our practises resonate with these communities.

The public engagement that I have had the joy of running, designing, evaluating and building over the last few years broadly falls into two categories; brief and entertainment-geared talks (Section 8.2.4), and longer-term community connection focused outreach (Section 8.2.1). I am pleased with the impact my fast-paced fun presentations and experiments have had, they have entertained audiences in the thousands across the local area, pulling in often sold-out crowds at Pint of Science talks (2017-2021) and the Warwick Christmas Lectures (online and in person; 2018, 2020, 2021, 2022) and has, I believe, improved the reputation of the department and university on a regional scale. However my most meaningful and impactful outreach is done at events designed to continue inspiring and informing long after the event finishes.

By focusing on long-term engagement I have pivoted to projects with an emphasis on science and art (see Section 8.2.1) which had a twofold goal; firstly it gives the audience an activity that they can take home– a physical reminder of the engagement which helps extend the longevity of the activity and therefore the impact. Secondly it provides science in a new and potentially less alienating context. I have centred much of my outreach on building connections with under-represented audiences. This was largely through working with schools that have high pupil premium (pupil premium is funding to improve education outcomes for disadvantaged pupils in schools in England). For example, I recently worked with The Polesworth School in Tamworth where historically a low proportion of students have considered university-level education. I targeted my outreach to break down some of the myths about what research, and life as a scientist, is and discussed bias and challenges in STEM, and adjusted my pitch to suit the appropriate age and expertise of the students. Testimony from the Y11 teacher, Dr. Millichamp, can be seen in the Appendix. I revised my 'standard' presentation and

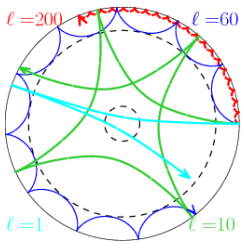

materials in advance of the event to emphasise the presence of scientists from similar backgrounds with less represented characteristics, and encourage the students to feel welcome. These characteristics include, but were not limited to; gender, sex, race/ethnicity, socio-economic background, sexuality, disabilities, accents, religious beliefs, learning difficulties, cultural backgrounds, language skills etc. My aim was to create material that resonates with a varied audience, and to provide a space for anyone who has an interest in science, centering on equality of opportunity.

I do acknowledge that including the public engagement and science communication work that I've carried out over the past 4-5 years is unorthodox for a physics Doctoral thesis. There are some who would consider this work, although well intended, to be unscientific and therefore not well placed for a scientific submission. I admit that the contents in the forthcoming sections are qualitative and are closer to a summary rather than a study. But I do believe this work has merit– it details what I have learnt, how I have carried out my outreach, how I have improved and evaluated my practises, and contains 'results' in the form of recommended future practices, evidence of impact, and testimonials from attendees and collaborators (which can be found in the Appendix of this thesis). In fact this may be the work I am the most proud of, because it covers the work that has by far had the largest impact during my time at the University of Warwick, potentially inspiring the scientists of tomorrow. I hope you see the value in this chapter and why I consider it an essential part of my thesis and worthy of attention equal to Chapters 5–7.

8.2 Summary of Engagement

Below I divide my work in public engagement into four categories; Art and Science, Academic/ professional engagement, Live talks and lectures, and School visits. Each of these sections discuss the contents of their respective event/ activities, and an evaluation of the practice. I close this chapter with a framework for those interested in doing effective science communication, based on my own experiences. Testimonials on my work in public engagement and science communication can be found in the Appendix of this thesis, alongside photographic evidence of some events I have run or worked on.

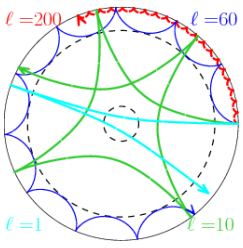

8.2.1 Art and Science

Embroider your own Sunquake!

This activity, advertised as "*Embroider your own Sunquake!*" combines art and science. An overview of the activity is as follows: I lead a conversation with the visitors on the interior structure of the Sun and the presence of p-modes (Sunquakes). Then visitors take part in a short coding exercise, in which they can design their own unique Sunquake design, which is transferred to an on-site embroidery machine. Their design is then sewn in 2-3 minutes, which the visitors can decorate, mount onto a coaster, and take home.

This activity was produced as part of the STEM connections program[3] which worked with schools that had diverse students and/or high numbers of pupil premium students. This project was made possible thanks to the STEM Connections grant; a Research England funded initiative that supported eleven researchers of various academic levels to develop their own outreach projects with a budget of up to £1000. The project, supported by Innovate Manufacturing and Future Materials Global Research Properties and Culture Coventry, took place over a period of nine months in which 10 researchers from the University of Warwick across several departments created outreach suitable to showcase at local schools, culminating in a day long event at Coventry Transport Museum (discussed in Section 8.3). A poster advertising my contributions to the program can be seen in Fig. 8.2. The initiative was strongly supported by Prof. Margaret Low, Dr. Phil Jemmett, and Rebecca Swan McAdam, all of whom were invaluable in the creation of this outreach. This successful engagement project was invited to be exhibited at NAM (the National Astronomical Meeting) at The University of Warwick on July 13th 2022 to an audience of over 80 families. Dr. Tomi Baike, from the University of Cambridge, and I were awarded a grant for £1200 from the Engineering and Physical Sciences Research Council (EPSRC) in New and Sustainable Photovoltaics, which enabled us to present this project at CISF (Caithness International Science Festival) on October 1st 2022 to an audience of over 200 children. This project was also exhibited to the following audiences:

- Cannon Park Primary School, Coventry (Year 6, 30 students)
- St Anne's Primary School, Chelmsley Wood (Year 6, 60 students)
- Earlsdon Primary School, Coventry (Year 6, 60 students)
- All Saints Primary School, Coventry (Year 6, 10 students)

[3] `warwick.ac.uk/fac/sci/wmg/about/outreach/stemconnections/`

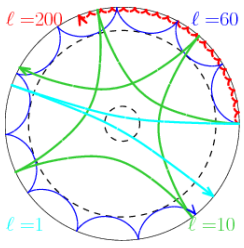

Figure 8.2: Poster from the **STEM Connections** event, showcasing the *"Meet the academic"* segment

- Meadow Park School, Coventry (Year 7, 20 students)
- Hill Farm Primary, Coventry (Year 6, 20 students)
- Match Foster Care at Warwick University (18 students mixed ages)
- Newton Park Primary, Wick, (P6–7, 85 students)
- Castletown Primary, Wick, (P5–7, 46 students)

I have designed the project to be accessible to audiences who e.g. may not have had much experience with computers, or don't use English as a first language, by incorporating a picture-based approach, with varying levels of complexity to suit the user. To ensure the longevity of this work I trialled it at test events, drew up budgets and risk assessments, and trained the public engagement volunteers in my department to ensure it can continue to run following the end of my postgraduate studies. I wanted to create a project that combined art and science, and took inspiration from the *Stitch*

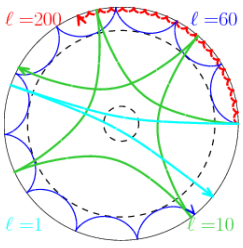

In Time project, supported by HVM Catapult, which makes use of Coventry's textile history and encourages children to create embroidery designs by learning basic coding skills [4]. *Stitch In Time* uses an online computer program called **Turtlestitch**[5] which allows a user to move a virtual turtle by combining pre-made basic code blocks. These blocks can be combined into for loops, with counters, iterators, and if statements. Using **Turtlestitch** students are able to explore the quickly scalable capabilities of code, and with few blocks students can build up increasingly complex patterns.

I built a custom block on **Turtlestich** which produces a pattern that resembles the path of a p-mode as projected on a circle. In order to make the project more appealing to the masses and to get the point across more efficiently, I dubbed these patterns sunquakes, analogous to earthquakes on the Sun. This terminology is not strictly correct in the academic sense, where sunquakes are more traditionally attributed to localised p-waves around flare sites. However in this instance I thought it appropriate to favour entitling the project something the audience would be able to quickly grasp the concept around, over being strictly scientifically accurate. I want to emphasise that I believe the dominant aim of science communication should not be to leave the audience with a list of fun facts, but to increase the understanding, appreciation, and inclusively of science. Having created the code to produce sunquakes as seen in Fig. 8.3a, I left three parametres to be user defined– the **bounce**, **curve**, and **depth** of the sunquake. A user is invited to pick any number between 0–10 for each of these parametres, producing an effectively unique design (out of 1331 possible patterns!). These values determine the number of bounces the sunquake presents, how quickly the sunquake curves in on itself, and how deep the wave penetrates into the solar interior respectively. I have taken some liberties in this code in the interest of speed of computation and in order to produce something that can be sewn. For example the sunquakes are not harmonics in my code, as they are on the Sun. Additionally I have restricted the values for bounce, curve, and depth, to prevent the over dense areas of stitches which eventually causes the embroidery machine to break. An example of the sunquake pattern that can be produced by **Turtlestitch** can be seen in Fig. 8.3b.

Once the Sunquake pattern is deigned by the student, the file can be transferred to a portable embroidery machine via USB to be sewn onto fabric (usually taking 1-3 minutes). I chose this system as the embroidery traces out the path of the sunquake in a similar way to how a p-mode physically travels. This allows me to discuss the path and behaviour of a wave with the waiting student and the student is usually quite excited to

[4] `warwick.ac.uk/about/cityofculture/get-involved/projects/stitchintime/overview`
[5] `www.turtlestitch.org`

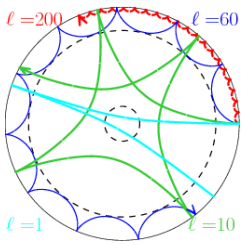

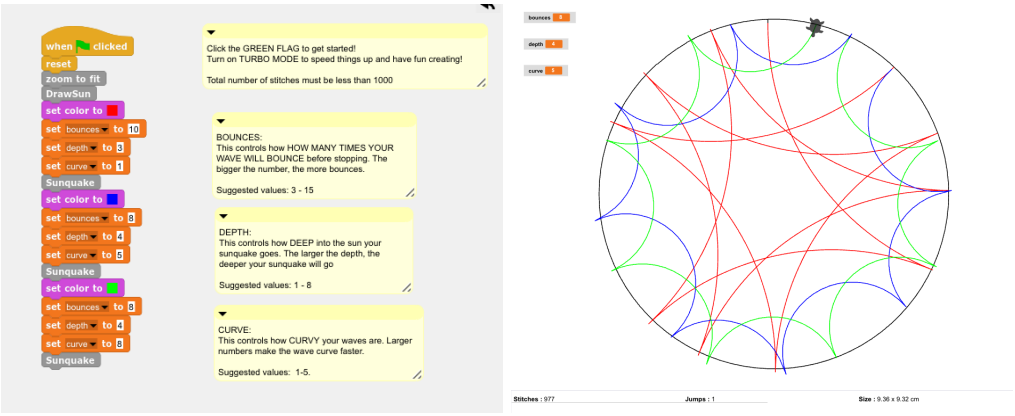

(a) (b)

Figure 8.3: *Left*: The code comprised of blocks in which the user can change the values for bounces, depth, and curve. *Right*: The resulting Sunquake

come across a machine that's outside of their everyday life and see their creation come to life. After the sunquake has been sewn, the student is encouraged to cut it out and attach it to a cork coaster (see Fig. 8.4) to take home. This is done with the intention that a take home resource will continue to jog their memory of a fun hands-on scientific activity in the future and provide longer term impact.

If you want to try designing your own sunquake, scan the QR code in Fig. 8.5 (please note that **Turtlestich** is optimised for a laptop or tablet).

This activity combines coding, creativity, discussions about engineering and computer science, helioseismology, and art. It allows for extended conversations with audiences which allows for personal connections to be made and break down barriers between myself the scientist and the non-scientific audience.

I came across several problems in the implementation of this activity– most prominently being the issue of scale. I had designed this activity as a 'drop-in' session for children aged between ∼5–13, wherein I planned to interact with up to three children/ families at a time– one designing on a laptop (that I provided), one having their design sewn, and one decorating their coaster, with approximately 5 minutes at each sub-stand, allowing for enough time for meaningful interaction with each child. However due to logistical reasons, the event plan pivoted into classroom style interactions– with up to twenty students in a singular 20 minute session.

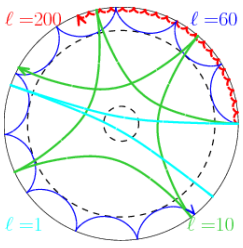

Figure 8.4: Sunquake coasters with patterns generated using **Turtlestitch**

Figure 8.5: QR code for the "Try it yourself!' **Turtlestitch** Sunquake activity. Alternatively you can access the program by following the link here: `www.turtlestitch.org/users/TishtryaMehta`

As each Sunquake needs 2-3 minutes to sew + 2 minutes of loading the pattern and the sewing machine, it was simply not feasible for every student to leave with a sunquake in this time frame. Similarly it's a difficult activity to scale with the bottleneck at the embroidery machines, which take a fixed amount of time to load and stitch. The session plan for the school visits in which I ran this activity underwent extensive last-minute alterations as I adapted this project from a 'drop-in' to a classroom group project. The group project sessions still had impact, with the majority of students engaging with the material, but had the significant drawback of too few laptops, meaning that the students had to code in groups. Naturally some students struggled to get involved with the coding part of the activity. Furthermore, as I could only sew 1-2 sunquakes per session, the 'long term' engagement of this activity was likely reduced as students couldn't take home a reminder of the event. I learnt

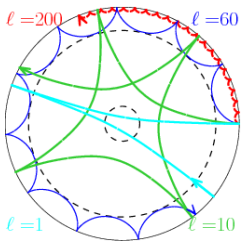

from this experience, and so when I reran the classroom style session two weeks later in Caithness, Scotland, I was able to ensure in advance every student had access to their own laptop and could code their own design. We also ensured everyone could take home some reminder of the event, and produced a display to be hung up in the class room, both of which were intended to improve the longevity of the event. My reflections on this project and an evaluation of running this event, including changes I made as a result, are included in Section 8.3.

Star-on-a-Stick!

Another activity I frequently ran or assisted with was the 'Star-on-a-Stick!' activity, co-created with Dr. Anne-Marie Broomhall. The project is again in the intersection of craft and science, encouraging children to make and decorate their own paper plate stars following a brief introduction into stellar classes and physical stellar phenomenon such as filaments and sunspots. Children were encouraged to decorate stars with blue, yellow, orange, red, white tissue paper, all reflecting the multitude of wavelengths emitted by stars. Pipe cleaners would be stapled on and positioned in ways to resemble prominences and coronal loops. The use of glitter glue made way for flares, and black paint for sunspots. Streamers made from thin sheets of reflective cellophane represented Coronal Mass Ejections and occasionally Solar wind.

After several iterations of running this activity, which were wildly successful in classrooms and libraries, Anne-Marie and I built on the existing activity and exchanged paper plates for polystyrene balls of various sizes, which could be stuck on to BBQ skewers and decorated as before. This iteration proved to be even more successful than the last. At events such as the Warwick Family Day 2019, or the Outreach festival at the National Astronomical Meeting 2022, a small procession of stars grasped in little hands could be seen walking across campus. Usually following a drop-in session or lesson, we would take the opportunity to discuss the range in sizes and colours, and arrange the class' creations into a temporary Hertzsprung-Russel diagram. This activity proved to be a great success, with students primarily enjoying the creativity and chance to make and take home something of their own. This usually led into wonderful discussions about space, e.g. "Can I have more than one star to decorate?", "Well, do you think you could have two stars next to each other? What do you think would happen?". This specific exchange led to a group of students learning about binary star systems for the first time, and started a discussion on the strength of gravity, and why two stars next to each other don't necessarily collide into each other. (This conversation also led to a

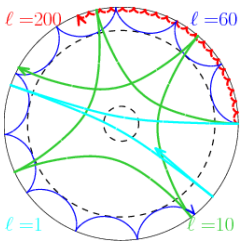

child very proudly walking away with a binary star system in either hand!)

Evaluating this activity, I would say it remains to be one of my favourites and one I would eagerly recommend to other science-communicators working with teenagers and younger. It's easy to set up, allows for a lot of creative control, facilitates brilliant discussions, and allows the child to create something to take home– increasing the longer term impact of the project. The significant hurdles are the physical and social environments. Firstly, the activity must be performed in an environment that can get a bit messy with PVA and glitter glue, and that can be cleaned with relative ease. Secondly it's easy for the science to get lost in a drop-in environment, as children are keen to get creating without understanding the 'how and why' of the event. We reflected on this issue and restructured our events slightly, by keeping the art side of the activity hidden until an initial presentation and Q & A session was finished. This allowed the audience to fully engage with the science and learn about the different stellar phenomena. The subsequent reveal of the art activity was met with controlled enthusiasm as we were then able to ensure the science wasn't lost in the session. After trying this approach and seeing its success, we firmly implemented this routine into our school visits. Finally a notable barrier that should be mentioned is cost; for each student to come away with a star, a number of resources are required, that can add up relatively quickly. We have been able to minimise this as much as possible by applying for grants, purchasing items such as PVA glue in bulk and diluting it down, and limiting the amount of craft materials available to the children at any given time (this last one was implemented after a student produced a 'Sun-on-a-stick' that had perhaps 20 pipe-cleaner coronal loops. While this was perhaps not an ideal use of resources, the student did comment that the Sun was at 'Solar maximum', so we considered it a success, and altered our practises for future events).

8.2.2 Outreach in academic or professional settings and mentorship

I have also been involved with scientific engagement within an academic setting. I wrote an article aimed at an academic audience [Mehta et al., 2022b]. This article presents the work done by the brilliant science communication professionals and volunteers on call at NAM's outreach festival and throughout the week. While this article is largely a celebration of the work that was done, it also functioned as as a means of networking between the different public engagement teams. This challenged me in a new way as I have far more experience communicating science in a casual way to children. From this, I was able to develop my professional writing skills, and improve the national reputation

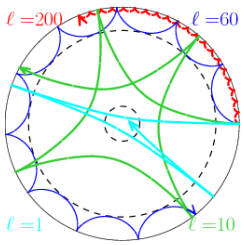

of the University of Warwick by showcasing its efforts in widening participation and outreach. I have also written a science communication aimed UKSP 'Nugget', largely based on Chapter 7, which was intended for an academic, solar based audience, which can be found here[6]. Science communication can still be meaningful within an academic audience of expert, when sharing the work that's perhaps outside of someones area of expertise.

I have extensively acted as a mentor (details of which can be seen in the Appendix), for example working with Undergraduate Research Support Scheme (URSS) students in my department the Centre for Fusion, Space and Astrophysics (CFSA), collaborating and advising on their research and practising their presentation skills with them. This is evidence of my work in mentoring and supporting students in Public Engagement schemes. I also have mentored my peers in good Public Engagement practises, encouraging them to co-present with me in Pint of Science talks and assisting them in taking the lead at outreach visits to local schools. This demonstrates evidence of public engagement focused teaching and comments from one of my peers whom I mentored can be found in the attached Appendix. On November 10^{th} 2022 I spoke as an Invited Speaker for a Leadership Seminar for the National Co-ordinating Centre for Public Engagement (NCCPE). I have also spoken as an invited panellist in Institute for Advanced Teaching and Learning (IATL)'s Postgraduate Public Engagement module in October 2021. Within these talks I discussed my recommendations for successful outreach and the importance of changing perceptions on why public engagement should be carried out. Other panels I've spoken on include 'Women like Me' and 'Early Career Network' events where I have trained peers on how to effectively engage with both a non-scientific and academic audience, and how to clearly communicate complex scientific principles in accessible and fun ways. I have also worked closely with Warwick Engages, leading activities around Canley, Nuneton, Whitnash, and worked closely with Warwick University led schemes, such as in British Science Week's Family Day where I co-designed and co-ran a host of art and sound-based activities to hundreds of visiting families.

8.2.3 Visiting Schools

One of my most common forms of outreach is to schools in Coventry, and the the wider West Midlands area. Within the last few years I have led or assisted in the outreach of well over 50 individual classes, usually each with 20 or more students. Usually the visit is set up by Ally Caldecote, or Anne-Marie Broomhall, and I either lead or help

[6] www.uksolphys.org/uksp-nugget/121-quasi-periodic-problems-whats-going-on-with-qpps/

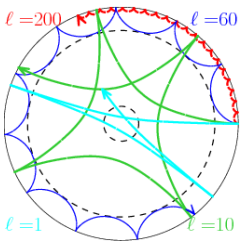

at a session, based on stars, magnets, light etc. Most often we work with children aged 8-12, staying for 1-2 hours. The format of the session is usually as follows: We begin with a short presentation on the Sun, why we care, asking "What is space weather?", "What do magnets have to do with space?", and similar questions. We then outline an activity which the students take part in for approximately thirty minutes. This may include one of the aforementioned art activities (Section 8.2.1), or an activity with beads that change colour under UV light, or a hands on activity involving magnets. All of our activities are interactive and in this time we get the chance to speak to all of the students individually, again with the focus on building trust and familiarity. We want the students to come away with the primary message of "the science we did/learnt was fun", and a secondary message of "I enjoyed meeting the scientists". This would encourage students to feel more welcome and inquisitive about science and space. We frequently close the sessions with a Q&A session, where (if appropriate) we may steer the conversation to improving equity in science, by prompting conversations on what a scientist looks like, who is welcome in science, what can hold us back and how we can overcome. I have also liaised with a number of local schools and Brownie groups to visit multiple times over months or years. This provided the opportunity for ongoing impact as testimonials from teachers (see attached evidence) confirmed that students would talk about the outreach long after the visit and younger students would be looking forward to their turn. This also allowed our department to build a partnership within the local community and strengthened community links.

Evaluating these visits, it's clear that the hands-on activities where the students can combine play and science are the most popular. Especially for students who are in primary school, our goal is to foster an enjoyment and appreciation for science rather than focusing on e.g. GCSE choices or career goals. Therefore we emphasise the fun of finding out the answers to questions, and the importance of asking 'why'. Again a danger is that the students become so engrossed in the activity that they lose focus in the science, or order is lost in the classroom. As a result, I keep a habit of incorporating the teacher into the lesson so that they can be in charge of being the class' attention together when needed, and are able to keep order better than I can as a visitor. Another difficulty is the added considerations of safeguarding when working with a school as a visitor. I have worked on this by attending multiple safeguarding training courses and always work to establish clear communication with the school and the class on what is unsafe during my visit (e.g. small magnets present choking hazards, telling students not to "stare directly at the Sun" with a naked eye when we bring telescopes on our visits etc. [See *Anti-Hero* in Swift & Antonoff, 2022]).

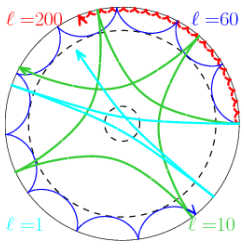

8.2.4 Live talks and lectures

I have performed in a vast array of public lectures and talks, primarily through **Pint of Science** or the **Warwick Christmas Lectures**. I have worked to increase the visibility of Warwick University and the research we do on a regional level, and as such have travelled across the West Midlands to promote, inform, entertain and deliver bespoke engagement.

For Pint of Science, I largely spoke about the Sun and solar phenomenon. In 2018 this was a talk on *"What to do when the Sun has a temper Tantrum"* at the Phoenix Pub (Coventry), in 2019 *"Who would win in a fight; the Sun or a trillion lions?"* co-written and co-presented with Dr. Alun Rees at The Old Clarence (Earlsdon), and in 2021 *"Escaping the Sun: a Photon's 100,000 Year Journey"* which was launched live online due to the COVID-19 pandemic. The movement of the Pint of Lectures to an online format was initially jarring, as much of my training in public speaking is based on the assumption that you're in front of a live audience. A lot of my 'stage-presence' had to be changed for an online format, e.g. how I stood and gesticulated, how loudly I spoke, getting used to referring to the inset video rather than a screen behind you. This was difficult to adjust to at first, and challenges arose, familiar to anyone who had had to attend a virtual conference in the last few years ("You're muted! Ah, and now the internet's gone!"). However this was combated with additional training provided by Duncan Yellowlees and Dr. Phil Jemmet, which smoothed the transition considerably. Upon reflection, the event was successful in still attracting a considerable audience. In some ways it was an improved format, as we were able to reach audiences in different countries, e.g. USA and Scotland, who usually would not have been able to attend. It was also a very valuable learning experience in trying to adapt experiments into the virtual world, and an exercise in relying more heavily on delivery and script than flashy demos.

I have also presented at six of the University of Warwick's Christmas Lectures, of which there are two per year, each to audiences of over 1000. In the Christmas Lectures in 2018, with Dr. Anne-Marie Broomhall, I co-wrote and co-lectured on *"Do you hear that Star Singing?"*. Following this lecture in 2020 I wrote and presented the virtual Christmas lecture *"How to measure distances in Space; The Astronomical Ruler"* available here: `www.youtube.com/watch?v=IKr9WOxtyqQ&t=33s`. In 2021 and 2022 I co-presented both of the Christmas Lectures alongside Ally Caldecote, which involved performing experiments live on stage. These included exploding Mentos and coca-cola, making smoke rings, setting off 100 Alka-Seltzer 'mini-rockets', and using a

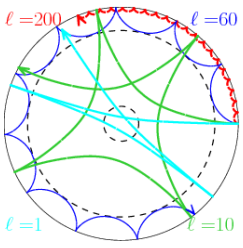

blowtorch to demonstrate convection. It's important to mention here that many of the experiments we have attempted have been cancelled, or altered at the very last minute (and sometimes on the day of the show!) due to safety or faulty equipment. I mention this because an essential tenet of public engagement is that something *will* go wrong. This is something I discuss more in Section 8.4.5, and is by far one of the most important lessons I've learnt during my years of outreach. At the first Christmas Lecture I spoke at in 2018, we had a demo cancelled on the day of the show, which left us worried and scrambling to alter the script. We were able to quickly find an alternative way of communicating the same science (albeit in a less exciting fashion) and move on with the day and accept the change. In 2021, we had a similar issue arise, but this barely impacted our plans. We were able to very quickly find replacement activities, revise our script, and ad-lib on stage when necessary.

The Christmas Lectures are a marvellous way of quickly showing some of the joy and brilliance in science to a very large audience. As there's very limited one-to-one interaction between the audience and the speakers, it's unlikely that a personal connection will be made. However the Lectures are a good format of quickly entertaining and hopefully informing an audience, and through a diverse set of speakers may be effective in proving the perceived inclusivity of science for an audience member. Shows of this format can be highly effective in making science 'fun' and 'cool' and do have a significant impact on showcasing the hugely varied careers available in STEM. The Vice Chancellor of Warwick, Stuart Croft contacted me directly following the Christmas Lectures in 2021 and commented: "Your skill at communicating both your expertise and enthusiasm is remarkable. Thank you for your excellent representation of the university to the public, and for your countless outreach events. It is very much appreciated and I wanted to give my sincere thanks". This is evidence that my contribution strengthens the Universities region role and improves the University's standing.

8.3 An evaluation of practises and the future of outreach and engagement

Evaluating an event: a case study

I worked at an all-day event at the Coventry Transport Museum as part of the STEM Connections partnership with Warwick Manufacturing Group (WMG). During this event we invited 110 students from four schools in the wider Coventry area to rotate around twelve stands at the museum, with myself running my Sunquake stand (Detailed in

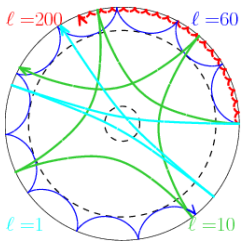

Section 8.2.1).

I took this as an opportunity to evaluate the impact of my outreach of six 20-minute sessions of the "Embroider a Sunquake" activity, each to an audience of about 10 students. Here I had two primary aims; firstly to educate the students about sunquakes– to introduce concepts such as stellar structure, transportation of heat in stars, waves, in a fun and interactive way, and secondly to present myself as a (minority background, female, art-enjoying) scientist hopefully widening their perception of who participate in science and what it means to be a scientist. I hoped they would leave with some new vocabulary and understanding or appreciation of scientific concepts, and having made some sort of personal connection/having enjoyed the session– which may make science feel more accessible to them.

To assess the impact I had blank posters which I encouraged them to write on before and after the session (Fig. 8.6a shows some of the comments written after the session). On the 'before' paper I wrote the prompt *'Write down everything you know about the Sun!'* and upon the 'after' paper I wrote *'What NEW things do I know about the Sun?'*. Some drawbacks to this method is that giving a child 1 minute to write down 'everything' they know about the Sun will not be a fair representation of their knowledge, and also will not necessarily be accessible to children with poor writing abilities or those who struggle with English. It is also difficult to ask questions about the children's opinions on their implicit biases about science or scientists at similar events as they will be influenced by the person asking and the setting they are in– they're less likely to answer unfavourably about their opinions on science when asked by a scientist in a position of power at a science event.

Because of these factors we expect to see some slightly more favourable responses than if we asked similar questions at a more neutral event. We also should expect to see fewer overall responses on the 'before' sheet due to the time restriction.

Here I evaluate the 'before' and 'after' responses. For the responses before the outreach, most of the words could be sorted into 5 categories; Size, Distance, Temperature, shape/composition, Astronomical features. Below is a condensed list of the responses, rephrased for convenience and with repeated statements omitted.

- **Size:** *99% of the galaxy, Big, 1,000,000 Earths, Huge, It's ginormous, massive*
- **Distance:** *Far Away, if you get close you will die*
- **Temperature:** *30,000, Hot, warm, burning, Very hot, will kill you, You will get burnt by it*

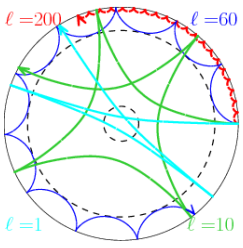

(a) (b)

Figure 8.6: Handwritten evaluations of the STEM Connections event at Coventry Transport Museum on September 16th 2022. *Left*: New words, facts and comments that audiences wrote after the session. *Right*: A comment from an audience member, comparing the sun to a 'jiggly jelly'

- **Shape/ composition:** *Circle, Lava*
- **Astronomical Features:** *Gives off light, It's a star, Light Source, Starry, It's an eclipse if it becomes one with the moon, The world's largest light source, It gives us light, It reflects on the Earth*

These responses varied in their scientific accuracy/ language from statements and numbers that were wrong (e.g. *[The Sun is] 30,000 [degrees]*), to more advanced and correct statements, discussing phenomenon such as eclipses. We see that the audience on the whole had some understanding that the sun was a star, and is very hot and very big. These sentiments were echoed in many different styles of writing but were the most common themes.

Following the activity I invited the attendees to write down any new things they had learned during the session. I present an updated list of the most common words/ phrases in these categories:

- **Size:** *Earth = small; Sun=Big, The sun is a million times bigger than the Earth,*
- **Distance:** No references
- **Temperature:** *The sun is hottest inside, the sun is 15 mil degrees, The core is 15 million degrees, it's hot, it's 15,000,000 in the core, the sun is hottest in the core, On the Sun the edge is colder than the middle*

- **Shape/ composition:** *It's made of plasma, the sun is a gas, When plasma explodes it makes sunlight, It's a bit wet, plasma sizzling, It's plasma!*
- **Astronomical Features:** T*he sun has sunquakes, There are sunquakes, sound cannot travel in space, the sun is like a jiggly jelly, sound cannot travel through space, Sunquake = MASSIVE, The Sun is like a Jelly, There are earthquakes on the Sun, The Sun burns continuously, The sun makes a kettle noise*
- **General comments:** *We had fun, It was amazing, we had so much fun, It's cool*

We see no significant differences in the size comments, with the same comparisons of the size of the Sun. Distance was not discussed in the session at length and no students remarked on anything new they had learnt in this area. However there's a marked difference when the students comment on the temperature with all of the comments either mentioning specific temperatures or how the temperatures relate to specific regions of the Sun. There's also an increase in scientific language (use of the words degrees, use of the word 'core'), which were not used before. Again there is a change in language as to how the students describe the composition of the Sun, with the very common use of the word 'plasma' which none of the student used previously. The most significant on changes is the extensive comments on 'sunquakes' which were the focus of the session. No student knew of Sunquakes before any of the sessions and following there were a very high number of comments about it. References were made to the sound of the Sun (something not previously commented on) and the movement of the Sun (the comment about a 'jiggly jelly' in Fig. 8.6b in in reference to a comparison I made frequently in the session, where I likened the oscillatory behaviour of the Sun to that of a shaking jelly). This increase in mentions, coupled with correct physics, proves that a new scientific concept has been has been effectively communicated. It's unlikely that the specific facts will be remembered in the weeks and months to come– the design and aim of the project was not to send the audience away with a barrage of facts to remember. It was to introduce science in a fun, hands on, creative way. It was also to provide a face to face meeting with a scientist and break down barriers and stereotypes that may surround science or a career in science. Audience unprompted came up to me with questions– some scientific "What will happen to the Sun when it does?" etc., and some personal; "What A-Levels did you do? How much do you earn? Why do you like science?". Being able to facilitate these questions that these audience might otherwise not have been able to ask is the real value of the outreach.

A reflection on what I learnt from this event:

Many things went well during the session. The children were clearly engaged and enthusiastic to learn, and responded well to the session plan. Many students asked questions unprompted, and started more personal conversations about their aspirations etc. which suggested that a comfortable environment had been set up. The session was largely successful, and students were happy to take materials back to their classroom, and several went out of their way to personally thank me for a fun session. There were also many things that I realised could be improved about the lesson plan. I built on these realisations and made several modifications when I repeated this activity two weeks later at the Caithness International Science Festival (CISF). These changes are listed below, split into the Limitation, the Difficulty as Coventry Transport Museum (CTM), and the change made at Caithness International Science Festival (CISF).

Limitation: 1 Embroidery Machine

Difficulty at CTM: There was only one embroidery machine, and I was the only person trained to use it. This caused delays when the machine broke and I had to interrupt what I was doing to fix it. Also halted the entire event when it needed maintenance.

Change made at CISF: I brought 2 Embroidery Machines to CISF, as well as training a volunteer on how to do simple maintenance, or how to takeover the session if I had to fix a machine. This also sped up the production of sunquake coasters.

Limitation: Ratio of volunteers to students

Difficulty at CTM: I had not effectively communicated how I wanted the session to the run (drop-in vs. timed fixed size group sessions) This meant that I was delivering outreach to a much larger audience than I expected, with an activity intended for 1-2 students. This made it difficult to meaningfully engage with all the students.

Change made at CISF: Recruited another volunteer, and effectively communicated that I wanted to run a drop-in style event. As such, I worked with the ratio I had planned the event for, and had meaningful interactions with all audience members.

Limitation: Overwhelming environment

Difficulty at CTM: At the Transport Museum I was stationed next to an exhibit that played loud music throughout the day (6 hours) which was very distracting, and at times irritating. The embroidery machine also can get loud, and this may have irritated the other science communicators at near-by stands.

Change made at CISF: I spoke to organisers to ensure my stand was placed away from sources of continuous noise. I also briefed the science communicators at nearby stands about the noise of the embroidery machines, ensuring they had the chance to raise any concerns, and offering to move if they did so. Reflecting on the busyness of the event previously and the amount of space the children took up when decorating the sunquake, I requested extra tables for the event, which were indeed needed.

Limitation: Constraints on take-home pieces

Difficulty at CTM: As mentioned, I did not have the time capacity to sew all of the attending children an individual sunquake. Therefore time constraints meant that only one Sunquake coaster was taken back to the classroom per group (about 10-20 children). This left some students disappointed as they wanted their own.

Change made at CISF: By changing the event to a drop-in session, we ensured everyone who interacted with the exhibit had the chance to design and take home a Sunquake. I planned by taking materials for over 100 students, and with spare Space themed stickers and Sunquake Spirograph templates so those who didn't have the 10 minutes to make a sunquake could quickly interact and still take something home.

Limitation: Marker pens didn't work

Difficulty at CTM: The pens we borrowed from the transport Museum didn't work, so students had to share, leading to bored students who were waiting, and hard to read responses.

Change made at CISF: Brought my own set of markers.

Limitation: Problems with electricity

Difficulty at CTM: I was only able to set up this activity on the morning of the event, and when I arrived I had issues in connecting the machines to the mains electricity. This was worrisome as the entire event relies on the machines.

Change made at CISF: I set up at CISF the day before the event, ensuring there was working electricity.

Limitation: Packing up equipment

Difficulty at CTM: Packing up the equipment at CTM took some time and it was difficult tracking down all the individual parts.

Change made at CISF: I set up a system of where everything should be placed during the event, and made a quick inventory to check through at the end.

On reflection, I learned a lot from these events, the most important being planning appropriately for your event. By this I mean that not all outreach activities can be adapted for a classroom, drop-in, lesson, or talk format. Although this event went well, it was designed for a drop-in session and it was not as effective as an alternative event, designed specially for groups of 10 in a 20 minute session could have been. As a result, I have learnt the importance of effective communication with the team in advance, as well as discussions of what resources are available and discussion of appropriate environments.

8.4 A framework for those interested in doing meaningful public-engagement or science communication

Here is my guide to effective outreach based on my experiences over the past five years. Please note that this advice is based on what I've learnt and may not be applicable to all researchers planning an outreach event.

8.4.1 What do you want to have changed by the end of your outreach?

First you need to consider what your intention is with the outreach. Are you trying to inform? Are you trying to educate? Are you trying to change the audiences perception of your field or your role. Consider carefully what do you want people to take away at the end of your session as this will massively change the direction you should take with your outreach. Also consider how you can fit your outreach format with the question. For example it is unlikely that you will be able to massively change the opinion of an audience of two hundreds with a one-off 10 minute talk. Consider realistic goals in line with the time and resources that you have available.
Examples of changes:

- "I want to showcase different career paths of scientists to *change* the perception of what a 'typical' scientists' journey is."
- "I want to *change* the audience's understanding of the scale of space and in doing so educate and entertain an audience
- "I want to educate to teachers and caregivers to *change* the way they speak about science to the children in their care, and move the emphasis from 'smart' scientists to passionate and hard-working scientists."

8.4.2 Consider effective solutions when inevitable restrictions arise.

The decisions you make at this stage are going to be largely influenced by restrictions; budget costs, location, time restrictions on creating or delivering the outreach. It's very likely that your original idea will have to evolve to accommodate these. However it's important to not sacrifice the intended goal of the outreach. There's a vast array of formats that outreach can take; online, in person, through the means of take home activities, or workshops etc. , most of which can be modified in some way to allow for your restrictions. The important thing is that you still use an appropriate format for your intended change and setting: E.g. making a poster may be a faster and cheaper but

not as effective way of educating 4 year olds. Instead a more hands on activity is likely to be more effective in engaging them. **At every stage consider will this format help you make the change that you are intending**. If not take a moment to stop and reconsider what your aim is.
Examples of modifying methods due to constraints:

- *Initial idea:* Change the perception of Y3's students about what the daily life of a scientist is by going to a local school and chatting to students for 1 hour with a Q and A
- *Constraint:* Location. School is in a remote village that takes 5 hours to drive to from your location
- *Ineffective solution:* Create a pamphlet and post it. This may have some impact, but is probably less effective as young children won't be as engaged and won't be able to ask questions live.
- *Effective solution:* Set up a live Zoom Q and A session to chat virtually to the students or recruit a more local colleague to attend in your stead.

8.4.3 Plan your evaluation.

So now do you know what you want to do and how you're going to do it consider what you're going to do afterwards aka how will you measure whether this has been effective. There is no point in doing engagement unless you assess how effective it has been and learn from it so that it can better inform any future work you do. It does seem strange to discuss the evaluation before the outreach has begun– but counter intuitively it is the perfect time to do so as the evaluation must be factored into the plan of the session. Surveys, discussion points, feedback forms etc. all must be created in advance, and thought must be given on how and when to distribute them to the audience, and how you'll get them back. Also consider what questions need to be asked to evaluate whether your change. How will you measure whether your outreach has made the change you hoped for?
Things to consider:

- The *format of your evaluation* may change what people say; people may be overly complimentary face to face and avoid stating their true thoughts. Make your evaluation fair and anonymous if possible

- Consider *what data needs to be collected*. Do you need to know your audiences' gender/age/marital status? Is it important to knowing whether your outreach was effective. If you include potentially identifying or personal questions, always give the option to 'opt out' with a N/A or 'Prefer not to state' option
- The *longevity of your impact*. While you may have exerted change after 1 session, see if that change can be tracked over weeks/months/ years. If possible re-collect evaluations at longer timescales and remember that the most effective outreach is one that continues to have ongoing impact.

8.4.4 Safeguarding and risk assessments

You must consider how you're going to keep the environment safe to the highest reasonable level. Often in outreach we work with audiences who are traditionally not represented in science, and these groups can have considerable cross over with the more vulnerable members of our society, e.g. people from foster homes, people with disabilities etc. We also commonly work with children or audiences under the age of 18, for whom additional safety measures should be taken. Above all, your activities must be safe– safety is an essential precursor to whatever activity is being planned. That is not to say that outreach cannot have some potentially dangerous activities– the trick is *finding the safe way to do any potentially dangerous activities*. Want to perform a chemical reaction involving a bright flash and the expulsion of hydrogen? That's great! But how can you ensure the audience are at a safe distance, and won't inhale anything they shouldn't? Can you ensure none of the audience will touch the equipment? Are you certain this has been communicated to all the audience– including those who may be hard of hearing or non-English speaking? Risk assessments are essential to the safe running of outreach– after all an unsafe activity is not effective outreach. A good risk assessment finds the risk levels for all equipment, taking into account the setting and audience, and is regularly updated. Also check the full safeguarding requirements given by your institution and look into what training is available. These requirements are not only there to protect children/ vulnerable audiences, but also to protect yourself from getting into situations where you can be blamed. If any incident arises always find yourself a senior member of staff and *report it immediately*.

8.4.5 What to do when things go wrong

First of all, embrace that **things will go wrong**. Equipment will go missing or break minutes before your outreach starts, staff will fail to show up, experiments won't work,

and you might find out the Hertzsprung-Russel diagram you drew on the board was completely back to front and have it corrected by an eight year old in the audience (true story). It's inevitable that something eventually will break and ruin your train of thought or force the lesson to change dramatically.

Try not to put too much stock in your original ideas and get familiar with becoming flexible with your plans– you might surprise yourself at how effective last-minute changes can be in delivering your intended message.

- *Pivot or persevere:* Is the lesson plan/ activity salvageable? Can you quickly amend a part or two of your plan and keep going? If so, do so; the audience won't know any better! If not, in general it's better to call it quits sooner rather than later. Always return to your original aim– what change do you want to make? Find a way of imparting that change as best you can in the situation you find yourself in. Start a conversation, find a resource online, but remember what you're aiming for and head in that direction as best you can.

- *Don't get attached:* The chances of something going perfectly to plan are essentially nil. Keeping your expectations realistic and being ready to abandon and replace parts, if not all, of your planned outreach and embracing whatever resources you have around you will allow you to move on quickly from disaster and create something that's still effective at last notice. Try to separate your activities from yourself– even the best planned activities sometimes don't reach an audience. You are not your output. Learn from mistakes and move on.

- *Practise thinking on your feet:* If you find yourself without a demonstration or equipment, it can be easy to get flustered and panic. Take a moment and remind yourself that your best resource is your enthusiasm and presence. Learn a few anecdotes or analogies on whatever you're presenting on and keep them up your sleeve in case of emergencies!

8.4.6 What makes a successful session

At the end of the day you are running the session to make an impact on the audience. This isn't always measurable in the traditional ways. An audience member may leave knowing exactly zero new facts about your topic, having spent the entire session just enjoying looking around. But you may have been successful in making the audience member feel more accepted, more represented, more comfortable in an environment they usually don't interact with.

Evaluation with your intended changes in mind can be the most valuable way of measuring your impact and will tell you a great deal about the success of your event, and help guide you into making more effective sessions. I would argue that the most important factor in judging whether a session is successful is the *connection* built between you and the audience. Audiences are less likely to remember what you spoke about 6 months down the line, but building a connection ensures they remember the friendly/funny/kind/thoughtful researcher. And ultimately this is what has the largest impact in helping create a welcoming, fun and inclusively environment. And the building of these environment allow more more people to feel comfortable in interacting with science, which can (on a much larger scale) improve our overall scientific literacy and communication between the sciences and wider audiences. I would always advocate to emphasise building a fun, inclusive and welcoming session over one that focuses on the facts or information (though the ideal session should encapsulate both).

Final suggestions for a successful session:

- *Follow the audience's train of thought:* Audiences, especially younger audiences, may be excited to speak to you about something that's not strictly on-topic but has caught their attention. Where possible, I'd suggest encouraging this conversation and engage – they're building a connection with you and it's important to not shut this down when they're opening up. When the moment presents itself, pivot the conversation back to your intended topic

- *Relate to the audience:* If appropriate, find a way to relate to your audience. Usually audiences are more engaged when they feel like they have something in common with the presenter and they're not being spoken down to. Bring up commonalities, in location, life experience, interests. Speak to your audiences as equals and find your commonalities.

- *Enjoy yourself:* At the end of the day you are aiming to make a fun activity both for your audience, but also for you. If you're not enjoying yourself they probably aren't either. So find a way to create something you'll enjoy doing– crack a joke, make your activities something that you'd actually enjoy running, and don't take it too seriously– it's not rocket science!

8.5 Conclusion

When I started doing public engagement four or so years ago, my aims were to educate, inform, and entertain audiences at schools and on stage alike, and bring the joy and beauty of science out from the lab and into the laps of new audiences. I hoped to achieve this for a large number of people, creating long lasting impact that positively influenced audience member's perception or attitude to STEM. I also aimed to build connections with local communities, e.g. in schools and youth groups, and to develop my skills in science communication.

I believe I have been largely successful in achieving these goals. I have worked at many events in which measurable impact has occurred, where audiences have left having learnt something new and have enjoyed doing so. I have received testimonies that evidence both the learning and fun that was had by attendees, which makes me confident that my work has had some measurable positive impact. I have also grown in skill and confidence in running these events as I have moved from being 'an extra pair of hands' in outreach events, as I was in my first year, to developing my own programs and showcasing them (often alone) across the UK.

There are still many ways in which I feel I have not achieved what I set out to do. For example, I had aimed to create long lasting impact, and I have failed at doing so. I later realised that long-term impact is extremely difficult to do with one-off events, such as school visits or stage shows. These visits may be greatly entertaining in the moment, but have a limited long term impact, as children may quickly forget about the content or the connection built. Although I have returned several times to the same school, I have visited different classes and so repeated visits to a specific audience are limited to those who actively seek out extra-curricular science (e.g. at the Christmas Lectures). This leaves behind those who may benefit from the intervention the most (those who do not actively interact with STEM outside of mandatory education). In the last year, I've tried to improve the longevity of my interactions by creating artistic activities that encourage students to produce something that outlasts my visit (e.g. Sunquake coaster, Sunquake poster), which can function of a reminder of the visit.

Moving forwards I would focus on building more meaningful interactions with smaller audiences and build up longer-term relationships with the same audiences over several months or years. I believe this would maximise the impact of the outreach and build the connections needed to facilitate trust and a welcoming environment in STEM. I would also change my approach to put evaluation at the forefront of my planning. I would start planning with the essential questions: *"What barriers exist at the moment?*

What can I do to reduce these barriers? What measurable *change can I make here, and is it feasible for me to do so?"*. This would improve the quality of the engagement from the outset as I would be able to make measurable, meaningful impact.

I believe over the past four years of running public engagement and outreach initiatives, my work has directly impacted close to 8000 people. This is through the non exhaustive following list of engagement activities I've worked on or run: five live Christmas Lectures, each with audiences of 1000; 600 views on the virtual Christmas Lecture; 85 attendees at NAM's outreach week; 110 attendees at the STEM Connections roadshow at Coventry Transport Museum; 200 at the Caithness International Science festival; a further 60 students in the West Midlands and 130 in Wick, Scotland while exhibiting the '*Embroider a Sunquake!'* activity to local schools; at least 500 students through 20+ individual school visits to local schools in Coventry, each with classes of 20-25 students; 100 students at the Warwick Family Day 2019; 100 children at the Warwick Engages Roadshow 2019; 100 in person attendees for two Pint of Science talks; 600 views for the virtual Pint of Science talk; 60 students for two separate Brownie group visits; 100 students at British Science Week at Warwick; 60 at the GNOSIS outreach event; 100 people for two panels on careers in science and outreach. This estimate does not take into account the number of teachers and group leaders I've worked with to provide additional learning resources and build connections with.

I want to acknowledge that the above figures is not equivalent to the number of lives I have meaningfully impacted. Indeed the vast majority of the audiences above have probably rarely thought of the outreach event since. Additionally, we must consider whether the fact that *I* did the outreach had any impact on the audiences at all – for example had I not spoken at a Pint of Science lecture, it's likely an equally talented, equally passionate speaker would have spoken instead and delivered an interesting talk of similar calibre. So for evaluate my overall impact we must consider *1.* What proportion of my audiences got something meaningful out of the initiatives I ran and *2.* Which events have I specially made a difference in.

For the first point, it's a difficult thing to definitely evaluate. Indeed I couldn't specifically tell you which of the many scientists with whom I interacted in my teenage years are responsible for inspiring me going on to do a PhD, but I'm certain that the interactions played a part. Furthermore, as I stated earlier in the chapter, something 'meaningful' to one attendee may be seeing themselves represented in science, and to another if may be newfound knowledge about the universe. Determining the number of people who found something 'meaningful' in my work is a subjective problem and not one I feel confident enough to answer. A conservative estimate of 1% of attendees

getting some 'meaningful' value from our interactions would suggest that my work has impacted the lives of ∼800 people – and if this is true, this is something I am deeply proud of.

The second point is easier to discuss. The areas where I've truly had the greatest impact is where I've *created* the opportunities for impact where they hadn't been before; in contacting schools and groups directly, in creating resources and new projects, in winning grants to take the work to schools that would otherwise have remained unvisited. Many of the aforementioned school visits were arranged by myself and would not have otherwise occurred (similarly for the Brownie group visits). Similarly all activities associated with the *'Embroider a Sunquake!'* activity (Caithness International Science Festival) are a direct result of my work and planning, and would not have occurred without me. Similarly several events such as my stand at NAM's outreach week and Warwick's Family Day, were I believe made more impactful by my being there verses my absence, as the stands I ran or co-ran were frequently among the busiest at the events. Adding up the number of attendees for the events I organised, plus 5% of the attendees at events in which my presence enhanced the impact of the outreach, I estimate that my work alone has impacted ∼400 further people. I believe this shows evidence that my being at or organising these events have made a meaningful difference compared to the null-case in my absence. I have created chances for impact and to those individuals I've created real change.

I hope this chapter has emphasised the importance and effectiveness of science communication, especially in this age of science hesitancy or scepticism. As scientists, we have the chance to change public perception and to influence the way forthcoming generations interact with STEM. I hope that I have convinced you that is is our responsibility to ensure the results from our research extend to audiences beyond conference centres. Through engagement and communication (whether that be with businesses, politicians, governments, charities, schools or any other institutions), we can use our expertise and passions to build a better world. A future wherein the answers to the mysteries of science are known and collectively rejoiced with the public is out there – if only the workforce exists to create it.

Chapter 9

Summary

Below is a brief summary of the results presented in this thesis. The summaries cover statistical studies on the presence and prevalence of overtones on datasets assessed by EMD (Section 9.1), the detection of the QBO in helioseismic data (Section 9.2) and a study on the behaviour and presence of non-stationarity in QPPs (Section 9.3). I also present a short overview and evaluation on my work in outreach and public engagement in Section 9.4. This chapter closes with a short discussion of some future work that could follow on from this thesis (Section 9.5).

9.1 Summarising the effective use of Empirical Mode Decomposition

In Chapter 5 we examined the presence of overtones from assessing simulated and real data with Empirical Mode Decomposition. We began by simulating datasets and assessed these using FFT and EMD and found evidence of overtones in both datasets, although the overtones were significantly more apparent in results found by EMD. We then tested the presence and distribution of overtones when changing the number of datapoints in the signal and the colour of noise present. We found that overtones were less common as the number of datapoints increases, and that the population of overtones increases to 10% of all detections (or more) when the number of datapoints in the signal is less than 100. We also found that overtones are more common for datasets containing only red noise compared to only white noise. We then examined simulated data with a sinusoidal trend and tested whether EMD can differentiate overtones from 'real' signals with periodicities close to overtone locations. We found that overtones obscure these detections where the overtone and the added periodicity were within twice the cadence

from each other. We finally tested real datasets from solar activity proxies with EMD and found evidence of overtones with populations consistent with our earlier studies. We summarise that EMD is a valuable tool is assessing non-stationary signals due to its competence at extracting complex signals, but should be used with caution for signals with short durations.

9.2 Summarising the search for the Quasi-Biennial Oscillation

Chapter 6 is closely based on Mehta et al. [2022a], and examines the presence of the QBO in helioseismic data and explores how the QBO population changes over Solar Cycles 23 and 24. We looked at intermediate degree p-mode frequency shifts from GONG and MDI/HMI data from 1996–2021. We sorted the frequency shifts according to their mode frequencies and lower turning points and assessed them using EMD, examining Solar Cycles 23 and 24 as a composite data series and then independently. We found evidence of the QBO in Cycles 23 and 24, most prominently around 500-800 d. We saw some evidence that the relative presence of the QBO is weaker in Cycle 24 compared to Cycle 23. We also found the presence of the QBO in p-mode frequency shifts was independent of the mode's lower turning point, suggesting that the QBO is caused by a near surface magnetic field that is interacted with by all modes. We also assess the presence of the QBO in solar activity proxies, the $F_{10.7}$ index and the MgII index, in Solar Cycles 21–24, by examining the data using EMD. We find evidence of the QBO in Cycles 22 and 23. We note that these were the more active solar cycles, which suggests that the QBO may be more prominent in higher activity cycles and vice versa. We also discuss the difficulties in differentiating the QBO from overtones, as most datasets had a low number of datapoints, making overtones highly visible in results.

9.3 Summarising the prevalence of non-stationarity in Quasi-Periodic Pulsations

Chapter 7 is based on two papers, which are both in the submission/ review process. Section 7.2 examines a case study of QPPs in an unusually long lasting flare from July 2012. Using AIA, GOES, and RHESSI data we set up a study to examine how the instantaneous periods of the QPPs change alongside the length of a loop at the flare site. We found that QPP period evolution and loop height were correlated in their

shapes, which may suggest some relationship between the characteristic time scales of QPPs and the length scales of the flare. The latter half of Chapter 7 (Section 7.3) examines the prevalence of non-stationarity in QPPs from 98 M- and X-class flares in Cycle 24. We obtained the flares that showed evidence of QPPs from GOES 1–8 Å data and assessed each flare's impulsive and decay phases separately using FFTs. We found 66% of QPPs examined showed evidence of an increase in period over the flare's duration, 14% showed a decrease in QPP period, and 19% showed no significant change. We saw for QPPs increasing in period, the decay period was approximately 1.4 times larger than the impulsive period. Most changes in period were between ±10 s. The presence of a CME and the flare's energy both had no impact on the magnitude or presence of a change in period.

9.4 Summarising my work in outreach, science communication and public engagement

Chapter 8 gives an overview of the outreach, science communication work I have carried out across the UK over the past four years and references the work in Mehta et al. [2022b]. I present the case for doing meaningful, measurable outreach and discuss my reasoning for integrating science communication into an academic career. I move on to discussing the different categories of outreach I've worked on, and summarised the benefits and difficulties of doing each. In Section 8.2.1 I describe the *'Embroider a sunquake!'* activity that I developed as part of STEM Connections project, and explain its conception, scientific value, mode of delivery, and outcomes. I then evaluate this activity as a case study of an outreach event in Section 8.3. I found that I had created a successful outreach activity and that it was enjoyed by attendees, but it was not appropriately planned for the audiences I interacted with. I closed Chapter 8 with my recommendations on how to host a successful outreach event, which are based on the years of experience and feedback I've received planning, running, and evaluating events. The recommendations cover planning, evaluation, presentation style, safe guarding and measurable impact.

9.5 Further work

The study of solar and stellar quasi-oscillatory signals is an ongoing and exciting field, and I am delighted to have contributed to it in my thesis. This thesis presents my recommendations for working with quasi-periodic data and contributes to the solar physics

community's understanding of the QBO and QPPs. However many unanswered research questions remain, such as what is the optimal method for assessing and detecting quasi-periodic signals, and what are the generation mechanism(s) producing the QBO and QPPs. I hope that with further research, perhaps done by generations of scientists yet to come, we might some day find answers to these exciting conundrums. Below, I outline some suggestions for further work that build on the research presented in this thesis which may bring us closer to understanding our Sun.

- *Automatic flagging of overtones*: The differentiation between overtones and signals of 'real' origins is difficult and relies on a user being familiar with concept of, and risk factors for, overtones. If we could find a physical characteristic or signature that differentiates overtones from 'real' signals, we could set up an system of automatically flagging overtones, leading to fewer false-positive detections.

- *Continued assessment of the QBO in helioseismic data in upcoming solar cycles* To date we only have intermediate degree helioseismic data from two solar cycles (23 and 24). We have reason to believe there may be a multiplicative relationship between the activity of the cycle and the prevalence of the QBO, but with only two data points we cannot draw any reliable conclusions. Ongoing work is required for further cycles to see if this relationship continues and with more data we obtain a higher number of datapoints, which reduces the likelihood of overtones.

- *Examining the latitudinal dependence of the QBO in helioseismic data*: In this thesis we only examine m-averaged p-modes, which is to say we removed the latitudinal dependence of the frequency shifts in favour of obtaining more data. As a result we have ignored any latitudinal dependencies in the datasets. It would be of interest to the solar physics community to look into the QBO in different hemispheres, as some mechanisms that have been suggested to generate the QBO show some hemispheric dependence (E.g. see Dikpati et al. [2018]).

- *Examining the flare site properties and non-stationarity in a larger study*: In this thesis we examine a single case study and see a correlation between the instantaneous period of QPPs and the flare site's associated loop. To examine this trend we need to repeat this study across many more flare sites and examine other flare site properties, such as ribbon length and active region size etc. and examine whether any flare site properties are linked with QPP period evolution.

- *Repeat QPP period evolution study with full time resolution*: In the interest of efficiency, in Chapter 7 we took a single period from the impulsive and decay

phases of a QPP and from this examine whether the QPPs appear to grow or shrink in period. A follow up study should use some analysis technique with time resolution (e.g. EMD or the CWT) to track the change in period in time. This will be extremely helpful in classifying different regimes of the change in QPP period and improve the accuracy of our findings. This work would be extremely valuable in helping discern which QPP generation mechanism(s) are creating QPPs.

- *Examination of what barriers are in the way of researchers doing meaningful measurable public engagement work*: While most researchers I interact with are supportive and encouraging with regards to my work in outreach, few researchers participate in running public engagement initiatives, usually citing reasons such as time constraints, poor pay, a lack of support from the department, and a deficit in public engagement training. We could combat this by carrying out a department-wide study to all staff on what hold them back from carrying out public engagement work, and what interventions are most needed to combat this. The study should also look into the perceived value in the work itself and the approximate cost of different interventions alongside their proposed benefits. In this way we may identify what support is needed to change perceptions and motivate meaningful public engagement.

Bibliography

Aerts, C., Eyer, L., & Kestens, E. 1998, Astronomy & Astrophysics, 337, 790

Ahmad, Q. R., Allen, R. C., Andersen, T. C., et al. 2001, Physical Review Letters, 87, doi: 10.1103/physrevlett.87.071301

Anguera Gubau, M., Palle, P. L., Perez Hernandez, F., Regulo, C., & Roca Cortes, T. 1992, Astronomy & Astrophysics, 255, 363

Appourchaux, T., Belkacem, K., Broomhall, A.-M., et al. 2010, The Astronomy and Astrophysics Review, 18, 197, doi: 10.1007/s00159-009-0027-z

Babcock, H. W. 1961, The Astrophysical Journal, 133, 572, doi: 10.1086/147060

Bahcall, J. N., Pinsonneault, M. H., Basu, S., & Christensen-Dalsgaard, J. 1997, Phys. Rev. Lett., 78, 171, doi: 10.1103/PhysRevLett.78.171

Balogh, A., Hudson, H. S., Petrovay, K., & von Steiger, R. 2014, Space Science Reviews, 186, 1, doi: 10.1007/s11214-014-0125-8

Barnes, W. T., Cheung, M. C. M., Bobra, M. G., et al. 2020, Journal of Open Source Software, 5, 2801, doi: 10.21105/joss.02801

Barnhart, B., & Eichinger, W. 2011, Solar Physics, 269, 439, doi: 10.1007/s11207-010-9701-6

Barthelemy, R. S., McCormick, M., & Henderson, C. 2016, Physical Review Physics Education Research, 12, 020119, doi: 10.1103/PhysRevPhysEducRes.12.020119

Basu, S. 2016, Living Reviews in Solar Physics, 13, 2, doi: 10.1007/s41116-016-0003-4

Basu, S., & Antia, H. M. 1997, Monthly Notices of the Royal Astronomical Society, 287, 189, doi: 10.1093/mnras/287.1.189

Basu, S., & Antia, H. M. 2008, Physics Reports, 457, 217

Bate, W., Jess, D. B., Nakariakov, V. M., et al. 2022, The Astrophysical Journal, 930, 129, doi: 10.3847/1538-4357/ac5c53

Bazilevskaya, G., Broomhall, A. M., Elsworth, Y., & Nakariakov, V. M. 2014, Space Science Reviews, 186, 359, doi: 10.1007/s11214-014-0068-0

Bazilevskaya, G., Fluckiger, E., Krainev, M., et al. 2001, in International Cosmic Ray Conference, Vol. 8, 3413

Beck, P. G., Bedding, T. R., Mosser, B., et al. 2011, Science, 332, 205, doi: 10.1126/science.1201939

Beckers, J. M., & Brown, T. M. 2013, in Astronomical Society of the Pacific Conference Series, Vol. 478, Fifty Years of Seismology of the Sun and Stars, 93

Bedding, T. R., Huber, D., Stello, D., et al. 2010, The Astrophysical Journal Letters, 713, L176, doi: 10.1088/2041-8205/713/2/L176

Berdyugina, S. V., & Usoskin, I. G. 2003, Astronomy & Astrophysics, 405, 1121, doi: 10.1051/0004-6361:20030748

Böhm-Vitense, E. 2007, The Astrophysical Journal, 657, 486, doi: 10.1086/510482

Boothroyd, A. I., & Sackmann, I.-J. 1999, The Astrophysical Journal, 510, 232, doi: 10.1086/306546

Bovensmann, H., Burrows, J. P., Buchwitz, M., et al. 1999, Journal of Atmospheric Sciences, 56, 127, doi: 10.1175/1520-0469(1999)056<0127:SMOAMM>2.0.CO;2

Brodrick, D., Tingay, S., & Wieringa, M. 2005, Journal of Geophysical Research: Space Physics, 110, doi: https://doi.org/10.1029/2004JA010960

Broomhall, A.-M. 2017, EPJ Web of Conferences, 160, 02009, doi: 10.1051/epjconf/201716002009

Broomhall, A. M. 2017, Solar Physics, 292, 67, doi: 10.1007/s11207-017-1068-5

Broomhall, A.-M., Chaplin, W. J., Davies, G. R., et al. 2009, Monthly Notices of the Royal Astronomical Society: Letters, 396, L100, doi: 10.1111/j.1745-3933.2009.00672.x

Broomhall, A. M., Chaplin, W. J., Elsworth, Y., & Simoniello, R. 2012, Monthly Notices of the Royal Astronomical Society, 420, 1405, doi: 10.1111/j.1365-2966.2011.20123.x

Broomhall, A. M., & Nakariakov, V. M. 2015, Solar Physics, 290, 3095, doi: 10.1007/s11207-015-0728-6

Broomhall, A.-M., Davenport, J. R. A., Hayes, L. A., et al. 2019, The Astrophysical Journals, 244, 44, doi: 10.3847/1538-4365/ab40b3

Brueckner, G. E., Howard, R. A., Koomen, M. J., et al. 1995, Solar Physics, 162, 357, doi: 10.1007/BF00733434

Callies, J., Corpaccioli, E., Eisinger, M., Hahne, A., & Lefebvre, A. 2000, ESA Bull., 102, 28

Campante, T. L., Schofield, M., Kuszlewicz, J. S., et al. 2016, The Astrophysical Journal, 830, 138, doi: 10.3847/0004-637X/830/2/138

Carmichael, H. 1964, NASA Special Publication, 50, 451

Chaplin, W. J., Appourchaux, T., Elsworth, Y., Isaak, G. R., & New, R. 2001, Monthly Notices of the Royal Astronomical Society, 324, 910, doi: 10.1046/j.1365-8711.2001.04357.x

Chaplin, W. J., Elsworth, Y., Miller, B. A., Verner, G. A., & New, R. 2007, The Astrophysical Journal, 659, 1749, doi: 10.1086/512543

Chaplin, W. J., Elsworth, Y., Howe, R., et al. 1996, Solar Physics, 168, 1, doi: 10.1007/BF00145821

Charbonneau, P. 2020, Living Reviews in Solar Physics, 17, 4, doi: 10.1007/s41116-020-00025-6

Christensen-Dalsgaard. 2003, Lecture Notes on Stellar Oscillations

Christensen-Dalsgaard, J. 1986, in NATO Advanced Study Institute (ASI) Series C, Vol. 169, Seismology of the Sun and the Distant Stars, ed. D. O. Gough, 23–53

Christensen-Dalsgaard, J. 2018, Helioseismology and solar neutrinos, 81–102, doi: 10.1142/9789811204296_0004

Christensen-Dalsgaard, J., & Gough, D. O. 1976, Nature, 259, 89, doi: 10.1038/259089a0

Christensen-Dalsgaard, J., Gough, D. O., & Thompson, M. J. 1991, The Astrophysical Journal, 378, 413, doi: 10.1086/170441

Clarke, B. P., Hayes, L. A., Gallagher, P. T., Maloney, S. A., & Carley, E. P. 2021, The Astrophysical Journal, 910, 123, doi: 10.3847/1538-4357/abe463

Cooley, J. W., & Tukey, J. W. 1965, Mathematics of Computation, 19, 297

Cowling, T. G. 1941, Monthly Notices of the Royal Astronomical Society, 101, 367, doi: 10.1093/mnras/101.8.367

Däppen, W., Gough, D. O., Kosovichev, A. G., & Thompson, M. J. 1991, in Challenges to Theories of the Structure of Moderate-Mass Stars, ed. D. Gough & J. Toomre, Vol. 388, 111, doi: 10.1007/3-540-54420-8_57

Daubechies, I. 1990, IEEE Transactions on Information Theory, 36, 961

Davies, G. R., Broomhall, A. M., Chaplin, W. J., Elsworth, Y., & Hale, S. J. 2014, Monthly Notices of the Royal Astronomical Society, 439, 2025, doi: 10.1093/mnras/stu080

Dikpati, M., & Charbonneau, P. 1999, The Astrophysical Journal, 518, 508, doi: 10.1086/307269

Dikpati, M., McIntosh, S. W., Bothun, G., et al. 2018, The Astrophysical Journal, 853, 144, doi: 10.3847/1538-4357/aaa70d

Dolla, L., Marqué, C., Seaton, D. B., et al. 2012, The Astrophysical Journal, 749, L16, doi: 10.1088/2041-8205/749/1/L16

Dominique, M., Zhukov, A. N., Dolla, L., Inglis, A., & Lapenta, G. 2018, Solar Physics, 293, 61, doi: 10.1007/s11207-018-1281-x

Dragicevic, P., & Jansen, Y. 2012, List of Physical Visualizations

Dubé, E., Laberge, C., Guay, M., et al. 2013, Hum Vaccin Immunother, 9, 1763, doi: 10.4161/hv.24657

Evans, J. W., & Michard, R. 1962, The Astrophysical Journal, 136, 493, doi: 10.1086/147403

Fletcher, S. T., Broomhall, A.-M., Salabert, D., et al. 2010, The Astrophysical Journal, 718, L19, doi: 10.1088/2041-8205/718/1/L19

García, R. A., Mathur, S., Salabert, D., et al. 2010, Science, 329, 1032, doi: 10.1126/science.1191064

Gelly, B., Lazrek, M., Grec, G., et al. 2002, Astronomy & Astrophysics, 394, 285, doi: 10.1051/0004-6361:20021106

Goldreich, P., Murray, N., Willette, G., & Kumar, P. 1991, The Astrophysical Journal, 370, 752, doi: 10.1086/169858

Green, E. M., Fontaine, G., Reed, M. D., et al. 2003, The Astrophysical Journal, 583, L31, doi: 10.1086/367929

Guenther, D. B., & Brown, K. I. T. 2004, The Astrophysical Journal, 600, 419, doi: 10.1086/379644

Hale, S. J., Howe, R., Chaplin, W. J., Davies, G. R., & Elsworth, Y. P. 2016, Solar Physics, 291, 1, doi: 10.1007/s11207-015-0810-0

Hall, O. J., Davies, G. R., van Saders, J., et al. 2021, Nature Astronomy, 5, 707, doi: 10.1038/s41550-021-01335-x

Hanser, F. A., & Sellers, F. B. 1996, in Society of Photo-Optical Instrumentation Engineers (SPIE) Conference Series, Vol. 2812, GOES-8 and Beyond, ed. E. R. Washwell, 344–352, doi: 10.1117/12.254082

Harvey, J. W. 1988, in Advances in Helio- and Asteroseismology, ed. J. Christensen-Dalsgaard & S. Frandsen, Vol. 123, 497

Harvey, J. W., Hill, F., Hubbard, R. P., et al. 1996, Science, 272, 1284, doi: 10.1126/science.272.5266.1284

Haxton, W. C. 1995, Annual Review of Astronomy and Astrophysics, 33, 459, doi: 10.1146/annurev.aa.33.090195.002331

Hayes, L. A., Gallagher, P. T., Dennis, B. R., et al. 2019, The Astrophysical Journal, 875, 33, doi: 10.3847/1538-4357/ab0ca3

Hayes, L. A., Gallagher, P. T., Dennis, B. R., et al. 2019, The Astrophysical Journal, 875, 33, doi: 10.3847/1538-4357/ab0ca3

—. 2016, The Astrophysical Journal, 827, L30, doi: 10.3847/2041-8205/827/2/L30

Hayes, L. A., Inglis, A. R., Christe, S., Dennis, B., & Gallagher, P. T. 2020a, The Astrophysical Journal, 895, 50, doi: 10.3847/1538-4357/ab8d40

—. 2020b, The Astrophysical Journal, 895, 50, doi: 10.3847/1538-4357/ab8d40

Heath, D. F., & Schlesinger, B. M. 1986, Journal of Geophysical Research, 91, 8672, doi: 10.1029/JD091iD08p08672

Hill, F., Stark, P. B., Stebbins, R. T., et al. 1996, Science, 272, 1292, doi: 10.1126/science.272.5266.1292

Hirayama, T. 1974, Solar Physics, 34, 323

Howe, R. 2009, Living Reviews in Solar Physics, 6, 1, doi: 10.12942/lrsp-2009-1

Howe, R., Christensen-Dalsgaard, J., Hill, F., et al. 2005, The Astrophysical Journal, 634, 1405, doi: 10.1086/497107

—. 2000, Science, 287, 2456, doi: 10.1126/science.287.5462.2456

Huang, N., Shen, Z., Long, S., et al. 1998, Proceedings of the Royal Society of London. Series A: Mathematical, Physical and Engineering Sciences, 454, 903, doi: 10.1098/rspa.1998.0193

Hughes, I., & Hase, T. 2010, Measurements and their Uncertainties: A practical guide to modern error analysis (OUP Oxford)

Hübner, M., Huppenkothen, D., Lasky, P. D., & Inglis, A. R. 2022, The Astrophysical Journal Supplement Series, 259, 32, doi: 10.3847/1538-4365/ac49ec

Inceoglu, F., Howe, R., & Loto'aniu, P. T. M. 2021, The Astrophysical Journal, 920, 49, doi: 10.3847/1538-4357/ac16de

Inceoglu, F., Simoniello, R., Arlt, R., & Rempel, M. 2019, Astronomy & Astrophysics, 625, A117, doi: 10.1051/0004-6361/201935272

Inglis, A. R., Ireland, J., Dennis, B. R., Hayes, L., & Gallagher, P. 2016, The Astrophysical Journal, 833, 284, doi: 10.3847/1538-4357/833/2/284

Inglis, A. R., Ireland, J., & Dominique, M. 2015, The Astrophysical Journal, 798, 108, doi: 10.1088/0004-637X/798/2/108

Jackman, J. A. G., Wheatley, P. J., Acton, J. S., et al. 2021, Monthly Notices of the Royal Astronomical Society, 504, 3246, doi: 10.1093/mnras/stab979

Jain, K., Tripathy, S. C., & Hill, F. 2009, The Astrophysical Journal, 695, 1567, doi: 10.1088/0004-637X/695/2/1567

Jiménez, A., García, R. A., & Pallé, P. L. 2011, The Astrophysical Journal, 743, 99, doi: 10.1088/0004-637X/743/2/99

Jørgensen, C. S., Karoff, C., Senthamizh Pavai, V., & Arlt, R. 2019, Solar Physics, 294, 77, doi: 10.1007/s11207-019-1465-z

Kiefer, R., Broomhall, A.-M., & Ball, W. H. 2019, Frontiers in Astronomy and Space Sciences, 6, 52, doi: 10.3389/fspas.2019.00052

Kiefer, R., Schad, A., Davies, G., & Roth, M. 2017, Astronomy & Astrophysics, 598, A77, doi: 10.1051/0004-6361/201628469

Kolotkov, D. Y., Anfinogentov, S. A., & Nakariakov, V. M. 2016, Astronomy & Astrophysics, 592, A153, doi: 10.1051/0004-6361/201628306

Kolotkov, D. Y., Broomhall, A. M., & Nakariakov, V. M. 2015, Monthly Notices of the Royal Astronomical Society, 451, 4360, doi: 10.1093/mnras/stv1253

Kolotkov, D. Y., Nakariakov, V. M., Holt, R., & Kuznetsov, A. A. 2021, The Astrophysical Journal, 923, L33, doi: 10.3847/2041-8213/ac432e

Kolotkov, D. Y., Pugh, C. E., Broomhall, A.-M., & Nakariakov, V. M. 2018, The Astrophysical Journal, 858, L3, doi: 10.3847/2041-8213/aabde9

Kopp, R. A., & Pneuman, G. W. 1976, Solar Physics, 50, 85

Kosak, K., Kiefer, R., & Broomhall, A. M. 2022, Monthly Notices of the Royal Astronomical Society, 512, 5743, doi: 10.1093/mnras/stac647

Kosovichev, A. G., Schou, J., Scherrer, P. H., et al. 1997, Solar Physics, 170, 43, doi: 10.1023/A:1004949311268

Kupriyanova, E., Kolotkov, D., Nakariakov, V., & Kaufman, A. 2020, Solar-Terrestrial Physics, 6, 3

Lacy, C. H., Moffett, T. J., & Evans, D. S. 1976, The Astrophysical Journals, 30, 85, doi: 10.1086/190358

Larson, T. P., & Schou, J. 2015, Solar Physics, 290, 3221, doi: 10.1007/s11207-015-0792-y

—. 2018, Solar Physics, 293, 29, doi: 10.1007/s11207-017-1201-5

Leighton, R. B. 1964, The Astrophysical Journal, 140, 1547, doi: 10.1086/148058

—. 1969, The Astrophysical Journal, 156, 1, doi: 10.1086/149943

Leighton, R. B., Noyes, R. W., & Simon, G. W. 1962, The Astrophysical Journal, 135, 474, doi: 10.1086/147285

Lemen, J. R., Title, A. M., Akin, D. J., et al. 2012, Solar Physics, 275, 17, doi: 10.1007/s11207-011-9776-8

Li, D., Ning, Z. J., & Zhang, Q. M. 2015, The Astrophysical Journal, 807, 72, doi: 10.1088/0004-637X/807/1/72

Libbrecht, K. G., & Woodard, M. F. 1990, Nature, 345, 779, doi: 10.1038/345779a0

Lin, R. P., Dennis, B. R., Hurford, G. J., et al. 2002, Solar Physics, 210, 3, doi: 10.1023/A:1022428818870

Lipa, B. 1978, Solar Physics, 57, 191, doi: 10.1007/BF00152054

Maehara, H., Shibayama, T., Notsu, S., et al. 2012, Nature, 485, 478, doi: 10.1038/nature11063

McLaughlin, J. A., Nakariakov, V. M., Dominique, M., Jelínek, P., & Takasao, S. 2018, Space Science Reviews, 214, 45, doi: 10.1007/s11214-018-0478-5

Mehta, T., Jain, K., Tripathy, S. C., et al. 2022a, Monthly Notices of the Royal Astronomical Society, 515, 2415, doi: 10.1093/mnras/stac1943

Mehta, T., McDonald, C., & Nealon, B. 2022b, Astronomy & Geophysics, 63, 5.21, doi: 10.1093/astrogeo/atac064

Molnar, M. E., Reardon, K. P., Chai, Y., et al. 2019, , 881, 99, doi: 10.3847/1538-4357/ab2ba3

Nakariakov, V. M., Inglis, A. R., Zimovets, I. V., et al. 2010, Plasma Physics and Controlled Fusion, 52, 124009, doi: 10.1088/0741-3335/52/12/124009

Nakariakov, V. M., Kolotkov, D. Y., Kupriyanova, E. G., et al. 2019, Plasma Physics and Controlled Fusion, 61, 014024, doi: 10.1088/1361-6587/aad97c

Nakariakov, V. M., & Melnikov, V. F. 2009, Space Science Reviews, 149, 119, doi: 10.1007/s11214-009-9536-3

Neupert, W. M. 2011, Solar Physics, 272, 319, doi: 10.1007/s11207-011-9825-3

Patsourakos, S., Vourlidas, A., & Stenborg, G. 2013, The Astrophysical Journal, 764, 125, doi: 10.1088/0004-637X/764/2/125

Pesnell, W. D., Thompson, B. J., & Chamberlin, P. C. 2012, Solar Physics, 275, 3, doi: 10.1007/s11207-011-9841-3

Phillips, K. J. H. 1995, Guide to the Sun

Pugh, Broomhall, & Nakariakov. 2019, Astronomy & Astrophysics, 624, A65, doi: 10.1051/0004-6361/201834455

Pugh, C. E., Armstrong, D. J., Nakariakov, V. M., & Broomhall, A. M. 2016, Monthly Notices of the Royal Astronomical Society, 459, 3659, doi: 10.1093/mnras/stw850

Pugh, C. E., Broomhall, A. M., & Nakariakov, V. M. 2017a, Astronomy & Astrophysics, 602, A47, doi: 10.1051/0004-6361/201730595

Pugh, C. E., Nakariakov, V. M., Broomhall, A.-M., Bogomolov, A. V., & Myagkova, I. N. 2017b, Astronomy & Astrophysics, 608, A101, doi: 10.1051/0004-6361/201731636

Ritzwoller, M. H., & Lavely, E. M. 1991, The Astrophysical Journal, 369, 557, doi: 10.1086/169785

Russell, B. 1961, History of Western Philosophy

Santos, A. R. G., Campante, T. L., Chaplin, W. J., et al. 2018, The Astrophysical Journal Supplement Series, 237, 17, doi: 10.3847/1538-4365/aac9b6

Savitzky, A., & Golay, M. J. E. 1964, Analytical Chemistry, 36, 1627, doi: 10.1021/ac60214a047

Scheiner, C. 1630, Apud Andream Phæum Typographum Ducalem

Scherrer, P. H., Bogart, R. S., Bush, R. I., et al. 1995, Solar Physics, 162, 129, doi: 10.1007/BF00733429

Scherrer, P. H., Schou, J., Bush, R. I., et al. 2012, Solar Physics, 275, 207, doi: 10.1007/s11207-011-9834-2

Schou, J., Antia, H. M., Basu, S., et al. 1998, The Astrophysical Journal, 505, 390, doi: 10.1086/306146

Schou, J., Scherrer, P. H., Bush, R. I., et al. 2012, Solar Physics, 275, 229, doi: 10.1007/s11207-011-9842-2

Schröder, K.-P., & Connon Smith, R. 2008, Monthly Notices of the Royal Astronomical Society, 386, 155, doi: 10.1111/j.1365-2966.2008.13022.x

Schunker, H., Schou, J., Gaulme, P., & Gizon, L. 2018, Solar Physics, 293, 95, doi: 10.1007/s11207-018-1313-6

Schwartz, R. A. 2009, in AAS/Solar Physics Division Meeting, Vol. 40, AAS/Solar Physics Division Meeting #40, 15.23

Severino, G. 2017, The Structure and Evolution of the Sun (Springer Cham), doi: https://doi.org/10.1007/978-3-319-64961-0

Simões, P. J., Hudson, H. S., & Fletcher, L. 2015, Solar Physics, 290, 3625

Simoniello, R., Finsterle, W., Salabert, D., et al. 2012, Astronomy & Astrophysics, 539, A135, doi: 10.1051/0004-6361/201118057

Simoniello, R., Jain, K., Tripathy, S. C., et al. 2013, The Astrophysical Journal, 765, 100, doi: 10.1088/0004-637X/765/2/100

Sokolov, I. V., van der Holst, B., Oran, R., et al. 2013, The Astrophysical Journal, 764, 23, doi: 10.1088/0004-637X/764/1/23

Sturrock, P. A. 1966, Nature, 211, 695

Suite, D Bril, R., Primm, A., & Harrison-Ross, P. 2007, Journal of the National Medical Association, 99, 879

Swift, T., & Antonoff, J. 2022, Midnights, Track 1

Tapping, K. F. 2013, Space Weather, 11, 394, doi: 10.1002/swe.20064

Tapping, K. F., & Detracey, B. 1990, Solar Physics, 127, 321, doi: 10.1007/BF00152171

Torrence, C., & Compo, G. P. 1998, Bulletin of the American Meteorological Society, 79, 61 , doi: 10.1175/1520-0477(1998)079<0061:APGTWA>2.0.CO;2

Tripathy, S. C., Jain, K., Simoniello, R., Hill, F., & Turck-Chièze, S. 2012, Proceedings of the International Astronomical Union, 8, 73–74, doi: 10.1017/S1743921313002263

Van Doorsselaere, T., Kupriyanova, E. G., & Yuan, D. 2016, Solar Physics, 291, 3143, doi: 10.1007/s11207-016-0977-z

Vaughan, S. 2005, Astronomy & Astrophysics, 431, 391, doi: 10.1051/0004-6361:20041453

Vaughan, S. 2005, Astronomy & Astrophysics, 431, 391, doi: 10.1051/0004-6361:20041453

Vecchio, A., Laurenza, M., Storini, M., & Carbone, V. 2012, Advances in Astronomy, 2012, 834247, doi: 10.1155/2012/834247

Viereck, R., Puga, L., McMullin, D., et al. 2001, Geophysical Research Letters, 28, 1343, doi: 10.1029/2000GL012551

Virtanen, P., Gommers, R., Oliphant, T. E., et al. 2020, Nature Methods, 17, 261, doi: https://doi.org/10.1038/s41592-019-0686-2

Weber, M., Burrows, J. P., & Cebula, R. P. 1998, Solar Physics, 177, 63, doi: 10.1023/A:1005030909779

Willis, D., Armstrong, G., Ault, C., & Stephenson, F. 2005, Annales Geophysicae, 23, doi: 10.5194/angeo-23-945-2005

Winget, D. E., & Kepler, S. O. 2008, Annual Review of Astronomy and Astrophysics, 46, 157, doi: 10.1146/annurev.astro.46.060407.145250

Woolfson, M. 2000, Astronomy & Geophysics, 41, 1.12, doi: 10.1046/j.1468-4004.2000.00012.x

Zaqarashvili, T. V., Carbonell, M., Oliver, R., & Ballester, J. L. 2010, The Astrophysical Journal, 724, L95, doi: 10.1088/2041-8205/724/1/L95

Zhilyaev, B. E., Romanyuk, Y. O., Verlyuk, I. A., et al. 2000, Astronomy & Astrophysics, 364, 641

Zimovets, I. V., McLaughlin, J. A., Srivastava, A. K., et al. 2021, Space Science Reviews, 217, 66, doi: 10.1007/s11214-021-00840-9

Appendix A

Appendix A contains Table A1, a QPP cataogue collated by the author, discussed in Chapter 7, which includes details on the QPPs' start and end times, peak energy, impulsive and decay periods, association with CMEs, and period drifts.

Table A1: Num gives the unique ID number of each flaring event. Date refers to the date that the flaring event began and T_{start}, T_{end}, and T_{peak} refer to the times corresponding to the start, end and peak flux of the flaring event, as measured in the long channel of *GOES-15*. GOES class gives the flaring class of the event. The CME column is ticked with a check mark if the flaring event is associated with a Coronal Mass Ejection. $Period_{Avg}$ is the mean period of the flaring event, found by taking the average of the impulsive and decay periods (given in columns $Period_{Impulsive}$, $Period_{Decay}$). Period drift is given in the final column of the table.

Num	**Date**	**T**$_{start}$	**T**$_{end}$	**T**$_{peak}$	**Duration** (seconds)	**GOES class**	**CME**	**Per**$_{Avg}$ (seconds)	**Per**$_{Impulsive}$ (seconds)	**Per**$_{Decay}$ (seconds)	**Period drift** (seconds)
01	2011-02-14	17:20:00	17:31:55	17:26:08	713	M2.2		$12.2^{+0.2}_{-0.2}$	$10.3^{+0.2}_{-0.1}$	$14.1^{+0.3}_{-0.3}$	$3.7^{+0.3}_{-0.3}$ †
02	2011-02-15	01:44:00	02:07:56	01:56:44	1431	X2.2	✓	$22.5^{+0.3}_{-0.3}$	$18.8^{+0.2}_{-0.2}$	$26.2^{+0.5}_{-0.5}$	$7.4^{+0.5}_{-0.5}$
03	2011-02-18	20:56:00	21:11:53	21:03:58	950	M1.3		$13.1^{+0.2}_{-0.2}$	$8.4^{+0.1}_{-0.1}$	$17.8^{+0.3}_{-0.3}$	$9.4^{+0.3}_{-0.3}$
04	2011-04-22	04:35:00	05:18:56	04:56:43	2625	M1.8		$19^{+0.1}_{-0.1}$	$15.6^{+0.1}_{-0.1}$	$22.4^{+0.2}_{-0.2}$	$6.8^{+0.2}_{-0.2}$
05	2011-05-29	10:08:00	10:57:54	10:33:15	2980	M1.4	✓	54.7^{+1}_{-1}	$33.8^{+0.4}_{-0.4}$	$75.7^{+2}_{-1.9}$	$41.9^{+2}_{-1.9}$
06	2011-08-03	13:17:00	14:18:57	13:47:56	3701	M6.0	✓	$57.4^{+0.8}_{-0.7}$	$42.4^{+0.5}_{-0.5}$	$72.4^{+1.4}_{-1.4}$	$30^{+1.5}_{-1.5}$
07	2011-09-07	22:32:00	22:43:52	22:38:44	709	X1.8	✓	$14.9^{+0.3}_{-0.3}$	$11^{+0.2}_{-0.2}$	$18.8^{+0.5}_{-0.5}$	$7.8^{+0.5}_{-0.5}$
08	2011-09-10	07:18:00	08:01:56	07:40:43	2625	M1.1	✓	$28.7^{+0.2}_{-0.2}$	$23.9^{+0.2}_{-0.2}$	$33.5^{+0.4}_{-0.4}$	$9.6^{+0.5}_{-0.5}$
09	2011-09-23	23:48:00	00:03:54 *	23:55:41	950	M1.9	✓	$12.3^{+0.1}_{-0.1}$	$11.6^{+0.1}_{-0.1}$	$13^{+0.2}_{-0.2}$	$1.4^{+0.2}_{-0.2}$ †
10	2011-09-24	17:19:00	17:30:55	17:25:33	713	M3.1		$13.2^{+0.2}_{-0.2}$	$10.7^{+0.2}_{-0.2}$	$15.7^{+0.4}_{-0.3}$	$5^{+0.4}_{-0.4}$
11	2011-09-25	09:25:00	09:44:54	09:35:56	1190	M1.5	✓	$16.1^{+0.2}_{-0.2}$	$18.4^{+0.3}_{-0.3}$	$13.8^{+0.2}_{-0.2}$	$-4.6^{+0.3}_{-0.3}$
12	2011-10-01	08:56:00	11:01:52	09:59:21	7516	M1.2	✓	$48.4^{+0.5}_{-0.5}$	13.9^{+0}_{-0}	$82.9^{+0.9}_{-0.9}$	$68.9^{+0.9}_{-0.9}$
13	2011-11-05	20:31:00	20:44:53	20:38:34	832	M1.8		$12.6^{+0.1}_{-0.1}$	$12.4^{+0.2}_{-0.2}$	$12.8^{+0.2}_{-0.2}$	$0.4^{+0.3}_{-0.3}$ †
14	2012-01-17	04:41:00	05:04:56	04:53:40	1431	M1.0		$12.1^{+0.1}_{-0.1}$	$14.6^{+0.2}_{-0.1}$	$9.5^{+0.1}_{-0.1}$	$-5.1^{+0.2}_{-0.2}$
15	2012-01-19	13:44:00	18:25:54	16:03:17	16834	M3.2	✓	$127.9^{+1.1}_{-1.1}$	$190.7^{+2.2}_{-2.1}$	$65^{+0.3}_{-0.2}$	$-125.8^{+2.2}_{-2.2}$
16	2012-03-02	17:29:00	18:02:55	17:46:26	2026	M3.3	✓	$33.4^{+0.4}_{-0.4}$	$31.1^{+0.5}_{-0.5}$	$35.6^{+0.6}_{-0.6}$	$4.5^{+0.8}_{-0.8}$
17	2012-03-05	02:30:00	05:47:56	04:08:34	11820	X1.1		$105.3^{+1.2}_{-1.1}$	$45^{+0.2}_{-0.2}$	$165.6^{+2.4}_{-2.3}$	$120.6^{+2.4}_{-2.3}$

Table A1 continued from previous page

Num	**Date**	**T**$_{start}$	**T**$_{end}$	**T**$_{peak}$	**Duration** (seconds)	**GOES class**	**CME**	**Per**$_{Avg}$ (seconds)	**Per**$_{Impulsive}$ (seconds)	**Per**$_{Decay}$ (seconds)	**Period drift** (seconds)
18	2012-03-07	01:05:00	01:22:47	01:15:25	1056	X1.3	✓	$27.1^{+0.9}_{-0.8}$	$12^{+0.1}_{-0.1}$	$42.2^{+1.8}_{-1.6}$	$30.2^{+1.8}_{-1.6}$
19	2012-03-09	03:22:00	04:23:53	03:53:19	3697	M6.3	✓	$34.3^{+0.5}_{-0.5}$	9.1^{+0}_{-0}	$59.5^{+1}_{-0.9}$	$50.4^{+1}_{-0.9}$
20	2012-03-10	17:15:00	18:12:52	17:43:55	3456	M8.4	✓	$47.7^{+0.9}_{-0.8}$	$18.5^{+0.1}_{-0.1}$	$76.8^{+1.7}_{-1.7}$	$58.3^{+1.7}_{-1.7}$
21	2012-05-06	01:12:00	01:23:55	01:18:05	713	M1.1		$13.3^{+0.2}_{-0.2}$	$14.3^{+0.3}_{-0.3}$	$12.2^{+0.2}_{-0.2}$	$-2.1^{+0.4}_{-0.3}$ †
22	2012-05-07	14:03:00	14:58:53	14:31:18	3338	M1.9	✓	$76.8^{+1.4}_{-1.3}$	$64.1^{+1.3}_{-1.2}$	$89.4^{+2.5}_{-2.3}$	$25.4^{+2.8}_{-2.6}$
23	2012-05-09	21:01:00	21:08:53	21:05:22	473	M4.1		$12.3^{+0.3}_{-0.2}$	$14.3^{+0.4}_{-0.4}$	$10.3^{+0.2}_{-0.2}$	$-4^{+0.5}_{-0.5}$ †
24	2012-05-10	04:11:00	04:24:54	04:17:50	832	M5.7	✓	$16.3^{+0.2}_{-0.2}$	$16.1^{+0.3}_{-0.3}$	$16.6^{+0.3}_{-0.3}$	$0.5^{+0.5}_{-0.4}$ †
25	2012-07-19	04:17:00	07:38:55	05:57:51	12057	M7.7	✓	$102.3^{+1}_{-0.9}$	$53.5^{+0.2}_{-0.2}$	$151.1^{+1.9}_{-1.9}$	$97.6^{+1.9}_{-1.9}$
26	2012-07-30	15:39:00	15:56:55	15:48:28	1072	M1.1		$16.9^{+0.3}_{-0.3}$	$10.3^{+0.1}_{-0.1}$	$23.5^{+0.5}_{-0.5}$	$13.2^{+0.5}_{-0.5}$
27	2012-08-11	11:55:00	12:44:54	12:19:52	2980	M1.0	✓	12.3^{+0}_{-0}	$15.7^{+0.1}_{-0.1}$	8.9^{+0}_{-0}	$-6.8^{+0.1}_{-0.1}$
28	2012-08-30	12:02:00	12:19:55	12:11:36	1072	M1.3		$14.2^{+0.1}_{-0.1}$	$15.3^{+0.2}_{-0.2}$	$13.1^{+0.2}_{-0.2}$	$-2.2^{+0.3}_{-0.3}$ †
29	2012-09-30	04:27:00	04:38:52	04:33:01	709	M1.3		$10.9^{+0.1}_{-0.1}$	$8.6^{+0.1}_{-0.1}$	$13.2^{+0.2}_{-0.2}$	$4.5^{+0.3}_{-0.3}$
30	2012-10-08	11:05:00	11:28:53	11:16:56	1427	M2.3		$12.8^{+0.1}_{-0.1}$	$14.6^{+0.2}_{-0.1}$	$10.9^{+0.1}_{-0.1}$	$-3.7^{+0.2}_{-0.2}$ †
31	2012-11-27	15:52:00	16:01:53	15:57:35	591	M1.6		$11.1^{+0.2}_{-0.1}$	$10.3^{+0.2}_{-0.2}$	$12^{+0.2}_{-0.2}$	$1.8^{+0.3}_{-0.3}$ †
32	2013-05-03	17:24:00	17:39:53	17:32:13	950	M5.7	✓	$23.1^{+0.6}_{-0.5}$	$14.2^{+0.2}_{-0.2}$	$32^{+1.1}_{-1}$	$17.8^{+1.1}_{-1.1}$
33	2013-06-05	08:14:00	09:39:55	08:57:28	5132	M1.3	✓	$72.9^{+1.3}_{-1.2}$	$33.2^{+0.2}_{-0.2}$	$112.5^{+2.5}_{-2.4}$	$79.3^{+2.5}_{-2.4}$
34	2013-08-17	18:49:00	20:16:55	19:33:47	5250	M1.4		$44.7^{+0.3}_{-0.3}$	$48.8^{+0.5}_{-0.4}$	$40.6^{+0.3}_{-0.3}$	$-8.2^{+0.6}_{-0.5}$
35	2013-10-13	00:12:00	01:13:54	00:43:36	3697	M1.7	✓	$20.8^{+0.1}_{-0.1}$	$20^{+0.1}_{-0.1}$	$21.6^{+0.1}_{-0.1}$	$1.6^{+0.2}_{-0.2}$ †
36	2013-10-17	15:09:00	16:12:53	15:41:00	3815	M1.2		$36.9^{+0.4}_{-0.4}$	$55.4^{+0.8}_{-0.8}$	$18.4^{+0.1}_{-0.1}$	$-37^{+0.8}_{-0.8}$
37	2013-10-28	01:41:00	02:24:53	02:02:57	2621	X1.0	✓	$16.7^{+0.1}_{-0.1}$	$17.5^{+0.1}_{-0.1}$	$16^{+0.1}_{-0.1}$	$-1.5^{+0.2}_{-0.2}$ †
38	2013-10-29	21:42:00	22:05:53	21:54:30	1427	X2.3	✓	$32.8^{+0.6}_{-0.5}$	$30.7^{+0.7}_{-0.6}$	$34.9^{+0.9}_{-0.8}$	$4.3^{+1.1}_{-1.1}$

Table A1 continued from previous page

Num	**Date**	**T**$_{start}$	**T**$_{end}$	**T**$_{peak}$	**Duration** (seconds)	**GOES class**	**CME**	**Per**$_{Avg}$ (seconds)	**Per**$_{Impulsive}$ (seconds)	**Per**$_{Decay}$ (seconds)	**Period drift** (seconds)
39	2013-11-05	18:08:00	18:17:56	18:12:57	595	M1.0		$12.5^{+0.2}_{-0.2}$	$8.8^{+0.1}_{-0.1}$	$16.2^{+0.5}_{-0.4}$	$7.4^{+0.5}_{-0.4}$
40	2013-11-21	10:52:00	11:29:55	11:11:07	2266	M1.2	✓	$49.1^{+0.8}_{-0.8}$	$43.3^{+0.8}_{-0.8}$	$54.9^{+1.4}_{-1.3}$	$11.6^{+1.6}_{-1.5}$
41	2013-12-07	07:17:00	07:40:53	07:29:41	1427	M1.2	✓	$13.8^{+0.1}_{-0.1}$	$9.9^{+0.1}_{-0.1}$	$17.7^{+0.2}_{-0.2}$	$7.7^{+0.2}_{-0.2}$
42	2013-12-31	21:45:00	22:10:56	21:58:07	1549	M6.4	✓	$26.3^{+0.3}_{-0.3}$	$24.9^{+0.4}_{-0.4}$	$27.7^{+0.5}_{-0.5}$	$2.8^{+0.6}_{-0.6}$ †
43	2014-01-01	18:40:00	19:04:10	18:52:03	1431	M9.9	✓	$14.1^{+0.1}_{-0.1}$	$19.7^{+0.3}_{-0.3}$	$8.5^{+0.1}_{-0}$	$-11.3^{+0.3}_{-0.3}$
44	2014-01-08	03:39:00	03:54:54	03:47:45	950	M3.6	✓	$18^{+0.3}_{-0.3}$	$15.1^{+0.2}_{-0.2}$	$20.9^{+0.5}_{-0.5}$	$5.8^{+0.5}_{-0.5}$
45	2014-01-30	07:54:00	08:28:17	08:10:51	1969	M1.1	✓	$20.6^{+0.3}_{-0.2}$	9.8^{+0}_{-0}	$31.3^{+0.5}_{-0.5}$	$21.5^{+0.5}_{-0.5}$
46	2014-02-11	16:34:00	17:07:54	16:51:43	2026	M1.8		$31.2^{+0.4}_{-0.4}$	$26.1^{+0.3}_{-0.3}$	$36.3^{+0.7}_{-0.6}$	$10.2^{+0.7}_{-0.7}$
47	2014-02-24	11:03:00	11:31:20	11:17:07	1667	M1.2	✓	$32.2^{+1}_{-0.9}$	$55.5^{+1.9}_{-1.8}$	8.8^{+0}_{-0}	$-46.6^{+1.9}_{-1.8}$
48	2014-03-10	04:02:00	04:13:55	04:08:17	713	M1.0		$11.7^{+0.2}_{-0.2}$	$8.4^{+0.1}_{-0.1}$	$15^{+0.3}_{-0.3}$	$6.6^{+0.3}_{-0.3}$
49	2014-03-12	10:55:00	11:14:54	11:05:09	1190	M2.5		$12.7^{+0.1}_{-0.1}$	$9.2^{+0.1}_{-0.1}$	$16.3^{+0.2}_{-0.2}$	$7.1^{+0.2}_{-0.2}$
50	2014-04-18	12:31:00	13:34:52	13:02:58	3815	M7.3	✓	$42.9^{+0.5}_{-0.5}$	$23.8^{+0.1}_{-0.1}$	62.1^{+1}_{-1}	38.2^{+1}_{-1}
51	2014-05-07	16:07:00	16:50:56	16:29:08	2625	M1.2	✓	$41.1^{+0.9}_{-0.8}$	$15.2^{+0.1}_{-0.1}$	$66.9^{+1.8}_{-1.7}$	$51.8^{+1.8}_{-1.7}$
52	2014-06-12	04:14:00	04:27:55	04:21:17	832	M2.0	✓	$11.8^{+0.1}_{-0.1}$	$11.6^{+0.2}_{-0.2}$	$12.1^{+0.2}_{-0.2}$	$0.6^{+0.2}_{-0.2}$ †
53	2014-06-12	18:03:00	18:22:54	18:13:54	1190	M1.3		$14.7^{+0.1}_{-0.1}$	$12.3^{+0.1}_{-0.1}$	$17^{+0.2}_{-0.2}$	$4.6^{+0.3}_{-0.3}$
54	2014-06-15	11:10:00	12:07:53	11:39:34	3456	M1.1		$28.7^{+0.3}_{-0.3}$	10.2^{+0}_{-0}	$47.2^{+0.7}_{-0.6}$	$37^{+0.7}_{-0.6}$
55	2014-07-10	22:29:00	22:38:56	22:34:15	595	M1.5		$10.4^{+0.1}_{-0.1}$	$10.3^{+0.2}_{-0.2}$	$10.5^{+0.2}_{-0.2}$	$0.2^{+0.3}_{-0.3}$ †
56	2014-08-21	13:19:00	13:42:53	13:31:41	1427	M3.4	✓	$37.2^{+0.8}_{-0.8}$	$27.6^{+0.5}_{-0.5}$	$46.7^{+1.6}_{-1.5}$	$19.1^{+1.7}_{-1.6}$
57	2014-08-25	20:06:00	20:35:56	20:20:50	1789	M3.9	✓	$28^{+0.4}_{-0.4}$	$20.8^{+0.2}_{-0.2}$	$35.3^{+0.7}_{-0.7}$	$14.5^{+0.8}_{-0.7}$
58	2014-09-03	13:20:00	14:27:55	13:54:11	4056	M2.5	✓	$37.2^{+0.3}_{-0.3}$	$49.1^{+0.6}_{-0.6}$	$25.2^{+0.2}_{-0.2}$	$-23.8^{+0.6}_{-0.6}$
59	2014-09-10	17:21:00	18:08:55	17:45:10	2861	X1.6	✓	$56.7^{+1.1}_{-1}$	$36.5^{+0.5}_{-0.5}$	$77^{+2.1}_{-2}$	$40.5^{+2.2}_{-2.1}$

Table A1 continued from previous page

Num	**Date**	**T**$_{start}$	**T**$_{end}$	**T**$_{peak}$	**Duration** (seconds)	**GOES class**	**CME**	**Per**$_{Avg}$ (seconds)	**Per**$_{Impulsive}$ (seconds)	**Per**$_{Decay}$ (seconds)	**Period drift** (seconds)
60	2014-10-09	01:30:00	01:55:55	01:43:23	1549	M1.3		$59.7^{+3.3}_{-2.9}$	$98.5^{+6.7}_{-5.9}$	$20.9^{+0.3}_{-0.3}$	$-77.6^{+6.7}_{-5.9}$
61	2014-11-03	11:23:00	12:22:54	11:53:30	3579	M2.2		$44.1^{+0.5}_{-0.5}$	$31^{+0.3}_{-0.3}$	$57.2^{+0.9}_{-0.9}$	$26.2^{+1}_{-0.9}$
62	2014-11-04	07:59:00	09:16:53	08:38:41	4651	M2.6	✓	$28.7^{+0.1}_{-0.1}$	$23.6^{+0.1}_{-0.1}$	$33.8^{+0.2}_{-0.2}$	$10.2^{+0.3}_{-0.3}$
63	2014-11-05	18:50:00	20:37:54	19:44:38	6444	M2.9	✓	$56.1^{+0.5}_{-0.5}$	$30.3^{+0.1}_{-0.1}$	$81.8^{+1.1}_{-1}$	$51.4^{+1.1}_{-1}$
64	2014-11-06	01:29:00	01:48:54	01:39:21	1190	M3.2		$19^{+0.2}_{-0.2}$	$17.4^{+0.3}_{-0.3}$	$20.7^{+0.4}_{-0.4}$	$3.2^{+0.4}_{-0.4}$ †
65	2014-11-06	21:53:00	22:38:49	22:16:01	2731	M2.5		$23.6^{+0.2}_{-0.2}$	$18.3^{+0.1}_{-0.1}$	$28.8^{+0.3}_{-0.3}$	$10.5^{+0.3}_{-0.3}$
66	2014-11-07	10:13:00	10:30:56	10:22:15	1072	M1.0		$17.1^{+0.2}_{-0.2}$	$14.7^{+0.2}_{-0.2}$	$19.5^{+0.4}_{-0.3}$	$4.8^{+0.4}_{-0.4}$
67	2014-11-15	11:40:00	12:25:55	12:03:21	2743	M3.2		$28.7^{+0.2}_{-0.2}$	$25.9^{+0.2}_{-0.2}$	$31.4^{+0.4}_{-0.4}$	$5.5^{+0.4}_{-0.4}$
68	2014-12-17	04:25:00	05:16:55	04:50:06	3102	M8.7	✓	$64^{+1}_{-0.9}$	$56.8^{+1.1}_{-1}$	$71.2^{+1.7}_{-1.6}$	$14.3^{+2}_{-1.9}$
69	2014-12-18	21:41:00	22:14:55	21:58:03	2026	M6.9		$29^{+0.3}_{-0.3}$	$22.8^{+0.3}_{-0.3}$	$35.2^{+0.6}_{-0.6}$	$12.4^{+0.7}_{-0.7}$
70	2014-12-20	00:11:00	00:44:55	00:28:00	2026	X1.8	✓	$21.3^{+0.3}_{-0.2}$	$10.6^{+0.1}_{-0.1}$	$31.9^{+0.5}_{-0.5}$	$21.2^{+0.5}_{-0.5}$
71	2015-03-02	15:10:00	15:45:56	15:28:16	2148	M3.7	✓	$41.1^{+0.6}_{-0.6}$	$48.9^{+1.1}_{-1.1}$	$33.3^{+0.5}_{-0.5}$	$-15.6^{+1.3}_{-1.2}$
72	2015-03-06	04:14:00	05:39:54	04:57:36	5132	M3.0	✓	$82.3^{+1.1}_{-1}$	$65.8^{+0.9}_{-0.8}$	$98.7^{+1.9}_{-1.9}$	$32.9^{+2.1}_{-2}$
73	2015-03-09	14:22:00	14:43:57	14:33:45	1312	M4.5		$11.9^{+0.1}_{-0.1}$	$14.1^{+0.2}_{-0.2}$	$9.8^{+0.1}_{-0.1}$	$-4.4^{+0.2}_{-0.2}$
74	2015-03-09	23:29:00	00:16:54 *	23:54:17	2861	M5.8	✓	$51.1^{+0.8}_{-0.8}$	$36.3^{+0.5}_{-0.5}$	$66^{+1.6}_{-1.5}$	$29.7^{+1.6}_{-1.6}$
75	2015-03-11	16:11:00	16:32:54	16:21:38	1308	X2.1	✓	$22.3^{+0.4}_{-0.4}$	$13.3^{+0.1}_{-0.1}$	$31.3^{+0.8}_{-0.7}$	$18^{+0.8}_{-0.7}$
76	2015-03-12	04:41:00	04:50:53	04:46:00	591	M3.2		$11.4^{+0.2}_{-0.2}$	$8.4^{+0.1}_{-0.1}$	$14.3^{+0.4}_{-0.3}$	$5.9^{+0.4}_{-0.4}$
77	2015-03-12	11:38:00	12:01:53	11:50:26	1427	M1.6		$21.3^{+0.3}_{-0.3}$	$15.9^{+0.2}_{-0.2}$	$26.7^{+0.5}_{-0.5}$	$10.8^{+0.5}_{-0.5}$
78	2015-03-12	12:09:00	12:18:53	12:14:23	591	M1.4		$17.1^{+0.4}_{-0.4}$	$21.1^{+0.8}_{-0.7}$	$13.2^{+0.3}_{-0.3}$	$-7.9^{+0.8}_{-0.8}$
79	2015-03-12	13:50:00	14:25:53	14:08:39	2144	M4.2		$14.5^{+0.1}_{-0.1}$	$13.1^{+0.1}_{-0.1}$	$16^{+0.1}_{-0.1}$	$2.9^{+0.1}_{-0.1}$ †
80	2015-03-13	03:47:00	04:14:54	04:01:49	1667	M1.2		$33.7^{+0.6}_{-0.6}$	$22.4^{+0.3}_{-0.3}$	$44.9^{+1.2}_{-1.2}$	$22.6^{+1.3}_{-1.2}$

Table A1 continued from previous page

Num	**Date**	**T**$_{start}$	**T**$_{end}$	**T**$_{peak}$	**Duration** (seconds)	**GOES class**	**CME**	**Per**$_{Avg}$ (seconds)	**Per**$_{Impulsive}$ (seconds)	**Per**$_{Decay}$ (seconds)	**Period drift** (seconds)
81	2015-03-16	10:39:00	11:16:53	10:57:59	2262	M1.6		$27^{+0.3}_{-0.3}$	$18.3^{+0.1}_{-0.1}$	$35.6^{+0.6}_{-0.6}$	$17.3^{+0.6}_{-0.6}$
82	2015-03-17	22:49:00	23:59:55	23:34:48	4235	M1.0	✓	$14.8^{+0.1}_{-0.1}$	8.7^{+0}_{-0}	$20.9^{+0.1}_{-0.1}$	$12.1^{+0.1}_{-0.1}$
83	2015-04-21	07:08:00	07:33:54	07:20:48	1549	M1.0		$19.1^{+0.2}_{-0.2}$	$15.7^{+0.2}_{-0.2}$	$22.5^{+0.3}_{-0.3}$	$6.8^{+0.4}_{-0.4}$
84	2015-06-21	02:04:00	03:03:32	02:36:26	3534	M2.7	✓	$86.9^{+1.6}_{-1.5}$	$76.4^{+1.7}_{-1.6}$	$97.4^{+2.8}_{-2.6}$	$21^{+3.2}_{-3.1}$
85	2015-06-21	02:06:00	03:05:51	02:36:45	3571	M2.6	✓	$84.8^{+1.5}_{-1.4}$	$75.4^{+1.6}_{-1.6}$	$94.1^{+2.5}_{-2.4}$	$18.7^{+3}_{-2.9}$
86	2015-06-22	17:39:00	19:06:55	18:24:42	5250	M6.5	✓	$20.2^{+0.1}_{-0.1}$	$21.2^{+0.1}_{-0.1}$	$19.2^{+0.1}_{-0.1}$	$-1.9^{+0.1}_{-0.1}$ †
87	2015-09-20	17:32:00	18:33:53	18:01:50	3697	M2.1	✓	$81.9^{+1.4}_{-1.3}$	$70.2^{+1.4}_{-1.3}$	$93.6^{+2.4}_{-2.3}$	$23.4^{+2.8}_{-2.7}$
88	2015-09-28	07:27:00	07:42:53	07:34:42	950	M1.1		$13.5^{+0.1}_{-0.1}$	$13.8^{+0.2}_{-0.2}$	$13.3^{+0.2}_{-0.2}$	$-0.5^{+0.3}_{-0.3}$ †
89	2015-10-02	17:08:00	17:27:54	17:18:27	1190	M1.0		$13.1^{+0.1}_{-0.1}$	$9.5^{+0.1}_{-0.1}$	$16.7^{+0.2}_{-0.2}$	$7.3^{+0.3}_{-0.2}$
90	2015-10-15	23:27:00	23:34:55	23:31:49	473	M1.1		$11.2^{+0.2}_{-0.2}$	$11.8^{+0.3}_{-0.3}$	$10.7^{+0.2}_{-0.2}$	$-1^{+0.4}_{-0.4}$ †
91	2015-10-16	06:11:00	06:20:53	06:16:31	591	M1.1		$18.7^{+0.5}_{-0.5}$	$23.1^{+0.9}_{-0.9}$	$14.2^{+0.4}_{-0.3}$	$-8.9^{+1}_{-0.9}$
92	2015-10-17	20:09:00	20:36:54	20:22:58	1667	M1.1		$18.7^{+0.2}_{-0.2}$	$9.3^{+0.1}_{-0.1}$	$28.1^{+0.5}_{-0.5}$	$18.7^{+0.5}_{-0.5}$
93	2015-11-04	11:55:00	12:10:56	12:03:17	954	M2.5		$13.1^{+0.1}_{-0.1}$	$10.8^{+0.1}_{-0.1}$	$15.4^{+0.3}_{-0.2}$	$4.6^{+0.3}_{-0.3}$
94	2015-12-21	00:52:00	01:13:57	01:03:04	1312	M2.8		$21.2^{+0.3}_{-0.3}$	$14.8^{+0.2}_{-0.2}$	$27.7^{+0.6}_{-0.6}$	$12.8^{+0.6}_{-0.6}$
95	2015-12-22	03:15:00	03:52:55	03:34:19	2266	M1.6		$32.3^{+0.4}_{-0.3}$	$27.1^{+0.3}_{-0.3}$	$37.4^{+0.6}_{-0.6}$	$10.4^{+0.7}_{-0.7}$
96	2015-12-23	00:23:00	00:56:54	00:40:46	2026	M4.7	✓	$38.1^{+0.6}_{-0.6}$	$29.1^{+0.4}_{-0.4}$	$47.1^{+1.1}_{-1.1}$	$18^{+1.2}_{-1.1}$
97	2016-07-23	05:00:00	05:31:52	05:16:43	1903	M7.6	✓	$20.9^{+0.2}_{-0.2}$	$17.3^{+0.2}_{-0.2}$	$24.6^{+0.3}_{-0.3}$	$7.3^{+0.4}_{-0.3}$
98	2017-04-02	07:50:00	08:13:56	08:02:56	1431	M5.3	✓	$22.6^{+0.3}_{-0.3}$	$19.5^{+0.3}_{-0.3}$	$25.7^{+0.5}_{-0.5}$	$6.1^{+0.5}_{-0.5}$

* indicates that the flaring event took place over midnight, so the end time of the flare occurs on the subsequent day to the Date indicated.

† indicates that the period drift is smaller in magnitude than 4.09 seconds (twice the data cadence) and therefore the QPP is deemed to exhibit no period drift in this study.